Alkali activated slag-fly ash binders: design, modeling and application

Xu Gao

/ Department of the Built Environment

bouwstenen 236

Alkali activated slag-fly ash binders: design, modeling and application

Xu Gao

De promotiecommissie is als volgt samengesteld:

Voorzitter:	
prof.ir. E.S.M. Nelissen	Technische Universiteit Eindhoven
1st supervisor/promotor:	
prof.dr.ir. H.J.H. Brouwers	Technische Universiteit Eindhoven
Co-supervisor:	
dr.ir. Q. Yu	Technische Universiteit Eindhoven
Leden:	
prof.dr. Z.H. Shui	Wuhan University of Technology
prof.dr. J.L. Provis	The University of Sheffield
prof.dr.ir. D.M.J. Smeulders	Technische Universiteit Eindhoven
prof.dr.dr. H. Pöllmann	Martin Luther Universität Halle Wittenberg
prof.dr. H. Justnes	Norwegian University of Science and Techonology

Technische Universiteit Eindhoven University of Technology

CIP-DATA LIBRARY TECHNISCHE UNIVERSITEIT EINDHOVEN

Alkali activated slag-fly ash binders: design, modeling and application / by Xu Gao.

ISBN 978-90-386-4422-6

Bouwstenen 236

NUR 955

Ph.D. Thesis, Eindhoven University of Technology, the Netherlands

Cover design: Xu Gao

Alkali activated slag-fly ash binders: design, modeling and application

PROEFSCHRIFT

ter verkrijging van de graad van doctor aan de
Technische Universiteit Eindhoven, op gezag van de
rector magnificus, prof.dr.ir. F.P.T. Baaijens, voor een
commissie aangewezen door het College voor
Promoties in het openbaar te verdedigen
op maandag 11 december 2017 om 14.00 uur

door

Xu Gao

geboren te Wuhan, China

Dit proefschrift is goedgekeurd door de promotor:

prof.dr.ir. H.J.H. Brouwers

Dedicated to:

Lovely parents: ZhiGang Gao, LiPing Xu
Teachers in life

Preface

Everytime when I recall my memory of the first arrival in the Netherlands, it was just like yesterday. The train was about to took me from Schiphol airport to Eindhoven, but it stopped in the middle, leaving me alone in a unknown small town for two hours with whipping winds. Finally I arrived safe and sound, then settled down. This experience is pretty like the process of my PhD study: with expectations at the beginning, go through some difficulties in the middle, and eventurally a happy ending. At the end of my PhD study, I suddenly realized that my personal skills were improved unconsciously, by the accumulation of every effort that was made, every minute that was spend on study. Then I noticed that as long as someone has the willingness to improve and put it into practice, he can reach his goal sooner or later. There were of course difficulties, frustrations, and unhappiness during the PhD study, but working and living in a lovely west country are for sure a lifetime memorable experience with mostly happyness.

I would like to firstly express my gratitude to both my master supervisor and the present supervisor, prof.dr.ir. Zhonghe Shui and prof.dr.ir. Jos Brouwers. Thank you for the “prepaid” trust of suggesting me to study abroad and accept me as a PhD student, respectively. Then I would like to thank prof.dr.ir. Jos Brouwers and dr.ir. QingLiang Yu for the supervision during the PhD study, for all your valuable guidance, suggestions, and patience that spend on me. I would never go this far without your kind carings. I also appreciate the financial and technical support from China Scholarship Council and Eindhoven University of Technology, as well as the cooperation of following company: Graniet-Import Benelux; Enci; Struyk Verwo and Inashco. I also would like to express my special thanks to prof.dr. FaZhou Wang and prof.dr. Wei Chen, from the State Key Laboratory of Silicate Materials for Architectures, Wuhan University of Technology, PR China, for the use of NMR instrument; and friend LiHua Shen from TU Eindhoven for his tremendous but anonymous support.

Further I wish to express my gratitude to the technicians and colleagues, who helped and gave me great support during the past four years; I really enjoyed working with you. You always give me sufficient and warm support when nessesary. The research group also experienced a great development and expansion during the past years. The graduates of the first generations already become irreplaceable persons in their position. And the second generations are about to or just start their careers. University is the place students keep coming and leaving, but the research group and the supervisor will be our bond forever. Eventually, I would like to express my appreciation to all the individuals that in any kind of form, either helped or frustrated, but finally enlightened me in my life.

Xu Gao

Eindhoven, September 2017

Contents

Chapter 1

Introduction

1.1 General introduction

Environmental impacts of cement industry

The cement industry is one of the most CO_2 production sectors around the world, nearly 21 billion tons of concrete are used and more than 4.6 billion tons of Portland cement are produced each year (USGS, 2017). Within the cement industry, the primary cause of CO_2 emission comes from the manufacturing process of ordinary Portland cement (OPC). Actually around 0.8 tons of CO_2 are emitted to the atmosphere with the manufacture of 1 ton of cement. According to the statistics, the cement industry should be responsible for about 7% of the total CO_2 emissions in the world (Palomo et al, 2007). Moreover, the production of cement has a tendency to increase with an annual increasing rate of nearly 3% (Rangan and Hardjto, 2005). The global demand for Portland cement would have increased almost 200% by 2050 from 2010 (Taylor, 2006).
The cement industry also emits other toxic gases like SO_3 and NO_x, which can cause the environmental problems such as greenhouse effect and acid rain (Anand et al, 2006). Climate changes caused by CO_2 emissions can lead to the rise of sea level and the occurrence of natural disasters. In particular, the energy demand associated with cement production is about 1700 to 1800 MJ/ton clinker (Taylor, 1997), including the calcination of raw materials, the grinding of raw materials, cement clinker and gypsum. The cement production consists about 5% of the total industrial energy costs around the world (Hendriks et al, 2004), it also consumes considerable amounts of raw materials like limestone and clay, approximately 1.5 tons of raw materials is needed when producing each ton of Portland cement (Rashad and Zeedan, 2011). Therefore, from the points of environmental protection and sustainable development of the cement industry, it is highly necessary to reduce those negative impacts.

Alkali activated materials as alternative binders

In order to reduce the environmental impacts and high energy consumptions of cement industry, approaches have been carried out on finding alternatives to ordinary Portland cement. Among those investigations, alkali activated materials have attracted great attention in recent years. In terms of the energy cost and environmental impacts, alkali activated materials are reported to generate nearly 80% less CO_2 than Portland cement (Duxson and Van Deventer, 2009).

Moreover, the global warming potential of alkali activated concrete is 70% lower than Portland cement concrete. In terms of the mortar and concrete performances, using alkali activated materials show various advantages. For instance, the heat released during the hydration process is reported to be lower than Portland cement (Chen and Brouwers, 2007), the mechanical properties are generally higher than cement based materials, especially the early strength development (Bakharev et al, 1999), excellent durabilities also reported like better resistance of sulfate and acid attack, improved freeze-thaw resistance due to the refined pore structure, significantly higher fire resistance (Rashad et al, 2012), higher resistance of chloride permeation (Roy et al, 2000), improved interface transition zones between aggregate and matrix (Shi and Xie, 1998). In overall, alkali activated materials have shown great potential to be an environmentally friendly alternative to ordinary Portland cement with comparable or even better performances. Thus it is promising to apply alkali activated materials to replace Portland cement based materials in various applications.

Development route of alkali activated materials

The development of alkali activated materials can be traced back to the 1895, and Table 1-1 below gives a brief outlook of the historical background about important events in the development of alkali-activated materials.

The first one who uses alkalis as a component in cement based materials is Kuhl in 1930, when he studied the setting of slag by using KOH solution. Since then many studies have been conducted to analyze the role of alkali plays in cementitious systems. The first milestone happened in 1940, when Purdon studied the clinker free cements consisting of slag and sodium hydroxide. An important breakthrough was made by Glukhovsky about the understanding and development of binders containing reactive aluminosilicates and alkaline metal solutions in 1967. These binders are called “soil cements”. The next few years have seen an exponential growth in research, Davidovits produced binders by mixing alkalis with a burnt mix of kaolinite, limestone and dolomite in 1982 (Davidovits, 1984). Geopolymers also generated some trademarks, the most famous one was Pyrament, but alkali activated binders have begun to acquire true technological significance in later ages. From nearly 2000 until now, key researchers such as Palomo, Van Van Deventer, Roy and Provis made some fundamental and systematic studies, and provide a more fundamental science base to this technology. Now the alkali-activation technology is well accepted from the point of science, but still not widely accepted in industry.

It is necessary to note that the term of Alkali activated material (AAM) has a broad classification, actually any binder system includes the reaction of an alkali metal source with a solid silicate powder can be called alkali activated materials (Shi et al, 2006). This solid powder can be calcium and silicate enriched slags or a more aluminosilicates-rich precursors such as metakaolin and fly ash. While the term ‘Geopolymers’ is usually used as a subset of ‘Alkali activated material (AAM)’, where the binding materials are almost exclusively silicate

and aluminum enriched aluminosilicates (Duxson et al, 2005), the available calcium content in the reacting components are usually very low, in order to form a zeolite like network structure (Provis et al, 2005). Low-calcium fly ashes and metakaolins are the most popular raw materials in geopolymer synthesis.

Table 1-1: Bibliographic history of alkali-activated cements (Li et al, 2010)

Author	Year	Significance
Whiting	1895	Slag-soda based cement
Purdon	1940	Alkali-slag combinations
Glukhovsky	1965	First called “alkaline cements”
Davidovits	1979	“Geopolymer” term
Roy	1984	Ancient building materials characterized
Davidovits	1985	Patent of “Pyrament” cement
Wu	1990	Activation of slag cement
Roy	1991	Rapid setting alkali-activated cements
Scivener	1995	Slag and alkali-activated microstructure
Shi	1996	Hardened properties of alkali-activated slag
Fernandez	1997	Kinetic studies of alkali-activated slag cements
Katz	1998	Microstructure of alkali-activated fly ash
Roy	1999	Challenges of alkali-activated cements
Puertas	2000	Alkali-activated fly ash/slag cement
Duxson	2006	Geopolymer technology: the current state of the art
Provis Van Deventer	2009	Geopolymers: structure, processing, properties and industrial applications

The difference between these two classifications is shown in Figure 1-1. It can be easily seen that geopolymers are here as a subset of alkali activated materials, with the highest Al contents and the lowest Ca concentrations. Different shadings indicate the approximately required alkali content to activate the raw material; darker shading means higher concentrations of alkali cations that are needed. Thus it is also possible to simply use the term of ‘Alkali activated

material (AAM)' to describe these types of material instead of geopolymer since the former has a broader meaning.

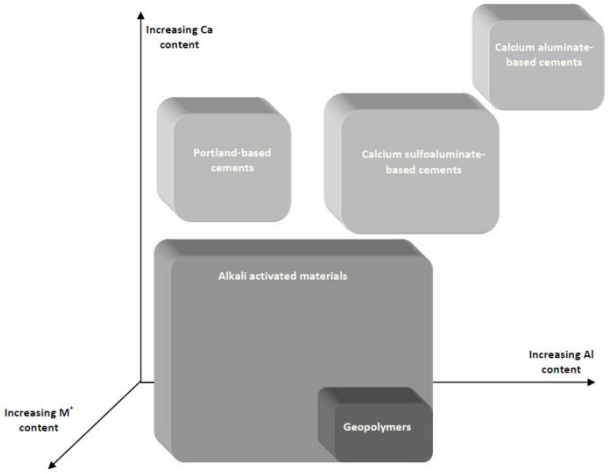

Figure 1-1: Classification of commonly used binders (Provis et al, 2014)

1.2 Alkali activated binders

Two typical binding systems

Theoretically, any raw materials containing reactive silica and aluminum can be used for alkali activation. And alkali activated materials are usually produced by mixing alkaline activator solutions with solid raw materials. Up to now, the most widely studied raw materials are blast furnace slag, class F fly ash (according to ASTM C618, similar to the EU standard of siliceous ash), metakaolin, also some relatively less commonly used ones such as kaolinitic clays, natural pozzolans and red mud. Two typical binding systems can be classified based on the chemical composition and the reaction mechanism of the starting materials: calcium and silica enriched (Ca + Si) system and aluminosilicates dominated (Si + Al) system (Li et al, 2010). The representice precursor of calcium enriched system is ground granulated blast furnace slag (GGBS), and the reaction product is a C-S-H (I) type gel with a lower Ca/Si ratio and a high Al incorporation (Brough and Atkinson, 2002). While the typical starting materials of Si + Al system are class F fly ash or metakaolin, having N-A-S-H type gels with three-dimensional network as the major final product (Granizo et al, 2002). Both systems exhibit distinct behaviors regarding alkaline and curing demands, setting and hardening processes, strength development due to their differences in reaction mechanism and the nature of the gel characteristics.

Alkali activated high calciums

Ground granulated blast furnace slag is a typical and most commonly used high calcium precursor. It contains relatively large amounts of calcium and low contents of aluminum in the glassy phase. The reaction process of slag with activator contains several steps, including the destruction of the raw material at the beginning stage and the condensation of the reaction products at later stages. Figure 1-2 provides an illustration of the dissolution mechanism of glassy Ca-Si particles that similar to the reaction process alkali activated slag. Additional bonds are not shown for clarity. Step A represents that, under the presence of alkalis in solution, the ionic exchange of H^+ with Ca^{2+} and Na^+ between the slag particle surface and the solution at the beginning stage. The removal of Ca^{2+} leads to serious damage of the original glassy structure, also the Na^+ cation, but the influence of divalent cation seems more significant because of the cation size.

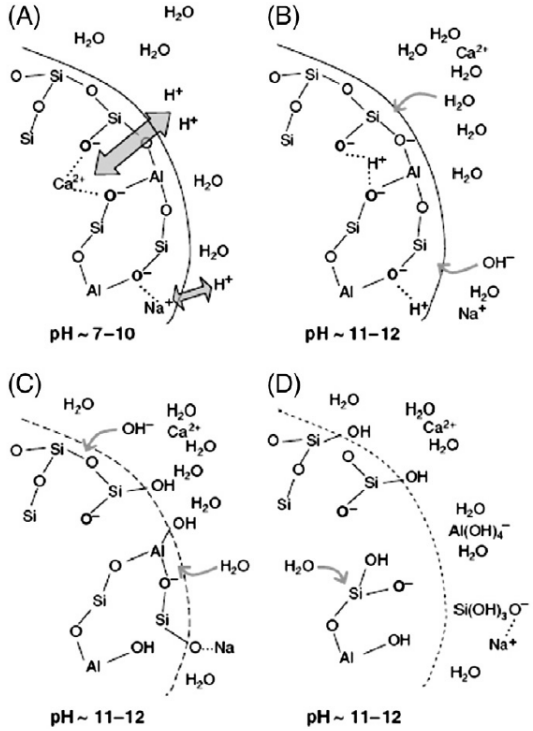

Figure 1-2: Dissolution mechanism of Ca-Si enriched phases (Duxson and Provis, 2008)

Step B represents the hydrolysis of Al-O-Si bonds, the destruction of the original slag bonds such as Ca-O, Mg-O, Si-O-Si, Al-O-Al and Al-O-Si begins after step A. Step C is assigned to

the breakdown of the depolymerized glass network, as many original bonds of the slag are broken, especially the Ca-O and T-O ones, the entire glassy phase begins to destroy. Step D shows the release of Si and Al monomers, then a Si-Al layer begins to form near the surface of slag particle and finally the formation of reaction products.

Other researchers suggested similar reaction mechanisms for activation of slag. For instance, a four step reaction process including the dissolution of the raw material particles, nucleation and growth of the initial products, interactions at the surfaces of the newly formed phases and the ongoing reaction at advanced times of curing (Fernandez et al, 1997); and a similar hydration process as Portland cement including dissolution and precipitation at early stage, and solid state reaction at later ages (Wang and Scrivener, 1995). However, the real case of activation of slag can be much more complicated than the illustrated route shown in the figure above. In short, the alkali activation of blast furnace slag can be summarized as: at the beginning, chemical attack takes place between the alkaline solutions and slag particle surfaces, ionic exchanges also take place between slag and the solution; due to the breaking down of original chemical bonds of T-O, Ca-O and the following dissolution of calcium and Si, Al units from slag particle, original glassy structure of slag begin to breakdown, then reaction products begin to form around slag surfaces or in the solution.

Alkali activated aluminosilicates

Although there are still many differences between fly ash and metakaolin, such as the particle shape and size, chemical composition and glassy type, one important character in common is that the main reactive phase in those materials is amorphous aluminosilicate. Thus researchers generally use the same reaction model to describe the reaction mechanism of fly ash, metakaolin and other silica and aluminum enriched raw materials. A descriptive model of the reaction process of alkali activation of fly ash is proposed and shown in Figure 1-3. The reaction begins with the alkali attack on the glassy shell surface of fly ash, then the reaction products form around the fly ash particle, ending up with final products that contain both fly ash with different reaction degrees and reaction products.

Besides, a general reaction mechanism for alkali activation of reactive aluminosilicate based raw materials is proposed. The reaction process mainly consists of the following parts: destruction, coagulation, condensation and crystallization. This first stage of reaction is the process from destruction of the raw material to coagulation, including the breakdown of the Me-O and T-O bonds in the starting material. The formation of Si-O-Na^+ bonds, which are stable in alkali solutions, making this reaction irreversible and working as the transport tools that is beneficial for the formation of coagulated structure. Similar effect happens on the Al-O-Si bond of starting material, the aluminate forms $Al(OH)_4$ or $Al(OH)_6$ under alkali attack. The second stage refers to the process from coagulation to condensation. The silica and aluminum monomers in the solution after alkali attack start to accumulate forming a coagulated structure,

which means the polycondensation are taking place. The last stage is from condensation to crystallisation, when the solid phases are gradually generated and crystallized.

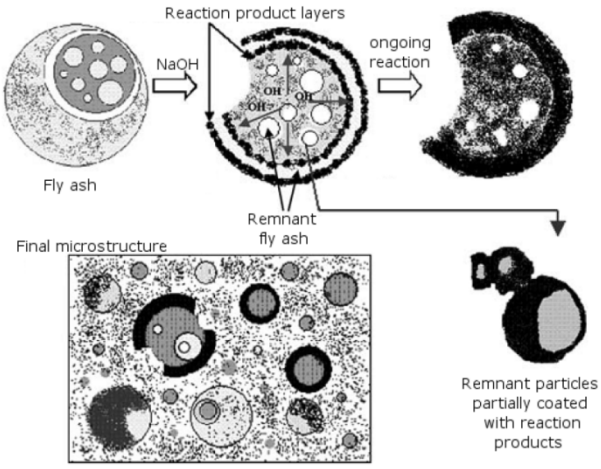

Figure 1-3: Microstructural description of alkali-activated fly ash (Fernandez et al, 2005)

A more detailed picture is provided later. As shown in Figure 1-4 that firstly the raw material dissolves under alkali attack, the aluminates and silicates that are released as monomers, then the smaller molecule monomers accumulate and form larger ones.

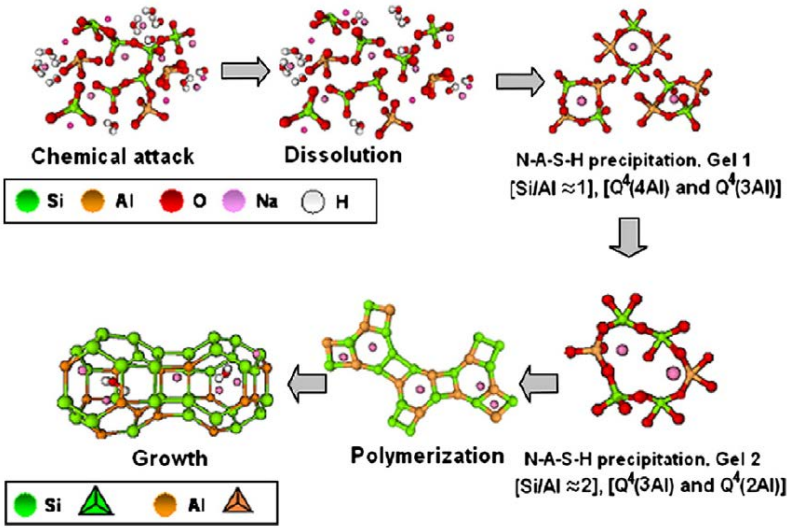

Figure 1-4: Modified descriptive model for activation of aluminosilicates (Shi et al, 2011)

The silicate and aluminate tetrahedral start to bond together to form rings with four tetrahedral units. The Gel 1 formed at early stage with a Si/Al ratio around 1 has relatively high aluminium content because of the Al release in the early hours of the reaction, Al-O bonds are weaker and hence more easily severed than Si-O bonds. As the reaction continues, more silica monomers are dissolved and gel 1 then has the tendency to transform into a more silica enriched gel (Gel 2, the Si/Al ratio is around 2). Afterwards the polymerization process occurs between Gel 2, large molecule reaction products are formed.

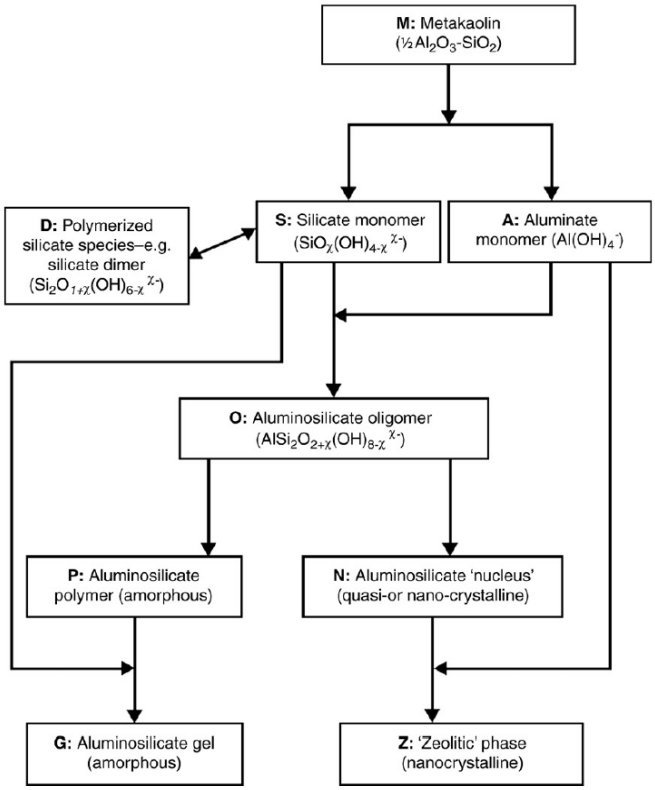

Figure 1-5: Schematic outline of the reaction processes (Provis et al, 2005)

A similar description on the reaction process was made by (Provis et al, 2005): the silicate and aluminate species release into the alkali solution, the 5 and 6 coordinated aluminate are transformed into 4 coordinated ones during the reaction. The release rate of aluminate seems to be faster than the silica, and dissolved aluminate reacts with silicate from the alkali solution to form aluminosilicate oligomers, then the reaction product N-A-S-H gel starts to form, grow and crystallize to form zeolites. Figure 1-5 presents a similar model of the reaction process. This model proposes the dissolution of starting material into aluminate and silicate single units, in concentrated alkali solutions, the silicate can form silicate oligomerization (species D); both

amorphous aluminosilicate gel (product G) and nanocrystallined zeolite phase (phases Z) can be formed as the final products.

Blended binders

The increasing interest has been focused on blended Na_2O-CaO-Al_2O_3-SiO_2 system by mixing Si + Ca and Si + Al type materials, as several improved properties can be resulted. For instance modified setting time (Lee and Lee, 2013), workability (Rashad, 2013; Yang et al, 2008; Collins et al, 1999), shrinkage (Aydin, 2013), mechanical properties (Kumar et al, 2010; Dougas et al, 1990; Shen et al, 2011) and durability (Sugama et al, 2005; Ismail et al, 2012; Guerrieri et al, 2009). Studies were also focused on understanding the gel compatibility and phase composition in the blended system: generally, both coexistence and interactions take place between C-A-S-H and N-A-S-H type gels (Escalante-Garcia et al, 2006). Two typical gels can form simultaneously within one system (Yip et al, 2005); the presence of calcium leads to the formation of C-A-S-H type gels and destroys the N-A-S-H gel structure to some degree by partially replacing sodium with calcium to form (N,C)-A-S-H gels (Garcia et al, 2005; Garcia et al, 2010), while the increased availability of aluminates strongly influences the C-S-H composition and structure (Garcia et al, 2009). In addition, a higher degree of cross-linking within the reaction products is achieved (Ismail et al, 2014). Those investigations in the microstructural understanding provide solid theoretical support for further researches on blended alkali activated system.

Activators

As mentioned before, the alkali activated materials can be synthesized by mixing raw materials and alkaline activators. It is also generally believed that the properties of activators have a decisive influence on the final performance of alkali activated materials. According to the summary from (Glukhovsky, 1980), the alkaline activators can be classified in six groups, where M represents the alkali ion:

(1) Alkalis, MOH.
(2) Weak acid salts, M_2CO_3, M_2SO_3, M_3PO_4, MF.
(3) Silicates, $M_2O + nSiO_3$.
(4) Aluminates, $M_2O + nAl_2O_3$.
(5) Aluminosilicates, $M_2O + Al_2O_3 + (2\text{-}6)SiO_2$.
(6) Strong acid salts, M_2SO_4.

The alkali sources used as activator can include alkali hydroxides, silicates, carbonates, sulfates, aluminates or oxides. Actually any soluble substance which can supply alkali metal cations, increase the pH of the solution and accelerate the dissolution of the solid raw materials can be used as activator. Table 1-2 below gives a short summary from Provis about different raw materials activated by different alkali activators and the compatibility between raw material

and the activator. Here 'Desirable' means the high performance binders and concretes can be synthesized by using this type of activator. 'Good' means good results can still be achieved even the general performance is slightly lower than the most desired ones. 'Acceptable' means the possibility of the formation of valuable alkali-activated binders, but significant drawbacks can be found in terms of strength development, durability, and/or workability. 'Poor' means strength development is generally insufficient. 'With OPC' means that it can only be used with the addition of ordinary Portland cement.

Table 1-2: Summery of activating efficiency of different activators (Provis and Van Deventer, 2013)

	MOH	$M_2O{\cdot}rSiO_2$	M_2CO_3	M_2SO_4	Other
Blast furnace slag	Acceptable	Desirable	Good	Acceptable	--
Fly ash	Desirable	Desirable	Poor	--	$NaAlO_2$ Acceptable
Calcined clays	Acceptable	Desirable	--	--	--
Natural pozzolans	Acceptable	Desirable	--	--	--
Volcanic ashes	Desirable	Desirable	--	--	--
Aluminosilicates	Acceptable	Acceptable	With OPC	With OPC	--
Synthetic glassy precursors	Acceptable or Desirable	Desirable	--	--	--
Steel slag	--	Desirable	--	--	--
Phosphorus slag	--	Desirable	--	--	--
Ferronickel slag	--	Desirable	--	--	--
Red mud	--	Acceptable	--	--	--
Bottom ash solid waste	--	Acceptable	--	--	--

The table also indicates that activator type of $M_2O{\cdot}rSiO_2$ is an ideal activator for most of the raw materials; actually it is commonly accepted as an ideal activator for high performance reaction products in most cases. MOH is efficient in activating low calcium fly ash and other silicate and aluminum enriched materials, but not suitable for high calcium raw materials such as slag. M_2CO_3 is only suitable for activating blast furnace slag because it is less caustic than MOH and can only provide high pH environment slowly, also because the glassy phase of blast

furnace slag is easier to break down compared to fly ash. The alkalinities provided by M_2CO_3 are not strong enough to fully activate low calcium raw materials. Other activators such as M_2SO_4 and $NaAlO_2$ are not commonly used due to the activation efficiency; relatively higher reaction temperature needed and lower final performances.

Similar to the situation of alkali activator type of MOH, there is also a limitation in choosing alkali cations in silicate activator ($M_2O+nSiO_2$) due to the cost and availability. The silicates of sodium and potassium are more practical in large scale production. Actually at present, the activator of $Na_2O+nSiO_2$ is the most commonly used one. Thus all mentioned silicate activators in this report are $Na_2O+nSiO_2$.

The activating solutions used in alkali activated systems are generally in the range of 1-10 M for MOH and 1-10 M for SiO_2, most of the silicate sites in the alkaline solution will be deprotonated to some degree due to different SiO_2/M_2O ratios. The deprotonating process will lead to a change in the respective pK_a values in the solution, the values obtained are given here in Table 1-3. Most silicate activators used in alkali activated systems are having a pH of about 11-12 mainly due to the silicate deprotonation equilibria. Due to the buffering effect to provide a ready source of basic species, the solution can provide a higher level of available alkalinity compared to hydroxide solutions at the same pH. Also when the reaction comes to the end, the pH will increase again because of the deprotonating equilibrium. This effect partly explains why silicate activators are the most accepted ones: because of the deprotonation equilibria, a constant high pH environment and soluble silica source can be guaranteed during the reaction process, then the reactions between raw material and activator continue rather than one time reaction, thus a more homogeneous reaction process and higher reaction degree of raw materials will take place.

Table 1-3: Equilibrium constants for deprotonations (Rimer et al, 2005)

Reaction	n					
	1	2	3	4	5	6
$SiO_{n-1}(OH)_{5-n} = SiO_n(OH)_{4-n} + H^+$	9.5	12.6	15.7	18.8	-	-
$Si_2O_n\ (OH)_{7-n} = Si_2O_{n+1}(OH)_{6-n} + H^+$	9.0	10.7	12.4	14.1	15.8	17.5

Figure 1-6 shows the viscosity of sodium silicate solutions as a function of composition. It can be found that the viscosity increases remarkably at higher silica contents, for most sodium silicates used for alkali activation, the SiO_2/M_2O ratio is usually between 1.0 and 2.0. Thus for high silica content activators, it may cause a problem that the fresh alkali activated binder mixtures tend to stick to the mixing machine, especially in the cases of activating fly ash or metakaolin, when high activator content is needed.

The significant decrease of viscosity due to the increase of temperature was also reported from (Yang et al, 2008). Thus additional attention should be drawn when preparing silicate based alkali activated materials under elevated temperatures. Presently, sodium silicate solution is the most widely used alkali activator; nearly most of the literatures that reported high performance alkali activated products are using sodium silicate as an activator. The commercial sodium silicate ranges with different SiO_2/M_2O ratio and water content, but generally the SiO_2/M_2O ratio is from 3.5 to 2.0, which are in the range of favored alkali activation parameters, and an ideal SiO_2/M_2O ratio can be achieved by incorporating sodium hydroxide into the silicate solution.

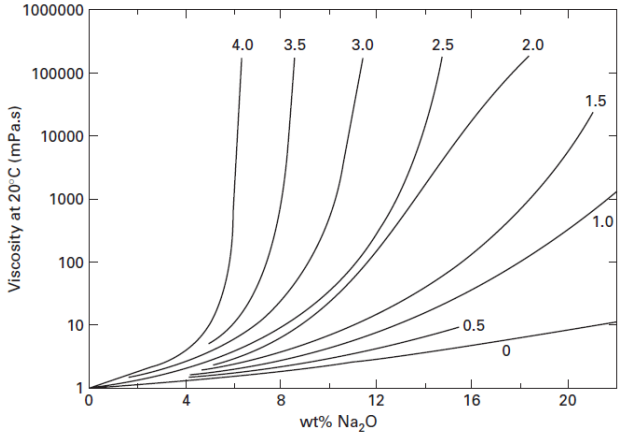

Figure 1-6: Viscosities of sodium silicate solutions (Vail, 1952)

1.3 Motivation and objective

Motivation

Applying alkali activated materials as alternative binder to Portland cement has been reported to show advantages in various aspects, including environmental issues such as carbon footprint, energy cost and the consumption of natural un-renewable materials; and also performances like mechanical properties and durability. Those intrinsic advantages give researchers the driving force of investigating this material. On the other hand, although solid basis has been established in understanding alkali activated materials, it is still necessary to carry out further studies in order to push this type of material closer to applications. Among those studies, the blended alkali binder system (C-A-S-H + N-A-S-H) has shown excellent performances and great potential in application in the past few years. Thus a better understanding of this blended binder would significantly contribute to both the academia and the industry.

Objective

The main objective of this study is to develop a blended alkali binding system based on ambient temperature cured, silicate activated slag and fly ash. Ground granulated blast furnace slag and class F fly ash are chosen as solid raw materials due to their worldwide availability and relatively stable properties, sodium hydroxide modified sodium silicate solutions are used as the activator because of their contribution in achieving high performance; and ambient temperature curing is applied because of its advantage in field applications. To develop and achieve a better understanding on the blended alkali activated materials, the following objectives are taken into consideration in this research: determination of key parameters in binder synthesis; modification of the binding system to achieve better performance and further lower environmental impact; mix design methodology and evaluation of fresh and hardened properties; reaction mechanism study and modeling of the blended binder system; small scale applications and performance identifications. Figure 1-7 presents a schematic description of the research objectives and strategy.

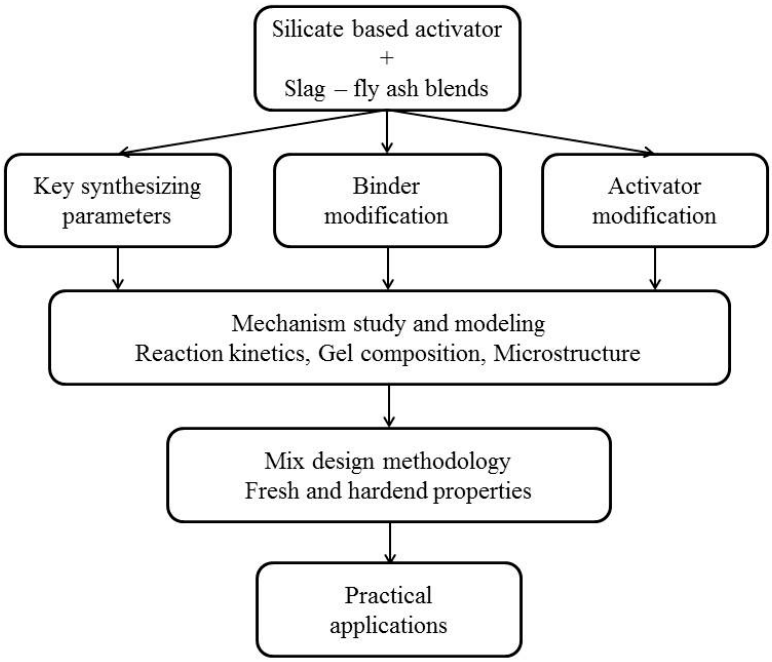

Figure 1-7: Schematic description of the research objectives and strategy

1.4 Outline of this thesis

This research aims at developing an ambient temperature cured, silicate activator based alkali activated slag-fly ash blends, with a better understanding of the reaction mechanism, further improved properties, reduced environmental impacts and identified performances that are related to different applications. The research framework of this thesis is presented in Figure 1-8. The contents of the chapters are explained in the following paragraphs.

In Chapter 2, the relevant physical and chemical properties of the starting materials used in the present study are characterized, for instance the chemical composition, particle size distribution and density. The applied solid materials include powder materials such as slag, fly ash, limestone powder, and aggregates. Testing methods used in this study are also introduced, for instance the isothermal calorimeter (IC), thermo-gravimetric (TG), Fourier transform infrared spectroscopy (FTIR), X-ray diffraction (XRD), Nuclear magnetic resonance (NMR) and Scanning electron microscope (SEM).

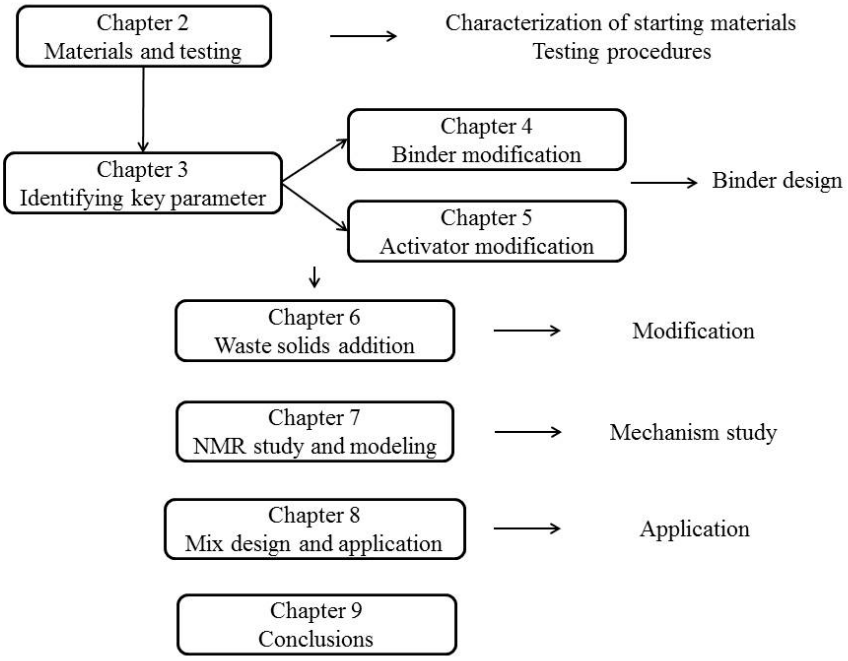

Figure 1-8: Outline of the thesis.

In Chapter 3, key synthesizing factors such as slag/fly ash ratios and activator moduli are identified by investigating their effects on early age reaction, mechanical properties, T-O bond conditions and thermal characteristics of the reacted gels; aiming at obtaining suitable starting

parameters for synthesizing alkali activated slag-fly ash blends with optimum mechanical properties, and clarifying how those parameters affect the micro structure. Determination of key synthesizing parameters would provide guide information for further steps of this research.

In Chapter 4, two additives are incorporated in the established alkali activated slag-fly ash binding system in order to achieve one or more of the following targets: enhanced sustainability, reduced cost, improved performance. The investigated additives are nano-silica and limestone powder. Their influences on fresh behaviors such as setting time and flowability; hardened properties like mechanical property and porosity; and reaction kinetics, gel structure are discussed in detail.

In Chapter 5, a study on the modification of the activator is carried out, aiming at developing a more sustainable activator with further reduced environmental impacts. A laboratory prepared olivine nano-silica is used to replace commercial water glass as alternative activator, and a comprehensive investigation is addressed by including detailed characterization of the prepared activator; comparison of the gel characteristics, important engineering properties and environmental issues such as costs, energy and carbon footprint.

In Chapter 6, the suitability of reusing industrial solid wastes in alkali activated materials is investigated. The applied wastes are incinerated bottom ash from urban wastes and granite powder from aggregate manufacturing. It shows advantages in reducing the treating costs of solid waste before application and immobilizing hazardous heavy metals. Besides, another solid waste, the waste glass, is ground and compared to silica fume in order to investigate its reactivity and application potential.

In Chapter 7, the effects of activator and precursor on reaction degree and gel structure of the reaction products are investigated by using ^{29}Si, ^{27}Al MAS NMR together with selective dissolution. The structural shift of the original Si and Al is tracked, and the contribution of the starting material (in terms of the Si and Al groups) on the reaction products is clarified in detail. Additionally, models concerning the gel formation under different activator and precursor conditions are proposed, primarily based on the NMR investigations.

In Chapter 8, mortar and concrete mixtures are designed based on the acquired insights of binders, and a particle packing model is firstly applied in this alternative binding system with adjusted methodology. Effects of starting parameters on several key performances related to engineering application are identified, such as fresh state behaviors, mechanical properties, porosity and shrinkage. Finally, two small scale applications are performed. One is the steel fiber reinforced alkali activated materials that are developed by using the particle packing model, which results in good mechanical property and stress-stain behavior. Another one is lightweight alkali activated composites with good thermal insulation and sound absorption properties.

In Chapter 9, comprehensive conclusions of the present work are drawn and recommendations for future research are proposed.

Chapter 2

Material characterization and testing procedures

2.1 Activators and liquids

The alkali activator used in this work was a mixture of the sodium hydroxide pellets of analytical level and commercial sodium silicate solution. The sodium silicate solution has a composition of 27.69% SiO_2, 8.39% Na_2O and 63.92% H_2O by mass. The desired activator modulus (Ms, SiO_2/Na_2O molar ratio) was achieved by adding the appropriate amount of sodium hydroxide pellets into the sodium silicate solution. Table 2-1 lists the composition of sodium hydroxide modified sodium silicate solution for the target moduli.

Table 2-1: Silicate/hydroxide ratios for a target activator modulus

Ms	Sodium silicate solution (g)	Sodium hydroxide (g)
2.0	100	7.64
1.8	100	9.69
1.6	100	12.25
1.4	100	15.55
1.2	100	19.94
1.0	100	26.10
0.8	100	35.33

Besides the activator modulus, another two parameters in the design of alkali activated materials are related to the activator: equivalent Na_2O content and water/binder ratio. The equivalent Na_2O content refers to the Na_2O from the activator divided by the binder material (by mass). For instance, an equivalent Na_2O content of 5% means 5 g of calculated Na_2O is used for 100 g of the binder. Usually a certain amount of distilled water is added in order to reach the desired water/binder ratios. In this study, the water refers to the ones that originally from the sodium silicate solution and the additionally added water. The mixed activator solution is cooled down to room temperature prior to further use. Besides the activator, a

commercial nano-silica slurry is used for binder modification in Chapter 4, the slurry has a solid content of 50 wt.%, a d50 of 0.12 μm and a density of 1.4 g/cm^3, and the solid fraction consist 98.7 wt.% of nano-silica.

2.2 Powder materials

The solid materials that will use in the following chapters are ground granulated blast furnace slag (GGBS, provided by ENCI, the Netherlands), Class F fly ash (supplied by Vliegasunie B.V., the Netherlands), limestone powder, silica fume and Portland cement (CEM I, 42.5 N, provided by ENCI). The specific density (kg/m^3) of used powder materials are listed in Table 2-2, it shows that all applied powders present similar level of densities while the fly ash and silica fume are relatively lightweight.

Table 2-2: Density of the applied powder materials

Powder	Density (kg/m^3)
Blast furnace slag	2930
Fly ash	2300
Limestone powder	2710
Silica fume	2320
Cement	2970

The major chemical compositions of those powders are analyzed by X-ray fluorescence (XRF) and shown in Table 2-3. Concerning the precursors, the slag presents similar content of Ca and Si, together with considerable amount of Al and MgO; while the fly ash mainly consists of Si and Al, a high amount of Fe and small amount of Ca and Mg.

Table 2-3: Major chemical composition of the powder materials

Oxides	Slag	Fly ash	Limestone Powder	Silica fume	Cement
CaO	37.42	4.44	53.96	0.86	63.54
SiO_2	34.44	54.62	0.84	90.84	19.82
Al_2O_3	13.31	24.42	0.24	-	5.36

MgO	9.89	1.43	1.01	0.67	1.27
Fe_2O_3	0.47	7.21	0.32	2.00	3.72
Na_2O	0.34	-	0.21	0.61	-
K_2O	0.47	1.75	0.34	1.12	0.09
SO_3	1.23	0.46	-	1.24	2.86
LOI	1.65	2.80	43.01	2.54	1.82

Their detailed particle size distributions, measured applying a light scattering technique using a Master sizer 2000 particle size analyzer, are given in Figure 2-1.

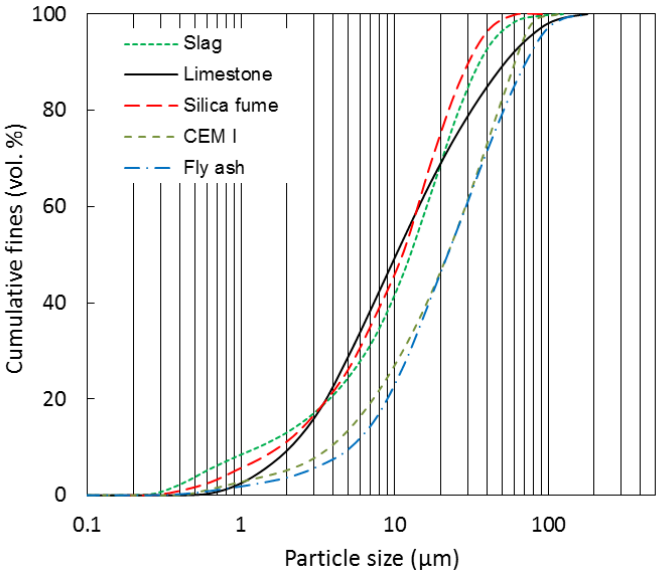

Figure 2-1: Particle size distributions of the applied powder materials

2.3 Aggregates and additives

Two types of sand were used as fine aggregates in this research: a micro sand with a specific density of 2720 kg/m^3 (0-1 mm, provided by Graniet-Import Benelux B.V., the Netherlands) and CEN standard sand (specific density of 2640 kg/m^3) with the fractions of 0-2 mm. Besides, two types of straight steel fibers were applied in Chapter 7: (1) fiber length of 13 mm with diameter of 0.2 mm; (2) fiber length of 6 mm with diameter of 0.16 mm. Commercial lightweight aggregates (expanded glass, provided by Rotocell) with three particle sizes (0.5-1

mm, 1-2 mm and 2-4 mm) are also used in Chapter 7, those three aggregates are with particle densities of 600, 550 and 500 kg/m^3, respectively.

2.4 Testing methods

Slump flow

The workability of the pastes and mortars are evaluated by the flow table tests according to (EN 1015-3). A Hägermann cone is employed for the slump flow test, the fresh samples were transferred into the cone and a free flow without jolting was allowed. Two diameters that are perpendicular to each other were determined and the mean value was recorded as the slump flow. Figure 2-2 shows the used Hägermann cone.

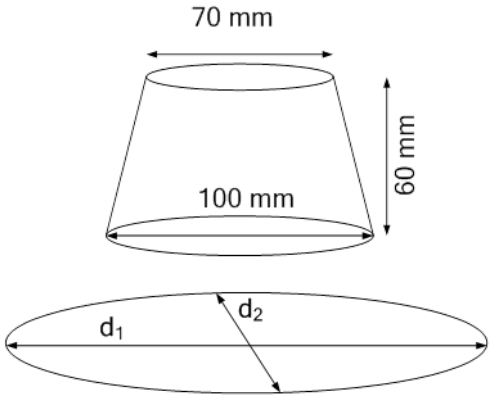

Figure 2-2: Hägermann cone used for flow test

Setting time

The initial and final setting times were measured by the Vicat needle method as described in (EN 196-3). The initial setting time is determined as the elapsed time that measured from zero to the time at which the distance between the needle and the base plate is (6 ± 3) mm; and the final setting time is recorded as the elapsed time that measured from zero to that at which the needle first penetrates only 0.5 mm into the specimen. The determined values were an average of three samples.

Early age heat release

The early age heat release of alkali activated material mixes were studied by an isothermal calorimeter (TAM Air, Thermometric). The solid raw materials were firstly mixed with the

activating solution externally for about 1 min and vibrated with an electrical vibrator, then the mixed paste was injected into a sealed glass ampoule and loaded into the calorimeter. All measurements were conducted for a designed period under a constant temperature of 20 °C. The heat release and heat flow results were normalized by mass of the binding materials.

Compressive strength

The compressive strength tests were carried out according to (EN 196-1). 40 × 40 × 160 mm^3 prisms were prepared and tested at the designed ages, and the strength value for each mix was obtained from the average of three specimens.

Stress-strain behavior

The flexural strength was tested using a Zwick Z020 instrument, under three-point loading using displacement control; the specimen sizes are 160 × 40 × 40 mm^3, and a mid-span deflection rate is 0.10 mm/min with a span of 100 mm. The pre-load was performed with a force of 5 N and a speed of 10 mm/min. The used testing speed was 50 N/s with a controlled force, the accuracy of the applied sensor is 0.1 N. The data was collected with a time interval of 0.1 s and travel interval of 1 μm. Figure 2-3 shows the setup of the stress-strain behavior test.

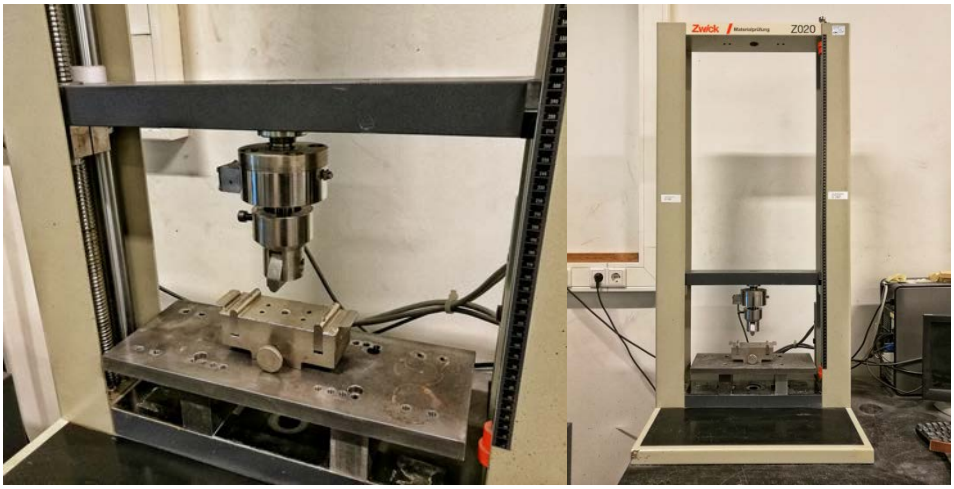

Figure 2-3: Setup of the stress-strain behavior test

Porosity

The water permeable porosity was measured by applying the vacuum-saturation technique following the description given in (NT Build 492). The water permeable porosity is calculated as:

$$P(\%) = \frac{Ms - Md}{Ms - Mw} \times 100\%$$

Where P (%) is the water permeable porosity, M_s (g) refers to the mass of the saturated sample in surface-dry condition in air, M_w (g) is the mass of water-saturated sample in water and M_d (g) is the mass of oven dried sample.

Drying shrinkage

The samples for drying shrinkage test were cast in molds with dimensions of 40 × 40 × 160 mm^3 and cured in sealed condition at a temperature of 20 °C. After 24 h of curing, specimens were exposed in a cabinet with a temperature of 20 °C and relative humidity of 50%, also the initial length (L_0) was measured at that time. Afterwards, the length (L_n) was measured once per day until the age of 28 d. The length change was calculated as:

$$L(\%) = \frac{L0 - Ln}{Li} \times 100\%$$

Where L_i is the effective initial length. A setup picture of the shrinkage test is shown in Figure 2-4.

Figure 2-4: Setup of the drying shrinkage test: constant humility curing and measuring

Fourier transform infrared spectroscopy

Fourier transform infrared spectroscopy (FTIR) measurement (KBr pellet method) was performed in a Varian 3100 instrument with the wavenumbers ranging from 4000 to 600 cm^{-1} at a resolution of 1 cm^{-1}, and each sample was scanned for 50 times.

Thermogravimetry

Thermogravimetry (TG) and differential scanning calorimetry (DSC) analysis was conducted in a STA 449-F1 instrument, grinded powder samples were heated up to 1000 °C at 5 °C /min with nitrogen as the carrier gas.

X-ray diffraction

The X-ray diffraction (XRD) analysis was performed using a Bruker 2D phase instrument, with a step size of 0.02° and a 2θ range from 5° to 60° using a Co or Cu X-ray tube with lynxeye-detector, 0.6 s/step and 1 mm fixed slit.

Scanning electron microscopy

The microstructure of the samples were characterized by a scanning electron microscopy (SEM, JEOL JSM-IT100) instrument operating in a high vacuum mode at an accelerating voltage of 10 kV. Testing specimens were extracted from the prepared samples, dried and coated with a thin gold layer for analysis.

Nuclear magnetic resonance

The solid-state Magic angle spinning nuclear magnetic resonance (MAS NMR) spectra were carried out using a Bruker Avance 400WB spectrometer, after 3 months of curing. The ^{29}Si NMR spectra were collected at 79.5 MHz on a 7 mm probe, with a pulse width of 6.5 μs, a spinning speed of 15.9 kHz and a relaxation delay of 10 s. The ^{27}Al MAS NMR spectra were obtained at 104.5 MHz on a 4 mm probe, with a pulse width of 6.5 μs, a spinning speed of 41.7 kHz and a relaxation of 2 s.
The liquid-state ^{29}Si NMR (99.361MHz) spectra were determined in a Bruker DRX 500 spectrometer, equipped with a 5mm Broadband probe. All spectra were obtained under the same conditions: 90º degree pulse (7 ms at -2 dB) and 5s of relaxation delay. Chemical shifts are reported in parts per million (ppm), calibrated to the TMS signal.

Chapter 3

Determination of key parameters in blended systems

3.1 Introduction

In alkali activated Ca + Si or Si + Al system, the silicate from activator participates in the formation of hydrated C-A-S-H or N-A-S-H gels together with solid silicate sources, and there exists an optimal silicate content in terms of mechanical properties, either insufficient or exceeding silicate supply may restrict the formation of an ideal gel structure and lead to a matrix with relatively low strength (Duxson et al, 2005). Also, the relations between the silicate content and mechanical properties were well established in the individual system (Wang et al, 1994). However, in the case of alkali activated blended systems such as slag/fly ash, the raw material composition plays a more complex role: the silicate from the activator may involve in the formation of all type of typical hydrated gels such as C-A-S-H, N-A-S-H and (N,C)-A-S-H; the silicate from different raw materials may exhibit different de-polymerization rates and availability under different conditions such as curing temperature and alkaline concentration.

Despite a consensus about the binding mechanisms has been reached in the previous studies, different conclusions were drawn in determining the optimal parameters in strength: some studies showed a decrease in compressive strength with the increase of fly ash content (Weiguo et al, 2011; Kumar et al, 2010 and Escalante-Garcia et al, 2006), while other studies indicated that there is an optimum ratio between slag and fly ash (Chi et al, 2013; Yang et al, 2012 and Zhang et al, 2007). Differences in critical raw materials' relative content and activator parameters were also reported (Puertas et al, 2000; Shi et al, 1999). Different used activators and curing conditions make it difficult to make valid comparison between those studies. Therefore, in order to tailor the properties of alkali activated slag/fly ash blends for desired applications, it is necessary to carry out a systematic study considering the effects of raw materials, activators and curing conditions simultaneously.

On the other hand, alkali activated materials manufactured under ambient temperature exhibit several superiorities in field application, but there exist limited studies about the combined influence of activator and raw materials on the comprehensive properties of room temperature cured slag/fly ash mixtures. In this chapter, a preliminary study for tailoring the properties of alkali activated slag/fly ash blends was carried out, and the influences of activator modulus and slag/fly ash ratios on hydration, gel characters and strength were addressed. Slag dominated mixes (at least 50% by mass) were chosen due to the superior mechanical properties under

room temperature, different slag/fly ash ratios were used to give different starting CaO-Al_2O_3-SiO_2 compositions.

3.2 Mechanical properties

In the mix design stage, the equivalent sodium oxide (Na_2O) content was kept at 5.6% by mass of the binder in all samples, five levels of activator moduli (Ms from 1.8 to 1.0) were used (assigned as A to E) to provide different extra silicate contents from activator to the solid material. The fly ash/slag ratios of 90/10, 80/20, 70/30, 60/40 and 50/50 by mass were used (represented as 1 to 5). The water/binder ratio was kept constant as 0.35; the water consisted of the water added from distilled water and the water contained in the original sodium silicate solution. The chosen Na_2O content and water/binder ratio were preliminarily determined that would provide sufficient alkalinity without efflorescence and satisfying flow ability, respectively. The detailed information of mix proportions is listed in Table 3-1.

Table 3-1: Mix proportions of alkali activated slag/fly ash pastes

	Slag/fly ash	Na%	Activator modulus					w/b
			A	B	C	D	E	
1	90/10	5.6	1.8	1.6	1.4	1.2	1.0	0.35
2	80/20	5.6	1.8	1.6	1.4	1.2	1.0	
3	70/30	5.6	1.8	1.6	1.4	1.2	1.0	
4	60/40	5.6	1.8	1.6	1.4	1.2	1.0	
5	50/50	5.6	1.8	1.6	1.4	1.2	1.0	

The compressive strength of samples with different starting material compositions and activator parameters after 7 days' curing is shown in Figure 3-1. It can be seen that all samples exhibit good strength after 7 days' curing under ambient temperature (between 56.24 MPa and 82.18 MPa). The compressive strength decreases when increasing the fly ash content in general. For a constant activator modulus, higher compressive strengths are observed in samples with higher slag contents in all cases, but the strength difference caused by slag content becomes less significant with the decrease of the activator modulus. The activator modulus has different effects on specimens with different fly ash substitution levels: for samples with a slag/fly ash mass ratio of 90/10, the highest compressive strength of 82.2 MPa is observed with an activator modulus of 1.8, then the strength decreases continuously as the decrease of activator modulus, reaching the lowest strength of 74.2 MPa at the activator modulus of 1.0; while for samples

with the slag/fly ash mass ratios of 80/20 and 70/30, the optimal activator modulus moves slightly lower to 1.6, and the compressive strength is 75.3 MPa and 72.4 MPa, respectively. Then a gradual reduction of strength takes place in both mixes, and the reduction rate is more prominent in the 70/30 mixes. On the contrary, for samples with higher fly ash contents such as 40% or 50% by mass, the compressive strength increases in general as the decrease of the activator modulus, and the highest strength appears at the Ms of 1.4 for 40/60 mixes (67.1 MPa) and 1.2 for 50/50 mixes (62.5 MPa).

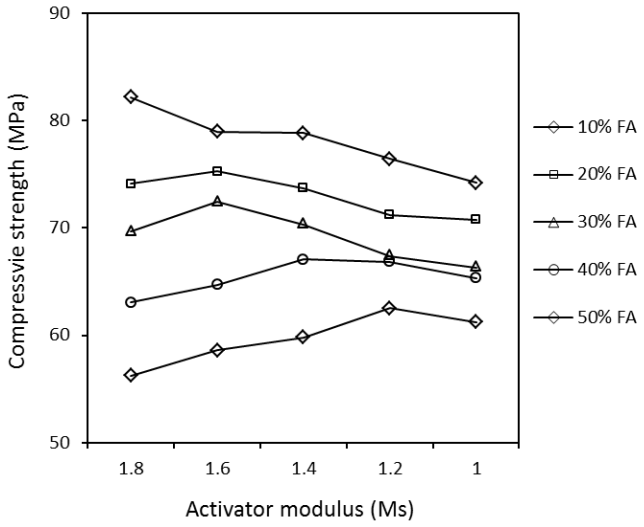

Figure 3-1: Compressive strength of alkali activated slag/fly ash blends at 7 days

The compressive strength of specimens at the ages of 28 days is given in Figure 3-2. The samples showed compressive strengths ranging from 71.6 MPa to 100.9 MPa, which is promising for high performance applications. It is obvious that a higher slag content leads to a higher compressive strength in general, which is similar to the 7 days strength results. As the activator modulus decreases, the strength variations are smaller when compared to the trend in 7 days. It may indicate that the influence of raw material composition on strength becomes more significant at longer ages. When the slag/fly ash mass ratio is kept constant, all mixes show a shift in optimal activator modulus for compressive strength. It is also similar with the tendency in 7 days' results that mixes with a higher slag content have a higher optimal activator modulus, and a lower slag content exhibits a lower critical modulus. It should be noted that there is an obvious increase in the compressive strength when the activator modulus decreased from 1.8 to 1.6 or increased from 1.0 to 1.2, which is different from 7 days results. It reveals that either a high or low modulus may have negative influence on strength at longer ages.

The compressive strength is increased by 25% to 30% for most of the specimens between 7 and 28 days and the increasing rate have weak correlations with either slag/fly mass ratio or activator modulus. It can be concluded that both slag/fly ash mass ratios and activator modulus have significant influence on compressive strength. The glassy phases of slag is more vulnerable to alkaline attack than the aluminosilicates enriched ones from fly ash under room temperature (Fan et al, 1999), and the slag generally has a higher content of reactive phase than fly ash (Duxson et al, 2007; Fernandez et al, 2006), thus a higher amount of Si and Ca will dissolve and more hydrated gels will be formed than fly ash, which can explain the decrease in compressive strength at both 7 and 28 days when the fly ash content is increased.

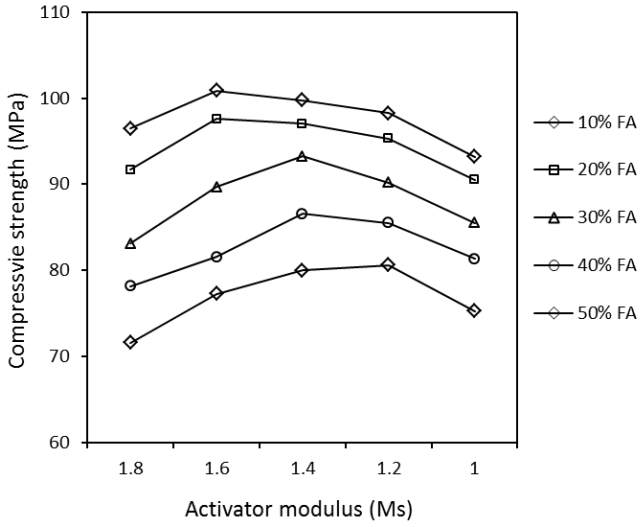

Figure 3-2: Compressive strength of alkali activated slag/fly ash blends at 28 days

It can be seen that samples with higher slag/fly ash mass ratios show a higher optimal activator modulus for strength, and this trend is more significant at early ages. This phenomenon is in accordance with the previous conclusions that a relatively high activator modulus has a positive effect on the dissolution of calcium and the formation of C-(A)-S-H gels (Phair et al. 2000), while a lower modulus has an opposite influence on the solubility of calcium from slag (Deira et al, 2014). As the fly ash content increases to a certain level, a relatively low activator modulus benefits the reaction process of Si and Al dominated structures of fly ash and leads to an increase in strength (Jaarsveld, 2000). Another possible explanation is that since the total Na_2O content is kept constant for all samples, a higher activator modulus provides a higher amount of extra silicate, mixes with different slag/fly ash mass ratios may exhibit different extra silicate demand to form an ideal gel structure, and the slag seems to exhibit a higher demand than fly ash under ambient temperature. The shifts in the optimum compressive strength indicate that the activator modulus and slag/fly ash ratio possess a synergetic influence

on strength, thus in order to achieve a desired strength, it is suggested to determine these two parameters simultaneously.

3.3 Early age reaction

The isothermal calorimetric analysis was conducted on the samples with the activator moduli of 1.8, 1.4, 1.0 (assigned as A, C, E) and slag/fly ash mass ratios of 90/10, 70/30, 50/50 (represented by 1, 3 and 5). Figure 3-3 illustrates the heat evolution curves within the first 72 hours. The entire reaction processes can be divided into four stages, namely initial dissolution, induction, acceleration and stable period. Two calorimetric peaks are shown in all samples: an initial peak with significant high heat flow during the first few minutes and an acceleration peak with relatively low intensity at around 6 to 24 hours. The occurrence of two typical peaks is in agreement with the heat evolution curves of silicate activated slag or its blends observed in previous studies (Chithiraputhiran and Neithalath, 2013). The first peak of heat flow corresponds to the initial wetting, dissolution of raw materials (primarily the breakdown of Me-O and T-O bonds of slag) within the first few minutes after mixing (Ravikumar and Neithalath, 2012), also partly due to the formation of the initial reaction products from the dissolved units such as Si, Ca and Na in the solution (Bernal et al, 2011).
The presence of the early peak is generally regarded as a physical rather than a chemical progress. The acceleration peak (i.e. the second peak) that observed at over 6 hours is assigned to the massive formation of reaction products (Shi et al, 1995). Figure 3-3 (a) shows the heat flow of samples with an activator modulus of 1.8 and slag/fly ash mass ratios of 90/10, 70/30 and 50/50 (A1, A3 and A5).

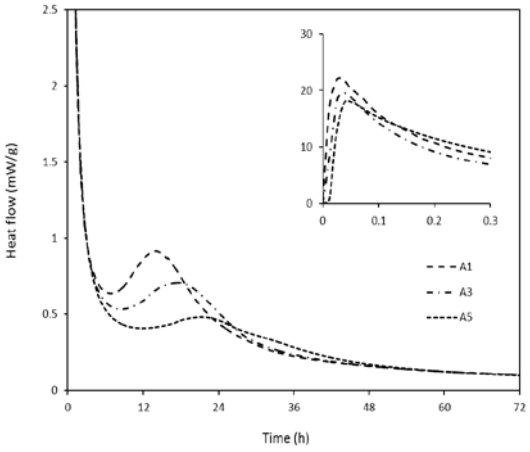

(a)

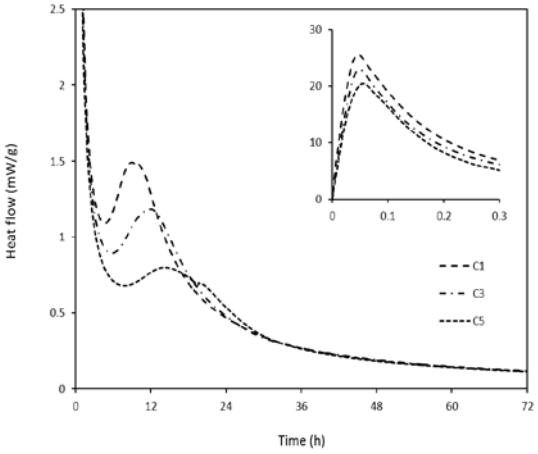

(b)

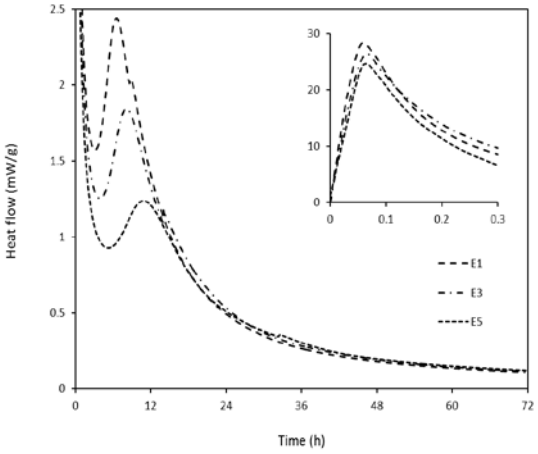

(c)

Figure 3-3: Heat evolution of AA-slag/fly ash blends [with Ms of 1.8 (a), 1.4 (b) and 1.0 (c)]

It can be seen that the initial dissolution peak appears at around 3-4 minutes, samples with higher slag content resulted in a higher dissolution heat flow, which demonstrates that slag is easier to dissolve than fly ash in alkali solutions under ambient temperature.

After the initial dissolution stage, all mixes exhibit an induction period that last about 4 to 10 hours before the second heat evolution peak. The dissolution of solid precursors in alkali solution leads to the dissolution of the glassy structure of slag and the release of Ca, Si and Al units. The newly formed reaction products from those released units may grow rapidly and

form a layer on the surface of unreacted slag particles, which limit the amount of available alkalis for slag dissolution and reduce the heat evolution. Because of the continuous alkali supply of sodium silicate and the penetration of alkalis through the newly formed layer (Brough et al, 2000), further reaction continues and the second peak of heat flow appears. Samples with higher fly ash content present considerably longer induction time, this is probably due to the low reactivity of fly ash, and it may mainly work as a nuclear site for the reaction products and has a negative contribution to the further reactions between alkalis and slag particles. The second heat evolution peak appears at around 13 hours for the sample with a slag/fly ash mass ratio of 90/10, this peak shifts to longer times with lower intensities and broader peak shapes as the fly ash content increases. For instance, when increasing the fly ash content from 10% to 50%, the acceleration peak is delayed for 9 hours and the peak height decreases by nearly 47%. Such significant changes are mainly due to the reduced total slag content that resulted in a smaller overall heat evolution, also partly because of the relatively low reactivity and a more moderate reaction process of fly ash under ambient temperature.

Figures 3-3 (b and c) exhibit the heat evolutions of slag/fly ash blends activated with the activator moduli of 1.4 and 1.0, respectively. It can be seen that as the activator modulus decreases, no significant change takes place in the time of dissolution peak, which proves again that the dissolution stage is more likely a physical process. However, the intensity of the initial peak is considerably increased for all slag/fly ash ratios, indicating a more intensive dissolution and reaction process at the beginning stage. Higher peak flows are also observed in the acceleration stage for all slag/fly ash mixtures, which may indicate a higher reaction degree due to the larger covered area under the peak.

The increased reaction caused by the reduction of activator modulus is also found in previous investigations (Krizana and Zivanovic, 2002). It was suggested that a decrease in activator modulus leads to a higher alkali concentration, thus enhancing the dissolution rate and reaction degree of slag, a higher alkalinity also increases the solubility of silica and alumina in solution that could benefit the formation of reaction products (Song and Jennings, 1999; Rothstein et al, 2002). For a constant slag/fly ash mass ratio, the duration of the induction time significantly decreases when lowering the activator modulus, as can be seen from those figures that the curves representing induction period become narrower and sharper. Furthermore, the commence time of the acceleration peak is decreased, such as from 13 to 6 hours in slag/fly ash mass ratio of 90/10 mixes and from 22 to 10 hours in slag/fly ash mass ratio of 50/50 mixes. Those reduced induction times and advanced second peak times also demonstrate an acceleration in reaction that is caused by the decreased activator modulus. It should be noted that the reaction process of samples with a high fly ash content was accelerated even more significantly, which indicates that the dissolution of Si-O and Al-O bonds in fly ash also increases to some extent in high alkalinities and contributes to the reaction processes (Fernandez et al, 2005).

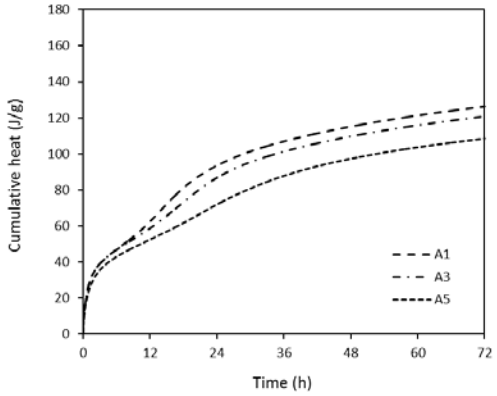

(a)

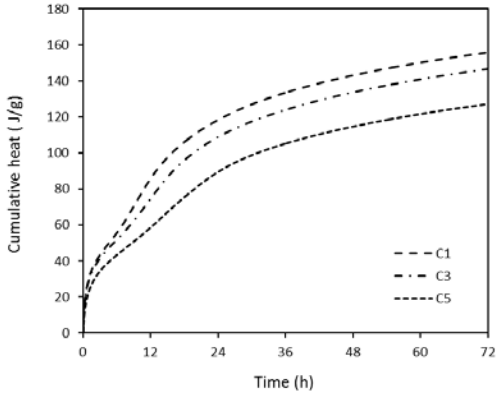

(b)

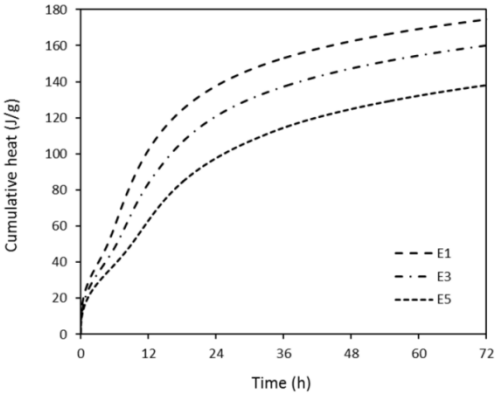

(c)

Figure 3-4: Cumulative heat of AA-slag/fly ash blends [Ms of 1.8 (a), 1.4 (b) and 1.0 (c)]

Figure 3-4 shows the cumulative heat evolution of all mixes. The sharp increase at the beginning corresponds to the initial wetting and dissolution of slag in alkali solutions; the relatively moderate increase after the initial stage is associated with the induction period; the acceleration/deceleration period is represented by the dramatic increase between 6 to 24 hours.
It can be seen that for a constant activator modulus, samples with a higher slag content exhibit higher total heat release, indicating that slag presents a higher reactivity than fly ash under ambient temperature; while for a constant slag/fly ash mass ratio, higher cumulative heat evolution appears in samples with lower activator modulus, this is owing to the better reactivity of both slag and fly ash in high alkalinity conditions.
The activator modulus has a more significant influence on the duration of induction time than slag/fly ash mass ratio, but both activator modulus and slag/fly ash mass ratio show a significant influence on the total heat release of acceleration/deceleration period. Additionally, it should be noted that the heat release after 24 hours consists of about 20 to 35% of the total heat release within the first 72 hours, this value increases with the increase in fly ash content and activator modulus, which demonstrates that the reaction process at longer ages still plays an important role in total reaction degree, especially for the samples with relatively low reactivity at early stages.

3.4 Gel structure identification

3.4.1 FTIR analysis

The influence of activator modulus and slag/fly ash mass ratio on gel character was investigated by FTIR. Figure 3-5 shows the infrared spectra of the unreacted slag and fly ash. The main vibration band for slag is at around 900 cm^{-1} and about 1020 cm^{-1} for fly ash, which is associated with the asymmetric stretching vibration of Si-O-T bonds (where T represents tetrahedral Si or Al units) (Rovnanik et al, 2013). The difference in the main band wavenumber is attributed to the different glassy phase structure of raw materials. The unreacted slag also shows an absorption band at around 670 cm^{-1}, which is associated with the asymmetric stretching of tetrahedral T-O groups (Kovalchuk et al, 2007). A small band at around 1450 cm^{-1} is also observed in slag, this band is corresponding to the asymmetric stretching vibration of O-C-O bonds (Yousuf et al, 1993), which may indicate that a slight degree of carbonation has already taken place in the raw material. For the fly ash, absorption bands located at around 1080, and 600 to 800 cm^{-1} indicate the presence of small amount of quartz (Gadsden, 1975).
Figure 3-6 shows the infrared spectra of samples with the activator moduli of 1.8, 1.4, 1.0 (represented by A, C, E) and slag/fly ash mass ratios of 90/10, 70/30, 50/50 (represented as 1, 3, 5 respectively) that after alkali activation. It can be seen that, regardless of the activator modulus and raw materials' relative content, all specimens exhibit similar location of absorption bands in general. Specifically, all samples showed OH groups at 1640 cm^{-1} and around 3200 cm^{-1} (since this is the only significant absorption bands after 2000 cm^{-1},

wavenumbers from 2000 to 4000 cm^{-1} are not shown in this figure), which indicates the presence of chemically bound water within the hydration products (Yu et al, 1999). The absorption bands at around 1420 cm^{-1} in all mixes correspond to the stretching vibrations of O-C-O in carbonates, and this band is more significant than that in the raw material, which reveals that the occurrence of carbonation during the reaction or curing process.

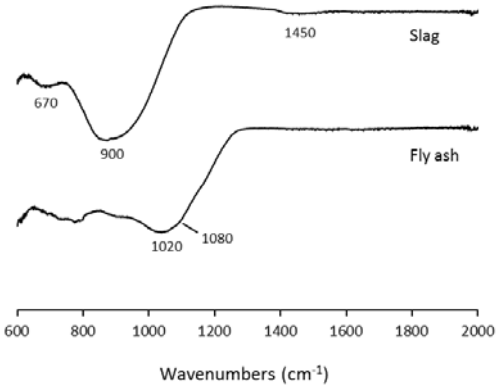

Figure 3-5: FTIR spectra of solid raw materials

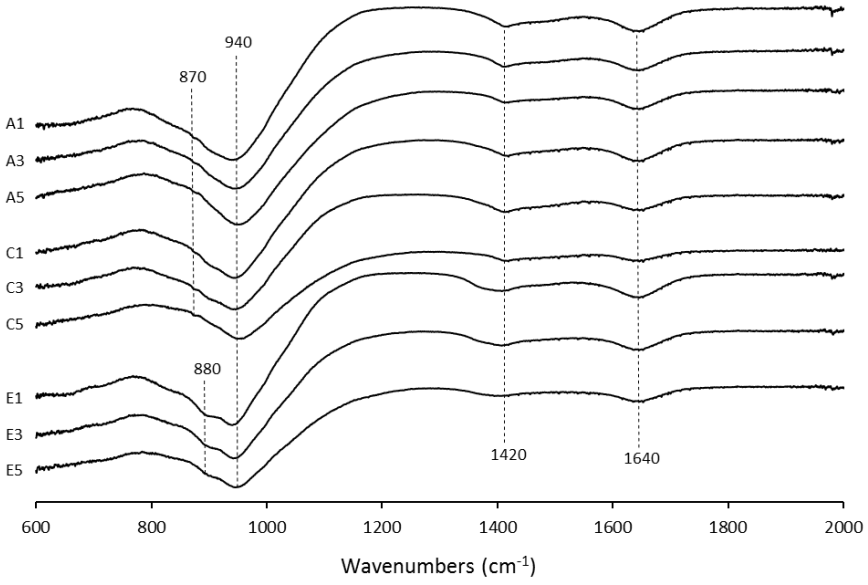

Figure 3-6: FTIR spectra of alkali-activated slag/fly ash blends

It should be noted that for a constant activator modulus, there is no significant change in the intensity and shape of carbonate absorption bands when changing the slag/fly ash mass ratio, but when shifting the activator modulus with a constant slag/fly ash mass ratio, slight changes take place. For instance, when comparing the samples with activator modulus of 1.8 (mix A) and 1.4 (mix C) respectively, the change in the absorption band is negligible. However, the absorption area becomes smoother and broader when the activator modulus decreases to 1.0 (mix E). It may reveal that the carbonation potential in alkali activated slag/fly ash blends has a more direct relation with activator modulus than the composition of solid raw materials. Considering that the FTIR spectra provides limited information about the quantitative analysis, more studies are needed to be carried out in order to identify the carbonation behavior of slag/fly ash blends in detail.

The main absorption band at 940 cm^{-1} is assigned to the asymmetric stretching vibration of Si-O terminal bonds (Zhang et al, 2012), also represented as non-bridging structures such as Si-O-Na (Lee and Van Deventer, 2003). This is the representative vibration bands of alkali activated slag that indicate the formation of C-A-S-H type gels with short chain structures. This Si-O bond was originally located at around 900 cm^{-1} in the unreacted slag; an increase in wavenumber indicates a higher polymerized Si-O network. The vibration of main Si-O-T bonds in this study shows a lower wavenumber than previous researches, this is probably due to the nature of the slag used in this study. It can be seen that when changing the slag/fly ash mass ratio or activator modulus, the main Si-O-T vibration bonds remain stable at 940 cm^{-1} in all mixes. It is generally concluded that the shifting of the absorption wavenumbers represents the changes of polymerization degree of a certain group, thus the unchanged main absorption band indicates that both fly ash incorporation and the amount of extra silicate from activator have limited influence on the polymerization degree of hydrated gels in slag dominated alkali activated slag/fly ash blends. This is consistent with the previous study that a low fly ash inclusion has limited effect on the gel networks of slag/fly ash mixtures (Ismail et al, 2014). Under ambient temperature and high slag content conditions, due to the low reactivity of fly ash and high dissolution rate of slag, the massive presence of Ca^{2+} in the solution prefers the formation of C-A-S-H type gels. The polymerization degree of C-A-S-H gel seems to be limited by its chain structure, thus there are no significant shifts in the absorption wavenumbers when changing the slag/fly ash mass ratio and activator modulus.

It can be noted that the absorption bands around 1000 to 1100 cm^{-1}, which are usually identified from alkali activated fly ash, are not observed in all mixtures. The absorption bands around this wavenumber are assigned to the asymmetric stretching vibration of Si-O-T bridge bonds (Hajimohammadi et al, 2011), which usually represent the high crosslinking networks such as silicate and alumina dominated geopolymers structures. The absence of this absorption band indicates that the typical structure of N-A-S-H gels is not obvious within the reaction products. One possible explanation is that the formation of N-A-S-H type gels requires the presence of soluble silica and alumina monomers in the solution, when those monomers reach a high concentration, the formation of oligomers and the following polymerization take place.

Also, the alkali cations participate in the reaction process as a charge balancer of tetrahedra T-O units. However, due to the vulnerable calcium enriched glassy structure of slag, large amounts of calcium are present in the solution at early ages, the silica and alumina units in the solution prefer to react with calcium to form precipitable C-A-S-H gels rather than continuously accumulating. The formation of C-A-S-H type gels reduces the concentration of Si, Al groups and consumes the alkali cations that are necessary for geopolymerization. Because of the calcium content is dominating in the mixes and the fly ash exhibits a low reactivity under ambient temperature, there may have no extra Si and Al existing after the calcium is fully consumed, or the remaining concentrations of Si, Al and alkalis are not sufficient enough to promote the formation of high polymerized structure.

3.4.2 TG/DSC analysis

The thermogravimetry results of all specimens are presented in Figure 3-7. It can be seen that all samples exhibit a significant mass loss before around 110 °C, this is mainly due to the loss of physically bound water within the matrix. The evaporable water content is around 15.5% in samples with an activator modulus of 1.8 (mix A), a slightly higher content of approximately 16.2% is observed in mixes with lower activator moduli (1.4 of mix C and 1.0 of mix E). The physically bound water content in the hydration products seems to be independent of the slag/fly ash mass ratio; also the activator modulus shows a very limited influence.

After a negligible mass loss between 105 and 180 °C all samples show a gradual decrease in mass until heated to around 600 °C, followed by a stable curve with remarkably low mass loss between 600 and 1000 °C. The mass loss after 180 °C is attributed to the gradual decomposition of hydration products. For a constant activator modulus, samples with a higher slag content show a higher total mass loss up to 1000 °C; while for a constant slag/fly ash mass ratio, samples with a lower activator modulus present a higher total mass loss. The mass losses after 105 °C in mixes with an activator modulus of 1.8 are from 6.05% to 5.02% when changing the slag content from 90% to 50%, this value is 6.27% to 5.5% in mix C and 7.2% to 6.39% in mix E, indicating that there is a very slight but distinguishable difference in thermal properties when changing the activator modulus or slag/fly ash mass ratio. It should be noted that there are no other abrupt mass losses observed between 105 and 1000 °C, which reveals that the reaction products of alkali activated slag/fly ash blends are mainly amorphous gels with the physically and chemically bound water.

Figure 3-8 shows the differential scanning calorimeter (DSC) results of all samples. The first sharp heat absorption peak at 110 °C is associated with the evaporation of physically bound water, as substantial mass loss observed at the same temperature range in the TG analysis. A smooth and broad peak with significantly low intensity appears at around 180 °C in all samples, the location of this peak corresponds to the beginning of the gradual mass loss after 105 °C in TG results, indicating the initial decomposition of the main hydrated products. Over 180 °C,

the gradual decomposition processes of hydrated gels containing the loss of chemical bond water and the following gel structure changes take place.

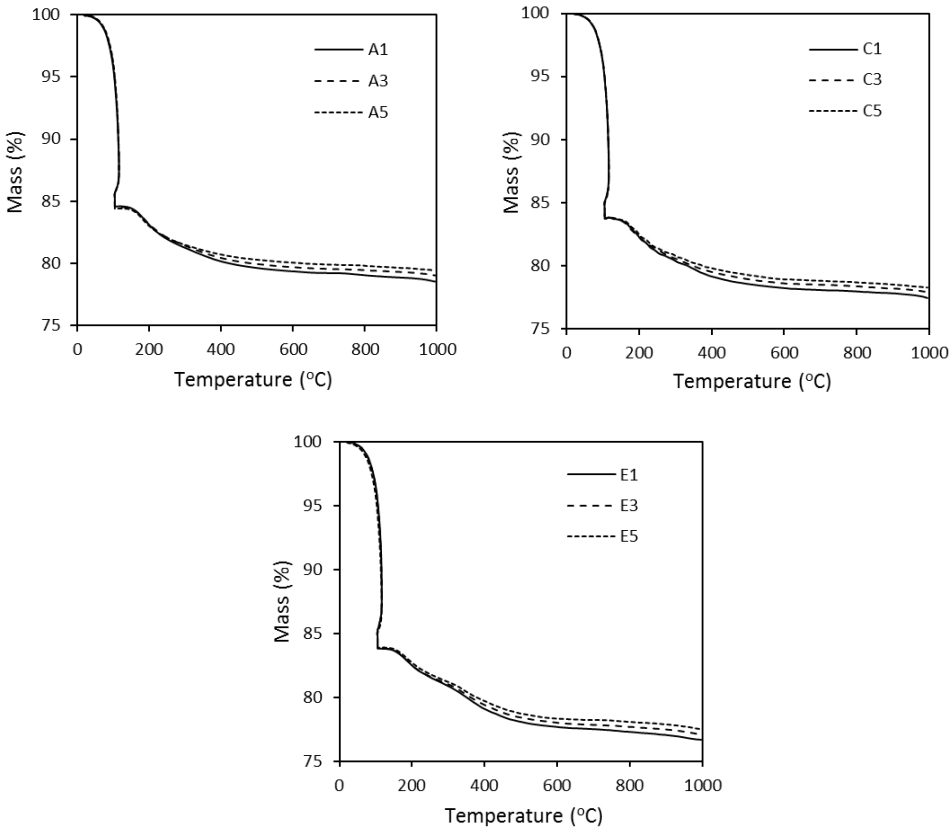

Figure 3-7: TG analysis of alkali activated slag/fly ash blends

It should be noted that the temperature of initial gel deterioration remain constant regardless of the changes in activator modulus and slag/fly ash mass ratio, also similar TG/DSC curves before 800 °C are shown in all mixtures, revealing that the reaction products of slag dominated alkali activated slag/fly ash blends present similar thermal characteristics in general within this temperature range, even though the raw material composition is significantly changed. All samples show an exothermic peak in the DSC curves at around 800 °C, while no remarkable changes appear in mass loss at the same temperature. The heat release at about 740 to 810 °C is due to the formation of new crystalline phases. One previous study showed that the C-A-S-H type gels completely lose the binding water when heated up to 800 °C, and the destroyed gel structure starts to form more ordered crystalline phases (Rovnanik et al, 2013); another possible explanation is that this peak is due to the devitrification of unreacted slag. It can be

seen that both slag/fly ash mass ratio and activator modulus are related to the location of this calorimeter peak: regardless of the activator modulus, samples with higher slag content exhibit a lower temperature of crystallization; while under the same slag/fly ash mass ratio, lower activator modulus presents a lower crystallization temperature. The raw material composition seems to have a more significant effect on this structural transformation.

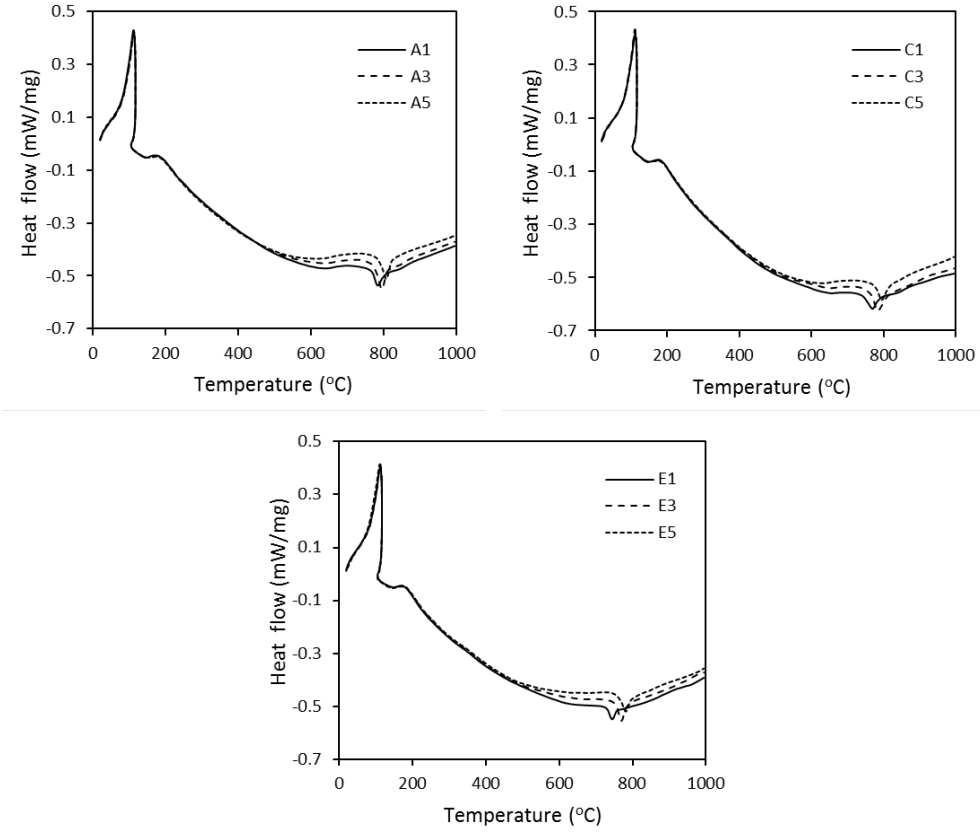

Figure 3-8: DSC analysis of alkali activated slag/fly ash blends

3.5 The synergetic effects of activator and solid precursors

The starting materials of silicate activated slag/fly ash blends consist of liquid activator (sodium silicate and sodium hydroxide), solid precursors (slag and fly ash) and water. When the equivalent Na_2O content, water/binder ratio and curing temperature are kept constant, the activator modulus and raw materials' relative content turn to be the only two dominating factors that influence the properties. These two compositional factors exhibit synergetic influences on a series of characters including the reaction kinetics, gel characters and

compressive strength under ambient temperature. Table 3-2 summarizes the influences of raw material, activator changes on early age hydration and gel structures. As concluded before, the early age reaction processes can be significantly accelerated by reducing the activator modulus and increasing the slag/fly ash mass ratio.

Table 3-2: Summary of the influences of activator modulus and slag/fly ash mass ratio on the hydration and gel structure characters

Analysis	Concerns	Activator modulus: From 1.8 to 1.4 and 1.0	Slag/fly ash ratio: From 5/5 to 7/3 and 9/1
Isothermal calorimeter	Acceleration peak intensity	Increased 64.6%, 158.6%	Increased 47.0%, 88.8%
	Acceleration peak location	Decreased 34.1%, 53.9%	Decreased 23.4%, 39.3%
	Total heat evolution	Increased 21.0%, 32.9%	Increased 14.5%, 21.9%
FTIR	Main absorption bands	Unchanged	Unchanged
	Terminal Si-O bands	Shift to 880 cm^{-1} in Ms of 1.0	Unchanged at 870 cm^{-1}
TG/DSC	Physically bond water content	Negligible change	Unchanged
	Gel decomposition temperature	Unchanged	Unchanged
	Total mass loss until 1000 ^{o}C	Slightly increased	Slightly increased
	Crystallization temperature	Decreased	Decreased

It can be seen from Table 3-2 that within the compositional ranges in this paper, the activator modulus exhibits a higher average increasing rate, indicating that the activator modulus shows a more significant influence on the early age reaction. This is because increasing the slag/fly ash mass ratios accelerates the reaction by increasing the total amount of high reactive phase, while lowering the activator modulus will show a more direct influence by remarkably increasing the alkalinity and providing extra silicate supply in a liquid form. Even though great changes take place in the early hydration stage, the main features of hydrated gel remain unchanged such as main Si-O-T structures, physically bound water content and thermal behaviors. It manifests that the main reaction products of alkali activated slag/fly ash blends in room temperature perform relatively stable properties regardless of the raw material composition and early reaction processes. But slight changes in terminal Si-O bonds and total mass loss show that the two investigated factors could cause the structural changes to some

extent, and the gel characters may change in a more significant way if larger compositional ranges are used.

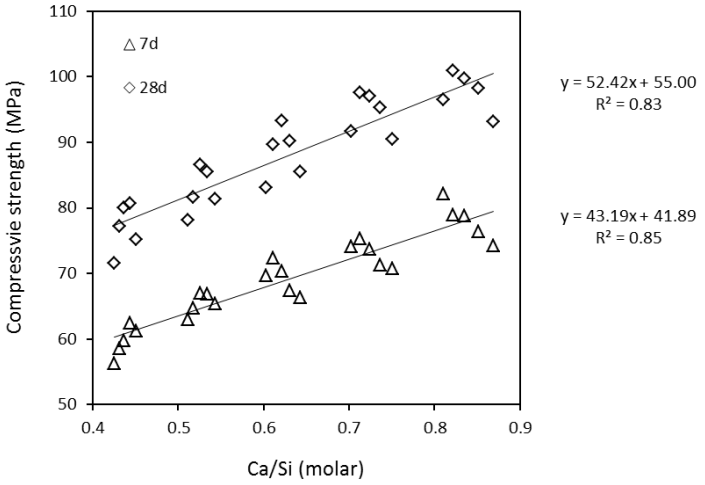

Figure 3-9: The effect of Ca/Si molar ratio on the compressive strength

Figure 3-9 shows the relations between the total Ca/Si molar ratio and the compressive strength after 7 and 28 days of curing, where the chemical composition of the starting materials, including solid precursors and liquid activator, are computed into the molar content. There are five obviously divided groups in both curing ages, this is due to the differences in slag/fly ash mass ratio, while the five points scattered in each group is caused by the changes in activator modulus. This Figure shows clearly that although slag/fly ash mass ratio has a dominating influence on the total Ca/Si ratio, the activator modulus still has a non-ignorable effect. Actually the extra silicate that is provided by the activator contains 6 to 9% by mass of the total binder (from activator modulus 1.0 to 1.8). It can also be found that the calcium content is positively related to the compressive strength in general, which is also confirmed by (Xu and Van Deventer, 2000). Possible explanations for the calcium related strength results are: higher calcium content represents higher amount of reactive phases and more reaction products in the matrix; and/or C-A-S-H type gels exhibit an intrinsic higher strength than other type of gels. It should be noted that the strength variation caused by the activator modulus is comparable with the effects of slag/fly ash mass ratio to some extent, and samples with a lower calcium content could still show a higher strength by adjusting the activator modulus. It reveals that silicate content is as important as calcium content in terms of compressive strength.

3.6 Conclusions

This chapter investigates the synergetic effects of activator modulus and slag/fly ash mass ratios on reaction kinetics, hydrated gel structures and compressive strength of room temperature cured alkali activated slag-fly ash blends. The activator modulus ranges from 1.0 to 1.8 and slag/fly ash mass ratios are between 90/10 to 50/50. The following conclusions can be drawn:

- All tested mixtures show the same typical reaction stages. The initial dissolution time is independent of slag/fly ash mass ratio and activator modulus, but the dissolution and reaction intensity, induction time, are strongly influenced by this two factors. Both increasing the slag/fly ash ratio and lowering the activator modulus would obviously increase the reaction intensity and shorten the main reaction processes, and activator modulus has a more significant influence than slag/fly ash ratio.
- The major reaction products in all mixes are C-A-S-H type gels with chain structure, the formation of this gel is attributed to the massive amount of available calcium in the solution. Highly polymerized N-A-S-H structures are not obviously observed within the mentioned compositional range. Changing the activator modulus and slag/fly ash content within the mentioned range shows very limited influence on the main gel structure.
- All samples show similar thermal properties such as the physically bound water content and gel decomposition temperature, and these characters are independent of activator modulus and slag/fly ash mass ratio. But lowering the activator modulus and increasing the slag/fly ash ratio will slightly increase the total mass loss and decrease the phase changing temperature.
- The compressive strength results show that when increasing the slag/fly ash mass ratios, the optimum activator modulus shifts to higher values in general, this tendency is more significant in early ages. But either too high or too low modulus (1.8 or 1.0 in this case) will lead to relatively low strength. The changes in the optimum parameters in strength indicate that both slag/fly ash ratio and activator modulus are dominating factors, and in order to achieve a desired strength, these two parameters are suggested to be considered simultaneously.

Chapter 4

Binder modification by nano silica and limestone

4.1 Introduction

Nano-silica (NS) has recently been utilized in Portland cement based systems as an effective supplementary cementing binder for the improvement of mechanical properties and microstructure (Pacheco et al, 2013). Due to its considerably fine particle size, nano-silica has been observed to accelerate the hydration process at early ages (Shaikh et al, 2014), refine the pore structure (Said et al, 2012) and enhance the mechanical properties even at small levels of replacement (Shih et al, 2006). Moreover, nano-silica also exhibits ideal pozzolanic activity owing to its amorphous nature and high specific surface area (Qing et al, 2007), which lead to the formation of additional C-S-H gel by reacting with calcium hydroxide and result in a denser matrix (Gaitero et al, 2008). Meanwhile, few attentions have also been paid to apply nano-silica in alkali activated systems. For instance a study on the effect of nano-silica on fly ash based geopolymers showing that increasing the nano-silica content results in the decrease of setting time and the increment of mechanical properties. Microstructure analysis revealed that nano-silica content up to 2% increases the reaction product and densifies the matrix, but higher nano-silica contents show negative effects (Phoo et al, 2014); nano-silica addition of up to 3% in metakaolin based geopolymers results in increased reaction products and an optimum nano-silica content of 1% in terms of strength and porosity was reported (Gao et al, 2013); a nano-silica content of 6% was reported to exhibits appreciable mechanical properties under ambient temperature in fly ash based geopolymers, as well as less water absorption and reduced chloride penetration test (Adak et al, 2014).

On the other hand, limestone powder has also been widely utilized for the purpose of energy saving and carbon reduction in Portland cement systems (Yilmaz and Olgun, 2008). A maximum limestone powder replacement of 35 wt.% is allowed in Europe. Beside the environmental benefits, limestone has also been known to improve the workability and strength by the filler effect (Antonia et al, 2012), to accelerate the hydration of C_3S by providing nucleation sites (Tyditat et al, 2014), to partly participate in the formation of C-S-H gels and to interact with aluminate-containing phases to form monocarboaluminate (Kakali et al, 2000; Bonavetti et al, 2001). Those studies indicate both physical and chemical modifications of limestone powder on the Portland cement system. Meanwhile, limestone also show some beneficial effects in alkali activated systems. A maximum limestone content up to 68 wt.% was applied in sodium carbonate activated slag, the mechanical properties were comparable to Portland cement, while the carbon emission and energy consumption were reduced by more

than 90% (Moseson et al, 2012). A calcite content of less than 20% is reported to benefits the compressive strength of silicate activated metakaolin, higher contents may lead to disruption of the gel structure (Yip et al, 2008). It was suggested that the increase of strength was not only due to the filler effect, as a small amount of released Ca^{2+} from calcite also plays a limited role. It was also reported that limestone slightly promotes the dissolution of metakaolin in alkali activated systems, and both activator concentrations and curing temperature significantly affect the leaching equilibriums of Ca, Al and Si (Cwirzen et al, 2014).

As can be noticed, previous studies showed the superiority of applying both nano-silica and limestone powder in alkali activated low calcium systems. However, there are limited mechanism studies and performance evaluations concerning the their roles in the blended alkaline system, where large amounts of reactive calcium, silica and alumina units are present simultaneously, different reacted gels are coexistent, and the synthesizing parameters and curing conditions exhibit a more sensitive influence on the final performance. The purpose of this study is to understand the influence of nano-silica and limestone powder on some fresh behaviors, early age reaction kinetics, mechanical properties and reaction products of alkali activated blended systems, and evaluate the feasibility of applying them as additives.

4.2 Nano silica modification

4.2.1 Flowability and setting times

The activator used in this work has an equivalent sodium oxide (Na_2O) content of 5% and an activator modulus of 1.4 for all mixes. The water/binder ratio was kept constant as 0.35 in all mixtures. The slag/fly ash ratios of 70/30 and 30/70 by mass and nano-silica replacement from 0% to 3% by mass were used. The detailed mix proportions are listed in Table 4-1.

The slump flows of the fresh alkali activated slag-fly ash pastes with nano-silica replacements from 0% to 3% are depicted in Figure 4-1. It shows that with a constant nano-silica content, a lower slag/fly ash ratio exhibits a better workability. For instance, in samples without nano-silica addition, when the slag/fly ash ratio changes from 70/30 to 30/70, the slump flow increases from 30.7 to 32.4 cm; similar results are also found in mixes with the nano-silica replacements. This phenomenon is in agreement with previous studies that a lower slag to fly ash ratio exhibits a better flowability in their blends, which can be explained by the morphology differences between slag and fly ash, as slag shows a higher water demand than fly ash due to its angular particle shape and larger surface area (Yang et al, 2009). On the other hand, compared to the effect of slag/fly ash ratio, the nano-silica content exhibits a more prominent influence on flowability even at small dosages. The slump flow dramatically decreases with the increase of nano-silica content: for the samples with a slag/fly ash ratio of 70/30, the slump flow is decreased by 18.2%, 32.2% and 45.9% when the nano-silica content increases from 1% to 2% and 3%, respectively; similarly, decreasing rates of 16.8%, 30.8% and 42.2% are shown in mixtures with a slag/fly ash ratio of 30/70.

Table 4-1: Mix proportions of AA slag-fly ash blends with nano-silica addition

Mixture	Activator	Solid raw materials (wt.%)			w/b
		Slag	Fly ash	Nano-silica	
A730	Na_2O: 5% Ms: 1.4	70	30	0	0.35
A370		30	70		
A731		69.3	29.7	1	
A371		29.7	63.9		
A732		68.6	29.4	2	
A372		29.4	68.6		
A733		67.9	29.1	3	
A373		29.1	67.9		

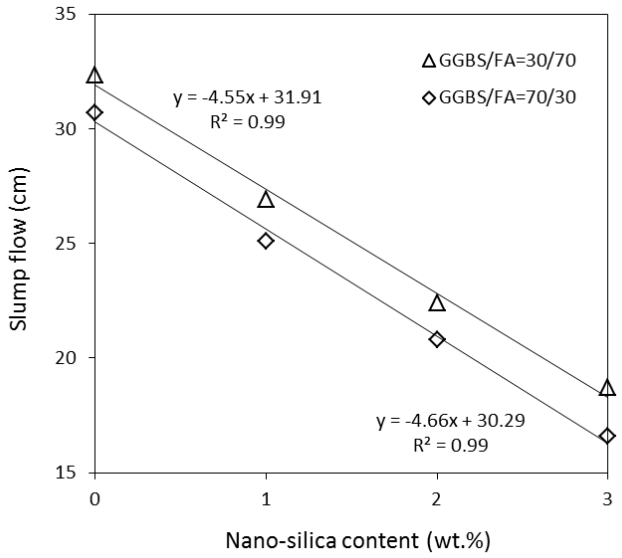

Figure 4-1: Slump flow of AA slag-fly ash blends with nano-silica addition

The remarkable reduction of slump flow could be attributed to the much finer particle size of nano-silica (d50 of 0.12 μm) than slag and fly ash (d50 of 12.43 and 22.06 μm, respectively), therefore an especially large surface area in total is presented as a result, which leads to a decrease in slump flow. Meanwhile, due to the high reactivity of nano-silica particles that contain unsaturated Si-O bonds, a certain amount of water in the solution can be retained around the nano-silica particles with the formation of Si-OH (Mukharjee and Barai, 2014; Boshehrian and Hosseini, 2011). This process may also contribute to the significant reduction of slump flow by decreasing the total effective mixing water.

Figure 4-2 presents the influence of nano-silica and slag/fly ash ratio on the initial and final setting times of alkali activated slag-fly ash blends. It can be seen that for a constant nano-silica content, samples with a lower slag/fly ash ratio exhibit longer initial and final setting times in general. For instance, the sample with a slag/fly ash ratio of 70/30 and without nano-silica shows an initial setting time of 27 mins, while this value increases to 76 mins in the sample with a slag/fly ash ratio of 30/70; and the final setting time also increases from 71 mins to 128 mins. The significant influence of slag content on the setting times of alkali activated salg-fly ash blends is also reported in previous study (Jang et al, 2014). The acceleration effect of slag on setting times is mainly due to its vulnerable amorphous structure that consists of large amount network-modifying cations (especially Ca), which exhibit high reactivity under alkali conditions. Thus a faster reaction process and shorter setting time are shown as a result of the faster dissolution rate of Ca, Si and Al units from slag and higher total amount of dissolved units in the slag-fly ash blends.

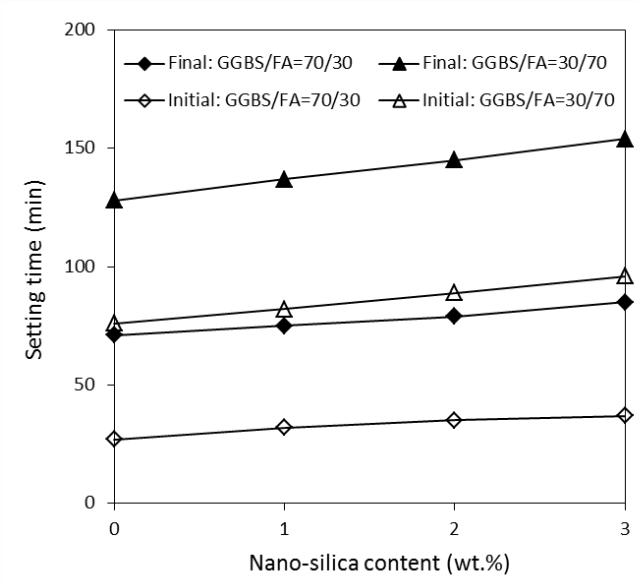

Figure 4-2: Setting time of AA slag-fly ash blends with nano-silica addition

Concerning the effect of nano-silica, it can be seen that both initial and final setting times are gradually increasing with the increase of nano-silica content, and its effect on setting time is more significant in mixtures with a lower slag/fly ash ratio. Specificly, the initial/final setting times of slag/fly ash ratio of 70/30 mixes increase from 27/71 mins to 37/85 mins when the nano-silica replacement increases from 0% to 3%; while for samples with a slag/fly ash ratio of 30/70, the increment is from 76/128 mins to 96/154 mins. However, this result is contrary to most of the investigations about the effect of nano-silica on setting time in Portland cement systems (Luciano et al, 2009; Zhang et al, 2012), in which cases the nano-silica provides additional nucleation sites for the formation and growth of reaction products, so the reaction process is accelerated.

4.2.2 Reaction kinetics

The normalized heat flow of alkali activated slag-fly ash blends (with a slag/fly ash ratio of 70/30 and nano-silica replacement from 0% to 3%) within the first 72 h are shown in Figure 4-3. The heat release peaks in the dissolution stage are not shown in this figure due to their much higher magnitude. It can be seen that for samples without nano-silica addition, the heat release peak in the acceleration stage is located at around 8.3 h after mixing; while as the nano-silica content increases, this peak slightly shifts to longer times with lower intensities. Such relatively slight but detectable changes during the main reaction stage indicate that the reaction of alkali activated slag-fly ash blends is retarded to some extent in the presence of nano-silica.

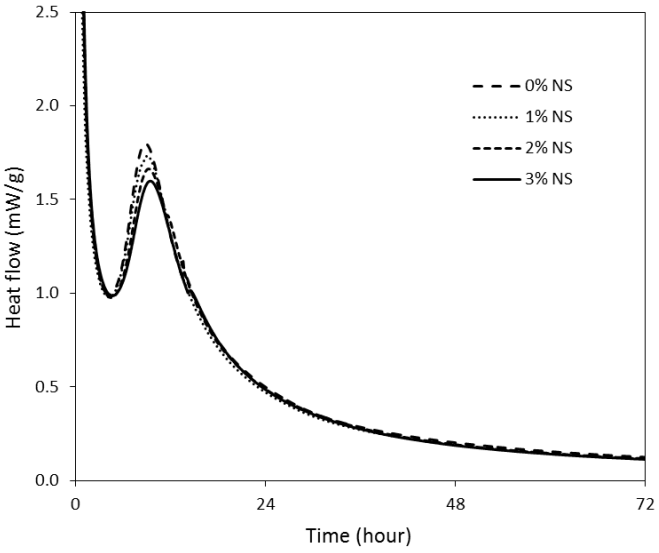

Figure 4-3: Normalized heat flow of AA slag-fly ash (70/30) pastes with nano-silica addition

This phenomenon is in agreement with the setting time results in this study and confirms again the retarding effect of nano-silica on the early age reaction. It is suggested that the isothermal calorimeter results observed in this study is a combined effect of the following factors: (1) a certain amount of nano-silica is dissolved during the early age and leads to an increment of the initial silica content in the solution, which delays the reaction of slag and fly ash. It has been known that the first step of alkali activation is the dissolution of raw materials, and during this process the Si, Ca and Al units are dissolved from the solid precursors and become available in the solution for the further reaction. Due to the fine particle size and high surface area of nano-silica, the dissolution of Si units also takes place in nano-silica particles and faster than that in slag and fly ash, which increases the initial silica content in solution and retards the dissolution of Si from slag and fly ash to some extent. Finally, the heat release peak is delayed as a result. (2) The addition of nano-silica accelerates the reaction process. The fine nano-silica particles that are not dissolved initially work as additional nucleation sites, which promote the formation and growth of reaction products from the dissolved units. Consequently, the reaction process is accelerated. (3) The incorporation of nano-silica leads to a decrease of effective slag content in the system, which leads to the decrease of the reaction intensity. In this case the nano-silica addition decreases the total slag content, therefore less presented slag (available Ca, Si units) results in a less intensive reaction process.

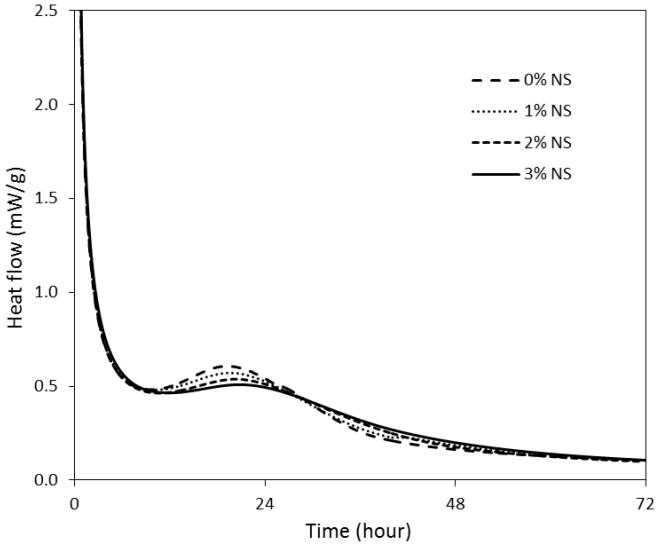

Figure 4-4: Normalized heat flow of AA slag-fly ash (30/70) pastes with nano-silica addition

In overall, as a final apparent result of the three influential factors analyzed above, the reaction process is slightly delayed with lower peak intensities when nano-silica is added. However,

more studies are needed to be carried out in order to clarify the behavior of nano-silica in detail. Figure 4-4 illustrates the normalized heat flow of samples with a slag/fly ash ratio of 30/70 and nano-silica replacement from 0% to 3%. Compared to the samples with a slag/fly ash ratio of 70/30, it can be seen that both the induction and acceleration stages are remarkably retarded. For instance, the induction period is located at around 3.7 h in mixes with a slag/fly ash ratio of 70/30, while it delays for approximately 4.5 h when changing the slag/fly ash ratio to 30/70. Similarly, the acceleration peak shifts from about 8.3 h to 20 h, also the peak intensity decreases from about 1.5 mW/g to 0.5 mW/g. Those changes demonstrate that the slag/fly ash ratio shows a dominant influence on the early age reaction, namely increasing the slag content can effectively accelerate the main reaction stage and result in a more intensive reaction. This is due to the intrinsic differences in the amorphous structure between slag and fly ash, where slag has a higher Ca content that leads to a more disordered glassy framework than aluminosilicates dominated structure, thus the slag exhibits a much higher reactivity than fly ash under alkali activation. In addition, based on the presented experimental results, it can be concluded that the early age reaction is mainly controlled by the relative slag content in the alkali activated slag-fly ash blends. Besides, similar to the results that are shown in Figure 4-3, the addition of nano-silica also slightly retards the reaction and decreases the intensity of the main reaction peak, but its influence on the reaction process is relatively small compared to effect of slag content.

4.2.3 Thermal analysis

The thermogravimetry results of samples with a slag/fly ash ratio of 70/30 and nano-silica additions up to 3% are presented in Figure 4-5. It can be seen that all mixes exhibit a significant mass loss before around 110 °C, mainly due to the loss of physically bound water within the paste. The evaporable water content is around 15.8% in all samples, indicating that the nano-silica addition has a limited effect on the physically bound water content.
Afterwards, all mixtures show a negligible mass loss between 105 °C and 160 °C, followed by a gradual decrease in mass until heated to around 700 °C. The continuous mass loss after around 160 °C is assigned to the gradual decomposition of the reaction products which leads to the release of chemically bound water within the generated gels. After around 700 °C, all mixes present a slight and moderate mass loss until 1000 °C; also no other abrupt mass losses are shown between 105 °C and 1000 °C. The thermogravimetry results reveal that the reaction products are mainly amorphous gels with bound water. It can be seen that as the nano-silica content increases, there is a slight but detectable increase in mass loss between 160 °C and 1000 °C. For instance, when increasing the nano-silica content from 0% to 3%, the mass loss between 160 °C and 1000 °C gradually increases from 4.69% to 5.47%. It implies that the addition of nano-silica slightly increases the amount of chemically bound water content. This is probably due to the fine particle size and high reactivity of nano-silica, which may not only

work as a nucleation site, but also provide extra reactive silica source, and both effects help to bond more water within the matrix.

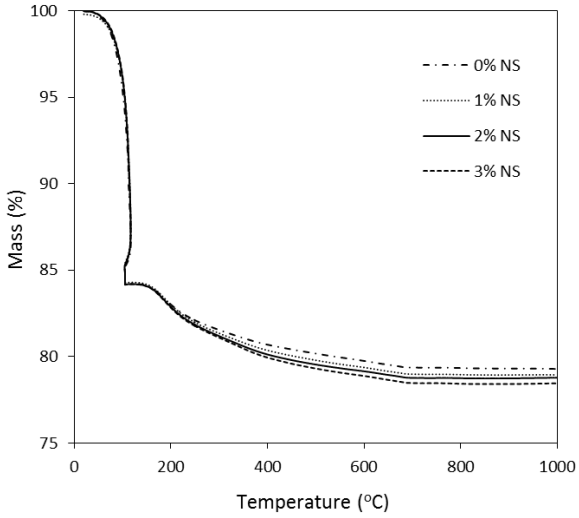

Figure 4-5: TG analysis of AA slag-fly ash (70/30) pastes with nano-silica addition

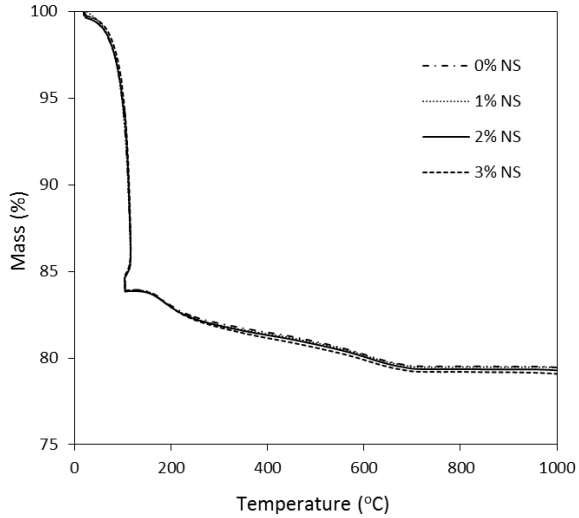

Figure 4-6: TG analysis of AA slag-fly ash (30/70) pastes with nano-silica addition

Figure 4-6 depicts the thermogravimetry results of samples with a slag/fly ash ratio of 30/70. It is obvious that these mixes exhibit a similar mass loss procedure as the ones with the slag/fly

ash ratio of 70/30. All samples show an evaporable water content of around 16.1%, which is at the same level as the ones shown in Figure 8. Also, the mass losses between 160 °C and 1000 °C in samples without nano-silica are similar, which is 4.69% and 4.31% in samples with a slag/fly ash ratio of 70/30 and 30/70, respectively. However, there is a slight difference in the mass loss between 160 °C and around 500 °C, as can be seen that samples with a slag/fly ash ratio of 70/30 present a more abrupt decrease. Concerning the effect of nano-silica, it is clear that its beneficial effect on chemically bound water content becomes less significant. It is shown that when increasing the nano-silica content from 0% to 3%, the mass loss between 160 °C and 1000 °C is increased by 16.6% in mixes with a slag/fly ash ratio of 70/30, while this value is only 7.7% in mixes with the slag/fly ash ratio of 30/70. It is indicated that the nano-silica may increase the bound water content by mainly influencing the reaction of the calcium enriched slag, since the main reaction product is a Ca and Si dominated structure with high silicate contents; while the benefit of nano-silica may become limited when large amount of silicate is present (slag/fly ash ratio of 30/70), and its main contribution may turn into the filler effect.

4.2.4 Compressive strength

The compressive strength of samples with a slag/fly ash ratio of 70/30 and nano-silica content from 0% to 3% is shown in Figure 4-7. For mixes without nano-silica addition, the compressive strength is 53.5 MPa after 3 days of curing; and it increases to 66.6 MPa at 7 days and 90.2 MPa at 28 days. It has been known that the alkali activated slag usually exhibits relatively high strength at both early and later stages, and the results in this study show that satisfying strengths that suitable for high performance applications can be obtained in ambient temperature cured slag-fly ash blends.

When nano-silica is incorporated, the compressive strength is slightly increased at 3 days, and it can be seen that when increasing the nano-silica content from 0% to 3%, the compressive strength gradually increases from 53.5 MPa to 57.9 MPa. It should also be noted that when the nano-silica content reaches 2%, the strength increment is no longer significant when more nano-silica is incorporated. Similarly, at the age of 7 days, the compressive strength is increased from 66.6 MPa to 71.6 MPa when increasing the nano-silica content up to 2%, but the strength is slightly reduced to 69.5 MPa when the nano-silica content increases to 3%. It indicates that a nano-silica content of around 2% is the optimum in terms of strength in both cases. In addition, it can be observed that the strength increasing rate is decreased as the increase of nano-silica content. For instance, the compressive strength is increased by 6.4% when increasing the nano-silica content from 0% to 1%, while this value is only 1% when the nano-silica content changes from 1% to 2%. Compared to the effect of nano-silica on strength in cement based system, the nano-silica exhibits a less significant influence in alkali activated systems (Kuo et al, 2006; Ye et al, 2007). One possible explanation is that in cement based system, the nano-silica not only works as a micro-filler that refines the pore structure, but also

effectively consumes the calcium hydroxide which leads to the formation of extra hydrated gels; then the strength can be remarkably increased.

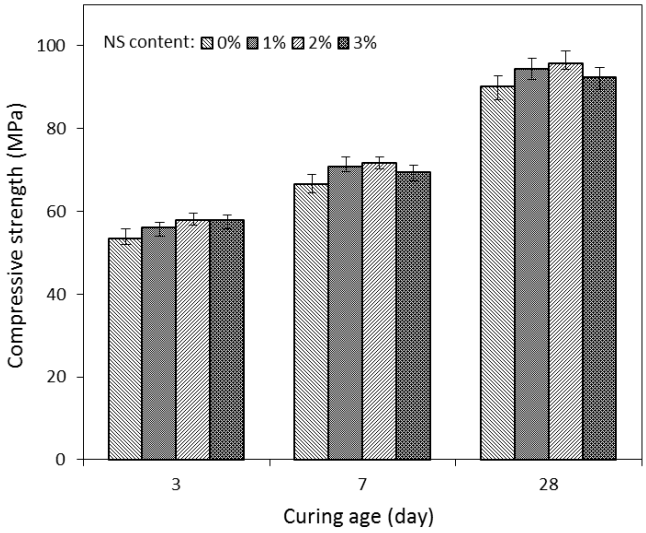

Figure 4-7: Compressive strength of AA slag/fly ash blends (70/30) with nano-silica addition

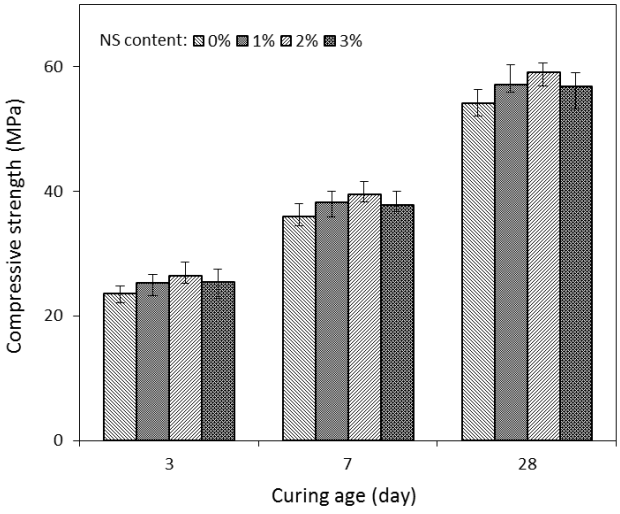

Figure 4-8: Compressive strength of AA slag/fly ash blends (30/70) with nano-silica addition

While in alkali activated system, as can be seen from the TG/DSC analysis, no significant amount of calcium hydroxide is presented, thus the pozzolanic effect of nano-silica is limited. Therefore, the nano-silica may only benefit the compressive strength by pore refinement due to the filler effect, as well as the additional bound water due to the extra provided silica from nano-silica. Concerning the 28 days strength, when increasing the nano-silica content up to 3%, the compressive strength firstly increases from 90.2 MPa to 95.9 MPa, then decreases to 92.4 MPa, showing again an optimum nano-silica content of around 2%.

Figure 4-8 depicts the compressive strength results of samples with a slag/fly ash ratio of 30/70. It is obvious that the strength is remarkably lower than those with a slag/fly ash ratio of 70/30. This is because of the significant effect of slag content on strength, which has been well discussed in the previous studies. It can be seen that without nano-silica addition, the 3, 7 and 28 d strength are 23.6 MPa, 35.9 MPa and 54.1 MPa, respectively. The compressive is increased by 52.1% and 129% at these three typical curing ages, while in samples with a slag/fly ash ratio of 70/30, these values are 24.5% and 68.6%, indicating that there is a difference in strength development between samples with different slag/fly ash ratios. In other words samples with a higher slag content shows a higher early strength and a lower increasing rate. Similar to the results in Figure 4-7, the compressive strength firstly increases when increasing the nano-silica content up to 2%, and then slightly reduces when the nano-silica content reaches 3%; and this tendency becomes more significant at longer ages. The optimum nano-silica content of 2% in terms of compressive strength is shown in all mixes, and the highest strength present in samples with 2% nano-silica are 26.4 MPa at 3 days, 39.4 MPa at 7 days and 59.1 MPa at 28 days, respectively.

4.2.5 Water permeable porosity

Figures 4-9 shows the relations between the strength, nano-silica content and porosity of alkali activated slag-fly ash blends after 28 days of curing. It can be seen that the compressive strength increases with the reduction of porosity in general; it confirms again the inverse relationship between the strength and porosity in porous materials.

Also, the porosity decreases with the increase of nano-silica content in general, while when increasing the nano-silica content up to 3%, the reduction of porosity becomes less significant or even slightly increases. As presented in Figure 4-9 (a), when increasing the nano-silica content from 0% to 2%, the compressive strength increases from 90.2 MPa to 95.9 MPa while the porosity decreases from 26.4% to 24.2%. However, the further increase of nano-silica content to 3% leads to a slight decrease of strength and increase of porosity. One possible explanation for this phenomenon is that a suitable content of nano-silica will refine the pore structure by filler effect and generate more reaction products; while higher contents lead to a significant reduction of workability (increased cohesiveness), which may result in an increase of the air content within the paste, then the porosity is increased as a result. Figure 4-9 (b) shows the results of samples with a slag/fly ash ratio of 30/70, it is obvious that when

compared to the results in Figure 4-9 (a), higher porosities as well as lower compressive strengths are presented. This is due to the relatively low reactivity of fly ash under ambient temperature and its relatively high content in the slag/fly ash blends, which result in a lower content of reaction products, thus less dense matrixes and lower strengths are exhibited. Specifically, when increasing the nano-silica content from 0% to 3%, the porosity decreases from 30.5% to 27.2%, while the compressive strength firstly increases from 54.1 MPa to 59.1 MPa, then slightly decreases to 56.8 MPa at the nano-silica dosage of 3%.

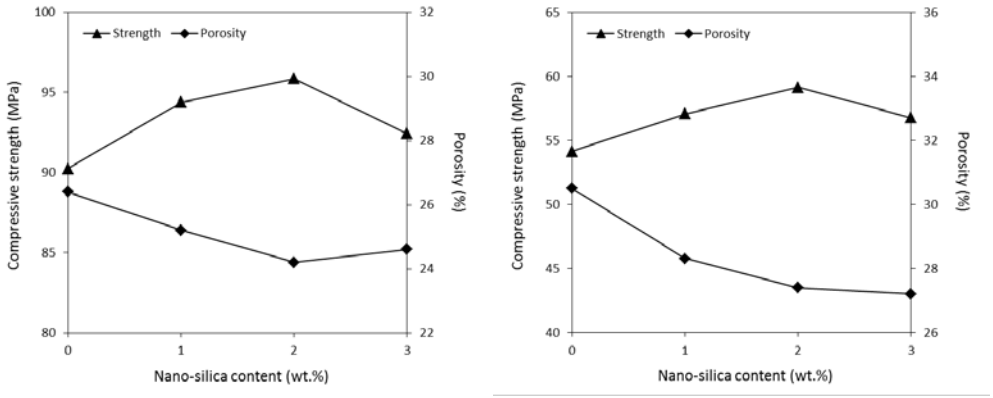

(a) (b)

Figure 4-9: Relations between 28d strength, porosity and nano-silica content (a: slag/fly ash = 70/30; b: slag/fly ash = 30/70).

4.3 Limestone powder modification

4.3.1 Fresh behaviors

The activator used in this study has an equivalent sodium oxide (Na_2O) content of 5.7% and an activator modulus (Ms) of 1.4 for all mixes, determined based on a preliminarily study, which would provide sufficient alkalinity without efflorescence. Three levels of slag content (60, 50 and 40% by mass) and limestone additions from 0% to 30% by mass were used. The water/binder ratio by mass was 0.35 for pastes and 0.45 for mortar specimens. The binder/sand ratio was 1/3 for all mortar samples. The detailed mixture proportions are listed in Table 4-2.
The slump flow of the fresh alkali activated slag-fly ash-limestone pastes is presented in Figure 4-10. All samples show satisfying flowabilities that range from 29.3 to 33.5 cm. For samples without limestone powder addition, the slump flow increases from 29.3 to 31.4 cm when the slag content decreases from 60% to 40%. A similar tendency is also found in samples with a constant limestone powder replacement, namely that a lower slag content exhibits a better flowability. This is in agreement with previous studies that indicated that alkali activated fly

ash shows better workability than slag, and a higher fly ash content in the slag/fly ash mixes leads to an improvement of flowability (Nath and Sarker, 2014; Deb et al, 2014). This phenomenon can be explained by the higher water demand of slag caused by its angular particle shape and larger surface area compared to fly ash. Besides, the addition of limestone powder also exhibits a positive effect on flowability. It can be seen that in samples with a constant slag content, the slump flow increases with the increasing limestone content in all cases.

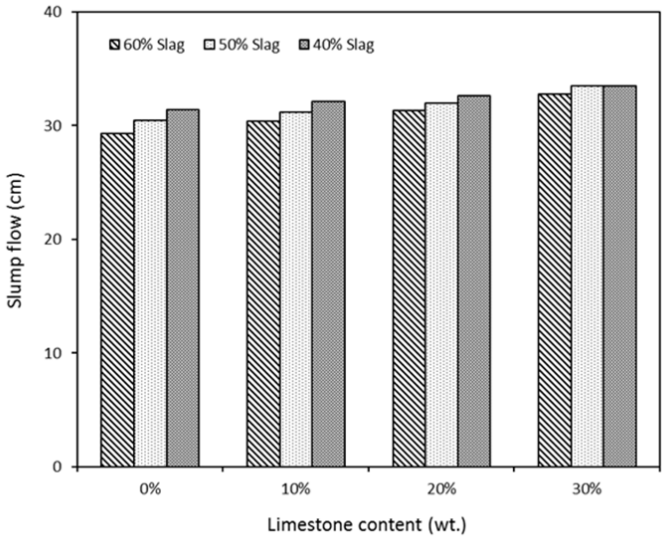

Figure 4-10: Slump flow of AA-slag-fly ash-limestone pastes with a w/b of 0.35

The influence of the slag content on workability seems to be weakened when a higher limestone content is used. It should be noted that for a constant slag content, the increased limestone replacement will also lead to the reduction of fly ash content in the slag-fly ash-limestone ternary blends. The improved flowability in samples with higher limestone contents may imply that the limestone powder presents a better flowability in alkali solutions than fly ash in this case. Another possible explanation for the improved flowability is that the particle packing of the paste also affects the water demand. By using fine limestone powders in slag and fly ash mixes, more fine particles with relatively low water demand will be filled in the micro voids, then a better particle packing is achieved; therefore, more available water can be provided to lubricate the particles resulting in a higher slump flow (Yu, 2010).

In terms of the mortar mixtures, a higher water/binder ratio of 0.45 was used in order to meet the water demand of the fine aggregates. The relations between the binder composition and the slump flow for mortars are depicted in Figure 4-11. All mixes show ideal slump flows between 23.2 and 27.4 cm without jolting, with no segregation observed. Similar to the results of paste

samples, the workability is improved when lowering the slag content and/or increasing the limestone content.

Table 4-2: Mix proportions of alkali activated materials with limestone addition

	Activator	Solid raw materials			Sand (g)	w/b
		Slag (wt.%)	Fly ash (wt.%)	Limestone wt.%		
S60F40L0	Na_2O: 5.7% Ms: 1.4	60	40	0	0 (paste) 300 (mortar)	0.35 (paste) 0.45 (mortar)
S50F50L0		50	50			
S40F60L0		40	60			
S60F30L10		60	30	10		
S50F40L10		50	40			
S40F501L0		40	50			
S60F20L20		60	20	20		
S50F30L20		50	30			
S40F40L20		40	40			
S60F10L30		60	10	30		
S50F20L30		50	20			
S40F30L30		40	30			

Figure 4-12 depicts the influence of the starting materials' composition on the initial and final setting times of alkali activated slag-fly ash-limestone blends. It can be seen that both the initial and final settings are retarded when lowering the slag content. For instance, the mixtures with a slag content of 60% show an initial setting time of 45 min, which increases to 55 and 68 min when the slag content is reduced to 50% and 40%, respectively. Similarly, the final setting time increases from 93 min to 115 min as the slag content decreases from 60% to 40%. The significant influence of slag on setting times is attributed to its high reactivity under alkali conditions, as the relatively fast dissolution rate of Ca, Si and Al units from the slag and the higher total amount of those units (especially Ca) that are present in the solution accelerate the formation rate of reaction products and the setting processes.

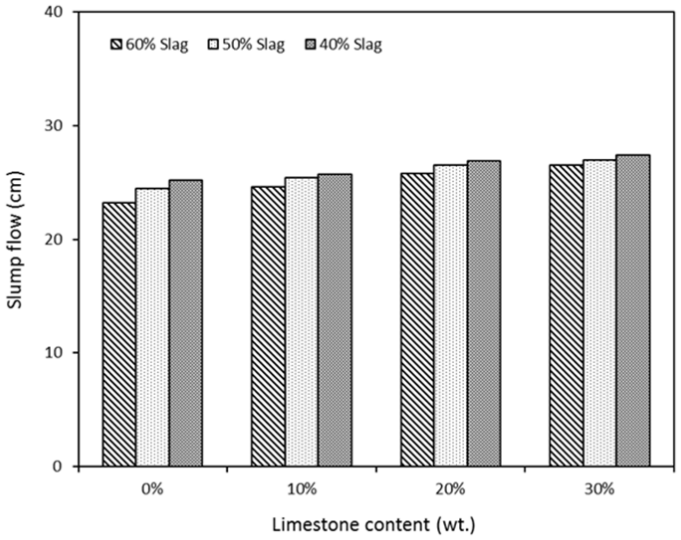

Figure 4-11: Slump flow of AA-slag-fly ash-limestone mortars with a w/b of 0.45

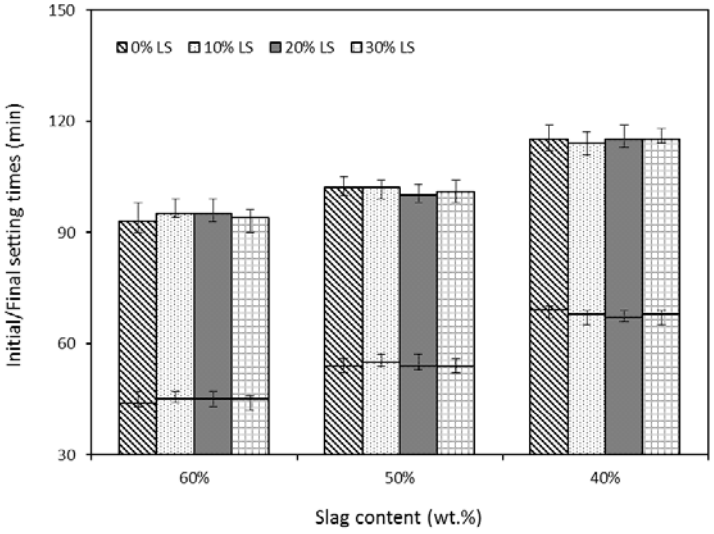

Figure 4-12: Setting times of AA-slag-fly ash-limestone pastes

On the other hand, for a constant slag content, it can be concluded that the influence of limestone and fly ash proportion on the initial and final setting times is negligible, since the variations in the initial and final setting times caused by the composition changes of limestone

and fly ash are within only 3 min in all cases. It also implies that the fly ash exhibits similar and very low reactivity as limestone powder during the initial stage of reaction. Thus from the angle of the raw material composition, the slag content appears to be the only key factor that influences the setting behaviors of the alkali activated slag-fly ash-limestone blends cured under ambient temperature.

4.3.2 Reaction kinetics

The normalized heat flow of alkali activated slag-fly ash-limestone blends (with a slag content of 60% and limestone addition from 0% to 30%) within the first 72 h are shown in Figure 4-13. It shows that as the limestone content increases, the heat evolution peak slightly shifts to earlier locations with higher intensities. It indicates that the reaction process of alkali activated slag-fly ash blends is slightly accelerated in the presence of limestone powder. This is in agreement with previous research on the effect of limestone powder in Portland cement hydration (Lothenbach et al, 2008). The incorporation of limestone powder brings more fine particles in the system, which provides additional nucleation sites for the formation and growth of reaction products, then as a result the reaction process is accelerated (Pera et al, 1999).

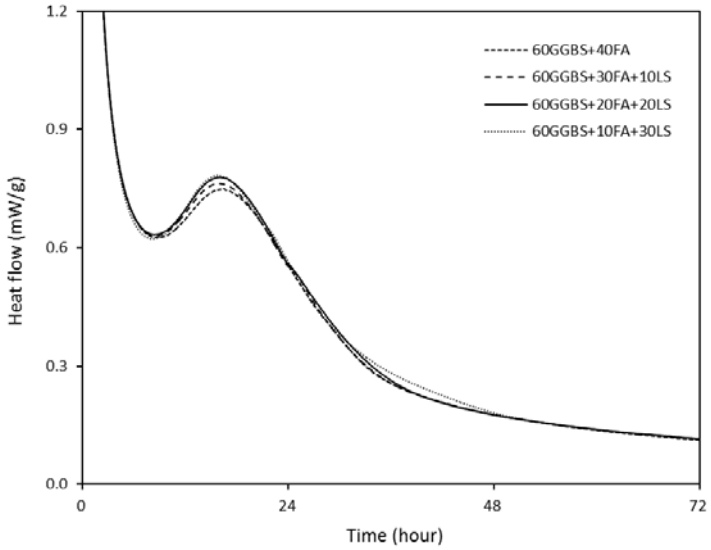

Figure 4-13: Normalized heat flow of AA slag-fly ash-limestone pastes with 60% Slag

It can be seen that the induction period is also slightly shortened with the increasing limestone content. During this stage, the newly formed reaction products cover the surfaces of unreacted particles (Rajaokarivony et al, 1990) and temporarily limit the reaction process. Further reaction continues when the alkalis penetrate the covered layers and reach the raw materials

again. Considering the induction period is promoted in a limited manner, it is more likely that the acceleration in this stage is due to the micro-nucleation effect of the fine particles from limestone powder and the better dispersion of slag, rather than a chemical process.

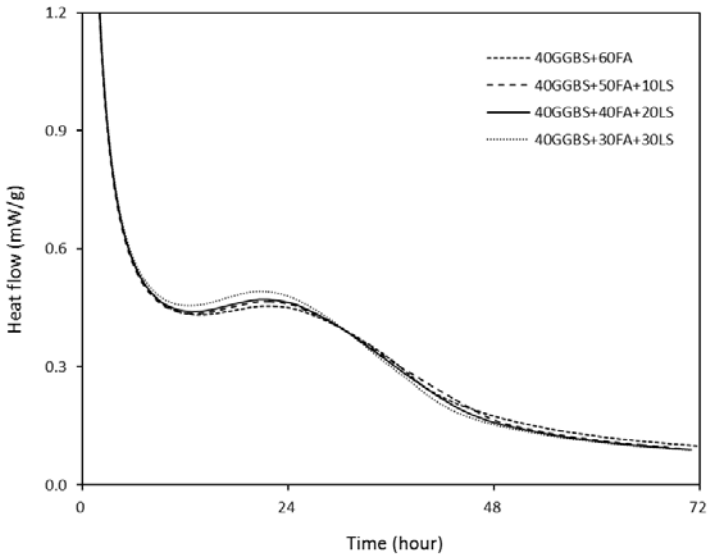

Figure 4-14: Normalized heat flow of AA slag-fly ash-limestone pastes with 40% Slag

Figure 4-14 illustrates the heat evolution curves of samples with a slag content of 40% and limestone additions up to 30%. It can be noticed that both the induction and acceleration stages are significantly retarded when compared to the mixes shown in Figure 4-13. For instance, the induction stage is around 7.5 h in samples with a slag content of 60%, while it shifts to approximately 11 h when the slag content decreases to 40%, also a considerably prolonged induction time and reduced heat flow can be observed. Similarly, when lowering the slag content from 60% to 40%, the acceleration peak shifts from about 16 to 20 h with a decreased peak intensity from about 0.8 to 0.5 mW/g. Those changes demonstrate the remarkable effects of the slag content on the early age reaction. The glassy structure of slag is mainly formed by Si and Al cations, and the Ca cation works as a network modifier. Under alkali activation, the breakdown of a calcium enriched structure is easier than Si and Al dominated structures such as fly ash. And this phenomenon is more significant at ambient temperature. Thus, a higher slag content will lead to a larger amount of available Si, Al and Ca units in solution, and consequently a more intense dissolution and reaction process. Similar to the results shown in Figure 4-13, an evident promotion in induction and acceleration stage due to the increase of limestone powder content is observed. But compared to the significant changes caused by slag, the effect of limestone powder on the early age hydration is at a relatively small scale.

4.3.3 XRD analysis

The XRD patterns (Cu radiation) of unreacted slag and fly ash are shown in Figure 4-15, as well as the samples with a slag content of 60% and limestone additions from 0 to 30%. It can be seen that the original slag is mainly amorphous without significant crystalline phases, and shows a peak hump between 25 and 35° due to the amorphous components; while the unreacted fly ash contains crystalline phases such as quartz (SiO_2), mullite ($Al_6Si_2O_{13}$), maghemite and hematite (Fe_2O_3) with a broad amorphous hump between 15 and 30°.

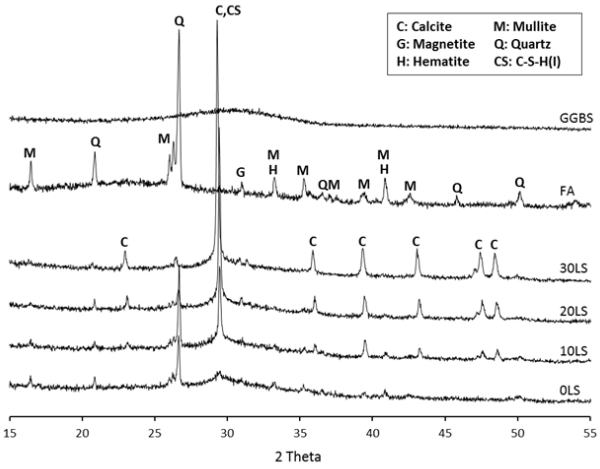

Figure 4-15: XRD patterns of slag, fly ash and AA slag-fly ash-limestone pastes

The differences in the location of the amorphous hump indicate the structural differences between the slag and fly ash. After activation, the characteristic peaks of quartz, mullite and maghemite/hematite from fly ash remain. The incorporation of limestone leads to the presence of calcite peaks. The intensity changes of those crystalline peaks in the reaction products are due to the different relative content of fly ash and limestone in each mixture. All samples show a main reaction product at around 29.5°, which is identified as a poorly crystallized C-(A)-S-H gel (type I, PDF#00-034-0002). This is in accordance with the previous study that the main reaction product is characterized by terminal Si-O bonds and chain structure. Besides, no significant newly formed crystalline phases are observed until the age of 28 d and the reaction products remain amorphous. As can be noticed, there is no significant change in the intensity and location of C-(A)-S-H peaks when slag content is kept constant, implying the limited influence of both limestone powder and fly ash content on the gel structure of the main reaction products until the age of 28 d.

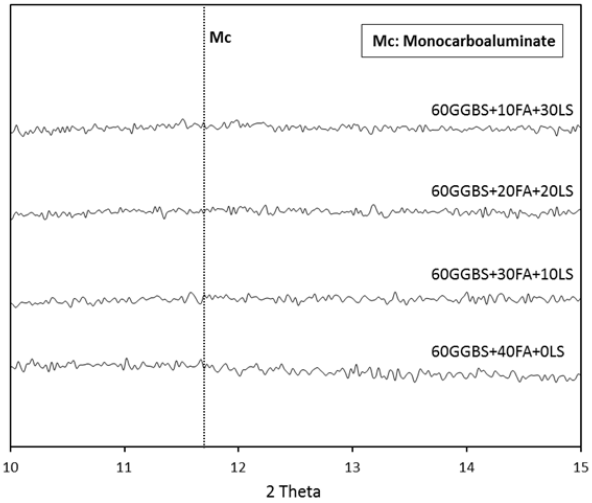

Figure 4-16: XRD patterns of alkali activated slag-fly ash-limestone pastes at low angles

In addition, previous studies concluded that the presence of limestone powder would lead to the formation of monocarboaluminate in both Portland cement and alkali activated systems, especially in high aluminate conditions (i.e. high C_3A, C_4AF content; fly ash/metakaolin addition), and the formation of those phases are detectable after 28 d of curing (Thongsanitgarn et al, 2014; Voglis et al, 2005). In order to identify whether this phase is formed in silicate activated slag-fly ash-limestone blends, an XRD observation that focused on low angles was conducted and the result is shown in Figure 4-16. It can be seen that the characteristic peak of monocarboaluminate, which is usually shown at around 11.7° (Weerdt et al, 2011), is not observed in this study. Thus, it can be concluded that no evident chemical reaction took place between the limestone powder and the aluminate units in this case, or the chemical reactions involving the limestone powder did not result in the formation of additional crystalline phases.

4.3.4 TG/DSC analysis

The thermogravimetry results of samples with a slag content of 60% and limestone additions up to 30% are presented in Figure 4-17. All samples exhibit a remarkable mass loss before around 110 °C, which is assigned to the loss of physically bound water within the paste. Specimens without limestone show an evaporable water content of 16.1%, which is slightly lower than the ones with limestone addition, but there is no further increase in this value when increasing the limestone content from 10% to 30%. After the evaporation of the physically bound water, all samples show a negligible mass loss between 105 and 180 °C, followed by a gradual decrease in mass until heated to around 600 °C. After around 600 °C, mixes without

limestone powder show a stable curve with only a slight mass loss until 1000 °C, and no other abrupt mass losses are observed between 105 and 1000 °C. This reveals that the reaction products are mainly amorphous gels with bound water. When the limestone powder is incorporated, samples show a remarkable mass loss between 600 and 800 °C, which is mainly due to the decomposition of the calcium carbonates.

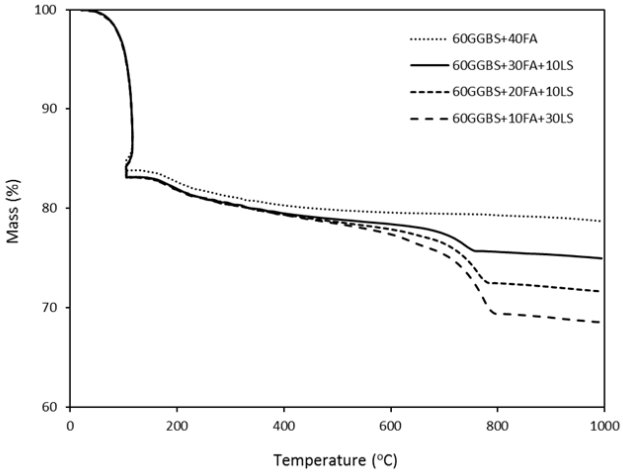

Figure 4-17: TG analysis of alkali activated slag-fly ash-limestone pastes

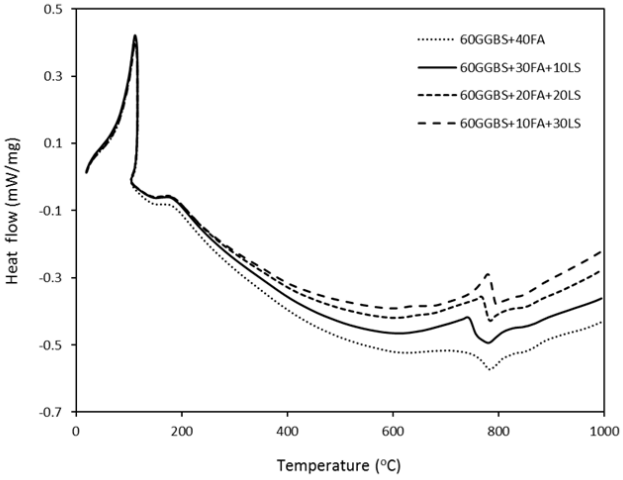

Figure 4-18: DSC analysis of alkali activated slag-fly ash-limestone pastes

The corresponding differential scanning calorimeter (DSC) results are depicted in Figure 4-18. The heat absorption peak at around 110 °C is associated with the evaporation of the physically

bound water. The smooth absorption peak at around 180 °C indicates the decomposition of the reaction products, then the gradual decomposition processes including the loss of chemically bound water take place. It can be seen that as the limestone powder content increases, the heat absorption peak at around 750 °C becomes more significant, representing a more intensive decomposition process due to the higher content of calcium carbonate. It should be noted that all samples also show an exothermic peak at around 800 °C, while no remarkable changes are observed in TG analysis at the same temperature. This heat release peak is attributed to the formation of more ordered crystalline phases under high temperature.

Based on the understandings above, a calculation on the physical and chemical bound water contents was carried out in order to study the effect of limestone powder on the composition of reaction products. The physically bound water content was calculated as the mass loss before 105 °C; the chemically bound water content in each mix is calculated by the mass loss between 105 °C and 1000 °C, with the exclusion of the mass loss due to the incorporated limestone. The mass loss of limestone between 105 °C and 1000 °C is 43.01% according to the TG analysis, this value includes the mass loss of calcium carbonate and the impurities from limestone powder; the calculated total mass includes the alkali activator and solid raw materials.

Table 4-3: Calculation of bound water content (wt.%)

	60GGBS 40FA 0LS	60GGBS 30FA 10LS	60GGBS 20FA 20LS	60GGBS 10FA 30LS
Mass loss between 105 °C -1000 °C	5.09	8.11	11.46	14.53
Limestone powder incorporated	0	6.70	13.38	20.07
Mass loss of limestone powder	0	2.88	5.75	8.64
Chemical bound water	5.09	5.23	5.71	5.89
Physical bound water	16.1	16.9	16.9	16.9

The results are presented in Table 4-3, where it can be seen that the addition of limestone powder leads to a slight increase in the total chemical water content. This phenomenon can be partly explained by the XRD results in this study that the addition of limestone powder does not evidently lead to the formation of additional reaction products, thus no remarkable amount of extra bound water can be observed. However, it is possible that the additional nucleation sites that are provided by the fine limestone particles promote the formation of hydrated gels and refine the pore structures, then result in a slightly increased physically and chemically

bound water contents; or a slight but non-ignorable amount of Ca^{2+} is released from the fine limestone particles under alkali activation, then participates in the reaction process and leads to a slight increase in the bound water content.

4.3.5 Compressive strength

The 7 and 28 d compressive strengths of alkali activated slag-fly ash-limestone pastes and mortars are shown in Figures 4-19 and 4-20, respectively. The water/binder ratio for paste samples is 0.35, and it is 0.45 for mortars. It can be seen that the paste and mortar samples show a similar tendency in the strength development, and mortar mixtures exhibit a lower strength in general, due to their increased water content. For samples with a constant slag content, both the 7 and 28 d compressive strengths are increased when increasing the limestone powder content. For instance, in the paste samples with a slag content of 60%, when increasing the limestone powder content from 0% to 30%, the 7 d compressive strength increases from 61.3 MPa to 68.9 MPa, and the 28 d strength also exhibits an increment from 76.5 MPa to 83.5 MPa. Similar results are also found in samples with other slag contents and the highest strength is shown in samples with the 30% limestone addition. This behavior should be attributed to the filler effect of limestone powder.

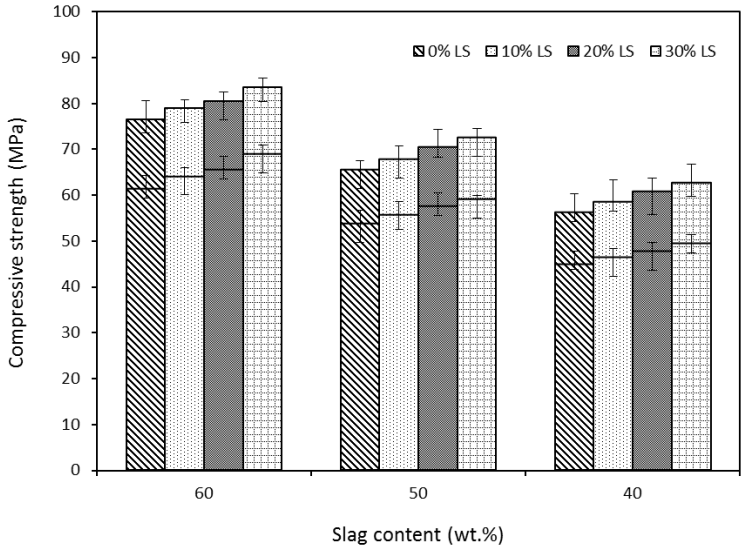

Figure 4-19: 7 and 28 days compressive strength of AA-slag-fly ash-limestone pastes

The addition of limestone powder will lead to a higher content of fine particles within the paste, which could work as micro aggregates and may reduce the total porosity, then results in an increment of strength. Moreover, the better reaction of slag due to the presence of limestone

also contributes to the strength improvement. Since the additional nuclear sites provided by the fine limestone particles promote the formation of the reaction products, as can be seen from the isothermal calorimeter results, a more homogeneous dispersion of the reaction products may result. The improved slump flow caused by the limestone addition could be an indication of the increased effective water content, which may result in an increase of the contact area between the slag particles and alkaline solutions.

It can be obviously seen that for a constant limestone replacement, higher compressive strengths are achieved in samples with higher slag contents at both 7 and 28 d. As shown in Figure 4-19, for samples without limestone addition, when reducing the slag content from 60% to 40%, the 7 d compressive strength decreases from 61.3 MPa to 44.8 MPa and the 28 d strength is reduced from 76.5 MPa to 56.3 MPa. Similarly, in samples with a 30% limestone content, where the highest strength is achieved in each slag level, the 7/28 d strength decreases from 68.9/83.5 MPa to 49.4/62.7 MPa respectively, with the shifting of the slag content from 60% to 40%. This should be attributed to the considerably higher reactivity of slag than the other components under ambient temperature. As can be seen from the results of the setting times and the reaction kinetics, the slag content shows a decisive impact on the reaction process, while changing the limestone/fly ash content based on a constant slag level exhibits limited influences.

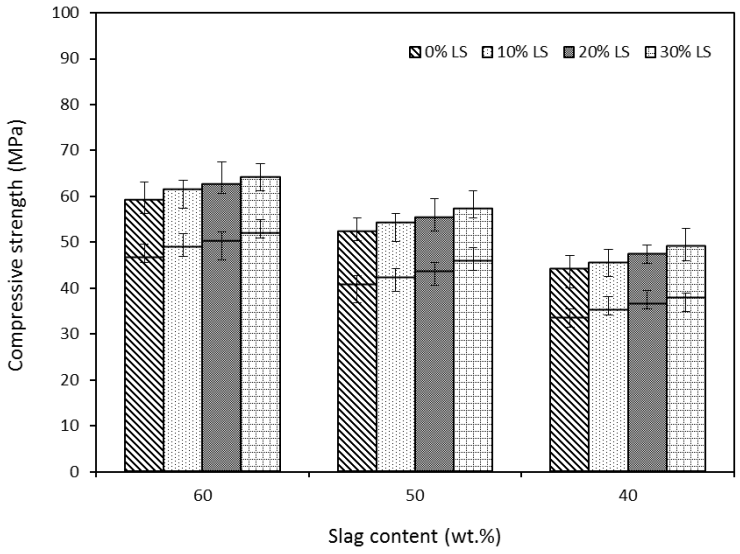

Figure 4-20: 7 and 28 days compressive strength of AA-slag-fly ash-limestone mortars

It can be noted that based on a constant slag content, mixes with different limestone contents show a similar rate of strength development between the 7 and 28 d. Considering that the

increased limestone content is at the expense of fly ash content in this case, it also demonstrates the low reactivity of fly ash until the age of 28 d under ambient curing conditions; or the dissolved Si and Al units from fly ash exhibits much less influence than the Ca from slag on strength in this case. Concerning the mortar mixes, the filler effect of limestone powder and the remarkable influence of slag on strength are also obviously presented. As shown in Figure 4-20, based on a constant slag level, the compressive strength increases with the increasing limestone content; also based on a constant limestone addition, both the 7 and 28 d strength increase with increasing slag content. The highest values are obtained in samples with a 60% slag and 30% limestone, showing 7 and 28 d compressive strengths of 51.9 MPa and 64.2 MPa, respectively. While the lowest 7/28 d strength of 46.6/59.2 MPa was shown in the samples with 40% slag and 0% limestone.

4.3.6 Role of limestone in blended alkali system

As commonly known, limestone powder exhibits both physical and chemical effects on Portland cement systems, which can be briefly summarized as follows: lowering the water demand of cement paste (Tsivilis et al, 1999); accelerating the hydration process; reacting with aluminate phases to form monocarboaluminate and affecting the strength. While in an alkali activated system, according to the investigations in this paper, the physical effect of limestone powder is obvious. As shown in the slump flow results, the low water demand of limestone powder promotes the workability of both pastes and mortars. Moreover, owing to the fine particles provided by the limestone powder, the hydration process is slightly accelerated; the higher intensities of the acceleration peak and the higher total heat release indicate an intensified reaction. The increment in compressive strength can also be attributed to the physical modification of limestone powder, as fine particles from the limestone powder modify the packing and result in a denser matrix.

However, the chemical effects of limestone powder in the blended alkali system are different from those in a Portland cement system. It has been known that the presence of limestone in calcium and high aluminates conditions modifies the Portland cement system following the mechanism expressed as:

$$A + 3CH + 8H + C\underline{C} \Rightarrow C_4A\underline{C}H_{11} \quad (1)$$

where: $A=Al_2O_3$, $CH=Ca(OH)_2$, $H=H_2O$, $C\underline{C}=CaCO_3$. This process increases the total volume of the solid phases and results in the increment of compressive strength in Portland cement systems. The occurrence of this reaction is highly dependent on the Al and Ca supply, while the limestone powder content and fineness plays a minor role (Weerdt et al, 2011; Zajac et al, 2014). In the case of alkali activated slag-fly ash-limestone blends, all the required elements for the reaction above are available, but the formation of $C_4A\underline{C}H_{11}$ is not observed according to the micro analysis (XRD) in this study.

One possible explanation is that the dissolved Ca, Si, Al units from the slag and fly ash prefer the formation of more stable structure of C-(A)-S-H type gels, when the formation of C-(A)-S-H gel is saturated, the remaining units may react with limestone powder to form $C_4A\underline{C}H_{11}$. However, it seems that the remaining components in ternary slag-fly ash-limestone blends do not meet the requirements of the equation above, the possible reasons can be as follows: (1) Absence of calcium. The C-S-H gels in alkali activated system (type I, tobermorite) show a Ca/Si of around 1.0-1.2 (Wang et al, 2003) and the Ca/Si (molar ratio) in the raw slag is 1.17. While the total Ca/Si in the system would be lower than 0.85 (in samples with 60% slag) when calculating the silicate from the activator, this value would be even lower when considering the silicate from fly ash. Thus no sufficient calcium will remain after the formation of C-(A)-S-H gels. (2) Absence of aluminate. It has been proven that the C-(A)-S-H gels in alkali activated systems also have the potential to contain a certain amount of aluminate (Richardson et al, 2004; Fernandez et al, 2003), and the total Al/Ca in C-S-H gels can reach around 0.2. Even though the Al/Ca ratio in original slag reaches 0.17, the dissolution of fly ash at ambient temperature may provide a limited amount of aluminate at early ages.

It is also possible that the dissolved aluminate from fly ash may be participating in the formation of low polymerized N-(C)-A-S-H type gels rather than reacting with limestone to form crystalline phases. Therefore, the reaction products of silicate activated slag-fly ash-limestone blends remain amorphous without crystalline phases. But it is still possible for the formation of monocarboaluminate in other alkali systems where additional Ca and Al groups simultaneously exist, such as systems with high calcium hydroxide and metakaolin/fly ash contents; further investigations on the formation mechanism of monocarboaluminate in alkali activated systems are being carried out. Besides, it should be noted that the dissolution of Ca^{2+} from calcium carbonates in alkali activated system was actually confirmed by (Cwirzen et al, 2014); also the satisfying surface binding between the limestone powder and alkali activated materials was suggested in the previous study (Yip et al, 2008). Thus, the slightly increased bound water content together with the continuously increased compressive strength in this case could be regarded as an indication that the limestone powder may not only work as a non-reactive filler, the release of Ca^{2+} from limestone powder and its topography characteristics may also make small but non-negligible contributions to the strength development and pore structure refinement by providing extra surface binding within particles. Overall, the utilization of extra fine particles (limestone powder) in hybrid alkali systems (alkali activated slag-fly ash blends) exhibits both physical and chemical modifications such as improving workability, promoting reaction processes, and achieving superior strengths with high level limestone replacements.

4.4 Conclusions

This chapter investigates the effects of nano-silica and limestone powder addition on slump flow, setting times, reaction kinetics, gel characteristics, porosity and compressive strength of

alkali activated slag-fly ash blends designed with different slag/fly ash ratios; and the role of both nano-silica and limestone powder in alkali activated system is discussed. The following conclusions can be drawn:

- The incorporation of nano-silica significantly decreases the slump flow of paste samples, while the flowability increases with the increasing limestone contens. Mixes with a lower slag/fly ash ratio contribute to a better flowability.
- Both the initial and final setting times are strongly influenced by the slag content, and a higher slag content leads to a decreased setting time. The setting times are slightly increased with the increase of nano-silica content, while limestone powder shows a negligible influence on setting.
- The slag content plays a dominant role during the early age reaction, since it is the main factor that affects the location and intensity of the induction and main reaction stage. The nano-silica replacement slightly retards the reaction process at early ages and also leads to a slight reduction of the peak intensity in the main reaction stage. This phenomenon is suggested to be the synergetic effect of several factors. The additional nucleation sites provided by limestone powder slightly accelerate the induction and acceleration stage of reaction.
- Gel character analyses show that the addition of nano-silica slightly increases the chemically bound water content. The gel structure remains stable regardless of the nano-silica content and slag/fly ash ratio; and the presence of limestone powder does not lead to the formation of new phases, but slightly increases both the physically and chemically bound water content.
- Samples with different slag/fly ash ratios show different rates of strength development. A nano-silica addition up to around 2% benefits the compressive strength at typical curing ages, while further higher nano-silica content shows negative effects. For a constant slag content, the compressive strength increases with an increasing limestone powder content up to 30%.
- Samples with a higher slag/fly ash ratio exhibit a lower level of porosity. The porosity decreases with the increasing nano-silica content, indicating the positive effect on nano-silica on pore structure refinement. All mixes show an optimum nano-silica content of around 2% in terms of porosity.
- The limestone powder shows mainly physical with slight but non-ignorable chemical modifications of alkali activated slag-fly ash blends. It is suggested that the absence of monocarboaluminate is due to the insufficient supply of additional calcium and aluminate in this case; and the small amount of the released Ca^{2+} from the limestone together with its filler effect results in the pore refinement and strength increment.

Chapter 5

Applying a green silica source as alternative activator

5.1 Introduction

In terms of the alkali activators, it is widely accepted that a mixture of silicates and caustic alkalis ($M_2O{\cdot}nSiO_2$ + MOH, where M commonly refers to Na or K) results in the best mechanical properties and lowest porosity (Puertas et al, 2014) compared with other types of activators, and the most commonly used cation is Na due to its relatively low cost and availability. This mixed activator benefits the reaction process by offering alkaline conditions in a moderate and continuous manner, meanwhile providing extra silicate sources that contribute to the formation of reaction products. However, the sodium silicate based activator is the main contributor of energy consumption and carbon emission in alkali activated materials (Lellan et al, 2011). The production of sodium silicates includes the melting of sodium carbonate and quartz sand at high temperatures (usually around 1400 to 1500 °C), and this process results in a total carbon dioxide release of 403 to 540 kg/ton and an energy consumption between 420 to 1250 MJ/ton (European Commission, 2007). Moreover, the estimated cost of one ton of equivalent silica from commercial sodium silicate solution is currently more than 2100 USD (Lazaro, 2014).

Therefore, in order to obtain a more sustainable alkali activated binder, it is of great interest to design new alkali activators with reduced environmental impacts and lower costs. Among those researches, using alternative silicate in the activator is reported to be an effective approach that balancing the costs and performances, such as use chemically modified nano-silica and MOH to activate class F fly ash (Rodriguez et al, 2013); apply modified silica fume as alternative activator in alkali activated slag (Zivica, 2006); using a mixed activator by dissolving industrial glass waste in NaOH/Na_2CO_3 solutions in alkali activated slag (Puertas et al, 2014); and the utilization of silica fume or rice husk ash with NaOH to activate metakaolin/slag blends (Bernal et al, 2012). These researches show that alternative silicate based activators could provide comparable mechanical properties and similar micro scale characters compared with commercial sodium silicate based ones. However, there are limited mechanism studies regarding the effect of alternative silicates as activator on the blended alkaline system. On the other hand, the olivine nano-silica, produced by the dissolution of olivine, exhibits advantages with regard to carbon emission, energy consumption and total costs (Lazaro et al, 2012). This type of amorphous nano-silica is produced under temperatures that lower than 95 °C and can have a specific surface area between 100 and 400 m^2/g and

primary particles as low as 10 nm. Thus it indicates the potential as a sustainable silicate source in the preparation of alkali activators while providing desirable reactive silica.
The aim of this chapter is to evaluate the olivine nano-silica as an alternative activator in alkali activated slag-fly ash blends. The effects of olivine nano-silica on activator characteristics, reaction kinetics, mechanical property and the structure of reaction products are analyzed. Micro-scale analyses are carried out by using an isothermal calorimeter, ^{29}Si and ^{27}Al MAS NMR spectroscopy and thermo-gravimetric/differential scanning calorimeter; and furthermore the total carbon emission of the related mixtures is computed. Also important engineering and application related properties of the products are studied and discussed, including flowability, setting times, mechanical properties, porosity and drying shrinkage.

5.2 Synthesis and characterization of olivine nano-silica

An alternative synthesis route to achieve amorphous nano-silica is the dissolution of silicate minerals in acid. The dissolution of olivine is a competitive alternative route compared to the existing methods of nano-silica production, due to the cheaper and greener process of olivine dissolution at low temperatures. The raw materials employed in this method are olivine ($(Mg,Fe)_2SiO_4$) and sulfuric acid. Olivine (an olivine gem-stone can be seen in Figure 5-1(a)) is the most common silicate mineral in the upper mantle and a common mineral in the earth's crust, which makes it a low-price commodity (currently between 75 and 150 USD/ton depending on the quality, location of the quarry and market oscillations).

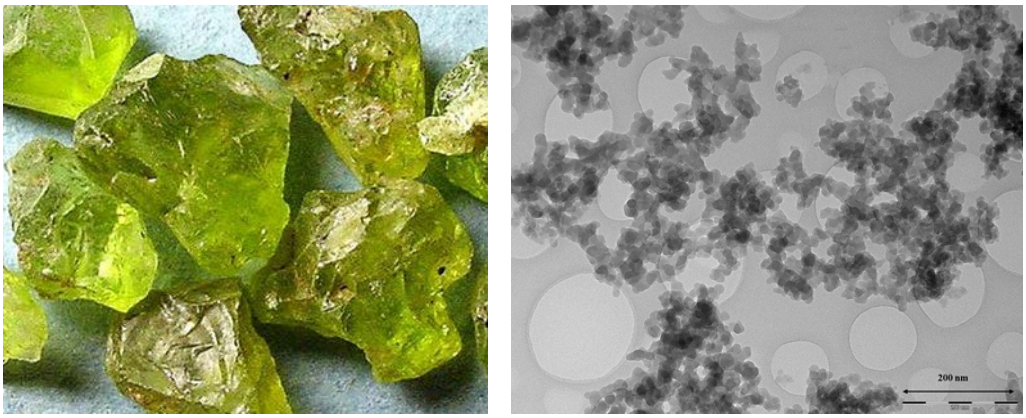

(a) (b)

Figure 5-1: A sample picture of the olivine gem-stone and a TEM image of produced olivine nano silica (Lazaro, 2014)

Amorphous silica can be produced through the following reaction (between 50 and 95 °C) (Lazaro et al, 2013):

$$(Mg,Fe)_2SiO_4 + 4H^+ = Si(OH)_4 + 2(Mg,Fe)^{2+}, 223\ KJ/mol \quad (1)$$

The dissolution yields a slurry consisting of a mixture of magnesium/iron salts, amorphous silica, unreacted olivine and inert minerals. Once the reaction is complete, the unreacted olivine and inert minerals are removed from the final suspension by sedimentation. Subsequently, the silica can be cleaned from the resulting mixture by washing and filtering. After the filtration, a cake with around 20 wt.% solid content of nano-silica is obtained. The synthesizing process is briefly presented in Figure 5-2.

In this study, amorphous silica is produced by mixing olivine stone with 3M sulfuric acid at 95 °C for periods of time between 4 and 6 hours. The grounded olivine used has a particle size range between 100 and 500 μm and a purity of 89 wt%, chemical analysis presents some other minor minerals (i.e., micas, serpentine minerals, chlorite, talc and enstatite) (Lazaro et al. 2015). After synthesis of silica, this material was cleaned by washing and filtering, and a filter cake product with around 20 wt.% solid content of nano-silica was then obtained.

The produced olivine nano-silica has a specific surface area between 100 and 400 m^2/g, primary particles between 10 and 25 nm (agglomerated in clusters) and silica content above 99%. The particle sizes and a typical TEM picture of produced olivine nano-silica is shown in Figure 5-1(b), nano particles with angular shape can be observed.

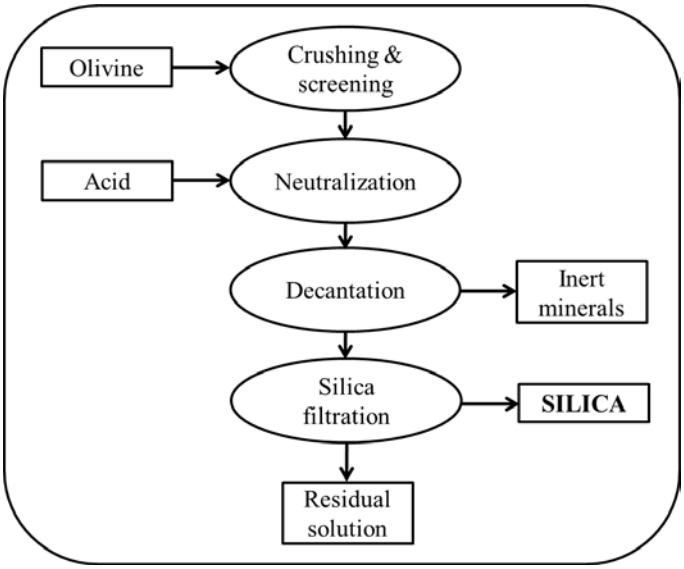

Figure 5-2: Chart flow of the olivine nano sililca production

In addition to the low temperature feature of this procedure (below 95 °C), it is remarkable that the process is exothermic with a reaction heat of 223 kJ per mole of olivine (Sun et al, 2006). The energy generation during the olivine nano-silica process for the hypothetical case of an adiabatic reactor is shown in Table 5-1, the used heat capacities of 25% sulfuric acid is 3.38 $J \cdot g^{-1} \cdot °C^{-1}$ according to (Faucon et al, 1999), while the forsterite and dunite are approximated to have the same value of 0.83 $J \cdot g^{-1} \cdot °C^{-1}$ (Robie et al, 1982). When 1.5 moles of olivine react with 1 L solution of sulfuric acid 25%, the temperature of the mixture will increase 79 °C. Therefore, the reaction generates more than enough energy to keep the system at the desired temperature (between 50 and 90 °C) provided the reactor is sufficiently insulated. In addition, the dissolution of concentrated sulfuric acid also generates a considerable amount of heat.

Table 5-1: Energy generation during the olivine nano-silica process

ΔH_r (kJ/mol)	$V_{H_2SO_4}$ (L)	$m_{H_2SO_4}$ (g)	n_{ol} (mol)	m_{du} (g)	X (%)	Q (kJ)	ΔT (°C)
223	1	1186	1.5	242	100	333.5	79.3

ΔH_r is the enthalpy of reaction, X is the conversion degree of the reaction and Q is the heat generated.

5.3 Activator characterization

5.3.1 Soluble content

The olivine nano-silica based activators are then produced by mixing the prepared nano-silica cake with sodium hydroxide pellets and distilled water. Three levels of activator modulus within the commonly used range are prepared: 1.0, 1.4 and 1.8. Reference activators with the same activator modulus were prepared by mixing sodium hydroxide pellets with commercial waterglass and water to achieve the same chemical composition of the corresponding nano-silica based activator.

It is commonly known that the silicates in both cases are mostly soluble silica; and differences in the silicate structure and pH might occur due to the origin of the silica source and the synthesizing parameters. The particle size distributions of the applied activators are shown in Figure 5-3. It can be seen that the un-dissolved silicates show particle sizes that centered at about 10 µm and some small fractions at around 0.8 µm, while no particle sizes are shown below around 200 to 300 µm. Then a 200 nm filter is used in order to identify the mass fractions of the dissolved silicates, since those dissolved ones show no information from the particle size measurement, the results are also shown in Figure 5-3.

It shows that the mass fraction of solids below 200 nm in activators with Ms of 1.0, 1.4 and 1.8 is 99.88%, 99.73% and 98.08%, respectively. According to (Iler, 1979), when the activator

modulus is lower than 2, there are no (or almost none) polymeric silica species (<2 nm); and the silica species are completely dissolved when the modulus is lower than 1. Thus it can be concluded that the silica in an olivine nano-silica based activator is almost completely dissolved for Ms of 1.0 and 1.4, and the sample with a Ms of 1.8 also reaches a high value of above 98%. It should be noted that there is a slight increase in the soluble solid content when lowering the activator modulus, which suggests again that higher alkalinity (pH) favors the dissolution of silicates. For the undissolved silicates, all the three samples present similar particle size distributions: a main particle size at around 9.8 μm together with a small amount of particles at about 0.7 μm. These micro particles could be practically the impurities from the olivine. But considering the small mass fraction within total amount of input silicate (0.27% to 1.92%), their influence should be limited.

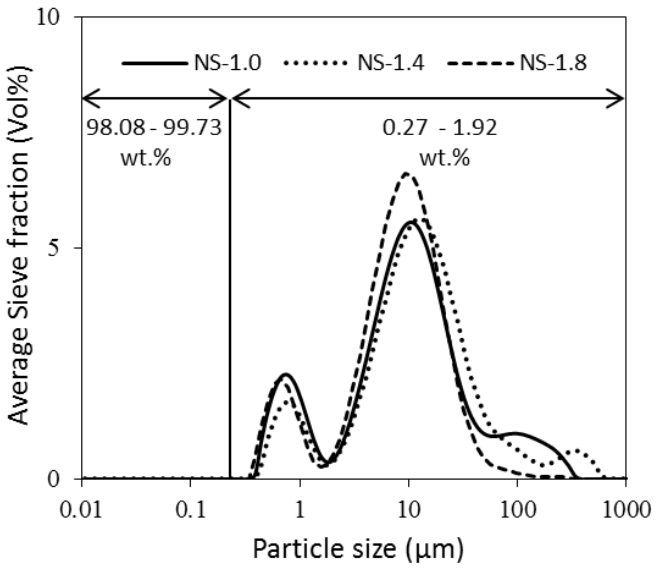

Figure 5-3: PSDs of the olivine nano-silica based activators

5.3.2 pH value

The measured pH values of all the six prepared solutions are shown in Table 5-2, each value is an average of three measurements. For the nano-silica based activators, very similar pH values are shown in general compared to the waterglass based ones with the same activator modulus, showing that the modulus exhibits a much greater influence than silicate origin in terms of the pH value. While as the modulus increases from 1.0 to 1.8, there is a gradual decrease of pH from 13.48 to 13.19, although those values will represent a high level, the pH variation is significant enough to cause changes in silicate solubility and consequently, reactivity of the activator. For a short summarize, the olivine nano-silica based activators are able to provide

comparable amounts of soluble silicate and alkalinity to the commercial waterglass based ones, thus similar macro performances upon activation can be expected.

Table 5-2: pH values of the activator solutions

Mix	pH
WG-1.0	13.49
WG-1.4	13.41
WG-1.8	13.17
NS-1.0	13.48
NS-1.4	13.39
NS-1.8	13.19

5.3.3 Liquid ^{29}Si NMR

Liquid ^{29}Si NMR was performed to all the six activators and the results are shown in Figure 5-4.

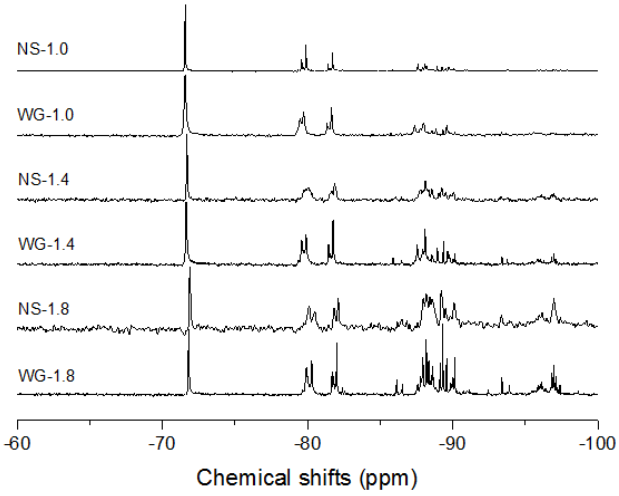

Figure 5-4: Liquid ^{29}Si NMR spectrum of activators

For activators with a modulus of 1.0, a significant sharp peak is located at around -72 ppm, indicating the presence of Q^0 monomers. Q^1 dimers and Q^2 trimers at around -80 and -82 ppm are observed (Bernal et al, 2013), as well as a certain fraction of Q^2 and Q^3 groups at about -85 to -90 ppm (Pardal et al, 2012). No significant peaks are shown in ppm ranges lower than -100, suggesting no Q^4 sites are present in the activator. When increasing the modulus to 1.4, the intensity of peaks at around -85 to -90 ppm (Q^2/Q^3 sites) becomes more evident, indicating the increasing fraction of Q^2 and Q^3 units within the activator solution. Also the Q^3 groups that located at around -95 to -100 ppm start to present. Further increment of the activator modulus to 1.8 results in a more significant peak intensity at around -85 to -90 ppm and -95 to -100 ppm, suggesting an increased amount of Q^2/Q^3 and Q^3 groups within the solution.

Table 5-3: Evaluation of the silicate structure compositions in alkali solution

Sample	Q sites and percentage (%)				
	Q^0	Q^1	Q^2	Q^2/Q^3	Q^3
NS-1.0	30	21	17	32	0
WG-1.0	32	23	16	29	0
NS-1.4	17	18	13	42	10
WG-1.4	20	21	16	37	6
NS-1.8	7	6	5	54	28
WG-1.8	9	14	10	49	18

These chemical shifts can be directly linked to the increment of the activator modulus, which lower the pH and therefore reduce the silica solubility, resulting in activator solutions with more polymerized silicates. Concerning the effect of silica origin, with a fixed activator modulus, olivine nano-silica derived activators exhibit the same typical peak locations compared to the commercial waterglass based ones, with slight differences in peak intensity and covered area, indicating a similar silicate structure composition in general. In order to further quantify the different silicate groups' fractions, an evaluation on the covered area of identified peak was carried out by using the software MestRec, and the results are listed in Table 5-3. It should be pointed out that the quantified calculation method is still open for discussion, and can only be used as an indication to show the structural differences. It shows that as the activator modulus increases, there is a general reduction of the low polymerized Q^0 and Q^1 groups, which usually present higher reactivity than the Q^n sites with higher n values. Meanwhile, the Q^2 and Q^3 contents show a significant increase. With a constant activator

modulus, the olivine nano-silica based activators show slightly lower contents of Q^0 and Q^1 groups, and relatively high fractions of Q^2 and Q^3 groups. Those slight but detectable structural differences may influence the properties of the resulting alkali activated materials.

5.4 Reaction kinetics

The mixtures used in this study had an equivalent sodium oxide (Na_2O) content of 5%, and the water/binder ratio was kept constant as 0.4. The slag/fly ash mass ratio was fixed at 70/30 and three levels of activator modulus (1.8, 1.4 and 1.0) were used. The detailed information of the mix proportions is listed in Table 5-4 (where WG and NS represent commercial waterglass and olivine nano-silica, respectively).

Table 5-4: Mix proportions of alkali activated slag-fly ash composites

Activator			Solid raw materials		w/b
Type	Na_2O	Ms	Slag	Fly ash	
A : WG+NaOH	5%	1.8	70	30	0.4
		1.4			
B: NS+NaOH		1.0			

The isothermal calorimetric analyses were conducted to all six mixtures and the results are illustrated in Figure 5-5. It can be seen that for the commercial sodium silicate based samples, the second heat evolution peak appears at around 12 hours with an activator modulus of 1.0; as the activator modulus increases to 1.8, this peak shifts to around 20 hours with a lower intensity. The prolonged induction stage with broader curves also indicates the decreased reaction intensity due to the increase of activator modulus. A similar tendency is also shown in nano-silica based mixes.

The more intensive reaction process due to the reduction of activator modulus is also found in the previous investigations (Krizana and Zivanovic, 2002). The peak change is primarily due to the increased silicate content in the activator solution and the resulted lower pH. When activators with lower moduli are used, the soluble silica exhibits a less polymerized structure in the solution than the ones with higher modulus due to the increased pH (Criado et al, 2008), thus a more direct interaction between the soluble silicates, alkali solutions and the raw materials is resulted. Besides, due to the silicate equilibrium based on the pH, the increased soluble silicate content at the beginning stage may negatively influence the dissolution of the silicate units from the original slag, consequently leading to an increased reaction time.

Concerning the nano-silica based mixtures, for each fixed activator modulus, the location of the main reaction peak slightly shifts to longer times. Besides, the peak intensities of those mixtures are slightly lower than the commercial sodium silicate based ones, together with less covered areas in all cases. It reveals that nano-silica based samples present a slightly less intensive reaction process during the first 72 h. Considering the facts that in the olivine nano-silica based activators, small fractions of the undissolved materials are present; slightly lower pH for a constant modulus is shown; and exhibit relatively high content of polymerized Q groups; which might explain the slightly reduced reactivity compared to the commercial sodium silicate activators.

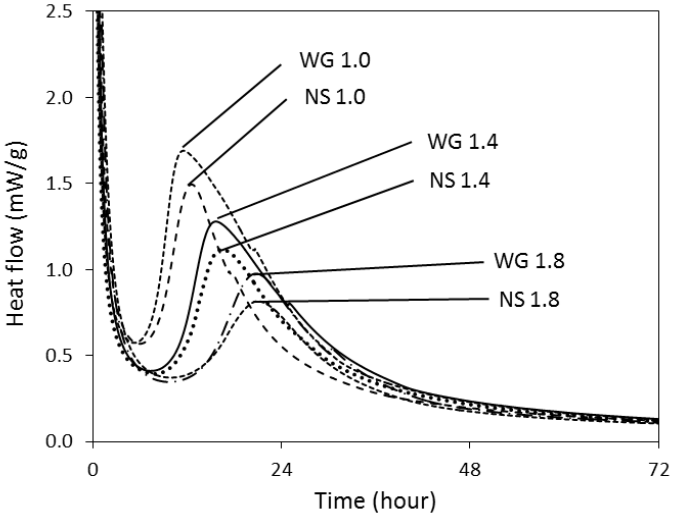

Figure 5-5: The normalized heat flow of AA slag-fly ash blends with different activator conditions.

5.5 Gel composition

5.5.1 TG/DSC

The thermal analyses of the mixes with different silicate sources and activator moduli are presented in Figure 5-6. Special attention is paid to the reacted gels and the initial mass after holding at 105 °C for 1 hour is calculated as the starting mass (i.e. 100%), in order to analyze the structural changes at higher temperatures. All the samples are cured for 3 months. It can be seen that after a negligible mass loss between around 105 and 160 °C, all mixtures exhibit a gradual mass decrease until 1000 °C. Between the temperature range of around 160 and 800 °C, all samples exhibit similar tendencies of mass loss, a representative DTG curve from sample WG-1.4 is shown in the figure, which reveals four DTG peaks that corresponding to the gradual decomposition of the C-A-S-H type gels (about 160 °C); hydrotalcite type phases

(around 330 °C) and carbonates (around 620 and 710 °C), respectively. The DSC results show two heat absorption peaks at around 160 and 700 °C (small shoulder), corresponding to the decomposition of reacted gel and carbonates, respectively. Besides, there are no other abrupt mass losses between 105 and 1000 °C, which reveal that the reaction products in this case are mainly amorphous gels with chemically bound water, while certain amount of carbonates are formed caused by the carbonation.

For a constant activator modulus, samples prepared using commercial sodium silicate exhibit a larger mass loss than the olivine nano-silica based ones between 105 and 1000 °C; and mixes with a higher activator modulus show a lower total mass loss in general. Specifically, in olivine nano-silica based samples, the mass loss after 105 °C is around 8.2%, 7.2% and 6.2% for mixes with an activator modulus of 1.0, 1.4 and 1.8, respectively. The corresponding values for sodium silicate based mixtures are 8.4%, 7.5% and 6.7%. The slight but noticeable difference in mass loss indicates that slightly more chemically bound water/reaction products are formed in commercial sodium silicate based mixes, and a lower activator modulus benefits the reaction rate.

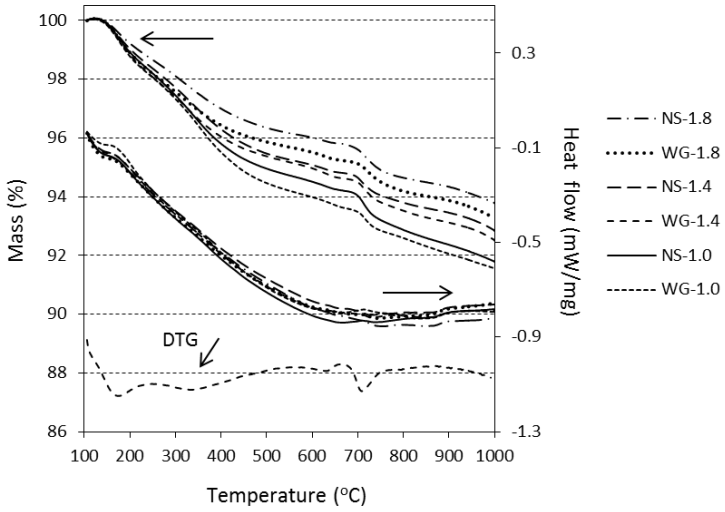

Figure 5-6: TG, DSC and DTG analyses of reaction products

These results are well related to the calorimeter results in this study, where the olivine nano-silica derived mixes exhibit less intensive reaction, and a higher activator modulus (higher amount of additional silicate from activator) slows down the reaction to some extent. Therefore, it is reasonable to state that the olivine nano-silica based activators present a slightly less activation efficiency compared to the commercial sodium silicate based ones, which is attributed to the silicate origin. Besides, the mass loss between 650 and 800 °C is about 1.04% to 1.39%, which mainly includes the decomposition of carbonates and a small amount of

chemically bound water, which provides a qualitative identification about the carbonation behaviors of this blended alkali system.

5.5.2 ^{29}Si MAS NMR

Figure 5-7 shows the ^{29}Si MAS NMR spectra of the unreacted slag and fly ash. The unreacted slag exhibits a broad peak in the range between -55 and -95 ppm, centered at around -75 ppm. In the later deconvolution work on the spectra, the contour of the raw slag after alkali activation is assumed to be unchanged, and its spectrum range is fixed and the intensity is rescaled by a certain factor to evaluate the contribution of raw slag in the corresponding overlapped areas. The spectrum of the unreacted fly ash presents a broad overlapped peak within the range of -80 and -120 ppm, assigning to the Q^4 structures with different aluminate substitutions: Q^4(mAl), m=0-4. The deconvolution of the overlapped peaks in fly ash is carried out in Origin Pro 9.0 by applying the Gaussian line model, constant peak widths and locations are used throughout the whole study. Peak locations and physical meanings are based on the analytical results from the software and the available literatures (Provis et al, 2009; Bernal et al, 2013; Wang et al, 2003; Palomo et al, 2004).

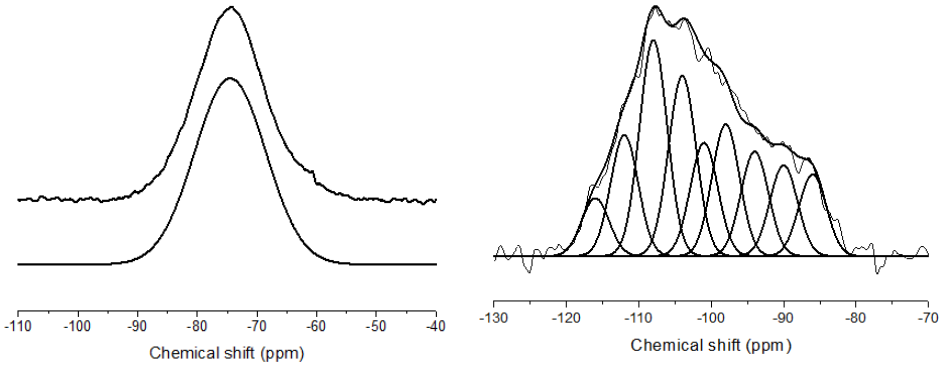

(a) (b)

Figure 5-7: ^{29}Si MAS NMR of starting materials (a: slag; b: fly ash).

Figure 5-8 and 5-9 shows the ^{29}Si MAS NMR spectra of slag-fly ash blends activated by commercial sodium silicate solutions and olivine nano-silica based ones after 3 months of curing, respectively. The fitting peak and deconvoluted peaks are presented below the obtained spectra in each figure. After activation, all mixes show obvious spectra of slag and Q^4(mAl) sites, indicating the presence of unreacted slag and fly ash. It should be noted that a small scaled formation of N-A-S-H gels (Q^4 structures) may also occur and the resulting spectra are overlapped with the original fly ash and Q^3(1Al) groups (around -80 to -120 ppm), making those phases difficult to quantify (Bernal et al, 2014). However, the main newly formed phases

within the range of -70 to -90 ppm are relatively easy to distinguish. The deconvoluted peak located at around -75.2 ppm refers to the Q^0 sites, two Q^1 peaks (non-bridging structure, $Q^{1\text{-}a}$, and $Q^{1\text{-}b}$) are identified at about -76.8 and -79.0 ppm, since a single Q^1 group is not sufficient to reach an ideal peak fitting. Previous studies also observed two Q^1 sites types in the C-(A)-S-H type gels, while the differences in the chemical environments of these two groups are not specified (Myers et al, 2013).

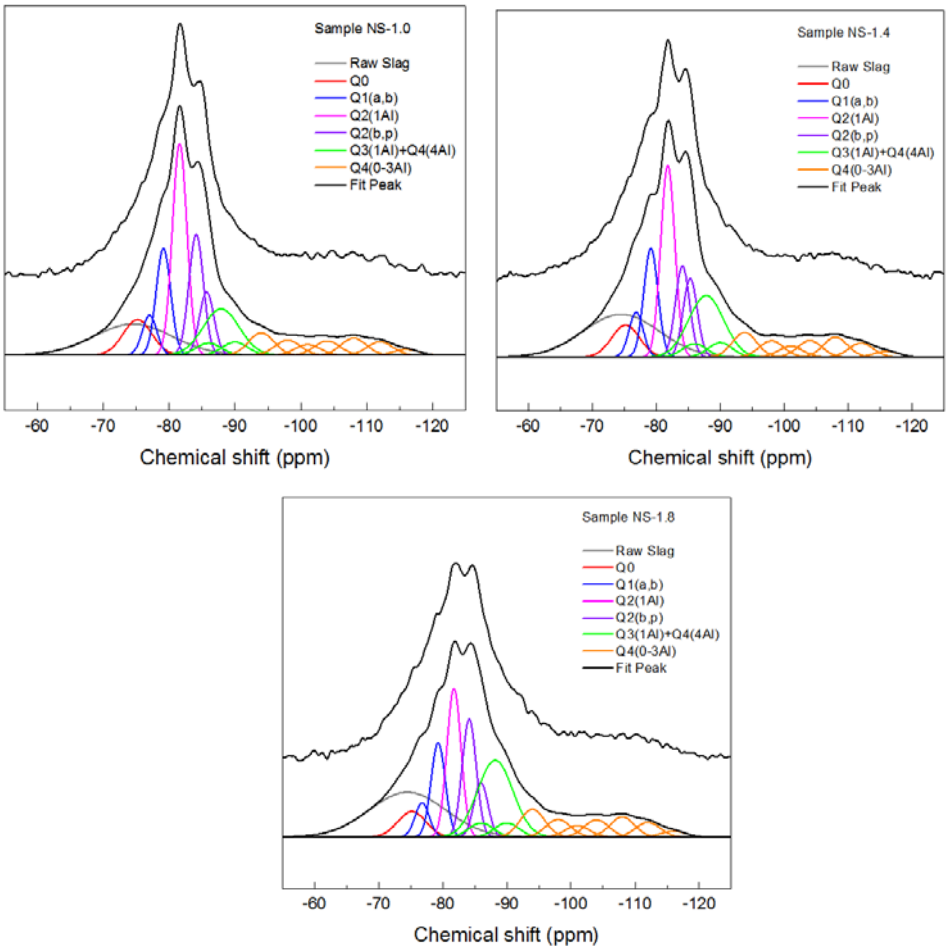

Figure 5-8: ^{29}Si MAS NMR of mixes based on olivine nano-silica

Peaks at approximately -81.6, -84.2 and -85.7 ppm are attributed to the bridging Q^2(1Al), $Q^{2\text{-}b}$, $Q^{2\text{-}p}$ sites within the C-(A)-S-H gels, respectively. Besides, three sites show an overlapped location at around -85 to -90 ppm, including two Q^4(4Al) groups that are observed in the original fly ash and a newly formed Q^3(1Al) groups; the strong presence of relatively high

crosslink Q^3(1Al) sites in alkali activated slag and its blends is also observed in the available literatures (Myers et al, 2013; Wang et al, 2003; Richardson, 2008).

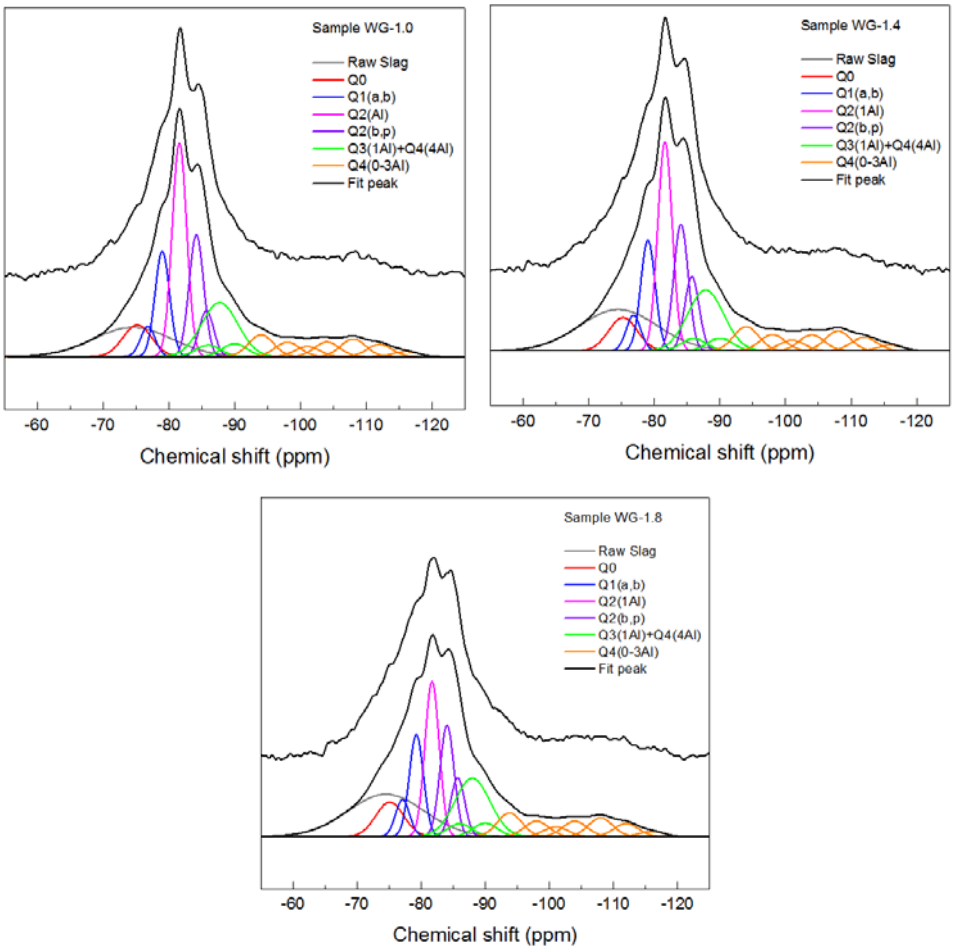

Figure 5-9: ^{29}Si MAS NMR of mixes based on commercial waterglass

The effect of activator modulus and alternative silica on gel structure is quantified based on the deconvolutions and the results are summarized in Table 5-5. The reaction degree of slag (RD, in terms of Si) is calculated as follows (in mol.%):

$$\mathrm{RD} = \frac{\mathrm{Si(Or)} - \mathrm{Si(Un)}}{\mathrm{Si\ (Or)}} \times 100\% \qquad (2)$$

Where Si(Or) is the input Si from the original slag, and Si(Un) is the unreacted Si in slag within the reaction products. When increasing the activator modulus from 1.0 to 1.8, the slag reactivity gradually decreases from about 72% to 58% in both commercial sodium silicate and olivine nano-silica based mixes.

Table 5-5: Summary of the deconvolution results fom ^{29}Si MAS NMR analysis

Chemical Shift (ppm,±0.5)	Sample ID	NS-1.0	NS-1.4	NS-1.8	WG-1.0	WG-1.4	WG-1.8
-55 to -95	Unreacted slag	15.2	19.3	20.5	14.6	18.2	20.3
	Slag reactivity	71.5	62.1	58.0	72.5	64.2	58.5
-75.2	Q0	6.3	5.3	4.3	5.8	5.4	6.1
-76.8	Q1-a	3.6	3.8	2.9	2.8	2.9	3.3
-79.0	Q1-b	9.6	9.1	8.0	9.6	9.0	9.0
-81.6	Q2(1Al)	19.0	16.0	12.6	19.8	17.1	13.8
-84.2	Q2-b	10.9	7.6	10.0	11.3	10.3	9.9
-85.7	Q2-p	5.7	6.6	4.6	4.3	6.1	5.2
-88	Q3(1Al)+Q4(4Al)	14.3	16.8	20.4	16.4	16.0	16.9
-94 to -116	Q4(0-3Al)	15.5	15.6	16.7	15.3	15.0	15.5

This result is inconsistent with the isothermal calorimetric and thermal analyses in this study that a lower activator modulus favors a more intensive reaction process which leads to an increased bound water content; and with a same activator modulus, olivine nano-silica derived mixes present a slightly lower reaction degree compared to the commercial ones. The Q^0 content slightly decreases with the increase of activator modulus in olivine nano-silica based samples, while it remains stable in waterglass based ones. Regardless of the silica origin and activator modulus, the content of Q^1 and Q^2 groups only shows slight shifts; the stable content of Q^4(0-3Al) groups may suggest a limited but constant contribution of fly ash during activation.

The most evident structural change is observed in the Q^2(1Al) groups, namely the increase of activator modulus results in a decrease of around 5% within the studied parameter range in this case, while the effect of silica origin is not obvious. It should be noted that the starting precursors (slag and fly ash) are the only aluminate sources in this case, and slag presents a

dominate effect in providing aluminate considering its content and reactivity. Thus it is highly possible that the reduction of $Q^2(1Al)$ sites is attributed to the decreased content of reacted slag and therefore less Al is available for the reaction. Another obvious structure shift is the high crosslink $Q^3(1Al)+Q^4(4Al)$ sites, their content is stable in commercial sodium silicate based mixes, regardless of the activator modulus. While in the case of olivine nano-silica based samples, there is an obvious increase of those sites when increasing the activator modulus.

5.5.3 ^{27}Al MAS NMR

Figure 5-10(a) shows the ^{27}Al MAS NMR spectra of the unreacted slag and fly ash. Similar to other blast-furnace slags, the original slag presents a broad resonance between 0 and 80 ppm and centered at around 55 ppm. This broad peak region is assigned to a combination of Al(IV), Al(V) and Al(VI) sites (Merwin et al, 1991), and cannot be identified as a single Al environment. This can be attributed to distribution of Al environments within the glassy phase of slag, which shows a broad amorphous hump and almost undetectable crystalline phases. For the unreacted fly ash, a broad peak at around 46 ppm and a relatively narrow one at around 2 ppm are identified, which can be assigned to the tetrahedral and octahedral Al environment, respectively (Sun et al, 2006). It has been reported that the resonance at around 2 ppm is assigned to the octahedral component in the mullite.

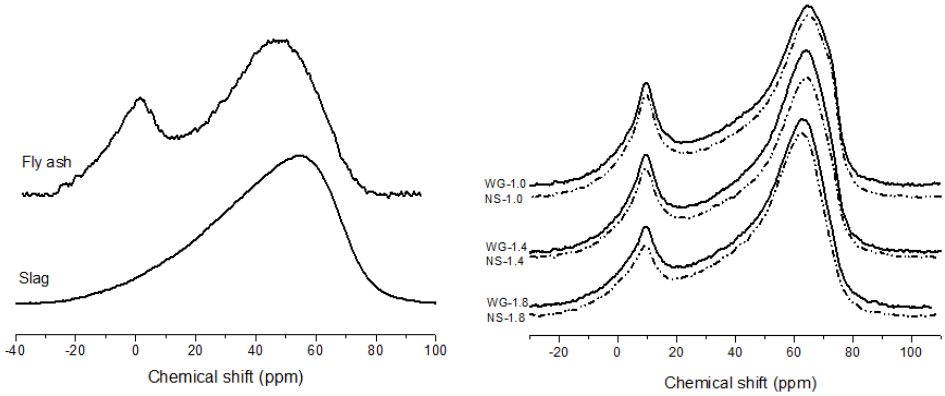

(a) (b)

Figure 5-10: ^{27}Al MAS NMR of starting materials and reaction products

As shown in Figure 5-10(b), after activation, all mixtures show a significant peak at around 64 ppm, and a narrow one with a relatively low intensity at about 10 ppm. The aluminate peak at 64 ppm is assigned to the tetrahedral Al(IV) that is incorporated in the $Q^2(1Al)$ and $Q^3(1Al)$ sites in C-A-S-H gels with bridging conditions (Saout et al, 2011), which is also proved by the ^{29}Si MAS NMR results in this study. It is also possible that a small amount of amorphous N-A-S-H type gels presents a contribution to this distorted Al(IV) region. The sharp peak centered at

10 ppm is commonly assigned to AFm and hydrotalcite type phases with octahedral coordination.

In this case, considering the identified crystalline phases (2 ppm with octa-Al) in the origin fly ash, and the relatively low content of fly ash in the total binder, the resonance centered at 10 ppm can be regarded as the hydrotalcite type phases from the alkali activation of slag (Mackenzie et al, 1993). It should be noticed that these phases are usually poorly crystalized and formed in the interlayers of C-A-S-H gels, making it difficult to be detected by XRD (Schilling et al, 1994), while the ^{27}Al MAS NMR verifies its presence. Besides, the unreacted slag and fly ash also contribute to the tetra-coordinated Al region (50 to 100 ppm), pentahedral region (30 to 40 ppm) and octahedral region (-10 to 20 ppm). For a constant activator modulus, the difference in Al environments between olivine nano-silica based mixtures and commercial sodium silicate derived ones is rather small; with two obvious peaks that representing newly formed Al(IV) and Al(VI) sites, also their peak locations remain unchanged, indicating a similar bonding environments surrounding the Al groups. Thus it is reasonable to conclude that the silica origin shows limited influence on the Al structures. When increasing the activator modulus, a slight decrease can be observed in the relative intensity of octahedral Al peak, compared to the tetrahedral one. It indicates that when the silicate content is increased in the system (from activator), more Al will participate into the C-A-S-H gels rather than form individual Al-rich phases.

5.6 Fresh behaviors

Mortar samples were also prepared to evaluate the fresh and hardened properties, the applied binder/sand ratio was kept constant at 1/3. The slump flows of the fresh alkali activated slag-fly ash mortars with different activator type and modulus are presented in Figure 5-11.

Mixtures with olivine silica based activators present a higher workability than the commercial sodium silicate based ones, and samples with higher activator moduli exhibit higher flowability in general. For instance, with a constant activator modulus of 1.0, the slump flow is 15.6/17.7 cm for the waterglass/olivine silica based activator, respectively. Similar results are also shown in mixes with other activator moduli. This can be explained by the silicate origin in the activator. In the case of commercial sodium silicate solutions, the higher contents of available oligomers exist in the solution, namely a lower modulus or higher pH, the faster of reaction rate will be. Therefore this leads to a reduced flowability by increasing the viscosity of the fresh paste.

The activator modulus also shows an obvious effect on the flowability, as can be seen from Figure 5-11 that the slump flow increases from 17.7 cm to 23.5 cm (for nano-silica based ones) when increasing the activator modulus from 1.0 to 1.8. It is commonly known that the increased silicate content in the sodium silicate solution will result in an increase of the viscosity (Provis et al, 2009); thus the mixture with a higher activator modulus should exhibit a lower workability.

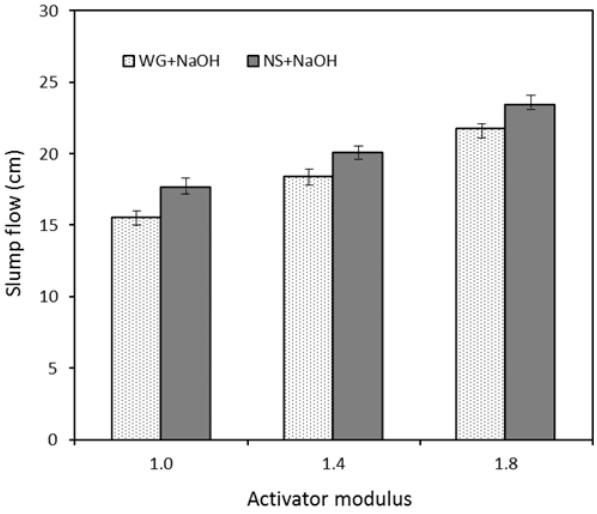

Figure 5-11: Slump flows of AA slag-fly ash mortars with different activator conditions

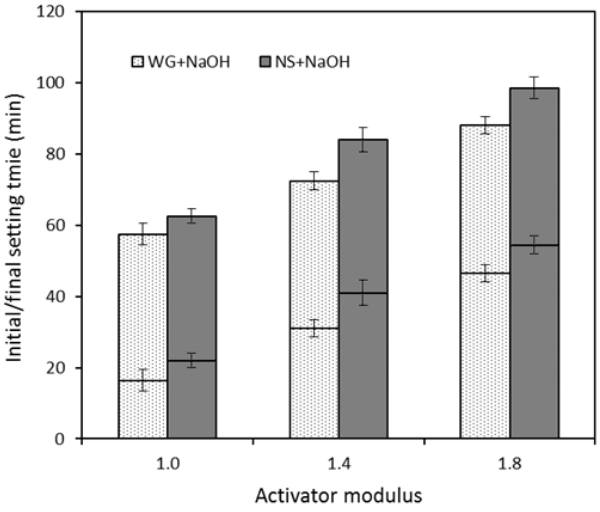

Figure 5-12: Effect of activator conditions on setting times

However, here the slump flow results are inversely related to the activator modulus. This phenomenon suggests that the chemical reaction between the solution and the raw materials play a more significant influence on the flowability than the viscosity of the activating solution alone. The initial and final setting times of all mixes are depicted in Figure 5-12. It can be seen

that the nano-silica based activators present longer setting times than the commercial sodium silicate based ones, and mixtures with a lower activator modulus exhibit faster setting times in general. For instance, the nano-silica based mixes show an initial/final setting time of 22/63 mins with an activator modulus of 1.0, and it gradually prolongs to 55/99 mins when the activator modulus increases to 1.8.

5.7 Compressive strength

The 7 and 28 d compressive strengths of mixtures with different activator moduli and silicate sources are depicted in Figure 5-13. For a fixed activator modulus, the olivine nano-silica based samples exhibit rather comparable while slightly lower compressive strengths than the commercial sodium silicate based ones. For instance, with an activator modulus of 1.0, the 7/28 d strength is 57.9/70.0 MPa for the nano-silica based ones, while for the for sodium silicate based mixes, this value is 64.7/75.4 MPa. A similar tendency is also shown in other activator moduli. Previous researches also indicate that samples synthesized by alternative silicate sources yield a lower strength than the traditional ones (Rodriguez et al, 2013; Bernal et al, 2012). This phenomenon can be explained by the generally lower reaction degree of the starting materials and therefore less formed reacted gels results in a lower mechanical property.

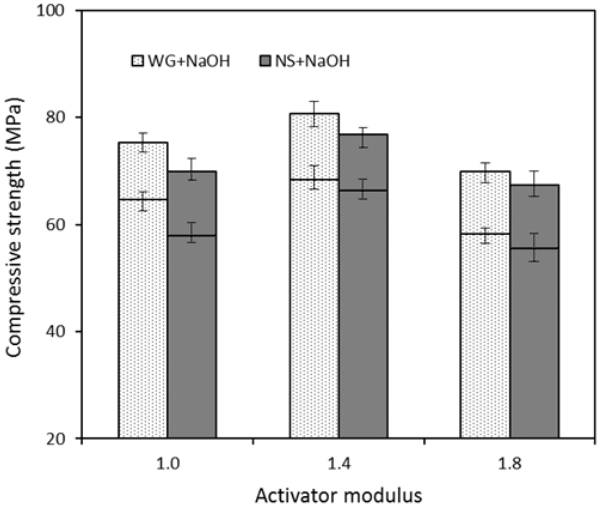

Figure 5-13: 7 and 28 d strengths of AA slag-fly ash blends with different activators

It should be noticed that although the olivine nano-silica based mixes exhibit lower strengths, these values are in overall within 10% less than the corresponding sodium silicate based ones. And their 7 d strengths range from 55.5 MPa to 66.3 MPa and the 28 d strengths are from 67.3 MPa to 76.8 MPa, which are still suitable for various applications. It is well known that the

activator modulus plays an important role in determining the compressive strength. The additional silicates from the activator participate in the reaction process and influence the Si/Ca and Si/Al ratios of the reaction products. It is important to notice that in terms of the effective silicate content, a large amount is provided by the activator. For instance, the silicate provided by the activator consists of around 14% to 25% of the total silicate in this study. Therefore, an efficient utilization of the additional silicate or using alternative silicate source is of great interest in terms of the costs and the environmental issues of this material.

It can be seen from Figure 5-13 that for mixes based on olivine nano-silica, the 7 d strength is 57.9 MPa with an activator modulus of 1.0, and it increases to 66.3 MPa when increasing the activator modulus to 1.4, a further increase of the modulus to 1.8 leads to a reduction of strength to 55.5 MPa. A similar tendency is also shown in the strength at 28 d, samples with an activator modulus of 1.4 exhibits the highest strength of 76.8 MPa. The presence of the optimal strength implies that there exists an optimum additional silicate content based on a certain composition of the starting material. However it is difficult to quantify this relation since several factors besides the total Si/Ca and Si/Al ratio also show an influence on compressive strength, such as the mineral composition, amorphous phase content and fineness of the starting materials, alkali concentration, curing conditions, flowability and porosity. On the other hand, changing the activator modulus from 1.0 to 1.8 leads to a strength variation up to 10.3 MPa. While besides the optimum strength, mixes with an activator modulus of 1.0 exhibit a slightly higher strength than the ones with modulus of 1.8. It is concluded that ideal compressive strengths can be achieved by using suitable content of additional silicate, since a further higher silicate content increases the cost and environmental impacts of the material but does not lead to an increased strength.

5.8 Porosity and drying shrinkage

The 28 d water permeable porosities of all mixes are shown in Figure 5-14. For the olivine nano-silica based mixes, the porosity is 20.9% with an activator modulus of 1.0, while it slightly decreases to 19.3% when increasing the modulus to 1.8. Similarly, the porosity of commercial sodium silicate derived samples decreases from 20.2% to 18.9% within the activator modulus range. It is suggested that the gradual reduction of porosity is attributed to the additionally provided silicate groups from the activator, which refines the pore structure by both filler effect and participating in the resulted gels. Therefore, if porosity would be the only consideration, adding extra silicate within a reasonable range may always be beneficial. However, the relations between porosity and other properties shown in this study suggest a reasonable utilization of the additional silicates. For instance, the reduced porosity does not always result in an increased compressive strength, and an an optimum activator modulus is shown in both cases. Regarding the effect of additional silicate source, it is easy to understand that commercial sodium silicate based samples exhibit a comparable level of porosity, since these mixes present similar strength when compared to the olivine nano-silica prepared ones.

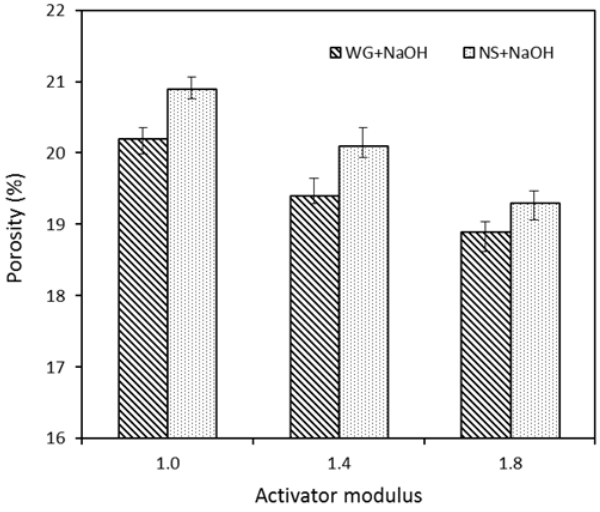

Figure 5-14: 28 d water permeable porosity of mixes with different activator conditions

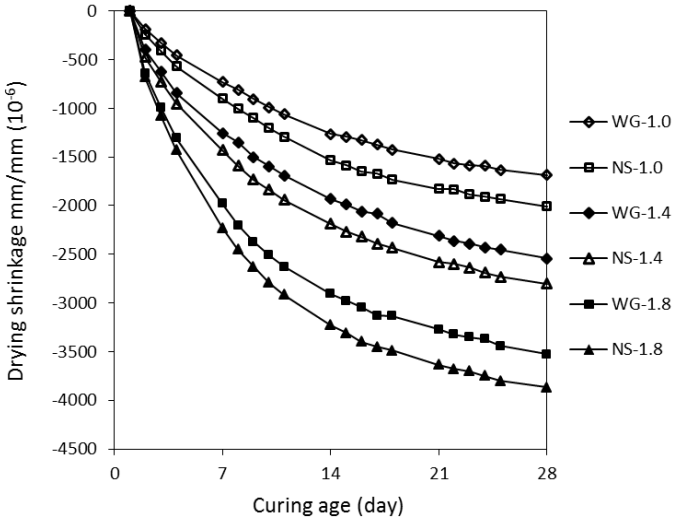

Figure 5-15: Drying shrinkage of mixes with different activator conditions

The drying shrinkage of all mixtures until 28 d of curing is presented in Figure 5-15. All mixes exhibit an obvious length change over time, and a higher drying shrinkage is usually shown when compared to the Portland cement, due to the nature of the reacted gels. It can be seen that both silicate source and activator modulus show a strong influence on the drying shrinkage. For instance, for the olivine nano-silica based samples, the length change at the age of 28 d is

around - 2006 × 10-6 for mixes with an activator modulus of 1.0, while it increases to -2803 × 10-6 and -3868 × 10-6 when increasing the activator modulus to 1.4 and 1.8, respectively. A similar tendency is also presented in commercial sodium silicate based samples, where a reduced shrinkage is observed. It is possible that the refined pore structure caused by the additional silicate may be linked to the shrinkage behaviours due to the self-desiccation. Therefore, if the shrinkage is the main concern of a certain application, reducing the activator modulus can be an efficient approach.

5.9 Advantages in sustainability

5.9.1 Energy and costs

It should be noted that in order to obtain commercial sodium silicate solution, the melting of quartz sand requires much higher temperature (usually over 1000 °C) and therefore significantly higher energy costs and carbon emissions than the olivine nano-silica process that performed under 95 °C. An estimation of the cost of the raw materials, the energy requirements and CO_2 emissions is below presented for both production processes. The average prices of dunite, sulfuric acid, sodium hydroxide and waterglass with a 2.5 SiO_2:Na_2O and silica content of 27 wt. % are 152, 113, 400 and 555 $/ton, respectively. The raw material cost of silica activator that produced from the dissolution of olivine sums up to 1148 USD per ton of silica equivalent, see Table 5-5 from (Lazaro, 2014). On the other hand, the price of commercial waterglass is almost twice as expensive as activators produced from olivine nano-silica, making a total of 2166 USD per ton of silica equivalent (Lazaro, 2014; Jonckbloedt, 1997).

Table 5-5: Estimated costs of sulfuric acid, olivine, sodium hydroxide for the production of 1 ton of olivine nano-silica

Cost of acid				Cost of olivine			Cost of NaOH		Overall cost
n_{NS} (kmol)	n_{H2SO4} (kmol)	m_{H2SO4} (kg)	C_{H2SO4} ($)	n_{ol} (kmol)	m_{Ol} (kg)	C_{ol} ($)	m_{NaOH} (kg)	C_{NaOH} ($)	C_{RM} ($)
16.64	33.29	4250	645	16.64	3355	377	313	125	1148

In addition, 403 kg of CO_2/ton is released during the production of waterglass, the required energy reported by several companies for the production of 2.0 sodium silicate liquor (SiO_2:Na_2O ratio of 2:1) with a 48% solid content (i.e., 32 wt.% of SiO_2) is between 420 and 1250 MJ/ton (European Commission, 2007). Taking the average of these two values and considering that 3900 kg of 27 wt.% waterglass is used per silica ton, results in an energy requirement of 2800 MJ/ton. The energy required during the synthesis of olivine nano-silica could be negligible since the reaction is exothermic. Thus, the energy requirement as well as

the CO_2 emissions from the olivine nano-silica production process represents an enormous reduction as compared to the sodium silicate production process.

5.9.2 Carbon footprint

An important driving force and potential benefit of applying this alternative silicate source is the reduction of the carbon emission of alkali activated binders. Therefore a calculation on the CO_2 footprint was carried out and the results are shown in Table 5-6. The carbon footprint is usually calculated as the sum of the CO_2 emissions of each component in unit volume of concrete. Considering that this value is highly related to the proportions of each particular component and the mix proportion of concrete can be largely varied; thus in this study, the evaluation is based on an assumed concrete recipe with an experienced binder content of 450 kg/m^3, and a Portland cement based sample is used as a reference. As listed in Table 5-6, the sodium silicate activator contains NaOH and commercial waterglass (Na_2O-$nSiO_2$-mH_2O), while the alternative activator consists of NaOH and olivine nano-silica ($xSiO_2$-yH_2O). Their corresponding contents are determined based on 450 kg/m^3 of binder, and those values are the effective solids contents excluding water. The carbon footprint used in this calculation: NaOH (1.915 tCO_2/t), commercial waterglass (1.514 tCO_2/t), OPC (0.82 tCO_2/t), slag (0.143 tCO_2/t), fly ash (0.027 tCO_2/t), fine aggregate (0.0139 tCO_2/t) and coarse aggregate (0.0459 tCO_2/t) are obtained from (Collins et al, 2010; Tumer et al, 2013), while the CO_2 footprint of olivine nano-silica (0.461 tCO_2/t) was estimated from a life cycle analysis performed by VTT (EU F7th project, ProMine internal report).

Table 5-6: Calculation of CO_2 emissions based on a sample concrete mix (kg/m^3)

Mix	Mix proportions						CO_2 emissions	
	Binder	NaOH	Na_2O-$nSiO_2$	Nano-silica	Fine aggr-	Coarse aggr-	From activator	In total
WG-1.0	315 Slag + 135 Fly ash	20.52	28.49	0	800	1000	82.44	188.16
WG-1.4		17.1	39.74	0			92.93	198.65
WG-1.8		13.64	51.35	0			103.82	209.54
NS-1.0		29.03	0	21.87			65.66	171.38
NS-1.4		29.03	0	30.51			69.66	175.38
NS-1.8		29.03	0	39.42			73.76	179.48
Ref	450 OPC	0	0	0			0	426.02

It can be seen from Table 5-6 that compared to the alkali activated material based concrete, the carbon emission of Portland cement concrete is more than doubled, indicating the clear benefit of using slag and fly ash as alternative binder in sustainable development. In terms of the alkali activated concrete, the carbon emission from activator consists of 43.8% to 49.5% of the total emission in commercial sodium silicate based mixes, and this value is around 38.3% to 41.1% in olivine nano-silica based ones, indicating a strong influence of activator in the total carbon emission. If concerning the activator alone, when olivine nano-silica is applied as the alternative silicate source for activators, the carbon emission per 1 m^3 of concrete is reduced by 20.4%, 25.0% and 29.0% in mixes with a modulus of 1.0, 1.4 and 1.8 respectively, compared to the commercial waterglass based ones. It is obvious that this reduction rate becomes higher when increasing the activator modulus. This is of great benefit since the alkali activated system usually requires additional silicate to improve its performance to a higher level, and when the olivine nano-silica is utilized to replace the commercial sodium silicate, a significantly reduced burden to the environment can be resulted. Moreover, the olivine nano-silica production could be still more sustainable if the heat produced during the reaction could be reused, the CO_2 footprint will be further reduced.

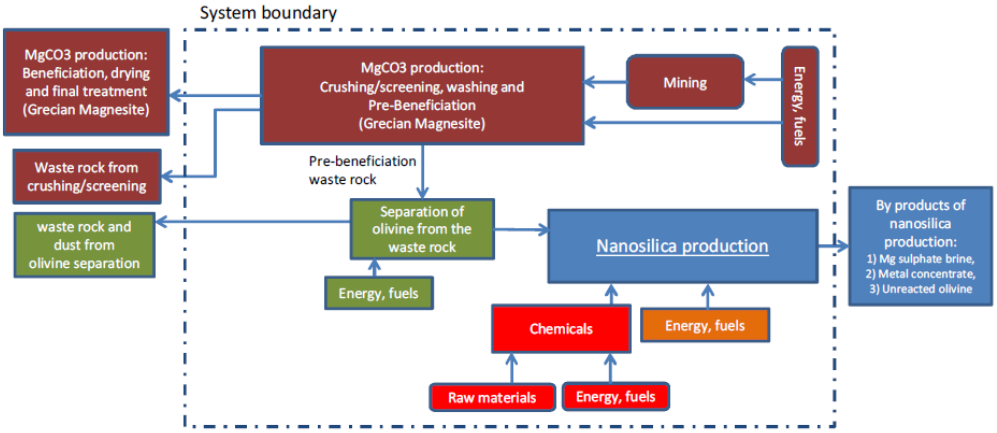

Figure 5-16: System boundary of the applied LCA analysis

It is important to note that the carbon footprint for olivine nano-silica shown here is an average European industrial case scenario, without make use of the heat that generated during the production of nano-silica, once this part of energy is reused, the carbon emission will be further reduced (see Equation 1 in Chapter 5.2). It should be mentioned that the nano-silica production data provided to the calculation is based mainly on laboratory and bench scale testing, and at this stage all amounts are based on reaction stoichiometric. The system boundary and data sources (obtained from either companies or research organizations) applied in the nano-silica

production LCA (life cycle analysis, a technique that addresses the overall environmental impacts of a product's life) is shown in Figure 5-16 and Table 5-7, respectively. The carbon footprint result used in this case (average European industrial scenario) is depicted in Figure 5-17.

Table 5-7: Data source of the applied LCA analysis

Process	Data Source
Olivine production	Grecian magnesite
Nano-silica production	Selor
Chemicals: H_2SO_4 and MgO	VTT's KCL-EcoData EcoInvent
Electricity and heat	
Fuels	
Transportation	VTT's LIPASTO database

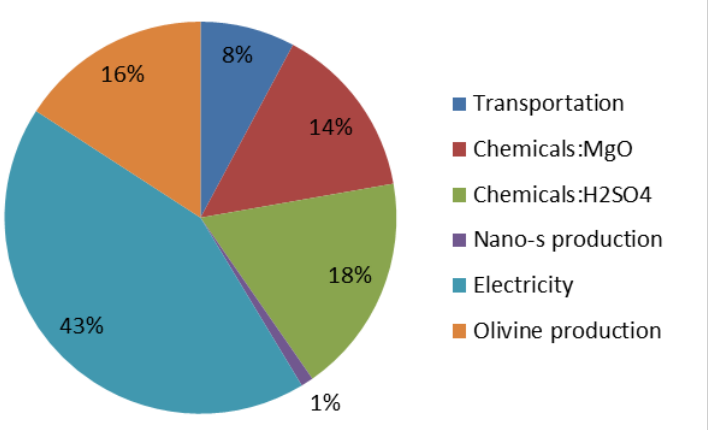

Figure 5-17: Composition of the carbon footprint during nano silica preparation

5.10 Conclusions

In this chapter, a green olivine nano-silica was synthesized and applied as an alternative alkali activator in alkali activated slag-fly ash blends; mixes with three different contents of additional silica were designed. Performance evaluations were carried out including activator characteristics, reaction kinetics, gel structure, compressive strength, fresh and hardend behaviors, and CO_2 footprint. Comparisons were made with commercial sodium silicate based mixes. The following conclusions can be drawn based on the results:

- The olivine nano-silica is well dissolved in a NaOH solution to prepare activators with the same chemical composition as the sodium silicate based ones. The soluble silicate in the nano-silica based activators is above 99%; except the one with a modulus of 1.8, which nevertheless has a soluble silicate content of 98.1%. ^{29}Si NMR characterizations on the alkali solutions show that increasing the modulus results in increased content of high crosslinking Q structures, and nano-silica based activators show relatively high percentage of Q3 sites.
- For the same activator modulus, the olivine nano-silica based mixes present similar reaction process compared to the commercial waterglass based ones, with a slightly less intensity. Mixes with a higher activator modulus also exhibit a delayed early age reaction with reduced reaction intensity.
- Solid-state ^{29}Si and ^{27}Al MAS NMR together with TG verify that when increasing the activator modulus, the reactivity of slag is reduced, as well as the Al incorporation in C-A-S-H gels; nano-silica derived mixes show an increase of Q3(1Al)+Q4(4Al) sites, while those groups in commercial waterglass based ones remain stable. The nano-silica replacement results in a slightly reduced chemically bound water content and compressive strength, compared to the sodium silicate based mixes.
- The investigation on the effect of activator modulus reveals both physical and chemical modification of the additional silicates from activator, and an optimum compressive strength is observed in mixes prepared with activator modulus of 1.4.
- Compared to the sodium silicate based mixes, the nano-silica replacement results in an increased initial/final setting time, flowability, porosity and shrinkage, and slightly reduced compressive strength. Nevertheless, the changes caused by the different silicate origin are rather limited.
- Alkali activated binders show much lower CO_2 compared to OPC. When olivine nano-silica is used as an alternative silicate source, the CO_2 emission from activator is reduced by 20.4% to 29.0% within the activator modulus range of 1.0 to 1.8; indicating a significant advantage towards carbon emission. In addition, the total CO_2 footprint can be further lower if the high amount of energy generated during the production of olivine nano-silica can be reused.

Chapter 6

Suitability of reusing solid wastes as substitutes

6.1 Reuse of MSWI bottom ash

6.1.1 Introduction

Besides the applications of alternative binders and activators, the reuse of solid wastes can also greatly contribute to sustainable development. One typical waste material is the municipal solid waste incineration (MSWI) bottom ash (BA). This is a by-product from municipal solid waste incineration, which may contain glass, metals, ceramics, minerals, stone, brick, and unburned organics (Chimenos et al, 1999). The incineration process shows benefits in massive reduction of the solid household wastes (Bosmans et al, 2013), energy reuse (Cimpan and Wenzel, 2013) and recycling of certain metals, paper and plastics (Wiles, 1996). And the resulting bottom ash is encouraged to be reused as a secondary building material in Europe especially considering the rapidly increased amount of land filling and to reduce the usage of natural gravels. In addition, applications of bottom ash as aggregate substitute in cement based materials were successfully carried out (Forteza et al, 2004; Lee et al, 2010).

However, there exists several significant drawbacks that limit the wide application of this waste material: generated cracks due to the presence of metallic aluminium (Bertolini et al, 2004), obvious alkali-silica reaction because of the glass residues (Juric et al, 2006) and leaching of heavy metals (Hjelmar et al, 2007). The primary environmental issue of MSWI BA comes from the leaching of heavy metals that could lead to severe damage on water resources (Birgisdottir et al., 2006) and human health (Song et al., 2013). In the Netherlands, a national regulation termed Soil Quality Decree limits the amount of leachable contaminants from construction materials in order to control the potential negative environmental impacts (Eikelboom et al., 2001). Thus appropriate treatments are usually required before a certain application. Besides, another grounded solid waste is the granite powder, which comes from the crushing and washing of high quality granite aggregates. Compared to waste bottom ash, it contains no risky contaminants to the environment but brings pressure to land filling. Therefore, a suitable application of these two solid wastes in construction and building materials will be of great benefit in reducing the environmental impacts.

It was reported that the alkali activated materials are proper binders to immobilize the heavy metals in bottom ash. For instance, the effective binding of Cr, Cd, Zn and Pb in alkali activated slag (Jan, 2002), and Pb, Cr, Cu and Sn in aluminosilicates dominated geopolymers (Rozineide et al, 2016). It reveals that reusing bottom ash in alkali activated systems shows

convenience in heavy metal treatment, which further results in reduced costs and wider applications. Depending on the nature and particle sizes of bottom ash, it shows the feasibility to be partial replacement of both binder (Chen et al, 2016) and aggregate (Xie et al, 2015). Besides, although limited attention was paid to reusing the granite powder, its similar origin to limestone powder may indicate an analogical application potential, which benefits both Portland cement and alkali activated binders by reducing the binder dosage and refining the pore structure (Bonavetti et al, 2001). As can be noticed, previous researches mainly focused on identifying the possibility of reusing bottom ash in alkali activated materials and the heavy metal binding effect; while limited attention was paid to the chemical effect of bottom ash on this new binding system such as early age reaction and gel composition.
The objective of this section is to carry out a comprehensive study on reusing two solid wastes, bottom ash and granite powder, as replacements of either binder or aggregate in alkali activated materials, and evaluating the performances from micro to macro scales. Firstly a systematic characterization of the starting materials is carried out, then suitable waste material dosages and their effects on reaction kinetics, mechanical properties, gel structure, micrograph and leaching behavior of the reaction products are investigated.

6.1.2 Characterization of waste materials

A detailed characterization of the MSWI bottom ash and granite powder was carried out. The moisture contents and densities were firstly identified. For the moisture content test, bottom ash and granite powder from different areas of the container were sampled and heated up to 105 ± 5 °C until the mass was constant. The average moisture content (of nine samples) for bottom ash and granite powder is 20.6% and 20.8%, respectively. The high free water content of bottom ash and granite powder slurry should be carefully considered during the design process. For the bottom ash, it can be used after evaporating the free water or applied directly by taking its water content into account. Considering the granite powders, it should be noted that the high free water content together with its fine particles may cause difficulties in dispersion of this material during the mixing. Thus a drying process or a pre-mixing/dispersion process is suggested. While in this study, waste bottom ash was dried to exclude the free water, in order to achieve a constant starting condition. The sticky granite powder was firstly dispersed in water with the addition of a superplasticizer, and this pre-dispersion process resulted in a well dispersed granite powder in water, which can be applied directly in mortar manufacturing. Their specific densities were measured by using the gas intrusion method employing an AccuPyc 1340 II Pycnometer, after drying. The measured value is an average of three samples, which is 2.72 $g \cdot cm^{-3}$ for bottom ash and 2.74 $g \cdot cm^{-3}$ for granite powder, respectively. Those values are similar to the commonly used fine aggregates and hydraulic materials such as slag, making it convenient in the designing processes that are based on both mass and volume.

The detailed particle size distributions (PSD) of the bottom ash and granite powder are shown in Figure 6-1, together with the other solids that will apply in this chapter. The PSD of granite was measured in liquid dispersion using the Mie scattering model as the measuring principle following ISO 13320 (2009); while the bottom ash was analyzed by sieve analysis according to the standard EN 933-1 (1997). It can be seen that the granite powder shows a particle size range from 100 nm to 400 µm, with a medium particle size of around 10 um, which is similar to the commonly used powder additives. Concerning the bottom ash, it shows a medium particle size of around 800 µm and a size range from 10 µm to 2000 µm. It should be noticed that a certain amount of smaller particles may aggregate with each other to form bigger ones, and those aggregated particles easily break during the sieving process, thus pre-treatments might be needed when applying them.

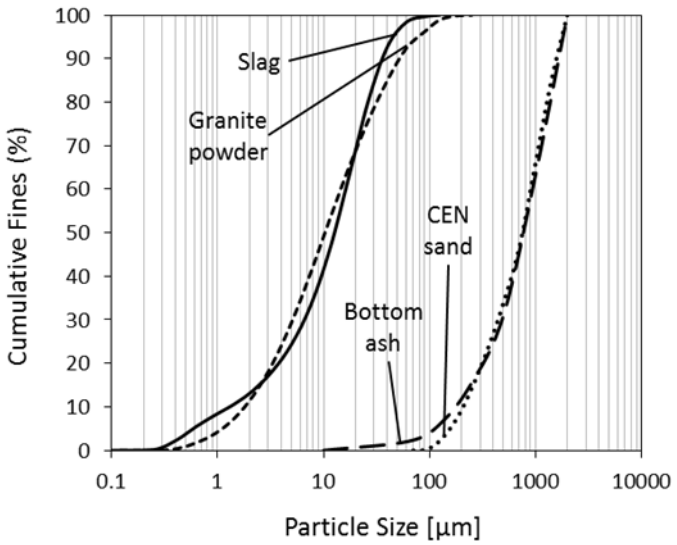

Figure 6-1: Particle size distributions of Bottom ash and Granite powder

Figure 6-2 presents the SEM picture of the waste bottom ash. Bottom ash particles with different sizes and shapes are observed, which are mainly a physical combination of various types of incinerated residues from urban wastes. Large amounts of pores are also identified, which is partly due to the nature of those starting materials, and partly caused by the incineration process. The porous structure will negatively influence the mechanical strength of the bottom ash when used as aggregates, and increase the water demand to some extent. However, if a suitable mix design is applied; those drawbacks can be largely reduced. Besides, porous aggregates are known to promote the late hydration process by the effect of internal curing, and how this bottom ash affects the reaction process in the long term is another research interest.

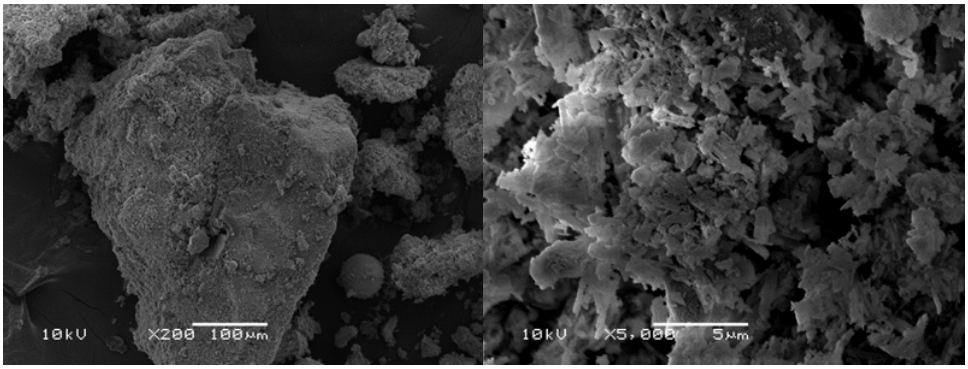

Figure 6-2: SEM picture of the bottom ash

The chemical compositions of bottom ash and granite powder are listed in Table 6-1, and their XRD patterns are shown in Figure 6-3. It shows that the granite powder mainly contains Si, Al and Ca; and limited amounts of heavy metals and sulfates. While the main mineral components identified are plagioclase ($NaAlSi_3O_8$-$CaAl_2Si_2O_8$), quartz (SiO_2), calcite ($CaCO_3$), and k-feldspars including orthoclase ($KAlSi_3O_8$). All those minerals, except for calcite, are typical compositions of natural granite, thus the granite powder in this case can be generally regarded as a mixture of natural granite and calcite powder. In the case of the bottom ash, the primary elements are also Ca, Si and Al, but with different contents compared to granite powder. Besides, certain amounts of environmental related components are presented such as heavy metals, chloride and sulfates, which should be carefully handled before application. The major minerals observed are calcite, and small amount of quartz and magnetite.

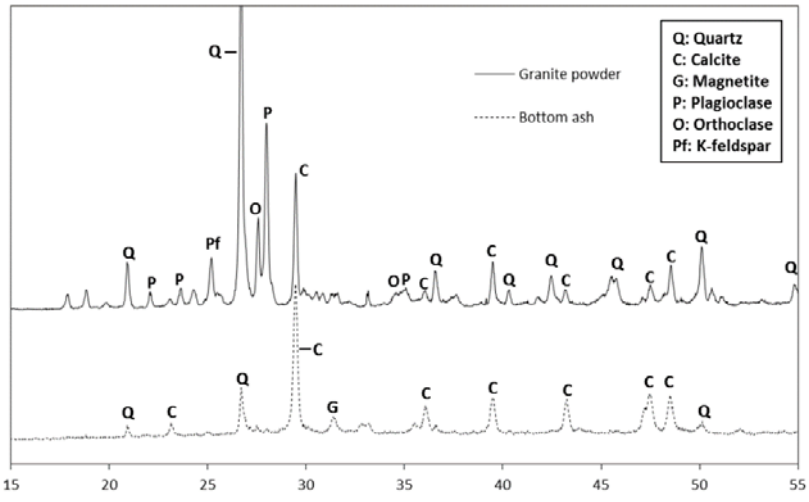

Figure 6-3: XRD patterns of Bottom ash and Granite powder

Table 6-1: XRF analysis of waste bottom ash and granite powder (wt. %)

Chemical compositions	Bottom ash	Granite powder
Na_2O	2.36	2.03
MgO	2.12	3.44
Al_2O_3	12.04	16.68
SiO_2	19.12	57.50
P_2O_5	2.63	0.05
SO_3	2.39	0.12
K_2O	0.85	4.52
CaO	43.12	9.13
TiO_2	2.48	0.84
Cr_2O_3	0.15	0.03
MnO	0.20	0.11
Fe_2O_3	9.31	5.35
NiO	0.04	-
CuO	0.87	-
ZnO	1.29	0.01
SrO	0.13	-
ZrO_2	0.04	0.02
Ag_2O	0.16	0.07
BaO	0.24	0.10
PbO	0.32	-
Cl	0.17	

6.1.3 Compressive strength

The activator used in this study had an equivalent sodium oxide (Na_2O) content of 5% and an activator modulus of 1.4. The used water/powder ratios were 0.5 and 0.55. Incinerated waste bottom ash contents up to 50% (by volume of the fine aggregates) and granite powder contents up to 20% (by volume of the binder) was applied. The detailed mix proportions of the used materials are listed in Table 6-2.

Table 6-2: Mix proportions (kg/m^3)

Mixtures	Binder content		Aggregate content		w/p
	Slag	Granite powder	Bottom ash	Sand	
S	450	0	0	1350	0.5/0.55
S+10BA	450	0	97.2	1215	0.5
S+20BA	450	0	194.4	1080	
S+30BA	450	0	291.6	945	
S+40BA	450	0	388.8	810	
S+5GP	427.5	20.9	0	1350	
S+10GP	405	41.8	0	1350	
S+15GP	382.5	62.7	0	1350	
S+20GP	360	83.6	0	1350	
S+25BA	450	0	243	1012.5	0.55
S+25BA+10GP	405	41.8	243	1012.5	
S+25BA+20GP	360	83.6	243	1012.5	
S+50BA	450	0	486	675	
S+50BA+10GP	405	41.8	486	675	
S+50BA+20GP	360	83.6	486	675	

The 7 and 28 d compressive strengths of mixtures with different waste bottom ash and granite powder contents are depicted in Figure 6-4. All mixes are having a water to powder ratio of 0.5.

For the reference sample, the compressive strength is 56.2 MPa at 7 d, and it increases to 69.6 MPa after 28 d of curing. When waste bottom ash is incorporated to replace fine aggregates, there is a continuous decrease in strength from 56.2 MPa to 27.5 MPa at 7 d and from 69.6 MPa to 34.61 MPa at 28 d. It should be noted that the strength decrement between 7 and 28 d is significant within the bottom ash content of 20%, while the strength shifts become relatively mild in mixes with bottom ash content from 20% to 40%. The obvious reduction in strength can be attributed to the porous structure of waste bottom ash after incineration, and therefore a lower strength of this aggregate. The reduced bond strength between aggregates and the binder (interfacial transition zone) can be another reason for the reduced compressive strength, which is caused by the relatively fragile structure of bottom ash (i.e. a low crushing strength) compared to the natural fine aggregates. Besides, it should be noted that the metallic aluminium from the bottom ash usually causes cracking and sometimes even initial failure when it is applied without suitable treatment (Aubert et al, 2004); while in the alkali activated system, no expansion and cracking were observed. It is suggested that this is due to the high alkali concentration (with pH value above 13) of the activators at the initial stage of mixing, which will dissolve those aluminates to some extent and reduce/eliminate the expansion. Those dissolved aluminates may also contribute to the reaction process since the alumina is one of the starting components of the alkali activated system. In addition, since the aluminate has no negative effect on the binder matrix and its extraction process can be ignored, the application of this bottom ash can be more cost effective. The effect of the metallic aluminate from bottom ash on the reaction process is an interesting issue, and it will be investigated in detail in future studies.

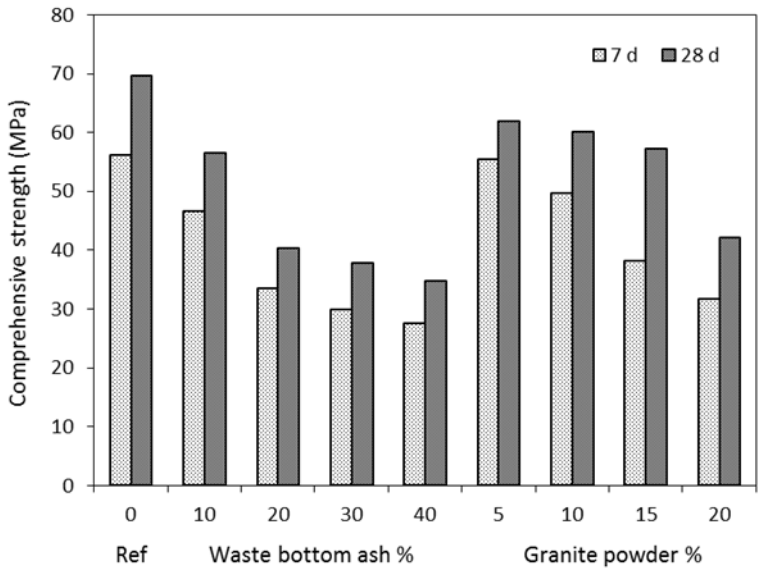

Figure 6-4: Compressive strength of mixes with bottom ash or granite powder (w/p = 0.5)

Concerning the effect of granite powder, the replacement up to 15% leads to a gradual decrease of strength from 69.6 MPa to 57.1 MPa (by 18%) after 28 d of curing. Further increment up to 20% results in a more obvious reduction of strength to 41.9 MPa. The effect of granite powder content on strength can be partly explained the filler effect: on the one hand the granite powder works as micro aggregates, reducing the total porosity and benefiting the strength; while on the other hand, its increased content negatively influences the binding matrix, resulting in strength reduction. The optimal dosage may vary from case to case. It should be noted that in Portland cement system, the suitable limestone powder content of up to 10% is usually observed, showing a similar tendency as the granite powder in this study. The replacement of granite powder within a reasonable range reduces the binder dosage in alkali activated system, and therefore reduces the total costs of the final products; also the reuse of this waste material contributes to the sustainable development.

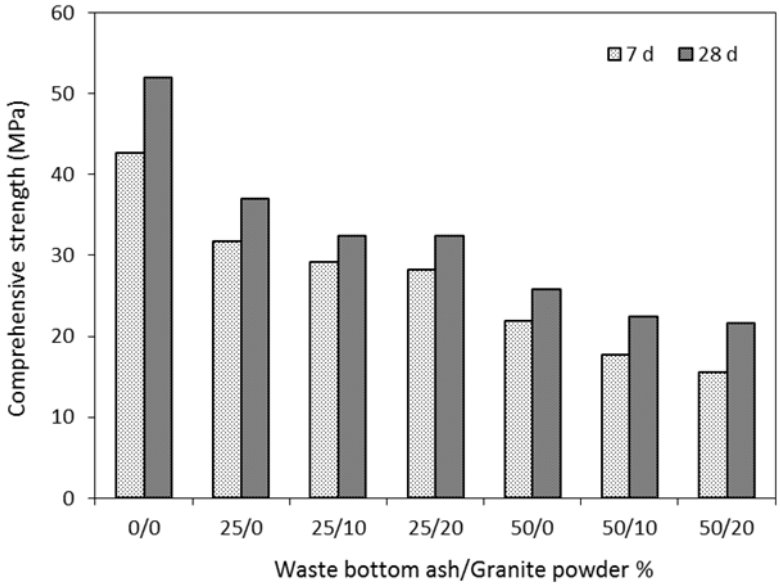

Figure 6-5: Compressive strength of mixes with bottom ash and granite powder (w/p = 0.55)

The effect of hybrid usage of bottom ash and granite powder on compressive strength is shown in Figure 6-5. In order to show the combined effect of those two materials on the strength, the bottom ash contents of 25%, 50% and granite powder contents of 10%, 20% are chosen, based on the results of their individual effect on strength. The used water to powder ratio is fixed at 0.55. Compared to the results from Figure 6-4, the increase of water to powder ratio leads to an obvious strength reduction in general. The reference sample shows a 7 d strength of 42.5 MPa and it increases to 52.0 MPa at 28 d. Similarly, the addition of bottom ash results in a

significant reduction of strength at both 7 and 28 d, because of its porous structure. For a fixed bottom ash content, the 10% replacement of granite powder only leads to a slight decrease of strength, and further increment to 20% presents very limited influence.
Mixtures with bottom ash/granite powder additions of 25/20 and 50/20 show compressive strengths of 32.3 MPa and 21.6 MPa, respectively. Additionally, it should be noticed that the addition of porous or fine particles would decrease the flow ability of the fresh samples, which also shows an effect on the mechanical properties (Huiskes et al, 2016). In the present study, increasing the bottom ash content up to 40% in the reference mix results in a reduction of slump flow from 21.5 cm to 18.9 cm. Similarly, the flowability reduces to 19.2 cm with the granite powder replacement of 20%. In summary, although significant reductions in strength are observed when large amounts of bottom ash are applied, the compressive strength range in this study shows excellent applicability for many applications; while suitable granite powder addition reduces cement consumption and shows limited influence on strength. Thus both solid wastes present promising application potentials.

6.1.4 Reaction kinetics

The compositional analyses have shown that both MSWI bottom ash and granite powder contain high amounts of CaO, SiO_2 and Al_2O_3, also crystalline phases containing these mineral oxides are clearly observed. While in the case of alkali activated system, any starting material that contains reactive Ca, Si and Al can be used for activation. Therefore, identifying the reactivity of waste bottom ash and granite powder is of importance since they have the potential to be applied as a binder substitute.

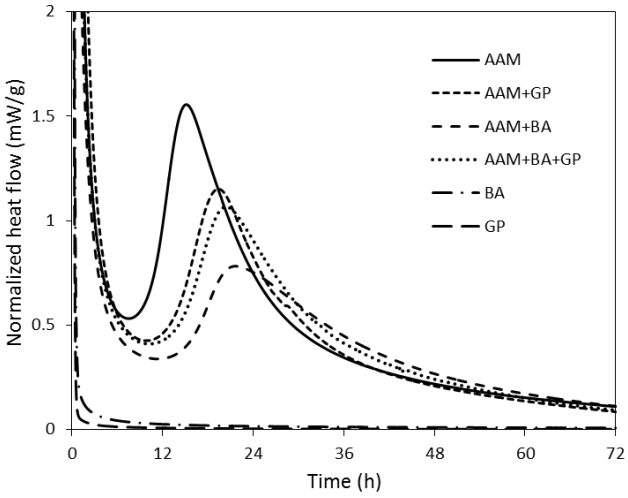

Figure 6-6: Normalized heat flow of AAMs, waste bottom ash and granite powder

The isothermal calorimeter is used in order to investigate the effect of these two solid wastes on the early age reaction process of the basic cementitious system. Figure 6-6 shows the normalized heat flow of six mixes within the first 72 h. The heat flow is normalized by mass of the binding material (slag), except for samples containing only Granite or bottom ash that are normalized by mass of the Granite or bottom ash. The used activator has a Na_2O dosage of 5% and total water to powder ratio of 0.5, which are the same parameters as used in the mortar samples. Samples labeled with "BA" and "GP" refer to the ones that contain purely waste bottom ash or granite powder that is mixed with the alkali activator, while "AAM" refers to the alkali activated materials. Paste samples are prepared and the bottom ash is grind to powder form.

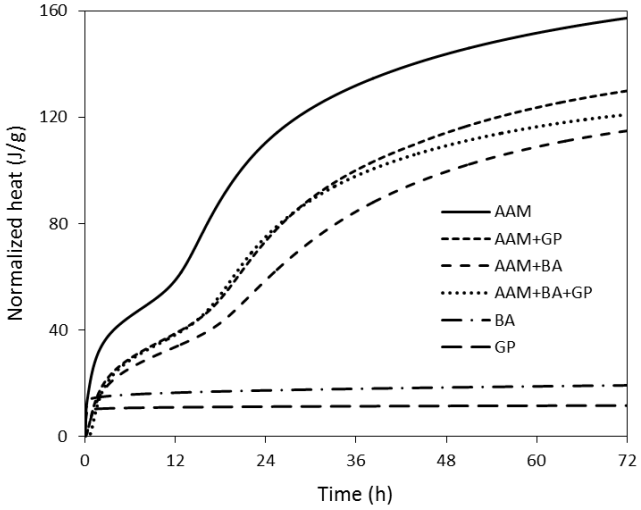

Figure 6-7: Cumulative heat release of AAMs, waste bottom ash and granite powder

It can be seen that the alkali activated slag exhibits obvious reaction peaks at around 14 hours, also with significantly higher heat flow than bottom ash and granite powder, revealing the occurrence of chemical reaction. The difference in reactivity is also shown in the cumulative heat evolution curves in Figure 6-7, where slag mix presents a continuously increased heat release, while different total heat release. Concerning the bottom ash and granite powder, both waste materials show negligible heat release after the initial dissolution, and the total heat release no longer increases afterwards. It indicates that these two materials may only work as non-reactive phases under alkali activation. This phenomenon is against the results from the literature that the potential reactivity of waste bottom ash was observed in both alkali activated systems (Lancellotti et al, 2013) and Portland cement systems (Tang et al, 2016). Considering the variations of the starting materials, an evaluation of the reactivity before application is suggested to be highly necessary. It is also believed that the origin of the starting waste

materials and the incineration process play a key role on determining the reactivity of the MWSI bottom ash.

The effect of the two solid wastes on the reaction of slag can be presented by investigating the mixture of them with slag. “AAM+GP” and “AAM+BA” refer to the mixture of granite powder and bottom ash addition by 20% of the slag, respectively. As shown in Figure 6-6, the main reaction peak for alkali activated slag is delayed from around 14.4 h to 18.4 h with a reduced intensity when granite powder is added. The reduced intensity can be explained by the decreased total amount of slag in the system, while the prolonged induction time together with delayed main reaction peak suggest that the granite powder replacement slightly delays the formation of reaction products.

Compared to the mix of “AAM+GP”, a more significant reduction in peak intensity and delayed presence of main reaction peak is found in mix “AAM+BA”, where the bottom ash has the same replacement level as granite powder, which indicates that the waste bottom ash exhibits a higher impact on the reaction process than granite powder. The inhibited reaction can be partly explained by the porous structure of bottom ash, which may absorb certain amounts of activator solution during the mixing, and therefore less activator is provided to activate slag. It is easy to understand that the mixture with both bottom ash and granite powder addition (AAM+BA+GP) presents a moderate inhibiting effect, since the total solids waste content are fixed at 20% (10% BA+10% GP). The cumulative heat release presents the similar tendency as the heat flow results, while the addition of solid wastes reduces the total heat release, and waste bottom ash presents a more significant influence on the reaction process than granite powder.

6.1.5 Gel structure

Figure 6-8 shows the infrared spectra of the unreacted slag, granite powder and waste bottom ash. The slag presents a broad main vibration band at around 900 cm^{-1}, which is associated with the vibration of Si-O bond, also a small absorption band at around 690 cm^{-1}, due to the asymmetric stretching vibration of T-O groups. Concerning the two solid wastes, both material exhibits a significant band at around 1450 cm^{-1} that assigned to the O-C-O bonds, indicating a certain amount of carbonates within the raw materials. A sharp absorption peak at around 880 cm^{-1} and a small shoulder at about 1180 cm^{-1} are also shown in both solids, corresponding to the Mg incorporated Si-O bond (Bobrowski et al, 2012) and bridge Si-O bonds in crystalline phases.

The waste bottom ash exhibits a terminal Si-O bond at 980 cm^{-1} and a bridge one at around 1120 cm^{-1}; while the granite powder shows an obvious bridge Si-O bond at 1000 cm^{-1} and 1090 cm^{-1}, which refer to the crystalline phases within the granite. Several vibration bonds that are observed between 600 and 800 cm^{-1} indicate the presence of asymmetric stretching Si-O-T bonds with slight structural differences (see the XRD spectrum in Figure 6-3). Upon activation, all mixtures show the presence of bound water at 1640 cm^{-1}, and the O-C-O from carbonates at

1450 cm^{-1}. It should be noticed that mixtures containing waste bottom ash present a more significant peak absorption at 1640 and 1450 cm^{-1}, suggesting a greater contribution in bound water (due to the porous structure and the resulting absorbed physically bound water) and carbonates (see the XRF analysis in Table 6-1). The main absorption band for the reaction product is at around 940 cm^{-1}, assigning to the asymmetric stretching vibration of Si-O terminal bond, which is a typical band that indicates the formation of C-A-S-H type gels with chain structures. The incorporation of both bottom ash and granite powder shows insignificant effect on the structure characters of the reaction products, the addition of granite powder increases the intensity of main absorption band, because of the obvious band in the raw material that at the same location.

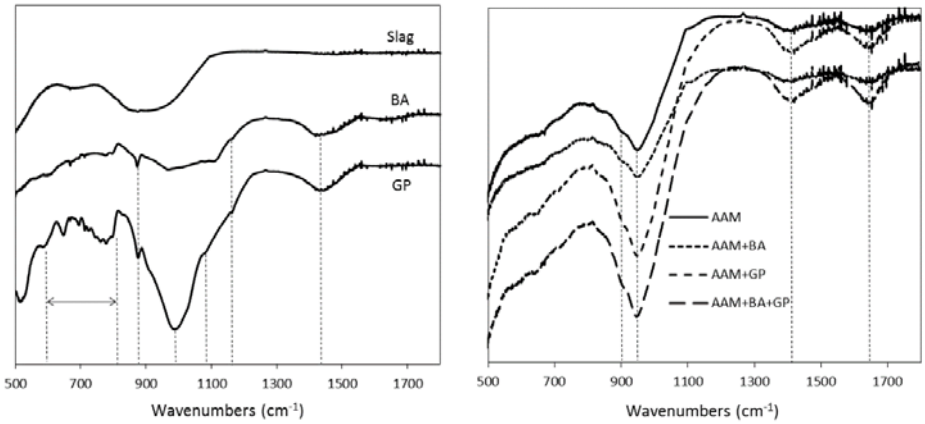

Figure 6-8: FTIR spectra of AAMs with bottom ash and Granite powder

In order to further characterize the effect of waste solids on gel structure, a TG/DSC analysis was carried out and the results are shown in Figure 6-9. All samples present an evident mass loss around 110 °C, attributed to the loss of physically bound water; except for granite powder, which exhibits one obvious mass loss of around 5% between 600 °C and 800 °C, due to the decomposition of carbonates. While the MSWI bottom ash presents a continuous mass loss of about 15%, up to 1000 °C, it is difficult to identify those phases in detail because of the complex origin of the starting wastes.

As for the alkali activated materials (AAM), the continuous mass loss after around 200 °C is assigned to the gradual decomposition of the reaction products, while the mass loss between 600 °C and 800 °C indicates a certain degree of carbonation during the reaction or curing process. When granite powder and bottom ash were both added, mixtures exhibit similar tendency of mass loss and typical mass loss regions, suggesting similar gel composition characteristics. The incorporation of these two solid wastes increases the overall mass loss up to 1.2%, attributed to the original mass loss of the two solids. Together with the calorimeter

and FTIR results in this study, it can be concluded that although the addition of the waste solids reduces the strength and delays the early age reaction, they present a negligible chemical influence on the binder structure. The DSC (differential scanning calorimeter) results are also presented in Figure 6-9, the sharp heat absorption peak at 110 °C is associated with the evaporation of physically bound water. The exothermic peaks at 720 °C and 850 °C are attributed to the decomposition of carbonates and the formation of new crystalline phases in high temperatures, respectively.

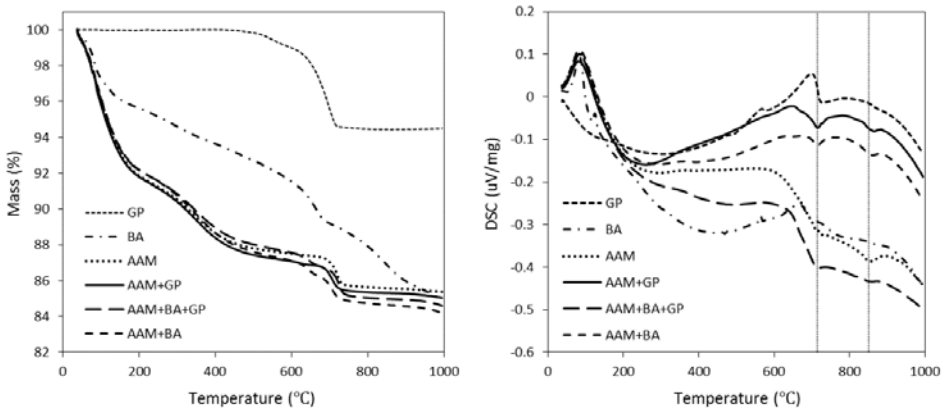

Figure 6-9: Thermal analysis of AAMs with bottom ash and Granite powder

6.1.6 Leaching behavior

The leaching test following (NEN 7383, 2003) was performed using a column leaching test with a liquid/solid ratio of 10 l/kg. Samples were crushed with particle sizes lower than 4 mm and placed in the testing column. Water was forced to flow through the particles for a 24 h. The concentration of chemical elements, the amounts of chloride and sulphate ions were analyzed using the ICP-AES according to (NEN 6966, 2005) and HPLC following (NEN 10304-2, 1996), respectively. The results were compared to the limited leaching values based on the Dutch legislation (Soil Quality Decree, 2008).

Seven mixes with different waste bottom ash and granite powder contents were prepared for the leaching tests. The reference sample was alkali activated slag with CEN standard sand as the fine aggregate. All mixes were having a water/binder ratio of 0.5. The bottom ash replacements of 25%, 50% and a granite powder content of 10% were used. Samples with the label of “p” mean that a pre-treatment was carried out, namely mixing the activator with bottom ash in advance for 5 mins. The purpose of this pre-treatment was to investigate whether the initial contact between bottom ash and concentrated alkali solution has an influence on the leaching behaviors. The other specimens were mixed by the following order: slag, granite powder, sand, bottom ash and then the activator. The leaching results are listed in Table 6-3

together with the Dutch legislation in non-shaped materials ("Niet-VormGegeven" (NVG)), which regulates the leaching behaviors of granulate materials used for civil technical purposes.

Table 6-3: Leaching results of AAMs with bottom ash and granite powder (mg/kg dm, NVG:Dutch legislation for leaching of non-shaped materials, "Niet-VormGegeven")

Items	NVG	BA Input	S	S 25BA	S 25BA,p	S 50BA	S 50BA,p	S 25BA 10G	S 50BA 10G
Sb	0.32	1.07	<0.039	0.13	0.095	0.18	0.2	0.13	0.14
As	0.9	<0.05	<0.1	<0.1	<0.1	<0.1	<0.1	<0.1	<0.1
Ba	22	NA	0.11	0.21	0.2	0.31	0.32	0.2	0.18
Cd	0.04	<0.01	<0.01	<0.01	<0.01	<0.01	<0.01	<0.01	<0.01
Cr	0.63	0.13	<0.1	<0.1	<0.1	<0.1	<0.1	<0.1	<0.1
Co	0.54	<0.01	<0.1	<0.1	<0.1	<0.1	<0.1	<0.1	<0.1
Cu	0.9	4.07	<0.1	0.78	0.59	**1.7**	**1.8**	0.58	0.69
Hg	0.02	NA	<0.001	<0.001	<0.001	<0.001	<0.001	<0.001	<0.001
Pb	2.3	<0.05	<0.1	<0.1	<0.1	<0.1	<0.1	<0.1	<0.1
Mo	1	1.36	<0.1	0.37	0.42	0.64	0.57	0.27	0.36
Ni	0.44	<0.05	<0.1	<0.1	<0.1	<0.1	<0.1	<0.1	<0.1
Sn	0.4	<0.05	<0.1	<0.1	<0.1	<0.1	<0.1	<0.1	<0.1
V	1,8(1)	<0.01	1.7	1.3	1.1	0.83	0.82	0.98	1.4
Zn	4.5	0.94	<0.2	<0.2	<0.2	<0.2	<0.2	<0.2	<0.2
F	55(2)	NA	9.7	7.1	6.6	7.1	6.6	5.8	7.8
Br	20(2)	NA	<2	6.9	5.2	8.7	11	5.5	6.8
Cl	616(2)	6980	110	**1100**	**920**	**1700**	**1900**	**930**	**1000**
SO4	2430	9010	1060	**3810**	**3110**	**6050**	**5820**	**2950**	**3620**

It can be seen that the components in the waste bottom ash above the NVG limitations are Sb, Cu, Mo, Cl and SO4, including both heavy metals and anions. The detrimental elements' type and content may vary depending on the source of the waste materials. In this study, the Mo concentration in the input waste bottom ash is slightly higher than the legislation, while the Sb and Cu contents are around 3 to 4 times higher. In terms of the anions, their concentrations are much higher than the limitation, especially for Cl. It should be noticed that this incinerated bottom ash also contains large amount of Al (12.0 wt.% of Al2O3 from the XRF analysis), although this element is not in the limitation list, it may cause potential expansion and therefore should be carefully considered in the mix design stage. The leaching results show that when waste bottom ash is applied as partial replacement of the fine aggregate, all mixtures pass the Dutch limitation in the leaching of heavy metals for construction materials, except the leaching of Cu in samples with a bottom ash content of 50%. For instance, the leached ion Sb in mixes with 50% bottom ash is around 0.19 mg/kg, which is 40% lower than the required value; similar phenomenon is observed for Mo, but with lower reduction rate. Cu is the main leaching issue of this waste bottom ash, because of the extremely high initial content, large amounts addition (50%) leads to a final high leaching value that exceeds the limitation, except one mix with 50% bottom ash and 10% granite. It can be attributed to the testing variations or the sampling. While there is no leaching problem in samples with 25% bottom ash. It can be seen that in order to reach the leaching regulations, reducing the effective bottom ash content in the final product can be a solution, then the final leaching value is reduced by the dilution effect. In addition, the pretreatment process presents no significant effect on the leaching behaviors, while the initial contact of bottom ash and high alkali solution may play a role in reducing the effect of metallic aluminates. Cl is highly responsible for the corrosion of steel in reinforced concrete and SO4 is associated with volume stability, thus a pretreatment process is needed to remove those two components before application. A simple water treatment is believed to be highly efficient considering the intrinsic characteristics of Cl and SO4 being highly mobile in mediums such as water. Actually the washing process is already known to be economically feasible for both Cl (Boghetich et al, 2005) and SO4 (Abbas et al, 2003). As the nornal treatment processes used to remove the heavy metals and Al can be neglected, a more cost effective application potential is foreseen.

6.1.7 SEM analysis

SEM analyses are used to characterize the reaction products with and without wastes solids additions. The mixtures after 28d of curing are presented in Figure 6-10. Samples with only alkali activated slag (Fig. 6-10A) exhibit a homogeneous paste matrix, which can be an indication of a reaction product of high strength in macro scale. The evenly distributed angular shaped phases refer to the partly reacted anhydrous slag particles that are surrounded by the reaction products. As can be seen in Fig. 6-10B, when 20% slag was replaced by granite powder, the shift in microstructure is not significant, and no evident change of phase

morphology was observed. This is in line with the gel structure investigations in this study that there is no evident chemical effect of granite powder on the gel characteristics. Thus it can be concluded that the granite powder mainly exhibits a physical filling effect and distributes within the reaction products. The matrix can also be characterized as homogeneous in general. The shifted compressive strength due to the granite powder addition can be attributed to the synergetic effect of several factors such as shifted effective slag dosage, particle packing and the influence of granite particles on the network of reaction products.

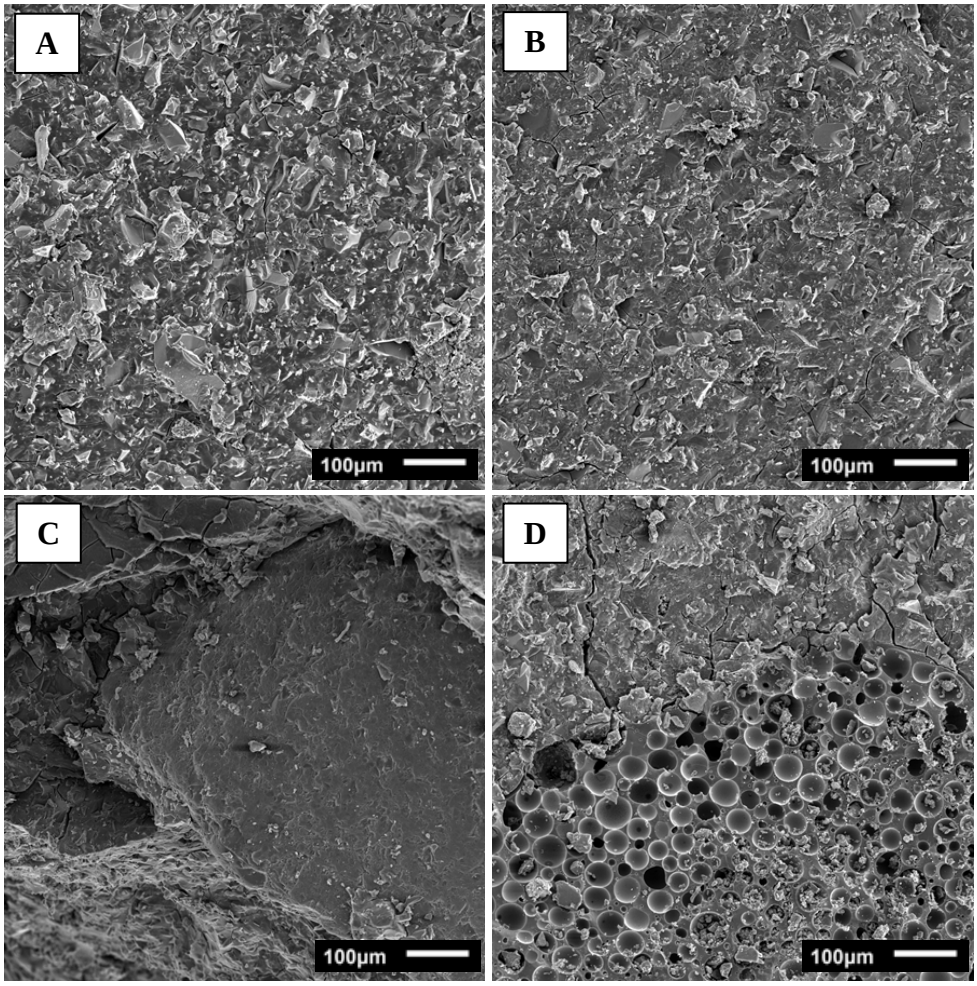

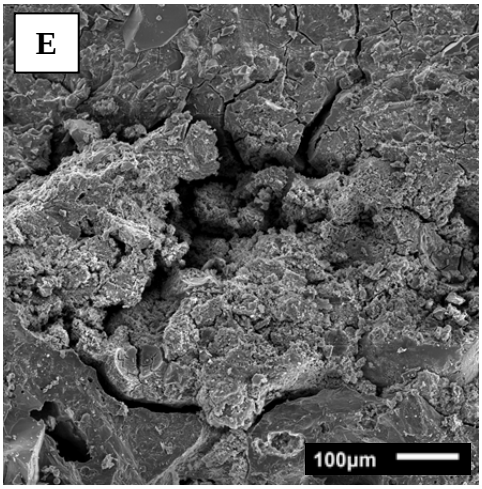

Figure 6-10: SEM images of mixtures with bottom ash and Granite powder

Figure 6-10C shows the micrograph of alkali activated slag with normal sand addition, working as a reference of mortar samples with commonly used aggregates in construction and building materials. The condensed and homogeneous area on the left side refers to a fine aggregate. The aggregate is well covered by the pastes and a well-connected interfacial transition zone (ITZ) can be observed. The slight cracks on the top area can be attributed to the sample preparation process. In a multi-phased composite such as concrete, the ITZ is the key area in terms of mechanical properties. Figures 6-10D and 10E depict two typical conditions of waste bottom ash addition in the alkali activated slag paste. Case D shows a bottom ash with a relatively large particle size and porous structure that works as an aggregate in the matrix, it is clear that compared to the normal sand (Fig. 6-10C), this aggregate is more fragile and less condensed. Then it is easy to understand that a lower compressive strength is shown when bottom ash is added, and the loss of strength can be attributed to the nature of the aggregate. The porous structure can also physically absorb a certain amount of activator solution after mixing, and then affect the early age reaction and bound water content to some extent. Another typical situation is the effect of bottom ash with smaller sizes, as shown in Figure 6-10E, the bottom ash itself presents an irregular particle shape together with porous structure, which leads to an unsatisfactory bonding in the interfacial transition zone and a heterogeneous matrix in general. Therefore a reduced compressive strength is resulted.

6.1.8 Conclusions

This section carries out a comprehensive study on reusing MWSI bottom ash and granite powder in alkali activated materials. The waste solids are thoroughly characterized. Besides the

key issues in evaluating the waste materials such as mechanical property and leaching behavior, the effect of two solid wastes on early age reaction, gel chemistry and micro structure are identified. The following conclusions can be drawn based on the results:

- The pre-treatment of the sticky granite powder in water with superplasticizer results in a well dispersed applicable slurry, suggesting a relatively new and cost-effective approach of applying this waste powder.
- Both bottom ash and granite powder slightly delays the early age reaction. But considering no evident effect on gel structure was observed, they can be considered as non-reactive components. Clarifying their effects on reaction kinetics and micro scale properties provide strong basis for further researches and applications.
- Bottom ash negatively influences the strength by its porous structure while granite powder features a filler effect. Compressive strengths of 20 to 70 MPa can be achieved by using those two solids with waste granite powder content up to 20% and waste bottom ash content up to 50%, suggesting wide application potentials and high reusing rate of waste materials.
- The leaching of the heavy metals meets the Dutch legislation, confirming again the advantage of using alkali activated binder; while economically feasible methods of treating the chloride and sulfate are suggested since these two chemicals are directly linked to the durability of the final products.
- The reuse of these two solid wastes in alkali activated materials contributes to the sustainable development, reduces the costs of handling the heavy metals and metallic aluminate, indicating the advantages of applying this composites.

6.2 Reuse of waste glass powder

6.2.1 Introduction

The utilization of alternative additives or waste materials in alkali activated systems as either reactive phases or fillers further exhibits an advantage in achieving a sustainable product with reduced environmental impacts. Waste glass is one of the solid wastes that may end with landfill. Although it can be reused in glass production, the collected waste glass mixture with different color makes its reuse inefficient; moreover, differences in type and compositions among the waste glass bring difficulty in quality control. Eventually up to around 30% of waste glass is not recyclable in Europe (Torres and Puertas, 2017). Previous studies have shown the possibility of using coarse waste glass fractions as aggregates in Portland cement based systems (Shi et al, 2007), which reduces the costs of waste glass handling and the consumption of natural resources (aggregates). Owning to the cooling process of glass production, disordered structures that are enriched of silica also show a possibility of acting as a reactive phase in cementitious materials. Suitable amounts of waste glass addition have been reported to show limited effect on the alkalis in cement chemistry (Chen et al, 2002; Xie et al, 2002); also

the pozzolanic reactivity of waste glass in Portland cement system has been verified (Khmiri et al, 2013).

Few studies investigated the suitability of using waste glass in alkali activated materials. The main elements in the waste glass are silica, sodium and calcium, which are also the input components for alkali activation; therefore the utilization of waste glass in alkali activated systems as alternative reactive phase can results in a more sustainable product with further lower environmental impacts. Waste glass is reported to be suitable of been used as both alternative silica sources in preparing activators to replace commercial waterglass (Puertas and Torres, 2014; Torres and Puertas, 2015) and supplementary binder material to replace solid precursors (Garcia et al, 2016).

The application potential of waste glass powder in two commonly used binder systems has already been proved, while limited attention was paid to compare the modification mechanism of glass powder to other supplementary additives, in different binder systems. The objective of this study is to investigate the reaction mechanism and characterize the microstructure of waste glass powder incorporated alkali activated materials using Portland cement (CEM I 42.5) based binder as a reference. Another silica enriched supplementary binder, silica fume, was used as a reference to evaluate the effects of glass powder. The effect of waste glass powder and silica fume addition on flowability, mechanical property, reaction kinetics and gel composition are evaluated and compared.

6.2.2 Flowability

A fixed water binder ratio of 0.45 is used for all mixes. For alkali activated slag, an equivalent sodium oxide (Na_2O) content of 5% by mass of the binder and an activator modulus of 1.4 are used. The ordinary Portland cement based samples are prepared by mixing solid powder materials with distilled water. Waste glass powder (from crushed bottles, ground to have similar PSD as Portland cement) replacement up to 20% (by mass of the initial binder) was used in both alkali activated and Portland cement systems, silica fume with the same replacement levels are also used in two binding systems as references because the main reactive phase is silica. The binder/aggregate ratio was fixed at 1/3 for all mortar mixes. The detailed mix proportions are listed in Table 6-4.

The slump flows of the fresh mortars containing different levels of waste glass powder and silica fume, in both alkali activated system and Portland cement system, are depicted in Figure 6-11. The data briefly illustrates the effect of powder addition and binder type on workability. It can be observed that for a constant powder replacement, the mixtures based on alkali activated materials exhibit higher slump flows than that in Portland cement. The slump flow of alkali activated slag without alternative powder addition is 27.2 cm, which is higher than 23.5 cm in pure Portland cement. It is generally believed that the water demand and the resulting flowability are directly related to particle size and surface area; however, differences may show when different binder systems are applied. It is suggested that the sodium silicate based

activator changes rheological characteristics of the fresh mixes. It should be noticed that in order to make comparison on the intrinsic property (flowability) of different binders, the effect of superplasticizers is not considered in this study. When glass powder was applied, the slump flow slightly increases with the increasing replacement level in alkali activated slag. The glass powder addition of 20% increases the slump flow from 27.2 to 29.1 cm (by around 7%). Similar tendency is also observed in Portland cement systems, glass powder replacement up to 20% results in an increased slump flow from 23.5 to 26.1 cm.

Table 6-4: Mix proportions of alkali activated slag and OPC (g)

Sample	Binders		Liquids			Glass powder	Silica fume	Fine aggr-
	Slag	OPC	Water glass	NaOH	H_2O			
OPC	0	100	0	0	45	0	0	300
OPC-nGP	0	90/80	0	0	45	10/20	0	
OPC-nSF	0	90/80	0	0	45	0	10/20	
AAM	100	0	24.4	3.8	29.4	0	0	
AAM-nGP	90/80	0	24.4	3.8	29.4	10/20	0	
AAM-nSF	90/80	0	24.4	3.8	29.4	0	10/20	

* "n" refers to the glass powder/silica fume replacement wt.%, n=10 or 20.

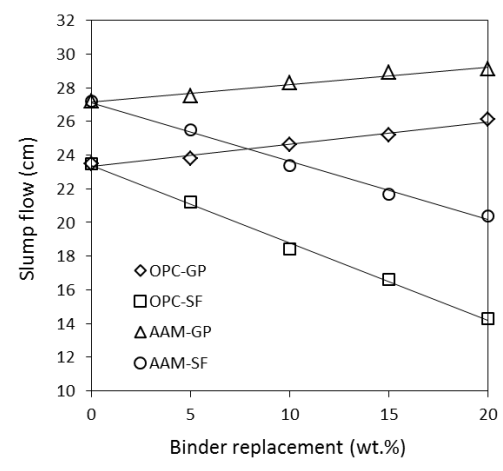

Figure 6-11: Flowability of fresh mortars with waste glass or silica fume addition

Contrary to the effect of glass powder, the addition of silica fume leads to a significant reduction of flowability in both Portland cement and alkali activated systems. For instance the slump flow is reduced from 27.2 to 20.4 cm (by 25%) when 20% slag is replaced by silica fume, and a reduction from 23.5 to 14.3 cm in cement based mixtures. For a fixed binder system, the shifts in flowability can be attributed to the particle shape and surface area of the applied solids, thus compared to the commonly used silica enriched additive: silica fume, glass powder exhibits an advantage in terms of the workability, and show different powder morphology, the beneficial effect of waste glass on flowability was also reported in previous studies (Topcu and Canbaz, 2004; Wang et al, 2010).

6.2.3 Reaction kinetics

The normalized heat flow and release of alkali activated slag with glass powder and silica fume addition within the first 72 h are illustrated in Figure 6-12, the heat flow is normalized by mass of the slag. For mixtures without additives, the main heat release peak is located at around 14.6 h and a peak intensity of 1.60 mW/g, the induction period is between around 5 to 10 h. As the glass powder replacement increases to 10% and 20%, the location of main reaction peak presents a delay to 15.9 and 17.3 h with slightly increased peak intensity, and the induction period shows a delay up to around 1.2 h. The slightly delayed location of the main reaction peak suggests that the amorphous phases within the glass powder exhibit lower reactivity than slag under alkali attack.

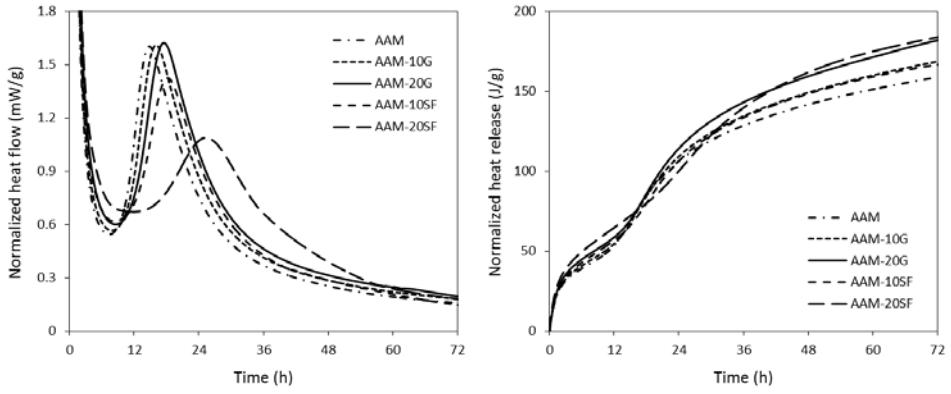

(a) (b)

Figure 6-12: Normalized heat flow and heat release of alkali activated systems

In terms of the silica fume, the same replacement level results in a more significant delay of the main reaction peak and an evident reduction of the peak intensity compared to the glass powder. As can be seen that the peak intensity of mixtures with 10% and 20% silica fume are 11.3% and 32.3% less than the relating ones with the same amount of glass powder; the peak

location is also show a delay of 2.3 and 8.0 h, respectively. It indirectly verifies that the glass powder presents a much higher reactivity than silica fume in alkali activated systems. As for the total heat release, alkali activated slag without additives presents the lowest heat of 158 J/g until the testing age of 72 h. The cumulative heat release per gram of slag increases as the increase of powder replacement in the system, indicating that both glass powder and silica fume shows a potential reactivity in under alkali conditions. Besides, although the addition of glass powder and silica fume show significant difference in heat flow, the overall heat release remain similar for a constant dosage, indicating their differences in reaction mechanisms and reactivity, but similar promoting effect on the overall reaction process.

Figure 6-13 illustrates the effect of two additives on early age hydration in Portland cement systems. The hydration process of Portland cement presents similar typical four stages as alkali activated materials, while with differences mainly regarding the induction and acceleration stage. This is attributed to the different hydration characteristics of the multiple phases such as C_3A, C_3S, C_2S and C_4AF within the clinkers. It can be seen that other than alkali activated slag, the addition of additives show very limited influence on the induction stage; due to the fact that this process is mainly controlled by the ettringite formation, while several factors such as the alkali concentration, the reactivity of starting materials show an effect on this stage in alkali activated system.

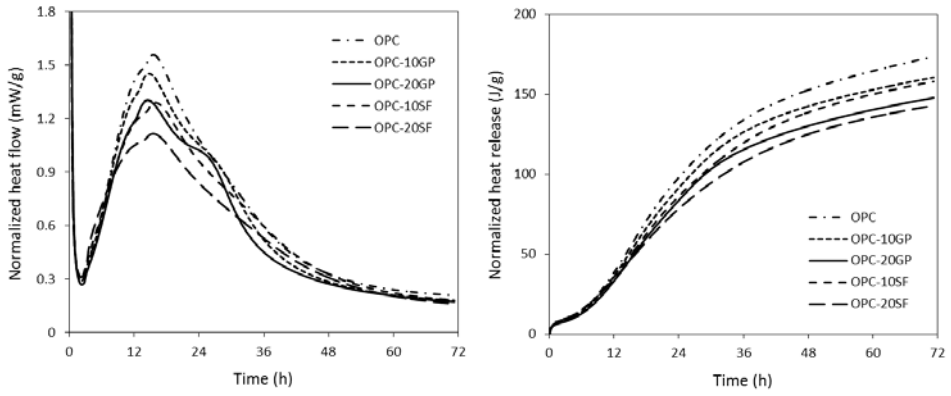

(a) (b)

Figure 6-13: Normalized heat flow and heat release of Portland cement systems

For mixtures without additives, the main reaction peak is located at around 14.7 h with a peak intensity of 1.54 mW/g, both values are similar to alkali activated pure slag. Different from the role of glass powder in alkali activated system, the addition of glass powder leads to the shift of main reaction peak earlier times with reduced peak intensity, indicating an acceleration effect. It also results in a more significant heat release at around 25 h, which is related to the formation of AFm phases. For the same replacement level, the addition of silica fume slightly retards the main reaction peak up to around 1 h with a more significant reduction of peak

intensity, and exhibits limited effect on the AFm related reactions. The cumulative heat release results in Figure 6-13(b) shows that contrary to the alkali activated system, the addition of glass powder and silica fume reduces the heat release of the original binder, indicating reduced binder reactivity. This is because that in alkali activated systems, any amorphous silica can be regarded as the precursors; while in Portland cement system, the main reaction process is only controlled by the cement clinkers.

6.2.4 FTIR

Figure 6-14 depicts the infrared spectra of mixtures upon activation after 28 d. Portland cement based samples show a main absorption band at around 950 cm^{-1}, which is attributed to the asymmetric stretching vibration of a terminal Si-O bond. The location of this band is higher than the relating ones in the original cement, indicating a slightly higher crosslinking structure of the hydrated C-S-H gels than the clinkers. Two types of tetrahedral T-O bonds are observed at around 875 and 820 cm^{-1}, the former one is from the original Portland cement, as can be seen that a sharp peak at the same location is shown in the starting material; while it is difficult to identify whether the latter one is newly formed since the cement clinker show a board and poorly defined shoulder in the similar location range.

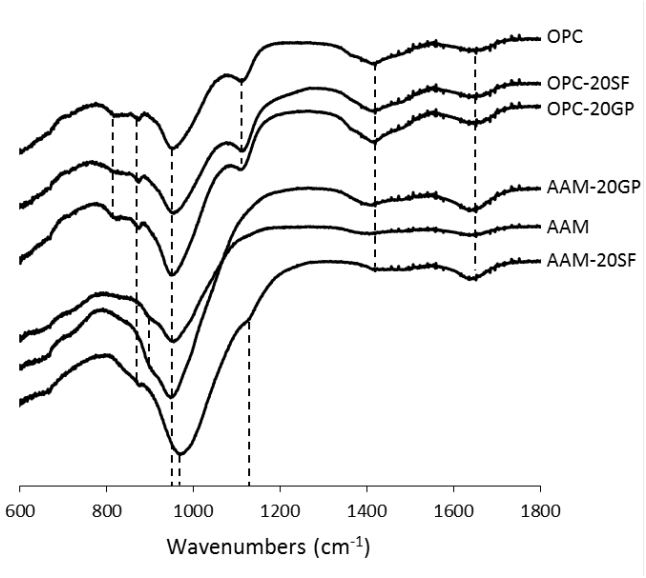

Figure 6-14: FTIR spectra of the reaction products

The broad band at around 1130 cm^{-1} in cement slightly shifted to 1120 cm^{-1} with increased intensity, indicating an increased amount of the bridge T-O-Si bonds during hydration. The absorption band at about 1420 and 1640 cm^{-1} indicates the strong presence of O-C-O bonds and chemical bond water within the hydration products. The location of the typical Si-O-T

bonds in the hydration products remains fixed with the addition of glass powder or silica fume, while the intensity of the main terminal Si-O bonds at around 950 cm^{-1} show an increment. This indicates their addition shows limited effect on the characteristics of the original Si-O structures, but increases the total amount of Si-O bonds in the reaction products.

The infrared spectra of alkali activated slag based mixes present some differences in terms of the Si-O bond composition, due to the differences in the starting precursors and reaction mechanisms. The main absorption band is located at around 950 cm^{-1}, which has the same location as the one in Portland cement. It is also reported that the tobermorite-like chain structured C-S-H type gels from alkali activated slag share a similar structure with the ones in Portland cement, and show differences in Ca/Si ratio and Al content. A small shoulder at around 890 cm^{-1} is shown in alkali activated slag and slag-glass powder blends, which is a terminal Si-O bond with less crosslink or more Al replacement than the main Si-O bond. The terminal Si-O bond at 820 cm^{-1}, 875 cm^{-1} and the bridge Si-O bond at 1130 cm^{-1} in Portland cement based samples are no longer significant in those alkali activated slag and slag-glass powder blends. Different from the effect of glass powder, the addition of silica fume show an absorption band at 875 cm^{-1} instead of 890 cm^{-1}. The presence of a bridge Si-O bond at 1130 cm^{-1} and the shift of main absorption band from around 950 to 970 cm^{-1} indicate a more polymerized structure is resulted.

6.2.5 XRD

The X-ray diffraction patterns (with Co radiation) of the starting materials are shown in Figure 6-15. The Portland cement show large amount of C_3S/C_2S, together with C_3A, C_4AF, gypsum, and limited amount of quartz. The original slag and glass powder are mainly amorphous without the presence of significant crystalline phases. The slag shows a peak hump between 30 and 40°, while a wider hump range can be observed in the waste glass from around 20 to 40°. Regarding the silica fume, a broad hump with relatively high intensity is shown between about 20 and 30°, as well as limited amount of crystalline phases such as quartz and hematite. The XRD patterns of the reaction products after 28 d are depicted in Figure 6-16. As can be seen that the hydration/reaction products in Portland cement and alkali activated systems present distinguish the characteristics, and the addition of glass powder and silica fume plays different role in different binder systems. Two evident crystalline peaks can be observed in Portland cement based mixtures: ettringite and portlandite, which are typical hydration products due to the presence of sulfates and considerable amount of calcium. Small amount of unreacted clinkers can be observed; especially the non-Al involved ones such as C_3S and C_2S. The main hydration product, C-S-H type gels, presents a sharp peak at around 34°. The addition of glass powder results in a reduced peak intensity of portlandite, indicating a reduced amount of it within the hydration products due to the well-known secondary hydration process.

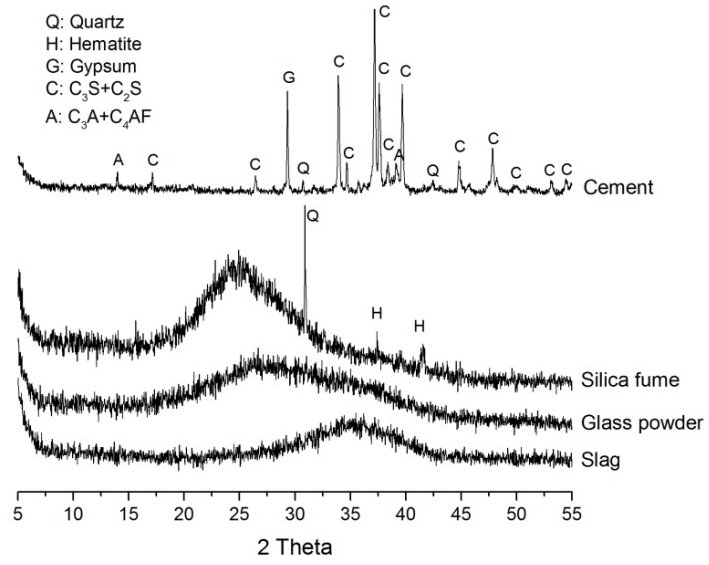

Figure 6-15: XRD patterns of the starting materials

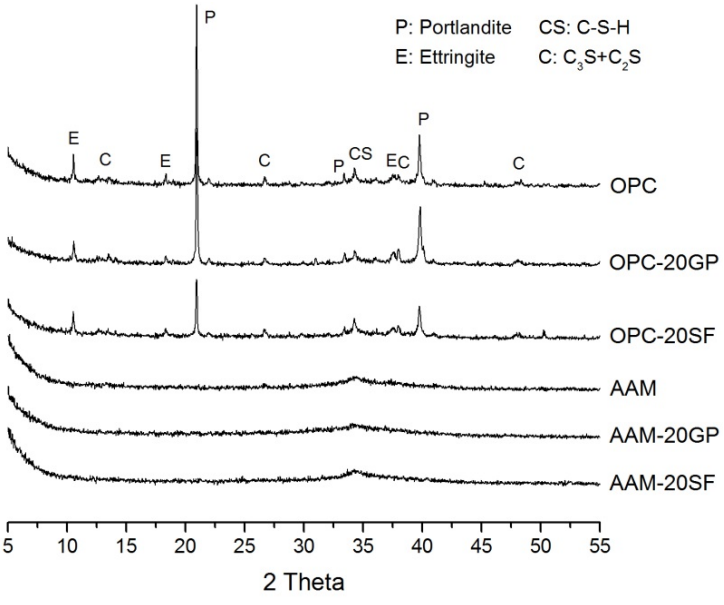

Figure 6-16: XRD patterns of the reaction products

The same replacement of silica fume instead of glass powder leads to a more significant reduction of Portlandite peak intensity, which reveals that the glass powder presents a lower pozzolanic reactivity than silica fume. As for the alkali activated materials, the main reaction product is a poorly crystalline C-S-H type gel. Compare to the C-S-H gels from Portland cement system, it has the same peak location while with much lower peak intensity, this gel is also known to have a higher Al content and a lower Ca/Si ratios. The addition of glass powder and silica fume, shows limited influence on the composition of the crystalline phases, and only slightly changes the crystallinity of the C-S-H type gels. Thus it can be concluded that the glass powder and silica fume, show different modification efficiencies in Portland cement system as supplementary binders that contribute to the secondary reaction; while exhibit similar reaction mechanism in alkali activated system, as starting precursors that change the overall Si content in the system, their modification efficiency in alkali activated systems will be further discussed in thermal analysis.

6.2.6 TG/DTG

The TG/DTG results of mixes with different starting compositions and binder systems are shown in Figure 6-17. In order to perform a clear view focusing on the mass loss of the reacted gels, the mass loss at 100 °C is calculated as the starting mass of 100%. Figure 6-17(a) depicts the mass losses of Portland cement based mixtures between 100 and 1000 °C. All mixtures exhibit similar characteristics of mass loss within the tested temperature range, including a continuous mass reduction before around 400 °C, a significant mass loss between around 400 and 480 °C, and a less evident one between 600 and 700 °C; then the mass loss remain stable and limited until 1000 °C.

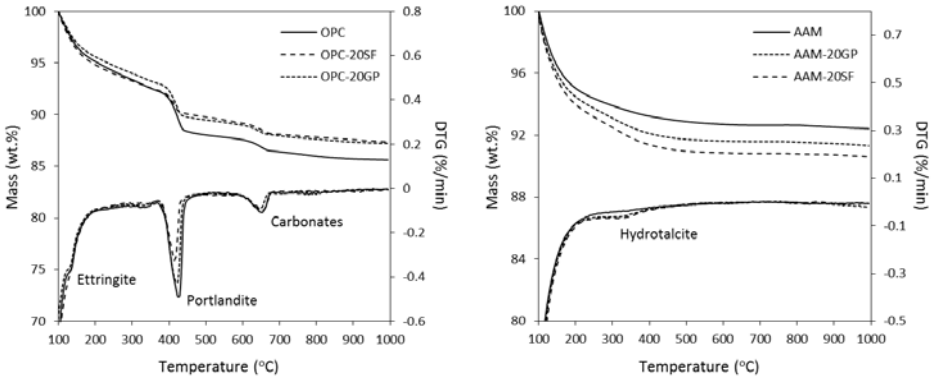

(a) (b)

Figure 6-17: Thermal analyses of the reaction products (a: OPCs, b: AAMs)

In relation with the abrupt mass losses in the TG results, the corresponding DTG curves indicate the presence of three typical phases within the hydration products: Ettringite, Portlandite and Carbonates, which are also observed in the FTIR and XRD analyses in this study and previous studies. It should be noticed that the gradual decomposition of the C-S-H gels and resulting loss of bound water also take place within this temperature range. The DTG curves reveal that the addition of glass powder shows limited effect on the content of Ettringite and Carbonates, while reduces the Portlandite content to some extent. The addition of silica fume shows a further reduction of Portlandite, which is in consistent with the XRD results. The mass loss between 370 and 450 °C, that mainly assigning to the loss of Portlandite according to the DTG curves, is around 4.1% for mixes with plain Portland cement. When replacing the OPC by glass powder with a dosage of 20%, this value reduces to about 3.4%, and the same replacement level of silica fume results in a higher reduction of around 2.4%, indicating a higher efficiency in terms of the secondary hydration. It should be noted that silica fume is commonly accepted as a commercial high efficient SCM, while the glass powder is an industrial solid waste. Therefore, when evaluating and comparing their effects on micro or macro level, their environmental impacts and costs should be considered together with the modification efficiency. Additionally, when excluding the mass loss of Portlandite, mixtures with glass powder or silica fume present a higher content of chemical bound water, confirming again the benefits of secondary hydration.

Concerning the alkali activated systems, as can be seen in Figure 6-17(b) that all mixes present a relatively evident mass loss till around 300 °C, and then become stable until 1000 °C without significant abrupt mass losses. This is in line with the XRD results that the reaction products are mainly amorphous gels without well-defined crystalline phases. Similar to the case of Portland cement system, the addition of glass powder increases the total mass loss (between 100 and 1000 °C) from around 7.6% to 8.7%, mainly attributing to the increased bound water, while the addition of silica fume exhibits a higher total mass loss of 9.4%. The DTG curves show a slight shoulder at around 330 °C, which can be assigned to the mass loss of Hydrotalcite. The presence of this phase is commonly reported in alkali activated materials, the minor amount together with the poorly crystalline nature make it almost undetectable from the XRD analysis in this study. To summarize, the TG/DTG analysis provides an additional approach in evaluating the effect of glass powder in two different binder systems, modifications in bound water and phase changes are identified. Quantitative comparison with silica fume gives a clear view on the modification efficiency of glass powder, which can also be linked to the results of other testing methods.

6.2.7 Compressive strength

The 7 and 28 d compressive strengths of all mixtures are presented in Figure 6-18. In Portland cement based mixes, the reference sample reaches a 7 d strength of 35.3 MPa and 28 d strength of around 46.2 MPa. The addition of glass powder up to 20% shows slight strength increment

at both 7 and 28d, as can be seen that the strength is increased by 1.3 MPa after 7 d of curing and 2.6 MPa at 28 d.

While in terms of silica fume, its incorporation up to 20% results in a more significant increase of strength compared to glass powder, especially at the dosage of 20%. For instance compared to the reference, the 7 and 28 d strength is increased by 4.4 MPa and 8.3 MPa respectively, when 20% silica fume is added, and the highest 28 d strength reaches 54.5 MPa. Compare to the effect of glass powder and silica fume, it reveals that the reuse of glass powder shows no negative effect on mechanical property, replacing Portland cement with 20% glass powder would result in a similar level of strength. Although the commercial silica fume shows better modification efficiency in terms of strength, its high purity of amorphous silica and high price should also be taken into consideration; while the glass powder is only an industrial waste with less silica content (see Table 6-5, measured by XRF) and lower intensity of amorphous phases (see the XRD pattern in Figure 6-15).

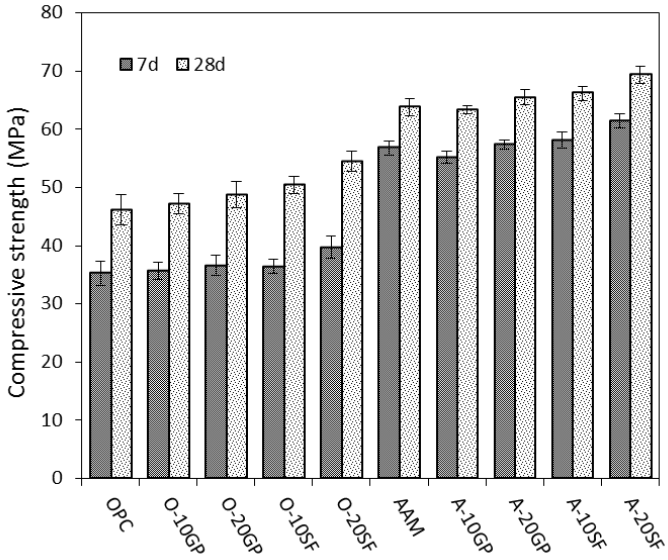

Figure 6-18: Compressive strength of the reaction products

As for the alkali activated materials, a higher compressive strength in general is clearly shown, partly because of the nature of the reacted gels and the nature of no calcium hydroxide within the reaction products. The reference sample presents 7 d strength of 56.8 MPa and 28 d strength of 63.8 MPa, which is much higher than the corresponding Portland cement based mixes. The effect of glass powder and silica fume on strength shows a similar tendency as the case in Portland cement binders. For a constant replacement level, the addition of silica fume leads to a higher increase of strength than glass powder at both 7 and 28 d. The silica

fume/glass powder dosage up to 20% show beneficial effect on strength, and the highest strength reaches around 61.4 MPa after 7 d of curing and 69.4 MPa at 28 d.

Table 6-5: Major chemical composition of glass powder and silica fume

Oxides (wt.%)	SiO_2	Al_2O_3	CaO	MgO	Fe_2O_3	Na_2O
Waste glass	69.51	0.91	10.52	1.28	0.30	16.38
Silica fume	93.06	-	0.89	0.69	2.06	0.63

6.2.8 Conclusions

This section discusses the suitability of reusing waste glass powder as substitutes to replace binding material in alkali activated systems. Silica fume is applied as a reference to evaluate the effect of glass powder, also Portland cement based mixes are used as references to investigate the role of glass powder in different binding systems. The effect of glass powder/silica fume addition on flowability, early age reaction, microstructure and mechanical property are identified. The following conclusions can be drawn based on the results:

- The addition of waste glass powder slightly increases the slump flow, while the silica fume significantly reduces the workability, in both alkali activated and Portland cement systems. For the same replacement level, alkali activated binder based mixes exhibit higher slump flow than Portland cement based ones.
- Waste glass powder shows different reaction mechanisms in alkali activated system and Portland cement system. In alkali activated system it works as a silica enriched precursor and slightly delays the reaction process, while in Portland cement system it slightly accelerates the reaction and affects the process of AFm formation.
- The gel structure identification reveals that the waste glass powder addition reduces the content of Portlandite in Portland cement system, indicating the presence of a secondary reaction, while the raction efficiency is lower than the commericial silica fume. As for the alkali activated system, glass powder addition increases the bonud water content, but shows limited effect on gel characteristics in general.
- The waste glass addition up to 20% does not show negative effect in terms of compressive strength, and slightly inceases the strength at both 7 and 28 d with a dosage of 20%, in both alkali activated system and Portland cement system. Besides, alkali activated materials show obviously higher strength than Portland cement based ones in general with the same water to binder ratio.

Chapter 7

^{29}Si, ^{27}Al NMR investigations and modeling

7.1 Introduction

Various types of analysing methods are applied in order to understand the chemistry, reaction process and products of this new binder system by using isothermal calorimetry, Thermo-gravimetric (TG), Fourier Transform Infrared Spectroscopy (FTIR), X-ray Diffraction (XRD), Inductively Coupled Plasma Optical Emission Spectrometry (ICP-OES) and Scanning Electron Microscopy with energy dispersive spectrometer. Together with those testing methods or works alone, Magic Angle Spinning (MAS) Nuclear Magnetic Resonance (NMR) spectroscopy presents new insights in phase evolution of the reaction products. For instance, in the alkali activated high calcium systems, the Al substitution in C-S-H gels as bridging tetrahedral and AFm, hydrotalcite-like phases from octahedral Al (not always XRD identifiable) were observed by using ^{27}Al NMR (Bonk et al, 2003). ^{29}Si MAS NMR resonances show the presence of Q^0 monomers, Q^1 dimers and Q^2 bridging groups (Palacios et al, 2006; Hakkinen, 1993). As for the alkali activated aluminosilicates, commonly investigated precursors are fly ash and metakaolin. The ^{29}Si MAS NMR spectra reveal that the silicates usually present in Q^4(mAl) structures, and their compositions are depending on the key synthesizing factors such as activator compositions and curing conditions (Fernandez et al, 2006; Peng et al, 2015). Moreover, the deconvolution of the obtained spectra makes quantitative analysis possible, especially on the ^{29}Si NMR, which provides further information about the structure changes, chain lengths, elements' ratios (mainly Ca/Si and Si/Al) of the reaction products. This method has gradually become an accepted approach to provide a qualitative investigation based on the quantified results (L'Hopital et al, 2015; Walkley et al, 2016).

Attentions have also been paid to using NMR to investigate more complex blended alkali systems, containing both high calcium and aluminosilicate phases (N-A-S-H + C-A-S-H). The existence of Q^0 to Q^3 and Q^4 silicon units determined by ^{29}Si NMR verifies the presence of two different types of reaction products in the blended system, while the gel interaction was observed by using ^{29}Si and ^{27}Al MAS NMR together with XRD, SEM/EDX and TEM/EDX. By tracking the structural shifts of Si and Al, it is observed that the mixture of C-S-H and N-A-S-H gels at initial stage is affected by the dissolved Ca and Al groups and gradually their composition are changed into C-A-S-H and N-C-A-S-H gels, respectively (Garcia et al, 2013). ^{29}Si MAS NMR with peak deconvolutions was also used to analyze the reactivity of the starting materials indirectly by quantifying the phase changes in the blended system, for instance the indirect quantitative analysis to study the effect of slag to fly ash ratios and

activator type on reactivity, quantifying the influence of carbonation on alkali activated slag and slag-fly ash blends by ^{29}Si NMR (Bernal et al, 2013), evaluating the phase composition of a chemically synthesized N-A-S-H/C-A-S-H mixture by TG, FTIR together with ^{29}Si NMR (Walkley et al, 2016), characterizing the phase composition, chain length, Si/Al ratios and reaction degree of hydroxide activated slag-metakaolin blends by applying ^{29}Si and ^{27}Al NMR (Buchwald et al, 2007).

Although great achievements have been made based on MAS NMR analysis, there are still remaining issues that deserve further discussions in blended alkali systems. One problem lays in the ^{29}Si NMR spectra of aluminosilicates, especially for the fly ash, both the starting precursor and reaction products show overlapped resonances that usually range from around -70 to -120 ppm, assigning to the Q^4(mAl) units (Oh et al, 2014); those overlapped peaks make it difficult to track their origins, therefore the quantitative analysis can only provide qualitative conclusions on the structural changes and it is impossible to identify the reactivity. However, previous studies proved feasible manner to separate the unreacted fly ash from the reacted aluminosilicates by HCl treatment (Fernandez et al, 2006; Puligilla et al, 2015), thus theoretically it is possible to quantifiy the reaction degree and Si structure shifts by comparing the ^{29}Si NMR results of samples before and after HCl treatment. Another issue is the commonly used silicate based activator; those additional silicates participate into the reaction process and become part of the reacted gels, and the activator dosage and modulus also strongly affect the silicate structure and reaction chemistry, while those findings are rarely linked to the reaction degree of blended alkali systems. Furthermore, alkali activated aluminosilicates are usually investigated in high alkali conditions with elevated temperatures to pursuit ideal mechanical properties, while in the blended systems, relatively low alkalinities and temperatures are more commonly used due to the calcium enriched precursors; how those starting conditions affect the original Si + Al systems need to be further clarified.

The aim of this chapter is to carry out a quantitative investigation on the reaction degree of ambient temperature cured silicate activated slag, fly ash and their blends based on the ^{29}Si and ^{27}Al MAS NMR spectroscopy, with special emphasis on the influence of precursors' interaction and activator modulus. The phase compositions are evaluated by deconvoluting the NMR peaks, and the reaction products are selectively dissolved in order to extract the unreacted phases. The effects of precursors and activators on reaction degree are discussed in detail, and subsequently a reaction model for blended alkali activated slag-fly ash is proposed based on the quantified NMR investigations.

7.2 Characterization of starting materials

The alkali activator used in this study had a constant equivalent sodium oxide (Na_2O) content of 5% by mass of the binder and activator moduli of 0.8, 1.6 and 2.4, respectively. The water/binder ratio was kept constant at 0.35. Three binder compositions were used: pure slag, pure fly ash and slag-fly ash blends (50/50 by mass). All specimens were cured at room

temperature and a relative humidity of 95% for 1 month. The ^{29}Si and ^{27}Al MAS NMR analysis of the starting materials are introduced in Section 5.5.2 and 5.5.3.

The ^{29}Si NMR spectra of the activator solutions are presented in Figure 7-1. The activator with a modulus of 0.8 shows an evident peak around -72 ppm, indicating the presence of Q^0 monomers. Besides, Q^1 and Q^2 groups with relatively low peak intensity can be observed, as well as limited amount Q^3 sites that located at around -98 to -100 ppm. Increasing the activator modulus results in a significant increase of Q groups with higher polymerization degree, as can be seen that shifting the activator modulus to 1.6 and then 2.4, the intensity of peaks for Q^1 dimers becomes more evident, indicating the increasing fraction of those units within the activator solution. Also, peaks for Q^2 and Q^3 units are obviously showing a higher intensity with larger covered area, especially for Q^3 groups that located at around -95 to -100 ppm. It should be noticed that no significant peaks are found lower than -100 ppm in all cases, which suggests that no Q^4 sites are present in the activator. It is already known that the different Q compositions of the activator is a combined results of the pH and silicate dosage, and less polymerized Q groups would present a higher reactivity during alkali activation (Jansson et al, 2015). It should be noticed that the Fe in fly ash will complicate the analysis by broadening the peaks and losing intensity, adding noise to the spectra.

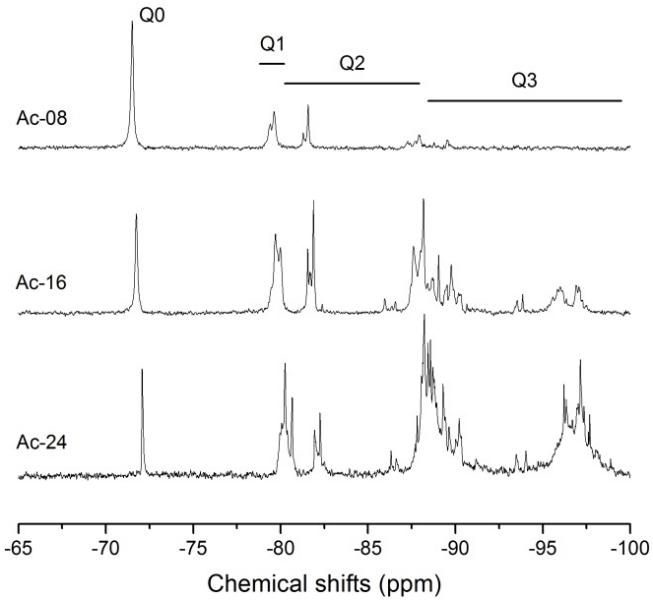

Figure 7-1: The ^{29}Si NMR spectra of the activators

7.3 Alkali activated slag

7.3.1 ^{29}Si MAS NMR

Figure 7-2 (a-c) shows the ^{29}Si MAS NMR spectra of alkali activated slag with activator modulus of 0.8, 1.6 and 2.4, respectively. The obtained spectrum, fitted peak and the deconvoluted results are presented. For mixes with the lowest activator modulus (i.e. Ms of 0.8), eight deconvoluted peaks are presented. The broad one from around -55 to -95 ppm refers to the unreacted slag. Its reactivity can be calculated indirectly by comparing its total content before and after reaction. The peak located at around -75.2 ppm refers to the Q^0 sites, suggesting the presence of isolated silica tetrahedral within the reaction products. Due to the fact that a single Q^1 group cannot perform an ideal peak fitting, two Q^1 peaks representing the non-bridging structure are separated: $Q^{1\text{-}a}$ and $Q^{1\text{-}b}$ that are located at about -76.8 and -79.0 ppm, respectively.

It is commonly agreed that this site mainly refers to the end of chain silicate tetrahedrals within the newly formed C-(A)-S-H type gels. Previous studies also observed two Q^1 sites within the reaction products of alkali activated slag and its blends (Bernal et al, 2014; Myers et al, 2013). Three types of Q^2 groups are observed in the reaction products: Q^2(1Al) sites located at around -81.6 ppm, $Q^{2\text{-}b}$ and $Q^{2\text{-}p}$ sites at approximately -84.2 and -85.7 ppm, respectively. Those Q^2 sites are assigned to the middle-of-chain silicates with either bridging or pairing conditions within the C-(A)-S-H gels (L'Hopital et al, 2015). In addition, there is a small amount of high crossliking Q^3(1Al) sites (around -89 ppm) that is in line with previous studies (Wang et al, 2003; Richardson, 2008).

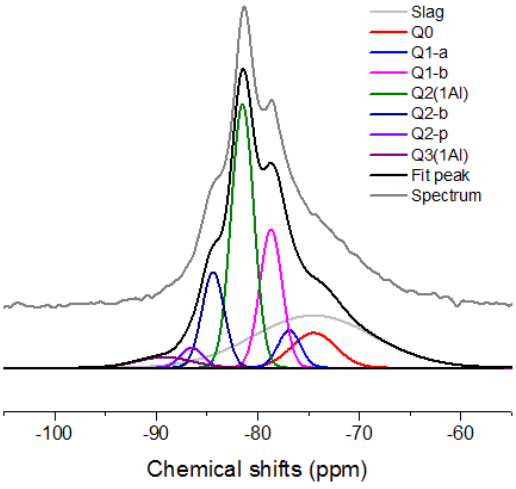

(a) Ms=0.8

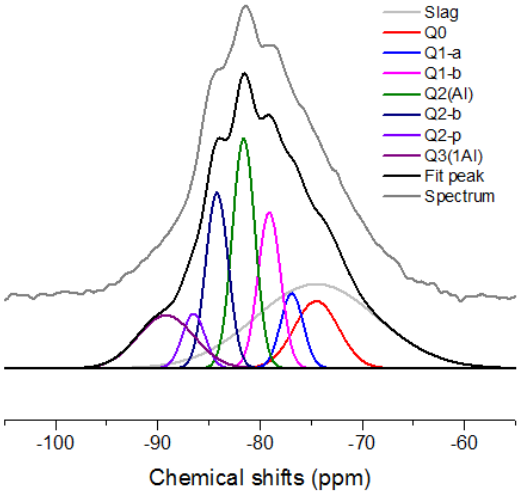

(b) Ms=1.6

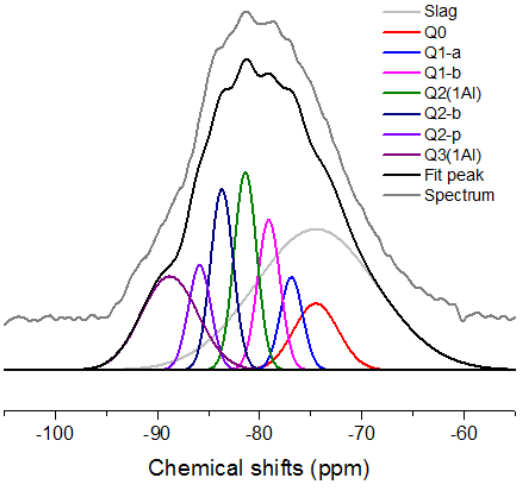

(C) Ms=2.4

Figure 7-2: The ^{29}Si MAS NMR spectra of alkali activated slag

As the activator modulus increases to 1.4 and then 1.8, there is an obvious increase of the covering area that refers to the original slag; indicating less starting precursor has reacted. This

result is in accordance with the previous investigations on the reaction kinetics and gel structures that a higher activator modulus leads to a delayed early age reaction with reduced reaction intensity, also the chemically bond water content exhibits a slight reduction (Faucon et al, 1999). Other obvious changes caused by the increased activator are the reduced relative content of Al substituted Q^2 groups and the increased Q^3(1Al) groups. The effect of activator modulus on the silicate structure compositions is quantified based on the deconvolution and the results are summarized in Table 7-1. It can be seen that the unreacted slag content in the reaction products is around 30.3%, 32.3% and 41.1% in mixtures with activator modulus of 0.8, 1.6 and 2.4, respectively. Considering the alkali solution also contributes to the total silica content, the reaction degree of slag (RD(s), in terms of Si) is calculated as follows (in mol.%):

$$\mathrm{RD(s)} = \frac{\mathrm{Si(Or)-Si(Un)}}{\mathrm{Si\ (Or)}} \times 100\% \quad (1)$$

Where Si(Or) is the input Si from the original slag, and Si(Un) is the unreacted Si in slag with the reaction products.

Table 7-1: Deconvolution results of ^{29}Si MAS NMR spectra of alkali-activated slag

Chemical shift (± 0.5 ppm)	Site type	Sample ID		
		AS-08	AS-16	AS-24
-74.51	Qs	30.28	32.27	41.09
-74.5	Q0	7.38	9.39	7.09
-76.9	Q1-a	4.03	5.31	5.00
-78.7	Q1-b	14.85	11.07	8.09
-81.5	Q2(1Al)	28.26	16.27	10.69
-84.4	Q2-b	10.24	12.44	9.75
-86.5	Q2-p	2.16	3.87	5.65
-89.2	Q3(1Al)	2.81	9.38	12.63

The result shows that when increasing the activator modulus from 0.8 to 1.6 and then 2.4, the reactivity of Si from slag decreases from 66.3% to 60.5% and 45.1%, respectively. It indicates that although additional silicate from the activator benefits the reaction in various aspects, its dosage should be limited to a reasonable level, otherwise a negative effect in terms of the slag efficiency may take place, as well as porosity and strength, especially in the case of mixes with

a high modulus of 2.4. It is suggested that the reduced pH due to the increased modulus and the increased available reactive silica at the initial age are the two reasons that lead to the reduced slag reactivity.

Besides, Q^1 groups (including $Q^{1\text{-}a}$ and $Q^{1\text{-}b}$) show a gradual reduction when increasing the activator modulus. In terms of the Q^2 groups, mixes with activator modulus of 0.8 and 1.6 exhibit similar content: 40.7% and 39.8%, respectively. When the modulus increases to 2.4, the Q^2 content significantly reduces to 26.1%. It is highly possible that the shifts of Q1 and Q^2 contents are related to the reaction degree of slag, since the terminal Q^1 and bridging Q^2 groups are the representative structures of the reaction products, and those parameters share a similar shifting tendency. Among the different types of Q^2 sites, the Q^2(1Al) groups present a significant reduction from 28.3% to 10.7%, due to the fact that the original slag is the only aluminate source in this case, the decreased amount of reacted slag leads to a reduction of Al supply in the solution, and therefore less Al is bonded into the C-(A)-S-H type gels. One dramatic increase as a result of the increased activator is the content of Q^3(1Al) sites, from about 2.8% to 12.5%. It is suggested that the silicate structure in the activator solution plays an important role, since the Q^n(0-4) groups are sensitive to the pH and Si/Na ratios in the solution. One previous investigation on the effect of activator parameters on silicate structures also showed that when activator modulus is around 1.0, the silicate is mainly shown in the form of Q^0 to Q^2 sites; when increasing the modulus to 1.7 or higher, the Q^0 to Q^2 sites content shows a sharp reduction while Q^3 groups become more significant (Jansson et al, 2015).

7.3.2 ^{27}Al MAS NMR

Compared to the original slag, the reaction products show two significant Al peaks. As shown in Figure 7-3, a significant and relatively broad peak is shown at around 62 to 72 ppm, which is assigned to the tetrahedral Al(IV) that is incorporated in the C-A-S-H gels with bridging conditions (Saout et al, 2011); the other one with lower intensity and sharper shape at around 10 ppm is usually regarded as octahedral coordinated Al in AFm and/or hydrotalcite typed phases (Mackenzie et al, 1993). These phases are usually poorly crystallined in the case of alkali activated system and therefore not always XRD detectable. Besides, the unreacted slag also contributes to the 4, 5 and 6 coordinated Al regions in the spectrum, since certain amount of raw slag is clearly identified by ^{29}Si MAS NMR. It is generally believed that the deconvolution of ^{27}Al MAS NMR peaks are more suitable for qualitative evaluation rather than quantitative calculation, due to their broad peak locations, asymmetrical natural and complicated linking environments (Oh et al, 2014). Therefore the deconvolution of Al spectra was not carried out in this study.

For mixes with an activator modulus of 0.8, the tetra-coordinated region seems to exhibit two resonances: a narrow one at around 71.5 ppm and a smooth one at around 65 ppm. The presence of more than one Al(IV) site within the reaction products of alkali activated materials is also observed in previous studies, and they are all identified as the tetrahedral Al in the C-A-

S-H type gels (Myers et al, 2013; Pardal et al, 2012). As the activator modulus increases to 1.6 and 2.4, the peak location of Al(IV) sites shifts to around 64 and 62 ppm, respectively; representing that slight changes occurred concerning the bonding environment surrounding the Al groups. The shifting of Al(IV) resonance into a lower chemical shift suggests a relatively high content of silicate is surrounded other than oxhydryl, therefore leading to a reduced electron density and lower ppm. This result is also in line with the ^{29}Si MAS NMR analysis that when increasing the activator modulus, less Q^2(Al) and more Q^3(1Al) groups are shown in the reaction products. Although the ^{27}Al MAS NMR resonances are not quantified in this case, it is still obvious that there is a decrease in the intensity of octahedral Al peaks compared to the tetrahedral ones. The reduced octa-Al intensity in the reaction products indicates that within the reacted phases, more Al is participated into the C-A-S-H gels rather than forming individual Al-riched phases. This can be explained by the Al uptake of C-A-S-H gels increases to some extent due to the increased total silicate input, which is in constant with (Carcia-Lodeiro et al, 2013; Ben et al, 2011).

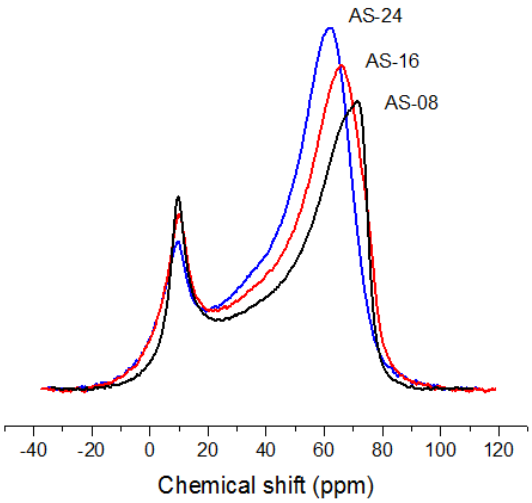

Figure 7-3: The ^{27}Al MAS NMR spectra of alkali activated slag

7.4 Alkali activated fly ash

7.4.1 ^{29}Si MAS NMR

Figure 7-4 depicts the ^{29}Si MAS NMR spectra of ambient temperature activated fly ash. By using different activator moduli, significant structural differences are resulted. The deconvolution results indicate that all mixes are having considerable contents of Q^4 groups, including both unreacted Q^4 sites from the original slag and newly formed ones. Depending on

the activator modulus, all mixtures also contain certain amounts of poorly polymerized Q^2 to Q^0 groups. It is commonly known that in order to achieve an ideal reaction degree, the activation of fly ash is usually carried out under elevated temperature and high alkali concentrations, resulting in mainly highly polymerized N-A-S-H type gels with Q^4 sturctures (Hai et al, 2014; Jaarsveld et al, 2002). Therefore a great structural variation can be seen in the activation of aluminosilicates when room temperature with moderate alkalinity is applied. Previous studies also observed the presence of Q^2 to Q^0 sites in room temperature cured fly ash (Peng et al, 2015).

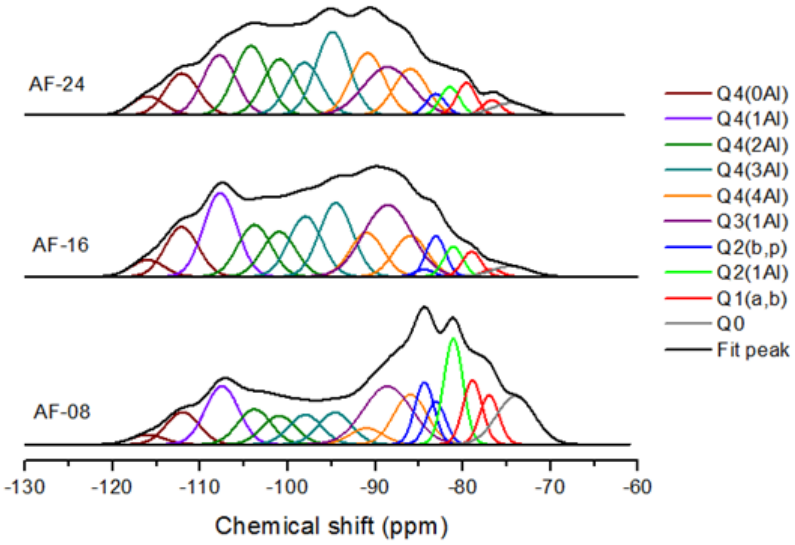

Figure 7-4: The ^{29}Si MAS NMR spectra of alkali activated fly ash

The deconvolution calculation of the effect of activator modulus on silicate structure of alkali activated fly ash is summarized in Table 7-2. Mixes with an activator modulus of 0.8 exhibit an obvious difference compared to the mixes with higher modulus. The total covered area of Q^2 to Q^0 groups in this mix is around 39.1%, while this value is only 11.7% and 11.1% for mixtures with activator modulus of 1.6 and 2.4, respectively. As a consequence, the Q^4 groups show a significantly lower value of 47.4% compared to 72.1% and 77.8% of the remaining two mixtures. It indicates that when the activator modulus is low to a certain degree, namely high pH and low additional silicate environment, a less polymerized structure is preferred under ambient temperature curing. For the isolated Q^0 groups, mixtures with activator modulus of 1.6 and 2.4 show a similar content of 1.9% and 2.2%, the total contents of end-of-chain Q^1 groups and Q^2(1Al) sites also remain on a similar level, while the content of Q^2 structures shows a decrease from around 4.3% to 2.0%. However, for the mixes with a modulus of 0.8, the total

covered areas of each above mentioned group is approximately 2 to 4 times higher. All three mixtures also show a significant presence of Q^3(1Al) groups around 11.1% to 16.1%, which is higher than that of alkali activated slag.

Table 7-2: The Deconvolution results of ^{29}Si MAS NMR spectra of alkali-activated fly ash

Chemical shift (± 0.5 ppm)	Site type	Sample ID		
		AF-08	AF-16	AF-24
-116.0	Q4(0Al)	1.57	2.59	2.99
-112.0	Q4(0Al)	5.17	7.72	6.61
-108.0	Q4(1Al)	9.42	13.02	9.52
-104.0	Q4(2Al)	5.66	8.05	10.99
-101.0	Q4(2Al)	4.66	7.00	8.88
-98.0	Q4(3Al)	4.77	9.12	8.35
-94.0	Q4(3Al)	5.43	11.45	13.19
-91.0	Q4(4Al)	2.63	6.83	9.87
-86.0	Q4(4Al)	8.03	6.37	7.36
-88.6	Q3(1Al)	13.56	16.13	11.09
-84.4	Q2-p	5.79	0.64	0.00
-83.1	Q2-b	3.97	3.64	1.95
-81.1	Q2(1Al)	9.88	2.68	2.63
-79.8	Q1-b	5.96	2.26	2.97
-77.0	Q1-a	4.60	0.66	1.38
-74.0	Q0	8.89	1.86	2.22

Concerning the Q^4(mAl) units, the peak intensity of Q^4(0Al) groups is around 10.3% and 9.6% in mixes with an activator modulus of 1.6 and 2.4, respectively. Also the percentage of Q^4(1Al) remains in a similar level of 21.1% and 20.5%. Those two types of Q^4 groups are generally regarded as the ones containing mainly crystalline phases with relatively low reactivity within

the original fly ash (Fernandez et al, 2006). However, certain amounts of glassy phases may also present in those groups and participate into the reaction process. Moreover, the silicate contaminated crystalline phases also have the potential to be reactive. Compared to the Q^4(0Al) and Q^4(1Al) sites, Q^4 structures with higher aluminate substitutes exhibit a higher intensity shifts from around 1% to 4% between samples with an activator modulus of 1.6 and 2.4. It thus shows that high alumina incorporated Q^4 groups tend to be more reactive.

The following discussion will examine the quantification of the fly ash in more detail. In order to investigate the reaction degree of fly ash, the selective dissolution was carried out. Samples were firstly ground and then dissolved in 1:20 HCl (vol.%). Specifically, 1 g of reacted powder was added into 250 ml of HCl solutions, the mixture was then stirred for 3 h and filtered by using a 2 um filter paper. The insoluble residues were washed with distilled water until a neutral pH is reached, then dried and stored until the analysis was carried out. Selective dissolutions were repeated 3 times for each mix. The acid attack decomposes the original structure of slag and its reaction products, as well as the N-A-S-H type gels or other reacted phases, leaving behind the unreacted fly ash as the only insoluble residue.

The dissolution results together with the calculation of reaction degree are summarized in Table 7-3. Each dissolution result is an average of three measurements. The reliability of this method on identifying the reaction degree was verified by (Fernandez et al, 2006) by using ^{29}Si MAS NMR together with Rietveld XRD. The fraction of inputted fly ash within the tested samples is calculated based on the designed recipes.

Table 7-3: Selective dissolution results of alkali activated fly ash

Sample ID	Weighed AA-FA	FA within weighed	Residual	Reaction degree
AF-08	2.00 ± 0.001	1.33 ± 0.004	0.45 ± 0.004	66.2%
AF-16	2.00 ± 0.001	1.30 ± 0.003	0.61 ± 0.001	53.3%
AF-24	2.00 ± 0.001	1.27 ± 0.004	0.66 ± 0.005	48.0%

The results indicate that similar to alkali activated slag, as the activator modulus increases from 0.8 to 2.4, there is a significant reduction of reaction degree from 66.2% to 48.0%. It also proves again that adding additional silicate and the consequently reduced pH exhibits a negative effect on the reaction degree. In order to further understand the contribution of the unreacted phases to the overall ^{29}Si MAS NMR spectra, XRF and ^{29}Si MAS NMR tests were carried out to the collected residuals (unreacted fly ash). The chemical composition analysis shows that the silica (SiO_2) contents in mixes with an activator modulus of 0.8, 1.6 and 2.4 are 54.73%, 59.92% and 53.94%, respectively. Their ^{29}Si MAS NMR spectra with the deconvolution analysis are depicted in Figure 7-5.

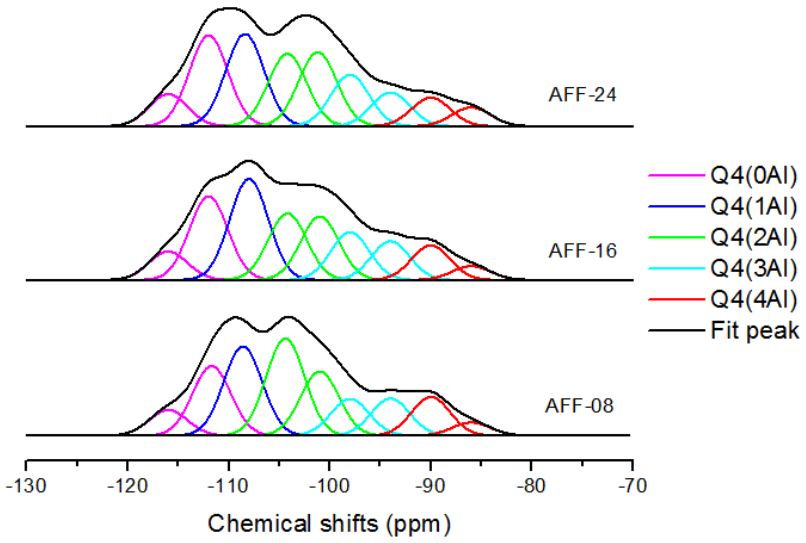

Figure 7-5: The ^{29}Si MAS NMR spectra of residuals after selective dissolution

It can be seen that compared to the spectrum of the original fly ash, there is a slight reduction mainly in the area representing Q^4(2Al) to Q^4(4Al) groups. It is easy to understand that the peak shape of the unreacted phases is overlapped within the overall spectra. Then the silica contribution of unreacted fly ash (Si(un)%) to the overall ^{29}Si MAS NMR peak is calculated as follows (in mol.%):

$$\mathrm{Si(un)\%} = \frac{\mathrm{Si(Res)}}{\mathrm{Si(FA)+Si\ (Ac)}} \times 100\% \qquad (2)$$

Where Si(Res) is the amount of Si from the filtered residuals, Si(FA) is the input Si from the original fly ash, and Si(Ac) is the input Si contributed by the activator.

Based on the calculation of reaction degree and XRF analysis, the value of Si(un)% can be obtained. The result shows that the contribution of unreacted silica to the total spectra is 31.6%, 44.9% and 42.4% for mixes with activator modulus of 0.8, 1.6 and 2.4, respectively. Then their peak shapes are fixed with a single factor that fits their area contributions, and subtracted from the overall NMR spectra, and by doing so the contribution of unreacted fly ash and reaction products to each Q structure can be calculated individually. The results are listed in Table 7-4. It can be observed that besides the unreacted phases, newly formed Q^4 groups upon activation consist about 15.7% to 35.4% of the total reaction products. When increasing the activator modulus, more reaction products are formed in Q^4 structures that with high aluminate

substitutions (Q^4(3-4Al)). A high activator modulus presents significantly higher contents of newly formed Q4 sites.

Table 7-4: Summary of the deconvolution and selective dissolution results

Site type	AF-08		AF-16		AF-24	
	Un-reacted	Newly formed	Un-reacted	Newly formed	Un-reacted	Newly formed
Q4(0Al)	6.38	0.37	10.53	<0.1	10.55	<0.1
Q4(1Al)	12.51	2.57	15.74	5.32	14.13	6.38
Q4(2Al)	6.76	2.67	10.45	5.66	10.75	6.48
Q4(3Al)	2.49	2.94	3.63	7.82	2.89	10.30
Q4(4Al)	3.48	7.18	4.55	8.65	4.06	13.17
Q3(1Al)	-	13.56	-	16.13	-	11.09
Q2	-	9.76	-	4.28	-	1.95
Q2(1Al)	-	9.88	-	2.68	-	2.63
Q1	-	10.56	-	2.94	-	4.35
Q0	-	8.89	-	1.86	-	2.22

7.4.2 ^{27}Al MAS NMR

Figure 7-6 shows the ^{27}Al MAS NMR spectra of alkali activated fly ash with three different activator moduli. Two significant peaks are shown at about 2 ppm and 59 to 54 ppm, representing Al(IV) and Al(VI) sites within the reaction products. Also a certain amount of Al(V) contributes to the spectra since there exists a hump between around 30 and 40 ppm. Compared to the spectra of unreacted fly ash, the location of Al(VI) groups remains unchanged, indicating that the alumina contaminated crystalline phases such as mullite show limited or negligible contribution to the activation process.

Besides, the relative intensity of the Al(IV) groups exhibits a significant increment, due to the massive formation within the reacted gels. The location of the Al(IV) peak in the original fly ash is at around 46 ppm, suggesting a lower silicon surrounded Al(IV) environment after activation. As the activator modulus increases from 0.8 to 2.4, there is a reduction on the relative intensity of the Al(IV) groups, together with less ordered peak shape and increased intensity of Al(IV) sites.

Based on the ^{29}Si MAS NMR analysis, those shifts can be partly attributed to the reduced reaction degree of fly ash, therefore more 4 to 6 coordinated Al groups from the original ash contribute to the overall spectrum, resulting in a lower Al(IV) to Al(IV) ratio. The obviously increased hump area around 20 to 40 ppm also indicates less Al(V) from the fly ash is transformed into the reaction products (tetra-Al). Meanwhile, the newly formed reaction products with mainly Al(IV) sites greatly contribute to a peak location, thus the mixtures with a higher reaction degree (lower activator modulus) present a more intensive Al(IV) peak.

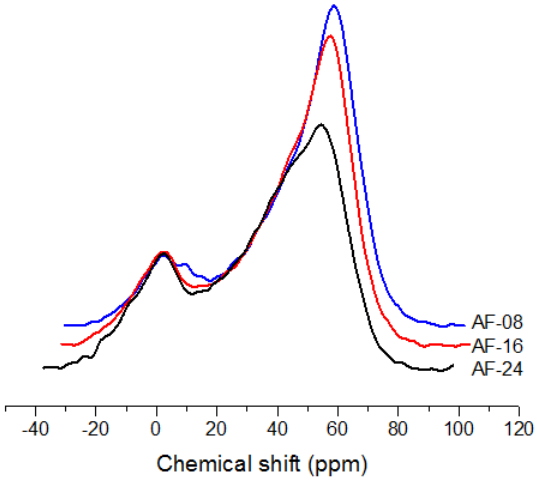

Figure 7-6: The ^{27}Al MAS NMR spectra of alkali activated fly ash

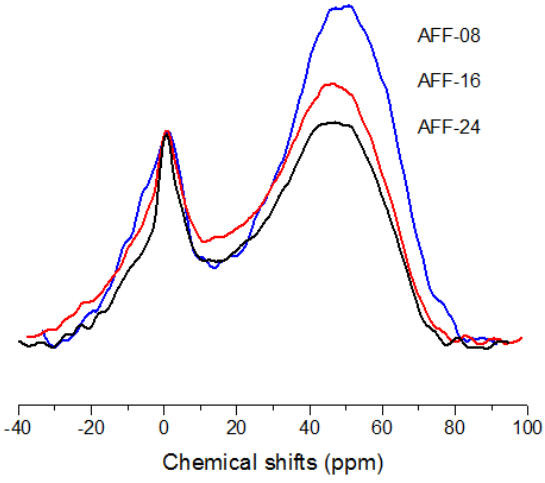

Figure 7-7: The ^{27}Al MAS NMR spectra of residuals after selective dissolution

The residuals of alkali activated fly ash after selective dissolution were also tested by ^{27}Al MAS NMR, and the results are shown in Figure 7-7. The residuals in this case are regarded as the unreacted components of fly ash after activation. The figure shows that the residuals exhibit two significant peaks at around 1 and 46 ppm, as well as a broad hump between around 20 to 40 ppm, assigning to the unreacted 6, 4 and 5 coordinated Al within the unreacted phases, respectively. The unreacted Al(IV) groups are centered at around 46 ppm, presenting the same location as the original fly ash. In terms of the Al(VI) groups, the peak location is shifted from 2 to 1 ppm and exhibits an obviously sharpened size compared to the raw fly ash. The changed peak shape of Al(VI) groups together with the reduced peak location may suggest that the Al(VI) sites in the original fly ash are partly reacted during the alkali activation, namely the Al(VI) from glassy Al phases and/or crystalline mullite participated into the reaction process.

7.5 Alkali activated slag-fly ash blends

7.5.1 ^{29}Si MAS NMR

Figure 7-8 shows the ^{29}Si MAS NMR spectra and deconvoluted peaks of alkali activated slag-fly ash blends with three different activator conditions. Similar to the spectra of alkali activated slag, the reaction products exhibit an obvious peak area between around -90 and -60 ppm, representing the large amounts of Q^0 to Q^2 groups within the reaction products.

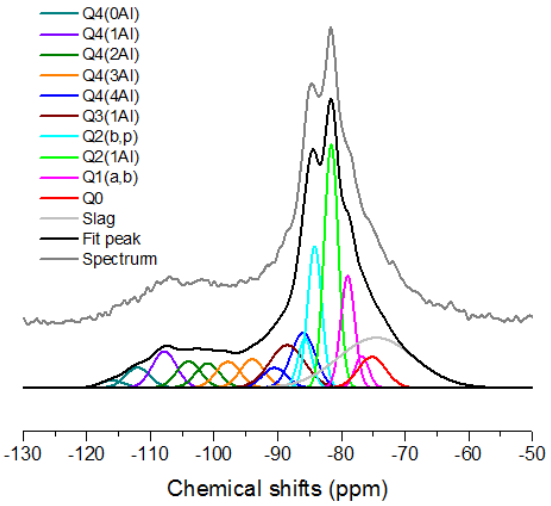

(a) Ms=0.8

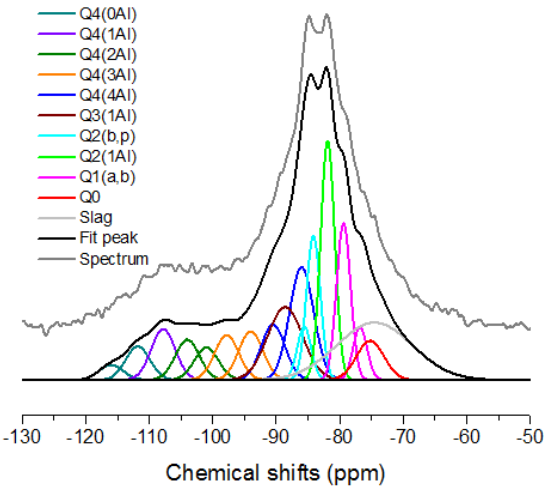

(b) Ms=1.6

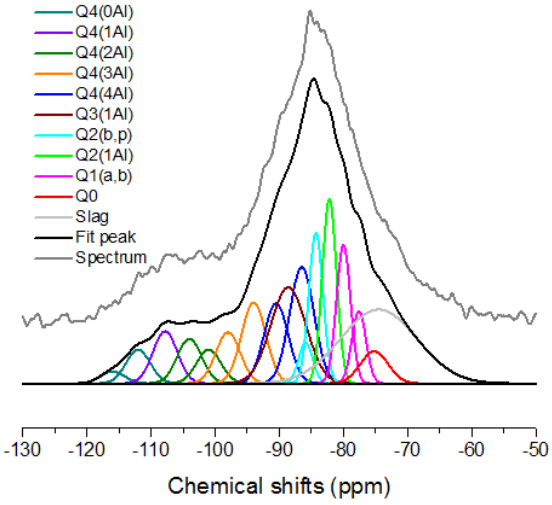

(c) Ms=2.4

Figure 7-8: The ^{29}Si MAS NMR spectra of alkali activated slag-fly ash blends

All peaks also show a large fraction of unreacted slag. The wide covered area at about -120 to -90 ppm is assigned to the Q^4 sites, mainly from the original fly ash and its reaction products. The deconvolution results are summarized in Table 7-5. The mixes show similar amount of

unreacted silica from the original slag around 15.8% to 18.8%. Also similar to the case of alkali activated slag, the fraction of Q^0 and Q^1 groups remains stable regardless of the activator modulus. When increasing the activator modulus from 0.8 to 2.4, the content of Q^2(1Al) and Q^2 groups shows a continuous reduction, up to around 8.4% and 4.4%, respectively.

Table 7-5: Deconvolution results of ^{29}Si MAS NMR spectra of slag-fly ash blends

Chemical shift (± 0.5 ppm)	Site type	Sample ID		
		ASF-08	ASF-16	ASF-24
-116.0	Q4(0Al)	0.89	1.33	0.95
-112.0	Q4(0Al)	2.44	2.94	2.68
-108.0	Q4(1Al)	4.37	4.47	4.16
-104.0	Q4(2Al)	3.16	3.55	3.58
-101.0	Q4(2Al)	2.93	2.85	2.69
-98.0	Q4(3Al)	3.14	3.94	4.08
-94.0	Q4(3Al)	3.44	4.28	6.46
-91.0	Q4(4Al)	2.42	4.85	6.38
-86.0	Q4(4Al)	6.62	9.90	9.29
-88.6	Q3(1Al)	7.40	9.28	11.13
-85.5	Q2-p	3.41	2.71	1.88
-84.2	Q2-b	9.84	7.34	6.95
-81.1	Q2(1Al)	16.92	12.16	8.54
-79.3	Q1-b	7.78	7.98	6.41
-77.0	Q1-a	2.18	2.69	3.35
-75.0	Q0	4.22	3.93	2.95
-74.51	Slag	18.83	15.81	18.51

The fraction of Q^3(1Al) groups shows a slight increase from about 7.4% to 11.1%, exhibiting a lower increment compared to the alkali activated slag. In terms of the Q^4 content, there is an

increase in general from 29.4% to 40.3% when increasing the activator modulus. This is mainly contributed by the Q^4(4Al) and Q^4(3Al) sites, which increase from around 12.5% to 22.1%; while the Q^4(2Al) to Q^4(0Al) group contents are less shifted, namely between approximately 16.9% and 19.1%.

The reaction degree of slag, in terms of the Si, is calculated using the same method as described in Section 7.3, while with the consideration of fly ash incorporation on the initial Si input, namely the initial silica consists of the ones from slag, fly ash and activator rather than only slag and activator. By applying the same methodology, the calculated silica reactivity from slag is 47.1%, 52.0% and 39.7% in mixes with the activator modulus of 0.8, 1.6 and 2.4, respectively. Those values are lower than the case of alkali activated slag, indicating a negative effect of fly ash incorporation on the slag reactivity.

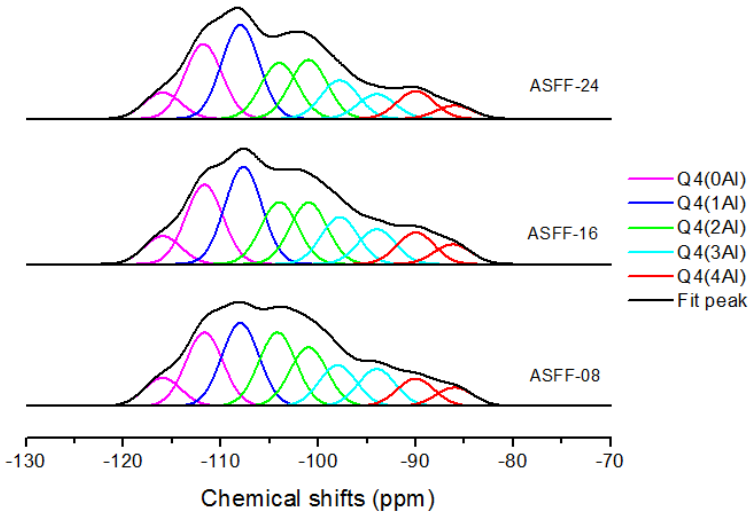

Figure 7-9: The ^{29}Si MAS NMR spectra of residuals from slag-fly ash blends

Similar to the measurements described in Section 7.4, the selective dissolution is carried out to the reaction products of alkali activated slag-fly ash blends, together with the XRF and ^{29}Si MAS NMR analyse of the undissolved residuals, based on the fact that slag will be well dissolved in HCl (Fernandez et al, 2006). Their ^{29}Si MAS NMR spectra with deconvolution are presented in Figure 7-9, and in mixes with with activator modulus of 0.8, 1.6 and 2.4, the silicate content within the residuals is 55.29%, 56.08% and 52.08%, respectively; and a dissolved fraction of 72.6%, 70.0% and 68.4%, respectively. The silica contribution of residuals to the overall ^{29}Si MAS NMR peak is calculated as by (in mol.%):

$$\text{Si\%} = \frac{\text{Si(Res)}}{\text{Si(FA)+Si(GGBS)+Si (Ac)}} \times 100\% \quad (3)$$

Where Si(Res) is the amount of Si in the residuals, Si(FA) is the amount Si from the initial fly ash, Si(GGBS) is the amount of Si from the initial slag, and Si(Ac) is the content of Si contributed by the activator.

The result shows that the unreacted silica contribution from the unreacted ash to the total spectra is 15.2%, 16.8% and 16.5% for mixes with activator moduli of 0.8, 1.6 and 2.4, respectively. Then the content of unreacted phases regarding each Q^4 structure within the reaction products is subtracted based on their deconvolution results and peak contributions. The results are listed in Table 7-6. It can be seen that the Q^3 to Q^0 groups are newly formed low polymerized structures, while the Q^4 sites include both unreacted phases and newly formed ones. Within the new phases, Q^4(4Al) and Q^4(3Al) exhibit an obvious increase with the increase of activator modulus, especially the Q^4(4Al) groups, which occupy more than half of the newly formed Q^4 structures. While the content of Q^4 groups with 0 to 2 aluminate substitutions remains a similar level, showing a total fraction of about 5% within the input silicate.

Table 7-6: Summary of the deconvolution and selective dissolution results

Site type	ASF-08		ASF-16		ASF-24	
	Un-reacted	Newly formed	Un-reacted	Newly formed	Un-reacted	Newly formed
Q4(0Al)	3.49	<0.1	3.91	0.36	3.98	<0.1
Q4(1Al)	5.39	2.14	5.81	2.21	5.77	1.78
Q4(2Al)	3.43	2.64	3.96	2.83	3.90	2.88
Q4(3Al)	1.27	2.16	1.27	3.01	0.99	5.47
Q4(4Al)	1.58	7.46	1.87	12.88	1.64	14.03
Q3(1Al)	-	7.40	-	9.28	-	11.13
Q2	-	13.25	-	10.05	-	8.83
Q2(1Al)	-	16.92	-	12.16	-	8.54
Q1	-	9.96	-	10.67	-	9.76
Q0	-	4.22	-	3.93	-	2.95
Slag	18.83	-	15.81	-	18.51	-

7.5.2 ^{27}Al MAS NMR

The ^{27}Al MAS NMR spectra of alkali activated slag-fly ash blends with three levels of activator moduli are depicted in Figure 7-10. Similar to the cases of alkali activation of sole slag or fly ash, all spectra present two typical peaks: octa-Al and tetra-Al, together with a broad hump assigned to the penta-Al. The location of Al(VI) groups is fixed at around 10 ppm, which indicates the presence of hydrotalcite type phases. Compared to alkali activated slag, this group shows the same chemical shift but with a relatively low peak intensity, revealing a relatively low content of these phases within the overall reaction products. It is easy to understand that this is due to the reduced absolute slag content in the slag-fly ash blends (slag/fly ash = 50/50). Compared to the alkali activated fly ash, the peak of Al(VI) sites at around 2 ppm seems to be covered by the newly formed hydrotalcite typed phases and becomes no longer significant, demonstrating its relatively low content compared to the one at 10 ppm. In terms of the Al(IV) groups, the peak location is at around 63 ppm, which is similar in general as the ones observed in alkali activated slag, but higher than the case of alkali activated fly ash, showing the slight difference of Al(IV) environments between C-A-S-H and N-A-S-H type gels, also in the blended system, the Al(IV) environment tends to be similar with the low polymerized C-A-S-H type gels. When increasing the activator modulus from 0.8 to 2.4, there is an obvious reduction of relative Al(VI) content, indicating a higher transformation rate of Al(VI) to Al(IV) groups.

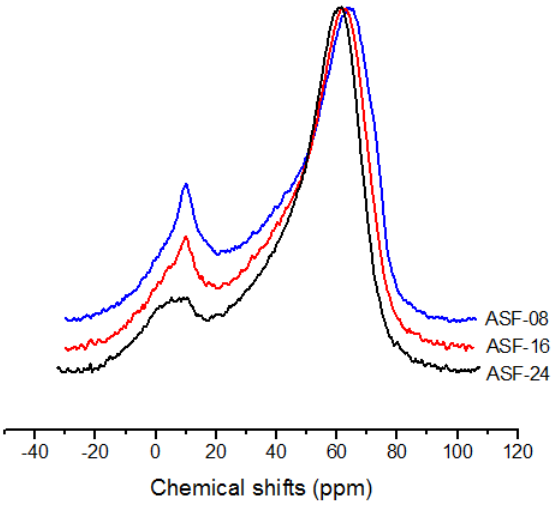

Figure 7-10: The ^{27}Al MAS NMR spectra of alkali activated slag-fly ash blends

The ^{27}Al MAS NMR spectra of insoluble residuals from alkali activated slag-fly ash blends are presented in Figure 7-11. Those spectra share a very similar peak location and intensity to the

residuals from the alkali activated fly ash, since they are intrinsically the same material with slightly different chemical compositions.

The location of Al(VI) sites in both cases is 1 ppm, while the Al(IV) peak location shifts to 1 ppm higher than the case of alkali activated fly ash, indicating a slight difference of the activation effect on fly ash when blended alkali system is applied. Besides, a sharper peak of Al(VI) sites can be observed in mixes with higher activator modulus, which may indicate that activator solutions with a low modulus exhibit a better interaction with the Al(VI) groups, resulting in a slightly lower amount of remaining octa-Al.

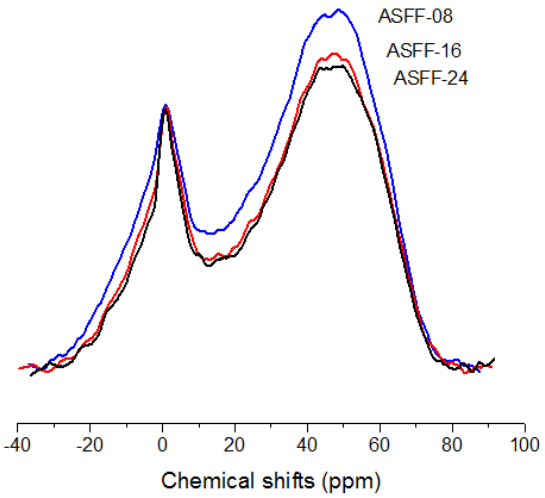

Figure 7-11: The ^{27}Al MAS NMR spectra of residuals from alkali activated slag-fly ash blends

7.6 Effect of activator and precursor on reaction degree

The chemistry, reaction kinetics, gel structure of alkali activated slag, fly ash and their blends are studied in great detail previous researches, providing strong basis for the understanding and application of this new type of binder. The results in this study show similar tendency towards the previous studies regarding the effect of activator and slag-fly ash blends on the reaction process during the alkali activation. For instance, the ^{29}Si MAS NMR analysis shows that the increased activator modulus leads to a reduction on the silica reactivity, which can correspond to the decreased reaction intensity with delayed main reaction peak, as shown in the isothermal calorimetric results; also slightly reduced bond water content was reported from the TG analysis.

The addition of fly ash into slag leads to a more complicated chemistry, and usually presents coexisting N-A-S-H and C-(A)-S-H type gels, identified by FTIR, SEM/EDX etc. (Garcia et al,

2010; Ismail et al, 2014; Bernal et al, 2013; Deira et al, 2014; Garcia et al, 2011); consistently, the ^{29}Si MAS NMR results in this study verify the formation of reaction products with both Q^4 and chain structures. Besides the previous investigations, this study gives a special focus on analysing the gel composition and reaction degree based on the deconvolution of ^{29}Si MAS NMR results, while the ^{27}Al MAS NMR spectra provide additional supporting information. Although the deconvolution analysis may not perfectly reflect the silica structures (content and type in the real situation), a consistent analyzing method applied throughout the whole study is still capable of investigating the structure shifts of alkali activated materials before and after activation. The quantified analysis provides some insights in understanding the reaction degree and reaction products, which can also be used as supplementary information of other micro scale analyses.

Figure 7-12 shows a comparison of the silica structure compositions (mol.%) between alkali activated slag-fly ash blends, and a physical mix of alkali activated slag and alkali activated fly ash (50/50 by mass), the gel composition of the latter mix is obtained from the ones shown in previous Sections in this chapter.

It should be noticed that although the unreacted fly ash and slag content remain relatively stable as the activator modulus increases, there is still a significant difference in reactivity of the raw materials, due to the shifted additional silicate content from the activators. The silicate from the activator presents a considerable amount of the total silica input, which is about 3.87, 7.72 and 11.58 g per 100 g of the precursors.

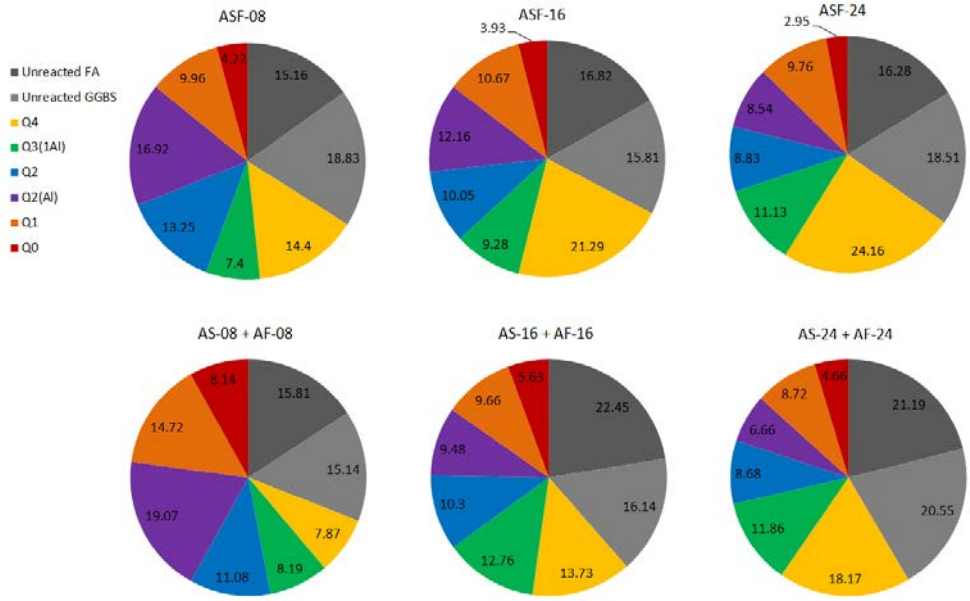

Figure 7-12: Comparison of the silicate compositions

Comparing the reactivity results in Sections 7.3 to 7.5, it is shown that when blended system is applied, there is a slight reduction of the slag reactivity and an increase of the reaction degree of fly ash, confirming an interaction between the precursors. The alkali activated slag-fly ash blends and the hypothesized AA-slag + AA-fly ash mixes are having the same starting compositions, the different silicate compositions in the reaction products also suggest an interaction. For mixes with an activator modulus of 0.8, the content of unreacted silica contains around 34.0% of the total silica, namely about 66.0% of the input silica is participated into the reaction products; while it should be noted that all the silicate from the initial activator (about 8% in sample ASF-08) is also considered as reaction products in this case, since it is impossible to distinguish their silicate origins from the reaction products. Compared to the AS-08 + AF-08 mix, the content of Q^0 and Q^1 groups is reduced by 3.9% and 4.8%, respectively; while the Q4 groups show an increment of around 6.5% (mainly contributed by Q^4(4Al)).

Table 7-7: Calculation of mean chain length and Si/Al of the reaction products

Sample ID	Si/Al in C-A-S-H	MCL	Si/Al in N-A-S-H
AS-08	4.21	7.80	-
AS-16	6.02	6.97	-
AS-24	7.33	6.80	-
AF-08	-	-	1.38
AF-16	-	-	1.47
AF-24	-	-	1.41
ASF-08	4.74	9.76	1.32
ASF-16	5.41	7.30	1.24
ASF-24	6.35	6.43	1.20

The reduced content of isolated silicate, end-of-chain structures together with the increased Q^4 sites suggest a higher polymerization and crosslinking in the blended system. Besides, the content of Q^3 and Q^2 groups remains similar, with slightly reduced Q^2(1Al) content of around 2.2%, increased Q^2 content of 2.2% and Q^3(1Al) shifts less than 1%. As the activator modulus increases to 1.6 and 2.4, the silicate from activator occupies 14.8% and 20.6% of the total silicate input. Thus although similar contents of unreacted slag and fly ash are presented, differences in reactivity are still shown by using the methodology described in Section 3.1 to 3.4. Compared to the physically mixed samples with a fixed activator modulus, there is a

reduction on the unreacted starting materials, indicating that the blended system benefits the overall reaction degree; with largely increased content of Q^4 structures, increased $Q^2(1Al)$ sites, slightly reduced $Q^3(1Al)$ and Q^0 groups, and similar Q^1 and Q^2 contents.
Based on the deconvolution results of ^{29}Si MAS NMR rspectra, the average chain length and Si/Al in the reaction products are calculated and listed in Table 7-7. The mean chain length (MCL), Si/Al of C-A-S-H and N-A-S-H type gels are calculated by:

$$MCL = \frac{Q1+\frac{3}{2}Q2(1Al)+Q2}{\frac{1}{2}Q1} \quad (4)$$

$$Si/Al_{CASH} = \frac{Q1+Q2+Q2(1Al)}{\frac{1}{2}Q2(1Al)} \quad (5)$$

$$Si/Al_{NASH} = \frac{\sum_{n=0}^{4} Q4(nAl)}{\sum_{n=0}^{4} \frac{n}{4}Q4(nAl)} \quad (6)$$

It can be seen that as the activator modulus increases, the mean chain length of the formed C-A-S-H type gels is slightly reduced with an obviously increased Si/Al. In the case of alkali activated fly ash, it should be noticed that only the newly formed Q^4 structures are applied in the calculation, the Si/Al in the N-A-S-H is relatively stable regardless of the activator modulus: between 1.38 and 1.47. When blended precursor is applied, mixes with an activator modulus of 0.8 exhibits a slight increase in Si/Al in terms of the C-A-S-H type gels, while the other two show a reduction. The mean chain length presents an increase in general except the mix with a modulus of 2.4. Concerning the Si/Al in the N-A-S-H type gels, there is a reduction as the activator modulus increases, compared to the alkali activated purely fly ash. All those shifts confirm again the gel interaction in the blended binder system.

7.7 Modeling of the gel formation under different conditions

7.7.1 Alkali activated slag

Based on the MAS NMR results, models that describe the gel formation under different activator and precursor conditions are then suggested. In the case of alkali activated slag, it is assumed that the slag particle is a homogeneous mixture of all involved oxides, and those oxides are reacting homogeneously during alkali activation. It is well known that the mian reaction product of alkali activated slag is a C-A-S-H type gel; while depending on the starting conditions, secondary phases also coexist such as hydrotalcite, AFm type phases and alumiate hydrates (Richardson et al, 1994; Ben et al, 2011; Bonk et al, 2003). Based on the experiments in previous chapters, hydrotalcite is identified as a secondary product and the only Mg-containing phase in this study; its chemical composition is estimated to be M_5AH_{13} based on

the description of (Chen, 2007). Due to the difficulties in identifying the amorphous and poorly crystalline phases, other secondary phases are considered together with the typical C-A-S-H gels as amorphous gels. Then the Ca-Si-Mg-Al related phase changes during alkali activation can be written as follows:

$$\begin{aligned} C_a{\cdot}Si_b{\cdot}M_c{\cdot}A_d\ (\text{Slag}) + Si_n\ (\text{Activator}) \\ = C_x{\cdot}Si_y{\cdot}A_z\ \ (\text{Amorphous CASH gels}) \\ + (M_5A_2)_t\ \ \ (\text{Hydrotalcite}) \end{aligned} \quad (7)$$

It should be noted that all symbols shown in the equations in this section are element in mole. By inputing the initial proportions of the precursor and activator (obtained from XRF analysis, in samples with an Ms of 0.8 shown in Section 7.3) in Equation (7), and recalculating the oxides into moles, then the starting composition can be calculated as follows (in mole, per 100g of slag):

$$\begin{aligned} C_{0.668}{\cdot}Si_{0.574}{\cdot}M_{0.247}{\cdot}A_{0.260} + Si_{0.064} \\ = C_x{\cdot}Si_y{\cdot}A_z \\ + (M_5A_2)_t \end{aligned} \quad (8)$$

Based on the information from the NMR analysis in this study and the literature, the compositon of the reaction products can be classified into several components: the unreacted slag, hydrotalcite, amorphous gels and isolated Q0. Then the following equation can be obtained:

$$\begin{aligned} C_{0.668}{\cdot}Si_{0.574}{\cdot}M_{0.247}{\cdot}A_{0.260} + Si_{0.064} \\ = C_{a1}{\cdot}Si_{b1}{\cdot}M_{c1}{\cdot}A_{d1}\ (\text{Unreacted slag}) \\ + (M_5A_2)_t\ \ \ \ \ \ \ \ (\text{Hydrotalcite}) \\ + Si_{n1}\ \ \ \ \ \ \ \ \ \ \ \ (\text{Isolated Q0}) \\ + C_{x1}{\cdot}Si_{y1}{\cdot}A_{z1}\ \ \ \ \ (\text{Amorphous CASH gels}) \end{aligned} \quad (9)$$

It is assumed that the involved oxides (Ca-Si-Mg-Al) are reacting homogeneously during the alkali activation, and all the reacted Mg is assumed to form hydrotalcite; besides, the reaction degree of slag, the mole content of the unreacted slag can be obtained from the NMR results. Therefore, the content of newly formed hydrotalcite can be calculated by calculating the reaction degree of the raw matetral, the amount of isolated Q0 groups can be directly obtained from the quantitative NMR results; the remaining oxides go into amorphous C-A-S-H gels. Then Equation (9) becomes:

$$C_{0.668}\cdot Si_{0.574}\cdot M_{0.247}\cdot A_{0.260} + Si_{0.064} = C_{0.225}\cdot Si_{0.193}\cdot M_{0.083}\cdot A_{0.088} + (M_5A_2)_{0.033} + Si_{0.047} + C_{0.443}\cdot Si_{0.397}\cdot A_{0.106} \quad (10)$$

It should be mentioned that the amorphous C-A-S-H gels might be a combination of one or more phases including typical non-crosslinking C-A-S-H type gels, crosslinked C-A-S-H type gels (Myers et al, 2013), AFm type phases and other amorphous/crystalline phases. Based on the literatures, it is known that the maximum A/S ratio in the typical C-A-S-H gel of alklai activated slag is around 0.2 (Wang et al, 2003), while this value is 0.28 in Equation (10), then another secondary phase Stratlingite is suggested in this system (Chen, 2007). And it is assumped that the Al favors in incorporating with the typical C-A-S-H type gels until it reaches the maximum Al content. And the remaining aluminate forms Strätlingite. Then a more detailed compostion of reaction ptoducts can be obtained (Ms=0.8):

$$C_{0.668}\cdot Si_{0.574}\cdot M_{0.247}\cdot A_{0.260} + Si_{0.064} = C_{0.225}\cdot Si_{0.193}\cdot M_{0.083}\cdot A_{0.088}\ \text{(Unreacted slag)} + (M_5A_2)_{0.033}\ \text{(Hydrotalcite)} + (C_2A_2S)_a\ \text{(Strätlingite)} + Si_{0.047}\ \text{(Isolated Q0)} + C_b\cdot Si_c\cdot A_d\ \text{(CASH gels)} \quad (11)$$

Using the molar balance of each element before and after reaction, together with the roles of forming reaction products that are mentioned above, the following equation can be obtained based on Equation (10):

$$\text{Ca balance: } 0.668=0.225+2a+b \quad (12)$$
$$\text{Si balance: } 0.574+0.064=0.193+a+0.047+c \quad (13)$$
$$\text{Al balance: } 0.260=0.088+0.033\cdot 2+2a+d \quad (14)$$
$$\text{Al/Si ratio balance: } 0.2d=c \quad (15)$$

Then the unkowns in Equation (10) can be obtiand by using the molar balances in Equations (12) to (15), yielding:

$$C_{0.668}\cdot Si_{0.574}\cdot M_{0.247}\cdot A_{0.260} + Si_{0.064}$$
$$= C_{0.225}\cdot Si_{0.193}\cdot M_{0.083}\cdot A_{0.088} \quad \text{(Unreacted slag)}$$
$$+ (M_5A_2)_{0.033} \quad \text{(Hydrotalcite)}$$
$$+ (C_2A_2S)_{0.015} \quad \text{(Strätlingite)}$$
$$+ Si_{0.047} \quad \text{(Isolated Q0)}$$
$$+ C_{0.412}\cdot Si_{0.382}\cdot A_{0.076} \quad \text{(CASH gels)} \qquad (16)$$

Similarily, the phase composition before and after activation in mixtures with activator modulus of 1.6 and 2.4, can also be calculated following the same methodology, and the results are listed below, respectively:

$$C_{0.668}\cdot Si_{0.574}\cdot M_{0.247}\cdot A_{0.260} + Si_{0.129}$$
$$= C_{0.264}\cdot Si_{0.227}\cdot M_{0.098}\cdot A_{0.103}$$
$$+ (M_5A_2)_{0.030}$$
$$+ (C_2A_2S)_{0.009}$$
$$+ Si_{0.066}$$
$$+ C_{0.386}\cdot Si_{0.401}\cdot A_{0.080} \qquad (17)$$

$$C_{0.668}\cdot Si_{0.574}\cdot M_{0.247}\cdot A_{0.260} + Si_{0.193}$$
$$= C_{0.367}\cdot Si_{0.315}\cdot M_{0.136}\cdot A_{0.143}$$
$$+ (M_5A_2)_{0.023}$$
$$+ Si_{0.054}$$
$$+ C_{0.301}\cdot Si_{0.397}\cdot A_{0.073} \qquad (18)$$

A brief view of the phase compositions before and after alkali activation with different activator modulus (mole %, in terms of the Ca-Si-Mg-Al) is shown in Figure 7-13.
It can be seen that with the fixed equivalent Na_2O dosage of 5%, the silica from the activator consists considerable amount of the starting composition, significantly contributes to the overall mole fraction. Increasing the activator modulus from 0.8 to 2.4 results in an increased additional silica fraction from 4% to 10%, while this in the meantime reduces the effective content of the starting precusor from 96% to 90%. Upon activation, the mole fraction of unreacted slag consists around 32% to 49% of the overall mixture; and the increase of activator modulus obviously reduces the reaction degree of slag, especially in the mix with an activator modulus of 2.4. It is easy to understand that the mole fraction of the typical C-A-S-H gels and the Hydrotalcite decreases with the increase of activator modulus, since their contents are directly linked to the reaction degree of slag. The increase of activator modulus also results in a reduced Ca/Si ratio in the typical C-A-S-H gels. Besides, the measured three mixtures show a similar isolated Q^0 content of around 3% to 4%, probably due to the silica equilibrium during the alkali activation; and the Stratlingite content decreases from 4% to 0% when increasing the

activator modulus from 0.8 to 2.4, indicating that the additional silicate from activator affects the phase composition by influencing the overall Si/Al and Si/Ca contents.

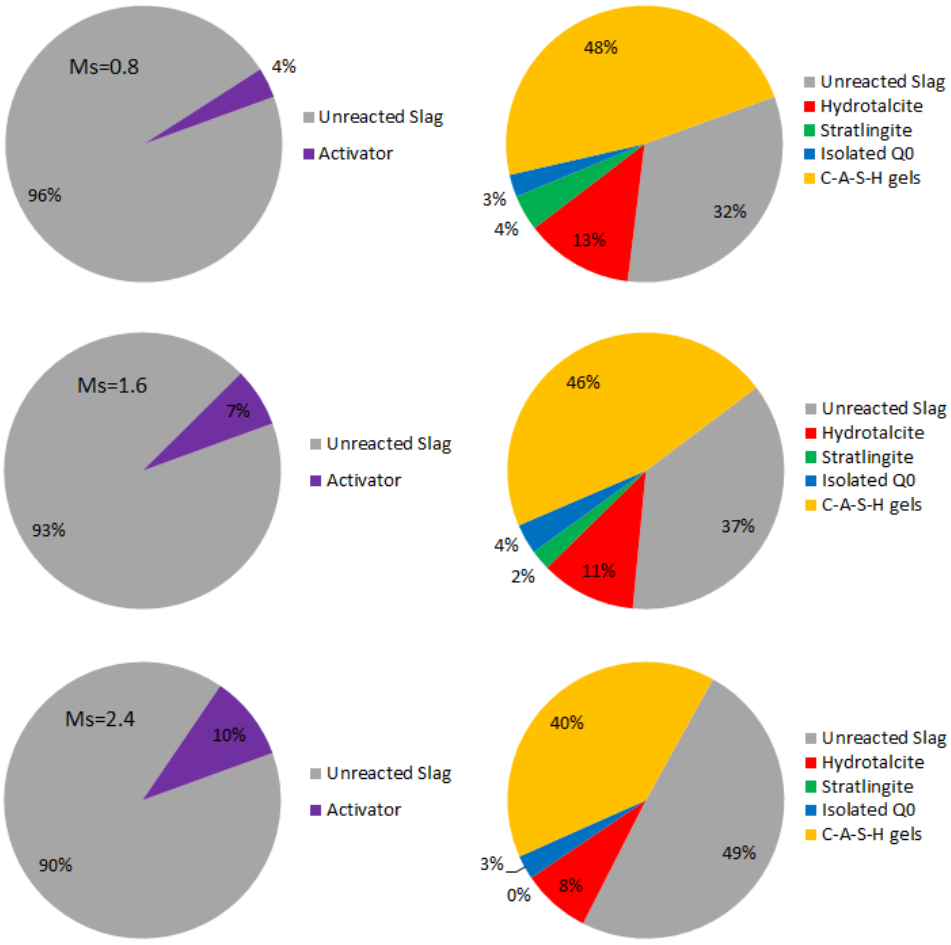

Figure 7-13: Ca-Si-Mg-Al based mole compositions before and after activation

7.7.2 Alkali activated fly ash

A similar calculation is also performed on alkali activated fly ash, based on the ^{29}Si MAS NMR results. Considering the very limited amount of Ca and Mg in this low calcium system, and the presence of crystalline phases such as quartz and mullite, it is assumed that the amorphous phases within the fly ash will be reacted prior to the crystalline phases and (C)-N-A-S-H gels are formed; and the amorphous Ca and Mg are fully reacted in order to simplify the

model. Then the Ca-Si-Mg-Al related phase changes during alkali activation can be generally assumed as follows:

$$C_a \cdot Si_b \cdot M_c \cdot A_d \text{ (Fly ash)} + Si_n \text{ (Activator)} = C_x \cdot Si_y \cdot A_z \text{ (Amorphous CNASH gels)} + (M_5A_2)_t \text{ (Hydrotalcite)} \quad (19)$$

Similar to the case of alkali activated slag, by inputing the initial proportions of the precursor and activator, and recalculating the oxides into moles, the starting composition can be calculated as follows (in mole, per 100g of fly ash, with a Ms of 0.8):

$$C_{0.079} \cdot Si_{0.910} \cdot M_{0.036} \cdot A_{0.497} + Si_{0.064} = C_x \cdot Si_y \cdot A_z + (M_5A_2)_t \quad (20)$$

Based on the information from the NMR analysis in this study and the literature, the compositon of the reaction products contains the following components: the unreacted fly ash that determined by the selective dissolution, hydrotalcite from reacted Mg, and some phases that observed by the NMR deconvolutions, which are typical N-A-S-H gels with Q4 structures, short ranged (C)-N-A-S-H gels and isolated Q0. Then the following equation with more details can be obtained:

$$\begin{aligned} C_{0.079} \cdot Si_{0.910} \cdot M_{0.036} \cdot A_{0.497} + Si_{0.064} = {} & Si_{a1} \cdot A_{b1} \text{ (Unreacted fly ash)} \\ & + (M_5A_2)_t \text{ (Hydrotalcite)} \\ & + Si_{n1} \text{ (Isolated Q0)} \\ & + C_{x1} \cdot Si_{y1} \cdot A_{z1} \text{ (CNASH gels)} \\ & + Si_{c1} \cdot A_{d1} \text{ (NASH gels)} \end{aligned} \quad (21)$$

The small amount of Mg is assumed to be fully incorporated in the Hydrotalcite, and the isolated Q0 content can be obtained directly from the NMR results. Then Equation (21) becomes:

$$\begin{aligned} C_{0.079} \cdot Si_{0.910} \cdot M_{0.036} \cdot A_{0.497} + Si_{0.064} = {} & Si_{a1} \cdot A_{b1} \text{ (Unreacted fly ash)} \\ & + (M_5A_2)_{0.007} \text{ (Hydrotalcite)} \\ & + Si_{0.087} \text{ (Isolated Q0)} \\ & + C_{x1} \cdot Si_{y1} \cdot A_{z1} \text{ (CNASH gels)} \\ & + Si_{c1} \cdot A_{d1} \text{ (NASH gels)} \end{aligned} \quad (22)$$

The reaction degree in alkali activated fly ash (in terms of silica) has been determined in Section 7.4, then the Si fraction of the unreacted ash in Equation (22) can be obtained, also the Si/Al ratio within the unreacted ash can be calculated by using Equation (6) together with the information of Q^4 compositions shown in Table 7-4. Similarily, the Si content and Si/Al ratio of the typical N-A-S-H gels with Q^4 structures can also be calculated using Equation (6) and the NMR deconvolution results shown in Table 7-4. Then the following equation can be obtained:

$$\begin{aligned} &C_{0.079}\cdot Si_{0.910}\cdot M_{0.036}\cdot A_{0.497} + Si_{0.064} \\ &\quad = Si_{0.308}\cdot A_{0.115} \quad \text{(Unreacted fly ash)} \\ &\quad + (M_5A_2)_{0.007} \quad \text{(Hydrotalcite)} \\ &\quad + Si_{0.087} \quad \text{(Isolated Q0)} \\ &\quad + C_{x1}\cdot Si_{y1}\cdot A_{z1} \quad \text{(CNASH gels)} \\ &\quad + Si_{0.153}\cdot A_{0.111} \quad \text{(NASH gels)} \end{aligned} \tag{23}$$

The remaining phases are suggested to be short ranged amorphous N-A-S-H gels with minor calcium addition based on the NMR results. The Ca, Si and Al contents within this gel can be easily calculated by using the overall Ca, Si and Al mole balance. Then the Equation (23) becomes as follows:

$$\begin{aligned} &C_{0.079}\cdot Si_{0.910}\cdot M_{0.036}\cdot A_{0.497} + Si_{0.064} \\ &\quad = Si_{0.308}\cdot A_{0.115} \\ &\quad + (M_5A_2)_{0.007} \\ &\quad + Si_{0.087} \\ &\quad + C_{0.079}\cdot Si_{0.426}\cdot A_{0.238} \\ &\quad + Si_{0.153}\cdot A_{0.111} \end{aligned} \tag{24}$$

Similarily, the phase composition before and after activation in mixtures with activator modulus of 1.6 and 2.4 are also calculated and shown below respectively:

$$\begin{aligned} &C_{0.079}\cdot Si_{0.910}\cdot M_{0.036}\cdot A_{0.497} + Si_{0.129} \\ &\quad = Si_{0.467}\cdot A_{0.171} \\ &\quad + (M_5A_2)_{0.007} \\ &\quad + Si_{0.019} \\ &\quad + C_{0.079}\cdot Si_{0.268}\cdot A_{0.100} \\ &\quad + Si_{0.285}\cdot A_{0.194} \end{aligned} \tag{25}$$

$$C_{0.079}\cdot Si_{0.910}\cdot M_{0.036}\cdot A_{0.497} + Si_{0.193}$$
$$= Si_{0.468}\cdot A_{0.167} + (M_5A_2)_{0.007} + Si_{0.024} + C_{0.079}\cdot Si_{0.210}\cdot A_{0.013} + Si_{0.401}\cdot A_{0.284} \quad (26)$$

The effect of activator modulus on the phase compositions of alkali activated fly ash before and after activation (mole %, in terms of the Ca-Si-Mg-Al) is briefly summarized in Figure 7-14.

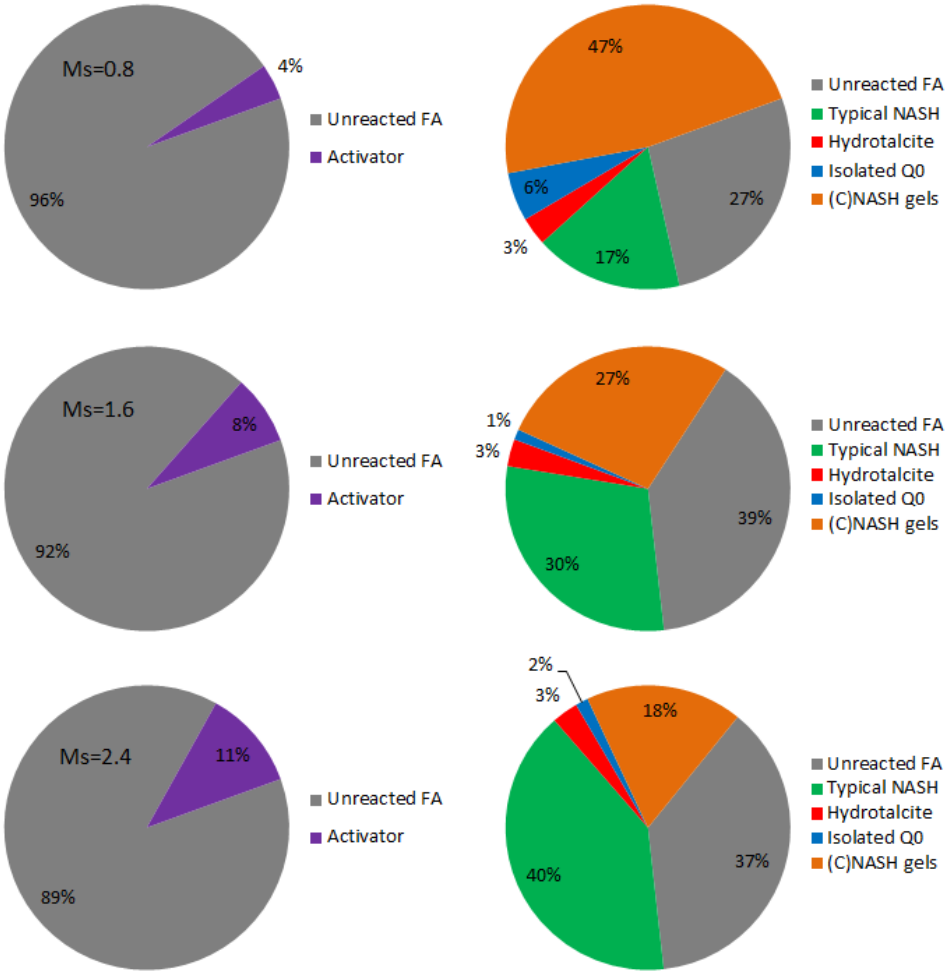

Figure 7-14: Ca-Si-Mg-Al based mole compositions before and after activation

It can be seen from the figure that although slag and fly ash show different chemical compositions, the silica from alkali activator shows a similar mole fraction among the overall Ca-Si-Mg-Al composition in both systems. After alkali activation, mixes with an activator modulus of 0.8 show a relatively high reaction degree of fly ash, and a higher content of Q^0, while those values remain similar in mixtures with higher moduli. In mixes with an activator modulus of 0.8, the amount of short ranged (C)-N-A-S-H gels and polymerized N-A-S-H gels (with Q^4 strucutres) accounts for 47% and 17% of the total moles of the phases after activation; when shifting the activator modulus to 1.6 and then 2.4, there is a significant reduction on the fraction of the short ranged (C)-N-A-S-H gels and an increase of polymerized N-A-S-H gels, indicating a phase transformation that is caused by the additional silicate from the activator. The increased activator modulus also results in a reduced Al content within the short ranged gels, and those reduced Al together with the additional silicate become parts of the polymerized N-A-S-H gels.

7.7.3 Alkali activated slag-fly ash blends

In the blended system, models regarding the phase compostion are also suggested based on the ^{29}Si MAS NMR results and the principles that are described in Section 7.7.1 and 7.7.2. Based on the deconvolution results that summarized in Table 7.6, the reaction products of alklai activated slag-fly ash blends contain unreacted raw materiasl (slag and fly ash), polymerized N-A-S-H gels (with Q^4 sturctures), isolated Q^0 and short ranged C-A-S-H gels (with Q^1 to Q^3 sturctures). Besides, hydrotalcite is regarded as the only Mg-contained phase. Thus the Ca-Si-Mg-Al related phase changes during the alkali activation can be written as follows:

$$\begin{aligned} &C_{a1}\cdot Si_{b1}\cdot M_{c1}\cdot A_{d1}\ \text{(Slag)} + C_{a2}\cdot Si_{b2}\cdot M_{c2}\cdot A_{d2}\ \text{(Fly ash)} + Si_n\ \text{(Activator)} \\ &\quad = C_{x1}\cdot Si_{y1}\cdot M_{z1}\cdot A_{t1} \quad \text{(Unreacted slag)} \\ &\quad + Si_{y2}\cdot A_{t2} \quad \text{(Unreacted fly ash)} \\ &\quad + (M_5A_2)_t \quad \text{(Hydrotalcite)} \\ &\quad + Si_{n1} \quad \text{(Isolated Q0)} \\ &\quad + Si_{y2}\cdot A_{t2} \quad \text{(NASH gels)} \\ &\quad + C_{x3}\cdot Si_{y3}\cdot A_{t1} \quad \text{(CASH gels)} \end{aligned} \tag{27}$$

Taking the mixtue of slag-fly ash with an activator modulus of 0.8 as an example, the initial composition (before activation) is based on 100g of slag plus 100g of fly ash. The composition of unreacted slag and fly ash can be determined by using the same methodology shown in Section 7.7.1 and Section 7.7.2, respectively. Then Equation (27) becomes:

$C_{0.668}\cdot Si_{0.574}\cdot M_{0.247}\cdot A_{0.260}$ (Slag) + $C_{0.079}\cdot Si_{0.910}\cdot M_{0.036}\cdot A_{0.479}$ (Fly ash) + $Si_{0.128}$ (Activator)

$$
\begin{aligned}
&= C_{0.354}\cdot Si_{0.304}\cdot M_{0.131}\cdot A_{0.138} && \text{(Unreacted slag)}\\
&+ Si_{0.244}\cdot A_{0.090} && \text{(Unreacted fly ash)}\\
&+ (M_5A_2)_t && \text{(Hydrotalcite)}\\
&+ Si_{n1} && \text{(Isolated Q0)}\\
&+ Si_{y2}\cdot A_{t2} && \text{(NASH gels)}\\
&+ C_{x3}\cdot Si_{y3}\cdot A_{t1} && \text{(CASH gels)}
\end{aligned}
\qquad (28)
$$

Besides, the amount of hydrotalcite can be calculated based on the amount of reated Mg, and the fraction of isolated Q^0 can be obtained directly from the ^{29}Si NMR analysis. As for the amount of NASH gels that with Q^4 structures, it can be calculated based on the deconvolution results shown in Table 7.6, and the rest reacted phases with Q^1 to Q^3 are regarded as amorphous C-A-S-H gels in general. Then Equation (28) becomes:

$C_{0.668}\cdot Si_{0.574}\cdot M_{0.247}\cdot A_{0.260}$ (Slag) + $C_{0.079}\cdot Si_{0.910}\cdot M_{0.036}\cdot A_{0.479}$ (Fly ash) + $Si_{0.128}$ (Activator)

$$
\begin{aligned}
&= C_{0.354}\cdot Si_{0.304}\cdot M_{0.131}\cdot A_{0.138} && \text{(Unreacted slag)}\\
&+ Si_{0.244}\cdot A_{0.090} && \text{(Unreacted fly ash)}\\
&+ (M_5A_2)_{0.030} && \text{(Hydrotalcite)}\\
&+ Si_{0.068} && \text{(Isolated Q0)}\\
&+ Si_{0.232}\cdot A_{0.176} && \text{(NASH gels)}\\
&+ C_{0.394}\cdot Si_{0.764}\cdot A_{0.274} && \text{(CASH gels)}
\end{aligned}
\qquad (29)
$$

The phase composition before and after activation in mixtures with activator modulus of 1.6 and 2.4 are also calculated usding the same method and shown below:

$C_{0.668}\cdot Si_{0.574}\cdot M_{0.247}\cdot A_{0.260}$ (Slag) + $C_{0.079}\cdot Si_{0.910}\cdot M_{0.036}\cdot A_{0.479}$ (Fly ash) + $Si_{0.258}$ (Activator)

$$
\begin{aligned}
&= C_{0.320}\cdot Si_{0.275}\cdot M_{0.118}\cdot A_{0.125} && \text{(Unreacted slag)}\\
&+ Si_{0.293}\cdot A_{0.109} && \text{(Unreacted fly ash)}\\
&+ (M_5A_2)_{0.033} && \text{(Hydrotalcite)}\\
&+ Si_{0.068} && \text{(Isolated Q0)}\\
&+ Si_{0.371}\cdot A_{0.299} && \text{(NASH gels)}\\
&+ C_{0.427}\cdot Si_{0.734}\cdot A_{0.141} && \text{(CASH gels)}
\end{aligned}
\qquad (30)
$$

$C_{0.668}\cdot Si_{0.574}\cdot M_{0.247}\cdot A_{0.260}$ (Slag) + $C_{0.079}\cdot Si_{0.910}\cdot M_{0.036}\cdot A_{0.479}$ (Fly ash) + $Si_{0.386}$ (Activator)

$$
\begin{aligned}
&= C_{0.403}\cdot Si_{0.346}\cdot M_{0.149}\cdot A_{0.157} && \text{(Unreacted slag)}\\
&+ Si_{0.304}\cdot A_{0.108} && \text{(Unreacted fly ash)}\\
&+ (M_5A_2)_{0.027} && \text{(Hydrotalcite)}\\
&+ Si_{0.055} && \text{(Isolated Q0)}\\
&+ Si_{0.452}\cdot A_{0.377} && \text{(NASH gels)}\\
&+ C_{0.380}\cdot Si_{0.608}\cdot A_{0.086} && \text{(CASH gels)}
\end{aligned}
\qquad (31)
$$

The structure of the amorphous C-A-S-H gels that are mentioned in Equation (29) to (31) is complex and difficult to distinguish in detail, since it is a combination of the C-A-S-H gels from alklai activated slag and the short ranged N-A-S-H gels from racted fly ash, and with gel interactions between those two. In order to evaluate the interactions between slag and fly ash during activation, the gel composition of alkali activated slag-fly ash blends is compared to the physically mixed alkali activated slag and alkali activated fly ash. In the physically mixed samples, the C-A-S-H gels from slag and the short ranged N-A-S-H gels are also computed together as amorphous C-A-S-H gels in general. When comparing the amorphous C-A-S-H gels alone, it is assumed that the Ca, Si and Al favor the formation of the typical C-A-S-H gel that is usually formed in alkali activated slag, which has a typical long term Ca/Si ratio of 1.0 and Al/Si ratio of 0.2 (Wang and Scrivener, 2003), then the remaining Ca, Si and Al interact with the typical C-A-S-H gels to form amorphous C-A-S-H gels with more complicated gel structures. It should be mentioned that this assumption may not exactly fit the real situation, but will bring convenience in studying the gel interactions. Then a comparision of the composition of the amorphous C-A-S-H gels between alkali activated slag-fly ash blends and alkali activated slag + alkali activated fly ash is listed in Table 7-8. A comparison of the overall reaction products is shown in Figure 7-15.

It can be seen from Figure 7-15 that compared to the physically mixed slag and fly ash, the slag-fly ash blends show a reduced reaction degree of slag, and an increased reaction degree of fly ash, owing to the effect of blended binder. The reduced reaction degree of slag results in a reduced content of the typical C-A-S-H gels, which can be partly assigned to the decreased amount of available calcium. Similarly, the increased reaction degree of fly ash leads to an increased supply of available Si and Al groups, which can be further linked to the increased fraction of the polymerized N-A-S-H gels. Besides, the content of isolated Q^0 and hydrotalcite remains stable or slightly reduced, indicating the slight and limited effect of blended binder on their mole fraction.

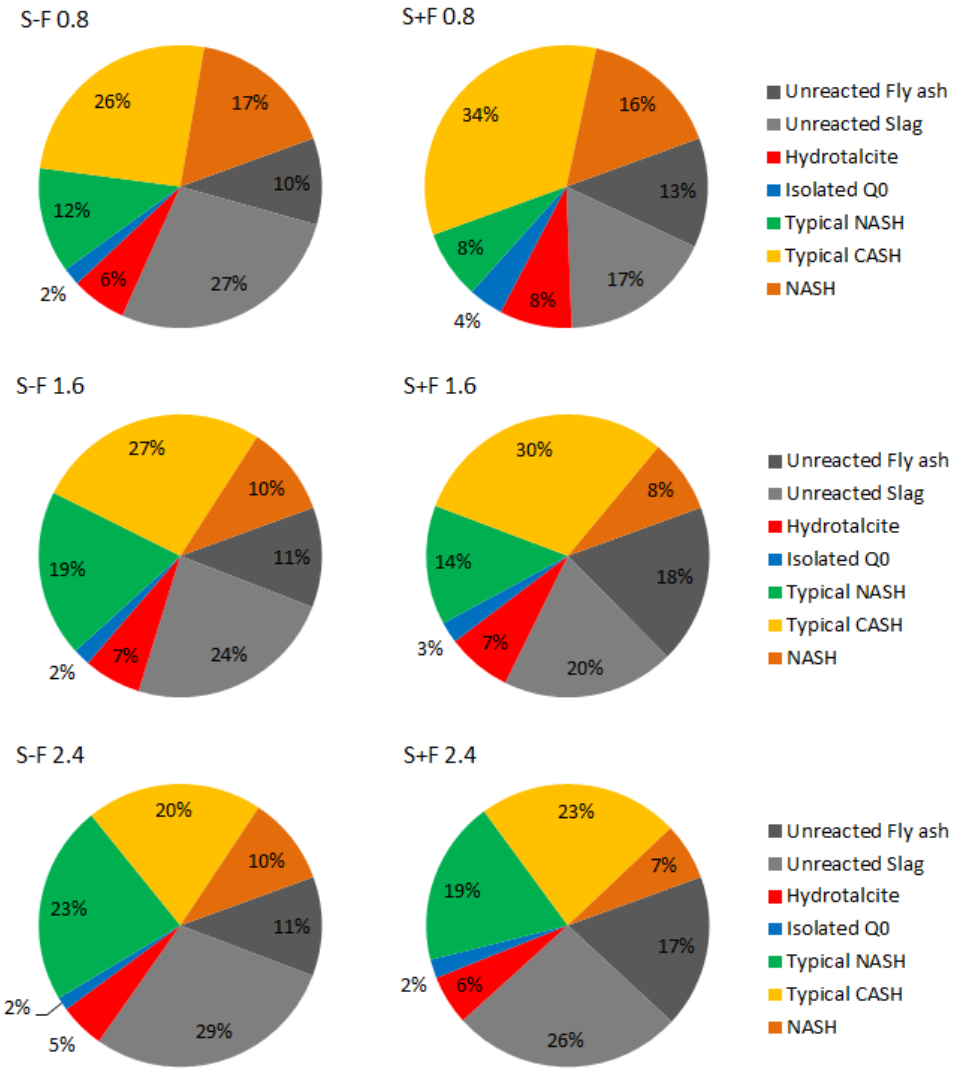

Figure 7-15: Comparison of the phase compositions

Based on the results shown in Figure 7-15 and Table 7-7, it is suggested that the gel interaction in the blended alkali system, on the one hand shows an effect on the content of polymerized N-A-S-H gels, and on the other hand influences the composition of the amorphous C-A-S-H gels. The content of amorphous C-A-S-H gels in slag-fly ash blends is very similar to the case of slag + fly ash mixes, except the mixtures with activator modulus of 0.8, which is 7% lower. While concerning their chemical compositions that are shown in Table 7-8, compared to the C-

A-S-H gels that typically formed in alkali activated slag, additional Si and Al groups are incorporated. The amount of additionally involved Si, Al groups in slag-fly ash blends is slightly higher than that in slag + fly ash mixes; and regarding these additional Si-Al sites, a higher Si/Al ratio is shown slag-fly ash blends than that in slag + fly ash mixes, resulting in a more silicate enriched gel with a higher total Si/Al ratio.

Table 7-7: Comparision on the amorphous C-A-S-H compositions (mole)

	Slag-fly ash blends		Slag + fly ash	
	CASH	NASH	CASH	NASH
Ms=0.8	C: 0.394 S: 0.394 A: 0.079	S: 0.370 A: 0.196	C: 0.522 S: 0.522 A: 0.104	S: 0.302 A: 0.241
Ms=1.6	C: 0.427 S: 0.427 A: 0.085	S: 0.307 A: 0.055	C: 0.483 S: 0.483 A: 0.097	S: 0.195 A: 0.101
Ms=2.4	C: 0.344 S: 0.344 A: 0.044	S: 0.368 A: 0.000	C: 0.380 S: 0.380 A: 0.076	S: 0.227 A: 0.010

7.8 Conclusions

This chapter investigates the reaction degree of alkali activated slag, fly ash and slag-fly ash composites with different activator moduli. The reaction degree is identified by applying selective dissolution and ^{29}Si MAS NMR spectra deconvolutions. ^{27}Al MAS NMR is also applied as a supplement to understand the gel structure. Models concerning the gel formation under different activator and precursor conditions are proposed. The combined application of these two methods brings a new approach in identifying the reactivity of the starting materials and characterizing the reaction products. The following conclusions can be drawn based on the results:

- For alkali activated slag, increasing the activator modulus reduces the slag reactivity from about 66% to 45%, with the reduced content of Q^2(1Al) groups and increased content of Q^3(1Al) sites. Hydrotalcite type phases are observed, and increasing the activator modulus reduces the relative content of Al(VI) within the reaction products.
- The unreacted fly ash and reaction products are separated by selective dissolution, which are then analysed by ^{29}Si, ^{27}Al MAS NMR, and XRF. Increasing the activator modulus results in an increased content of Q4 groups, while reduced reaction degree of fly ash. Both polymerized Q^4 structures and short ranged Q^2 to Q^0 sites are formed. The

contributions of unreacted ash and reaction products to a certain silica structure are identified.

- In the blended binder system, the slag reactivity is reduced while the reaction degree of fly ash is increased. Both C-A-S-H and N-A-S-H type gels are identified within the reaction products. The $Q^4(4Al)$ groups consist more than half of the newly formed Q^4 structures.
- Compared to the mixture of alkali activated slag and alkali activated fly ash with the same chemical composition, the blended binder exhibits higher contents of newly formed Q^4 groups with reduced Si to Al ratios, and reduced content of Q^0 groups, showing an gel interaction when blended binders is applied.
- The proposed model of gel formation based on the NMR results quantifies the Ca-Si-Mg-Al related phase compositions within the reaction products, which provides further insights on understanding the microstructure of alkali activated slag, fly ash and their blends.

Chapter 8

Mix design and applications

8.1 Mix design based on a particle packing model

8.1.1 Introduction

It is commonly accepted that an optimal packing of granular ingredients is the key for achieving excellent mechanical strength and durable structures (Husken and Brouwers, 2008; Hunger et al, 2009), and several mix design methods have been proposed in cement based system such as the Linear Packing Density Model, Solid Suspension Model and Compressive Packing Model (Larrard and Sedran, 2002; Fennis et al, 2009). Among those design methodologies, the modified Andreasen & Andersen particle packing model, which is based on the integral particle size distribution approach of continuously graded mixes (Andreasen and Andersen, 1930), shows conveniences by considering fine particles into the design process. While presently, when designing the recipes of alkali activated blended mortars and concretes, key manufacturing parameters from the aspects of activator and raw material are the main concerns, while to the authors' knowledge limited attention has been paid to the packing of the granular ingredients. It is possible that by giving additional consideration to the particle packing in the mix design stage, the binders in alkali activated system will be used in a more efficient manner, while certain fresh and hardened properties may also improve as a result.

Another important issue of alkali activated materials is the shrinkage, since it is well linked to the cracking tendency and consequently the durability related properties. The previous investigations revealed that the alkali activated high calcium system usually exhibits a higher degree of drying shrinkage than the cement based system (Collins and Sanjayan, 2000; Melo et al, 2008), while the alkali low calcium systems can show a lower value than OPC (Ma and Ye, 2015). It was also concluded the activator type and content, the physicochemical properties of the raw material and curing conditions are the key factors that affect the shrinkage behaviors (Shi, 1996; Fernandez et al, 2006). However, there still exists very limited study about the relationships between key synthesizing factors and the shrinkage in alkali activated blended systems. The objective of this work is to design the room temperature cured alkali activated slag-fly ash blended mortars by applying the modified Andreasen & Andersen particle packing model; while to perform a general evaluation on the effects of key synthesizing factors on the fresh behaviors, gel structure development, porosity, compressive strength and drying shrinkage.

8.1.2 Mix design methodology

The mixes of the alkali activated composites were designed following a mathematical model in order to achieve the optimized packing of the granular solid materials. Theoretically, a minimal porosity can be achieved by an optimal particle size distribution of all solid materials, as shown in Eq. (1):

$$P(D) = (\frac{D}{D_{\max}})^q \tag{1}$$

Based on this packing theory, a new model, so called the modified Andreasen and Andersen (A&A) model, was proposed by taking into account of the minimal particle size (Funk and Dinger, 1994), as shown:

$$P(D) = \frac{D^q - D_{\min}^q}{D_{\max}^q - D_{\min}^q} \tag{2}$$

Where P(D) is a fraction of the total solids materials that are smaller than the particle size D (μm), D_{max} is the maximum particle size (μm), D_{min} is the minimum particle size (μm) and q is the distribution modulus.

This modified Andreasen and Andersen (A&A) model was firstly applied in the design of concrete products by (Brouwers and Radix, 2005). Afterwards it was also successfully used in the optimization algorithms of self-compacting concrete (Hunger, 2010), zero-slump concrete (Husken, 2010), lightweight concrete (Yu et al, 2013) and nano-silica modified concrete (Quercia, 2014). In the present study, it is applied as a target function for the subsequent granular optimization of the individual solid materials.

The distribution modulus (q) in the model is fixed at 0.23 based on the previous experiences (Brouwers and Radix, 2005; Yu et al, 2012). By using an optimization algorithm based on the Least Squares Method (LSM), the proportions of each individual material in the mix are adjusted until an optimum fit between the composed mix grading curve and the target curve is reached (Hunger et al, 2009), namely minimized sum of the squares of the residuals (RSS) at defined particle sizes.

$$RSS = \sum_{i=1}^{n} (P_{mix}(D_i^{i+1}) - P_{tar}(D_i^{i+1}))^2 \tag{3}$$

Where P_{mix} is the composed mix, and the P_{tar} is the target grading calculated from Eq. (2). Then the optimized mixture is expected to possess a compact matrix because of the optimal packing.

It should be noted that this mix design methodology is based on the volumetric fractions of all used materials, including both solids and liquids. In Portland cement system, the liquid component is primarily water; while in the case of alkali activated system, the liquid (activator) consists of water, dissolved NaOH and sodium silicates. Based on the fact that both NaOH and the silicates in waterglass are well dissolved in the activator solution, their effect on the solids' packing is not taken into account here; while the densities of the liquid activator are calculated based on each individual mix and applied in the packing model.

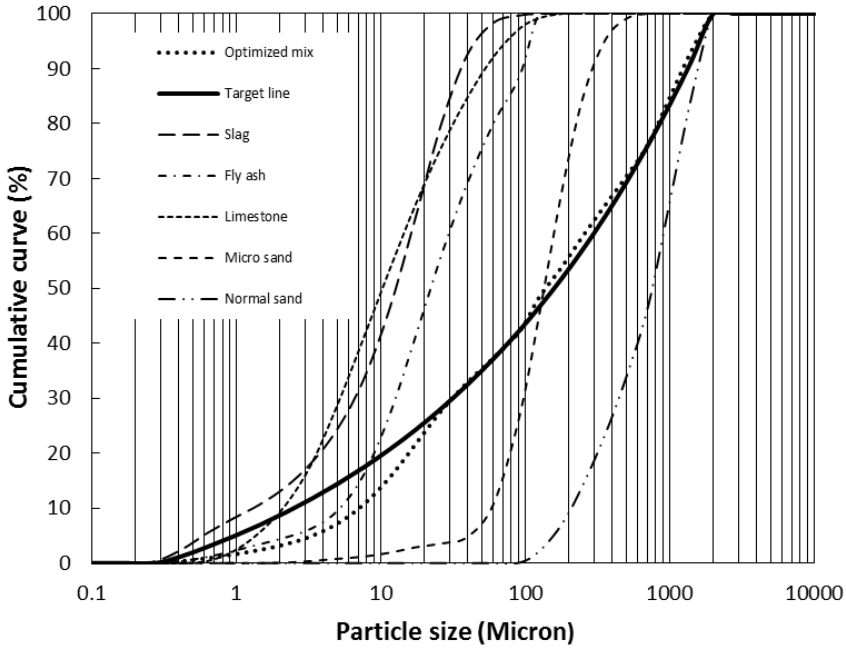

Figure 8.1-1: Particle size distributions of the raw materials, the target curve and the resulting integral grading line of a sample mix.

Concerning the mix proportions, the activator used in this study has an equivalent sodium oxide (Na_2O) content of 5% by mass of the powder and activator moduli of 1.0, 1.4 and 1.8. Besides the slag and fly ash, limestone powder was used as filler while a micro sand (0-1 mm) and a normal sand (0-2 mm) were used as fine aggregates. Slag/fly ash ratios of 80/20, 60/40 and 40/60 by mass were used and the water/powder ratio was kept constant as 0.4 in all mixtures. An example of the detailed mix designs based on the modified Andreasen & Andersen particle packing model is shown in Figure 8.1-1, and the detailed mix proportions of the used materials are listed in Table 8.1-1.

Table 8.1-1: Mix proportions of alkali-activated slag-fly ash composites (kg/m^3)

Mix	Activator	Slag	Fly ash	Limestone	Sand 0-1	Sand 0-2
M1-820	368.5	463.7	115.9	144.9	271.7	815.1
M2-824	379.8	461.9	115.5	144.3	270.6	811.9
M3-828	390.9	460.1	115.0	143.8	269.6	808.7
M4-640	364.4	343.9	229.3	143.3	268.7	806.1
M5-644	375.6	342.6	228.4	142.7	267.7	802.9
M6-648	386.7	341.3	227.5	142.2	266.6	799.9
M7-460	360.4	226.8	340.2	141.7	265.8	797.3
M8-464	371.5	225.9	338.9	141.2	264.7	794.2
M9-468	382.5	225.1	337.6	140.7	263.7	791.2

8.1.3 Fresh behaviors

The slump flows of the fresh alkali activated slag-fly ash mortars are presented in Figure 8.1-2. All slump flow values are measured after 4 mins' mixing. It can be seen that the activator modulus exhibits a more significant effect on the slump flow than slag/fly ash ratio in general. For instance, in samples with a constant activator modulus of 1.0, the slump flow increases from 16.4 to 18.7 cm when shifting the slag/fly ash ratio from 80/20 to 40/60. Similar results are also shown in mixes with other activator moduli. This can be simply explained by the different water demand between slag and fly ash that is caused by their morphology differences, where slag usually presents a more angular particle shape and larger surface area. On the other hand, compared to the effect of slag/fly ash ratio, a higher range of flowability is shown in samples with a different activator modulus. For a fixed slag/fly ash ratio of 80/20, when increasing the activator modulus from 1.0 to 1.4 and then 1.8, the slump flow is increased from 16.4 cm to 23.6 cm and 26.5 cm; the increase rate is 43.9% and 61.6%.

Dramatic increases in slump flow are also found in samples with other slag/fly ash ratios. One possible explanation for the higher influence of the activator modulus on flowability is that the additional provided silicate from activator benefits the workability due to the nature of the silicate groups, since higher activator modulus means a higher proportion of sodium silicate in the activator solution. In addition, compared to (Gao et al, 2005), similar flowability is achieved in this study while a lower water binder ratio is used. It is suggested that more available water can be provided to lubricate the particles by applying the packing model, this is

also confirmed by (Yu et al, 2011). This is especially important in the case of alkali activated systems, where no effective superplasticizers are available and limited solution leads to a poor workability. Activator with lower modulus usually exhibits a more intensive reaction at early stages; then it is also possible that a faster dissolution of the raw materials increases the viscosity of the fresh mortars and results in a reduced slump flow.

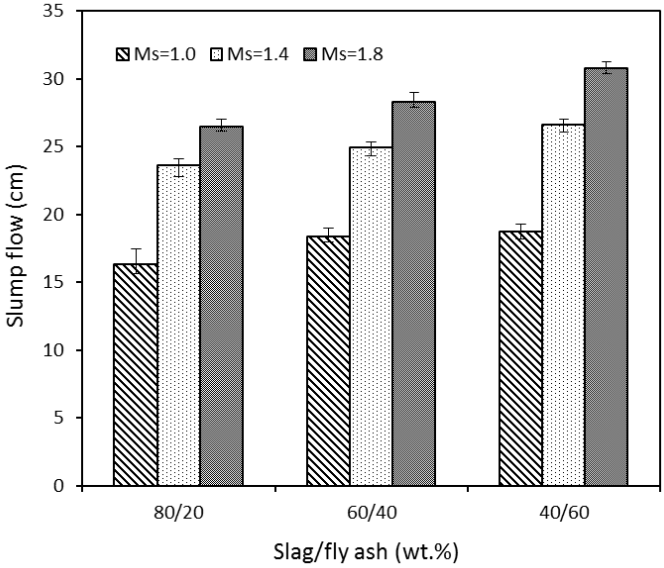

Figure 8.1-2: Slump flow of AA slag-fly ash mortars

Figure 8.1-3 depicts the initial and final setting times of alkali activated slag-fly pastes. It is clear that both slag/fly ash ratio and activator modulus have a significant effect on the setting times; samples with a lower activator modulus and a higher slag content exhibit faster initial and final setting times in general. For instance, when a constant activator modulus of 1.0 is used, the sample with a slag/fly ash ratio of 80/20 shows an initial/final setting time of 10/46 mins, whereas 48/84 mins in the sample with a slag/fly ash ratio of 40/60. A similar remarkable increment is also observed in samples with other fixed activator moduli when lowering the slag content in the mixture. This can be explained by the higher reactivity of slag than fly ash under ambient temperature. The amorphous structure of slag, with enriched network-modifying cations (primarily Ca), is easier to dissolve than the aluminosilicates dominated structure of fly ash under alkali conditions. Thus as a result of the faster dissolution rate of Ca, Si and Al groups from the precursors, a faster reaction process and a shorter setting time followed. Similar to the effect of the slag/fly ash ratio, dramatic increases of setting times are shown when the activator modulus is increased. For a constant slag/fly ash ratio of 60/40, the initial/final setting time increases from 29/69 mins to 60/110 mins when shifting the activator modulus from 1.0 to 1.8, the increasing rate is 107% and 59.4% for the initial and final setting

time, respectively. The corresponding increasing rate in samples with a slag/fly ash ratio of 40/60 is 73.9% and 59.3%, respectively. Such significant changes in the setting times indicate that the activator modulus may strongly affect the early age reaction kinetics. In overall, both of the discussed manufacturing factors strongly affect the fresh behaviors of alkali activated slag-fly ash blends; and a large variation in slump flow and setting time can be caused. Thus when designing the mix proportions of this type of material, attention should be firstly paid to the effect of the key synthesizing factors on the fresh behavior.

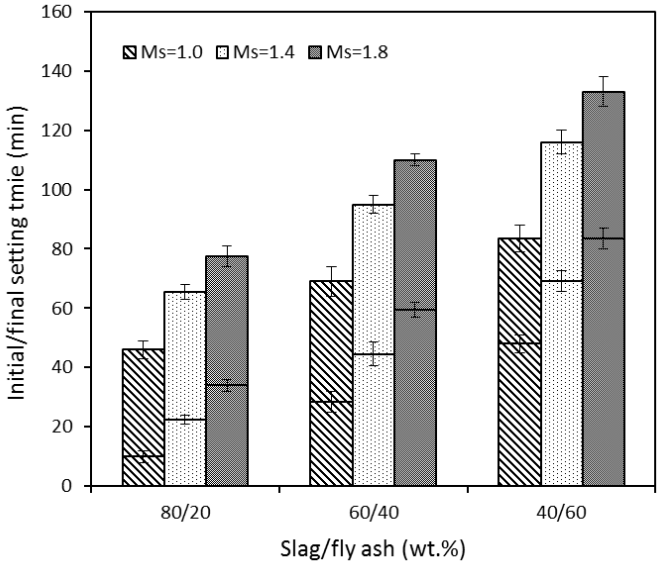

Figure 8.1-3: Setting time of AA slag-fly ash pastes

8.1.4 FTIR

Figure 8.1-4 presents the infrared spectra of alkali activated slag-fly ash pastes, at 1 and 28 days, respectively. Four mixtures with relatively remarkable differences in slag/fly ash ratios (8/2 and 4/6) and activator modulus (1.0 and 1.8) were chosen. Samples are labelled by the combination of slag/fly ash ratio, activator modulus and curing age, for instance “820-1” in represents the mixes with a slag/fly ash ratio of 8/2 and activator modulus of 1.0, after 1 d of curing.

After one day of activation, as can be seen from Figure 8.1-4 (a), all samples exhibit a main absorption band at similar locations that lies around 940 cm^{-1}, which is assigned to the asymmetric stretching vibration of the non-bridging Si-O bonds. Besides, it also shows that the gel structure of alkali activated slag-fly ash blends is relatively stable regardless of the activator parameters and raw material composition. Samples with higher slag content (80% by mass) present a more significant absorption band at around 640 cm^{-1}, which is associated with the

formation vibration of TO_4 groups (where T represents Si or Al). It is more likely that this band is shifted from 670 cm^{-1} (in the unreacted slag) and indicates that structural changes have also occurred to the tetrahedral T-O groups during alkali activation. The vibration bands at 1640 cm^{-1} in all mixes manifest the presence of bound water within the reaction products.

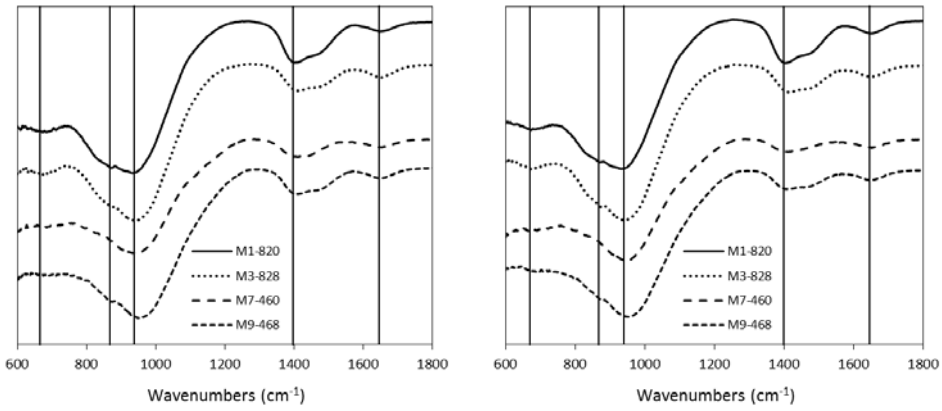

(a) (b)

Figure 8.1-4: FTIR spectra of AA slag-fly ash blends at 1 d (a) and 28 d (b)

Although all samples exhibit the same type of main reaction product (chain structured C-A-S-H type gels), slight differences in the location of the main absorption peaks are still observed within a subtle scale. As can be noticed, for samples with a slag/fly ash ratio of 80/20, the location of the main absorption band is almost fixed at around 940 cm^{-1}, the changes in the applied activator modulus does not lead to a significant shift of the band location; while in mixtures with a slag/fly ash ratio of 40/60, the main absorption band slightly shifts to higher wavenumbers, implying that the reaction products in those mixes have a relatively high polymerization degree. It is more likely that the shifted band location is due to the increased fly ash content, since the activator modulus in this case also shows a negligible effect. Concerning the gel structure development, no significant structural changes were observed during the age of 1 and 28 d, which manifested that the main reaction process may have already finished after 1 d of curing. It should be noted that until the curing age of 28 d, samples with a slag/fly ash ratio of 40/60 still exhibit a higher wavenumber of the main absorption peak, indicating that slight but detectable gel structure differences may remain in the long term.

8.1.5 TG

Figure 8.1-5 (a to d) depicts the thermogravimetric results of pastes with different slag/fly ash ratios (80/20 and 40/60) and activator moduli (1.0 and 1.8) at the age of 1, 7 and 28 days, respectively. Samples are labelled following the same rule as the ones in FTIR analysis. It is

clear that a significant mass loss before around 110 °C is shown in all mixes; due to the loss of physically bound water. All mixtures exhibit similar evaporable water content at the same curing age. Regardless of the manufacturing parameters and curing age, all samples present a negligible mass loss between around 105 °C and 150 °C, followed by a gradual decrease until heated to around 700 °C. Between around 700 °C and 1000 °C, only a very slight and moderate mass loss is shown in general.

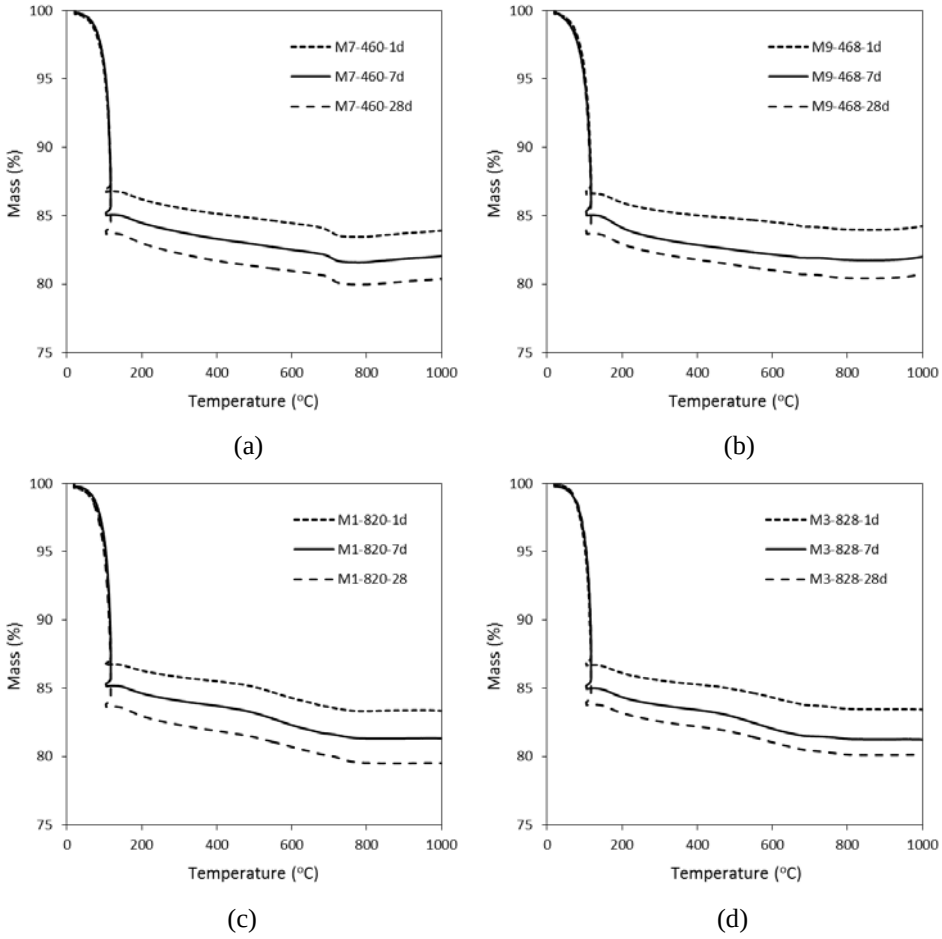

Figure 8.1-5: TG analyses of AA slag-fly ash blends at 1, 7 and 28 d

For samples with a slag/fly ash ratio of 40/60 and an activator modulus of 1.0, as shown in Figure 8.1-5 (a), the mass loss between around 105 °C and 1000 °C shows a small increment as a function of time, which increases from 2.9% to 3.3% between 1 and 28 d. It should be noted that the mass loss within this temperature range is not only due to the loss of chemically bound water from decomposed gels; the decomposition of the carbonates also plays a role. This

is confirmed by the relatively remarkable mass loss between 600 °C and 800 °C, and the presence of carbonates observed in the FTIR results in this study. The calculated mass loss in this temperature range (600 to 800 °C) is approximately 1.0%, and it does not obviously change with the increase of the curing time. When increasing the activator modulus to 1.8, as shown in Figure 8.1-5 (b), the mass loss between 600 °C and 800 °C tend to be moderate. It could be an indication that the samples with relatively low activator modulus may exhibit a higher tendency towards carbonation.

Besides, the total mass loss between 105 °C and 1000 °C is 2.3%, 3.0% and 3.0% at 1, 7 and 28 d, respectively. The slightly increased chemically bound water content after 1 d of curing suggests that the main reaction process may have already completed within the first day of curing, and the reaction at later ages present detectable but limited contribution. Previous researches on the early age reaction kinetics of silicate activated slag-fly ash blends also confirmed the completion of the main reactions during the first few hours (Chithiraputhiran and Neithalath, 2013; Gao et al, 2015). Combined with the FTIR results, it is reasonable to conclude that the slightly increased chemically bound water after 1 d is mainly attributed to the continuous formation of reaction products in a small scale, rather than generating new phases.

For a constant activator modulus, samples with higher slag contents (e.g. slag/fly ash ratio of 80/20), as presented in (c) and (d), exhibit a higher mass loss between 105 °C and 1000 °C in general. For instance, the calculated chemically bound water content in (c) is 3.4%, 3.9% and 4.2% at 1, 7 and 28 d, respectively; which is slightly higher at each curing age compared with the ones shown in (a). Additionally, for a fixed slag/fly ash ratio, a slightly increased mass loss between 105 °C and 1000 °C was also observed when lowering the activator modulus, it may imply that a relatively high amount of sodium hydroxide in the activator (sodium hydroxide modified sodium silicate) exhibits a better activation effect. However, further investigation is still needed in order to understand the relations between the key manufacturing parameters and certain macro performances.

8.1.6 Compressive strength

The 7 and 28 d compressive strength of mortars with different activator moduli and slag/fly ash ratios are depicted in Figure 8.1-6. Generally speaking, the samples exhibit compressive strengths that range from 52.8 MPa to 68.4 MPa at 7 d, and 67.4 MPa to 86.4 MPa after 28 d of curing. Similar strength levels are also reported by (Ng and Foster, 2013), in which case particle packing model was applied in the alkali activated slag-fly ash based composites. Besides, samples with higher slag contents show a relatively high strength and a medium activator modulus of 1.4 presents the optimum compressive strength in every case. Specifically, for mixes with a slag/fly ash ratio of 80/20, the 7 d strength is 61.8 MPa with an activator modulus of 1.0, and it increases to 68.4 MPa when increasing the activator modulus to 1.4, a further increase of the modulus to 1.8 leads to a reduction of strength to 65.3 MPa. Similar tendency is also shown at 28 d, samples with an activator modulus of 1.4 exhibits the highest

strength of 86.4 MPa; while both mixes with lower or higher activator moduli show a lower compressive strength: 79.5 MPa and 82.6 MPa, respectively.

However, it seems that the strength development is not well related to the activator modulus, since the strength increasing rate between 7 and 28 d is 28.6%, 26.3% and 26.5% for samples with activator modulus of 1.0, 1.4 and 1.8, respectively. The presence of the optimal activator modulus implies that within the parameter ranges in this study, both too high or too low activator moduli may present a negative influence on strength. One possible explanation is that compared to the samples with a higher modulus, mixes with an activator modulus of 1.0 exhibit a significantly lower slump flow, and the poor workability presents a less effective dispersion of the raw materials in the fresh mix, then a slightly lower strength is consequently shown. In addition, the extra silicates that are provided by the activator also participate in the reaction process, and reaction products with different silicate contents are resulting. It indicates a critical additional silicate content, which will exhibit a relatively high strength. Besides the highest strength in each case, there is no remarkable strength difference between samples with activator moduli of 1.0 and 1.8, implying that the effect of activator modulus on strength is non-negligible but limited.

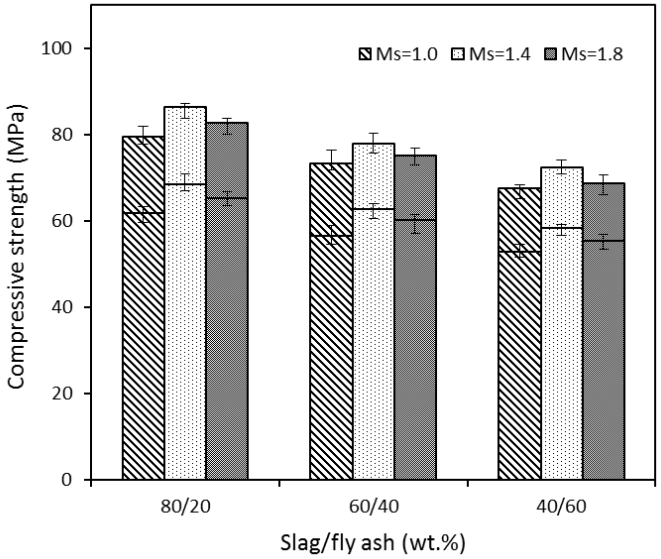

Figure 8.1-6: 7 and 28 d compressive strength of AA slag-fly ash mortars

Concerning the effect of raw materials' composition, there is a gradual decrease in compressive strength when lowering the slag/fly ash ratio. As shown in Figure 8.1-6 that for a constant activator modulus of 1.4, the 7 d compressive strength for mixes with slag/fly ash ratio of 80/20 is 68.4 MPa, which slightly decreases to 62.6 MPa and 58.4 MPa when lowering the slag content to 60% and 40%, respectively. The corresponding 28 d strength also decreases from

86.4 MPa to 77.8 MPa and 72.3 MPa, respectively. The positive influence of the slag content on compressive strength has been frequently reported in the previous studies. In addition, the strength variations caused by the raw materials' composition are larger than the activator modulus, indicating its relatively high dominant role in determining the mechanical properties. It should be emphasized that the mechanical property of alkali activated materials is particularly sensitive to the key manufacturing parameters such as activator type and dosage, raw materials' composition and origin, water to binder ratio and curing conditions. Thus due to the large variation of those mentioned factors, it is difficult to make effective comparison within the available literatures. However, equivalent or higher compressive strengths are achieved in general when compared to other alkali activated slag-fly ash blends (Rashad, 2013; Islam et al, 2014; Puertas et al, 2000). It is also clear that samples with large amounts of fly ash content in this case also exhibit excellent compressive strengths for relevant applications, for instance in samples with a slag/fly ash ratio of 40/60, the 7 d strength ranges from 52.8 MPa to 58.4 MPa while the 28 d strengths are between 67.4 MPa and 72.3 MPa. Besides, in the present study the system is investigated on the mortar level with the maximum aggregate size of 2 mm; it can be predicted that the effect of particle packing can be more prominent when larger aggregate sizes and wider particle size distributions are used.

8.1.7 Water permeable porosity

The 7 and 28 d water permeable porosities of mortar samples with slag/fly ash ratios of 80/20 and 40/60 are shown in Figure 8.1-7. It is clear that the mixtures with a lower slag content exhibit a higher porosity, and the porosity slightly decreases with the increase of the activator modulus. For mixes with an activator modulus of 1.0, the porosity is 21.4% at 7 d for samples with a slag/fly ash ratio of 80/20, while it increases to 23.6% when shifting the slag/fly ash ratio to 40/60. Similarly, when reducing the slag content from 80% to 40%, the porosity at 7 d is increased by 10.2% and 10.0% in samples with an activator modulus of 1.4 and 1.8, respectively. Depending on the different application levels, a balance between the setting times, slump flow, compressive strength and the costs can be achieved by the incorporation of fly ash; as can be seen that desirable strengths with other similar properties are shown in samples with high fly ash contents. It should be noted that relatively high porosities of alkali activated materials are also reported in other previous researches (Ma, 2013; Balczar et al, 2015; Ko et al, 2015), this is probably due to the relatively high physically bound water content of this type of material by nature. Between the curing age of 7 d and 28 d, a slight decrease of porosity is observed in all mixes. For samples with a slag/fly ash ratio of 40/60 and an activator modulus of 1.0, the water permeable porosity is 23.6% after 7 d of curing, and it reduces to 22.8% at 28 d.

The porosity also decreased by 3.5% and 3.2% in samples with an activator modulus of 1.4 and 1.8, respectively. The slight decrease of porosity is probably attributed to the formation of reaction products at a small scale at later ages, since the slight increase in bound water is found

in the thermogravimetric analysis in this study and the strength development can also be an indication. Additionally, it can be observed that there is a gradual reduction of porosity when increasing the activator modulus from 1.0 to 1.8. For instance, in samples with a slag/fly ash ratio of 80/20, the porosity at 7 d is 21.4%, 20.6% and 20.1% for mixes with activator modulus of 1.0, 1.4 and 1.8, respectively; and these values are 20.7%, 19.8% and 19.4% at the age of 28 d. It can be seen that the porosity results are not well related to the ones from compressive strength, where an optimum activator modulus is shown. It demonstrates that the porosity is not the only indication of the compressive strength in this case. When concerning the porosity alone, an increase of the activator modulus within a reasonable range (from 1.0 to 1.8 in this case) may always refine the pore structure due to the increased additional silicate groups.

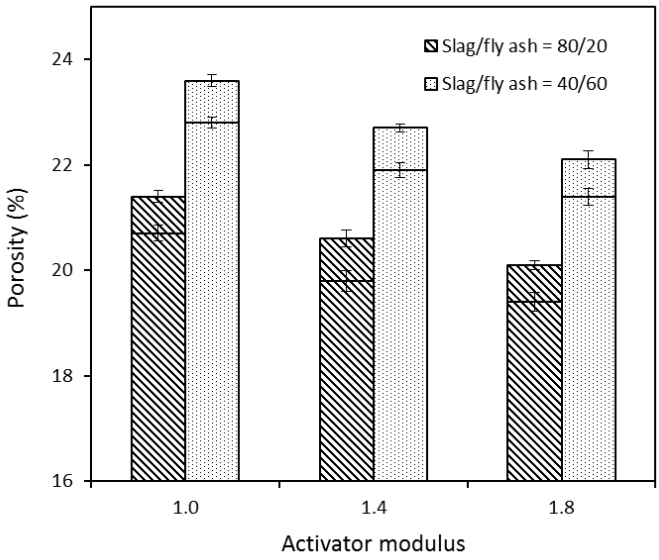

Figure 8.1-7: 7 and 28 d porosity of AA slag-fly ash mortars

8.1.8 Drying shrinkage

The drying shrinkage of samples with slag/fly ash ratios of 80/20 and 40/60 are presented in Figure 8.1-8. It can be seen that all mixes exhibit an obvious length change over time, and the drying shrinkage is strongly affected by the raw materials' composition and the activator modulus. It is commonly known that the drying shrinkage is caused by the evaporation of free water from the pores of the hardened mortar, and a higher drying shrinkage is usually shown when compared to the ordinary Portland cement. The TG results in this study may partly explain this phenomenon since all mixes present a relatively high proportion of physically bound water. As shown in Figure 8.1-8, samples with a lower slag content and a lower activator modulus show a lower drying shrinkage in general. For example, with a constant

slag/fly ash ratio of 80/20, the length change at the age of 28 d is around -3364 × 10^{-6} for mixes with an activator modulus of 1.0, while this value increases to -3996 × 10^{-6} and -4864 × 10^{-6} when increasing the activator modulus to 1.4 and 1.8, respectively. Similarly, when shifting the activator modulus from 1.0 to 1.8, the length change is increased by 29.1% and 71.3% in samples with a slag/fly ash ratio of 40/60 at 28 d. Thus it is clear that a significant increase of drying shrinkage will result when increasing the activator modulus. This is in agreement with the previous study on the drying shrinkage of alkali activated slag-fly ash blends that the higher extra silicate content from the activator is, the higher drying shrinkage is (Ma and Ye, 2015). Based on the results of the porosity test in this study, it seems that the refined pore structure caused by the increased additional silicate content (increased activator modulus) may be linked to the shrinkage behaviours due to the self-desiccation. In addition, the result also implies that using activators with a lower modulus can effectively reduce the drying shrinkage to some extent.

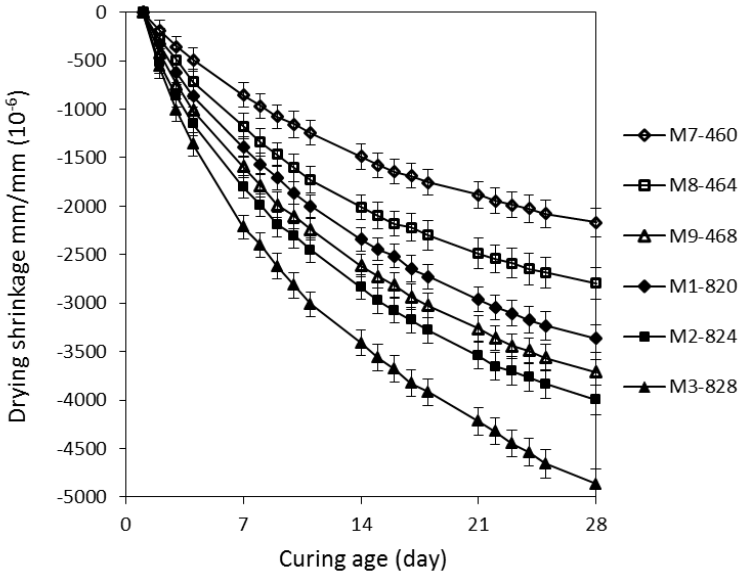

Figure 8.1-8: Drying shrinkage of AA slag-fly ash mortars

A significant reduction of drying shrinkage is presented when a lower slag content is used in the slag-fly ash blends. It can be seen that with a constant activator modulus, taking 1.4 as an example, the 28 d length change is -3996 × 10^{-6} for mixtures with a slag/fly ash ratio of 80/20; while it decreases to -2797 × 10^{-6} (by nearly 30.0%) when lowering the slag/fly ratio to 40/60, suggesting that replacing slag by fly ash is an ideal approach to reduce the dry shrinkage. This result is in accordance with the previous investigations that reducing the slag content in the slag-fly ash blends will lead to a decrease of drying shrinkage (Chi and Huang, 2013; Lee et al, 2014). As shown in the FTIR analysis of this study, the main reaction product in the alkali

activated slag-fly ash blends is a C-A-S-H type gel, which is similar to the one in alkali activated pure slag. It is possible that the typical C-A-S-H gels with low Ca/Si ratio exhibit a high tendency of shrinkage by nature, and the addition of fly ash may modify this characteristic. In overall, both the incorporation of fly ash into slag and lowering the silicate content from activator are efficient methods of reducing the shrinkage.

8.1.9 Conclusions

This section addresses the properties of alkali activated slag-fly ash mortars that are designed by using the modified Andreasen and Andersen packing model. Furthermore, the effects of two key manufacturing factors (slag/fly ash ratio and activator modulus) on slump flow, setting times, gel structure development, compressive strength, porosity and drying shrinkage are analysed. Based on the results, the following conclusions can be drawn:

- A large range of slump flow (from 16.4 to 30.8 cm) and setting time (from 10/46 to 84/133 mins) can be caused by both slag/fly ash ratio and activator modulus. Increasing the fly ash content in the slag-fly ash mix leads to an increased slump flow and prolonged initial/final setting time; while an increase of the activator modulus results in an increased flowability and delayed setting times. The activator modulus exhibits a more considerable effect on the fresh behaviours than the raw materials' composition.
- Gel structure development shows that the main reaction product is a C-A-S-H type gel, and it remains stable after 1 d of curing regardless of the key synthesizing factors in general. But samples with high fly ash contents show a slightly higher main absorption band. The chemical bond water content is around 3% to 4% after 28 d of curing. Slight gel development is still observed at later ages.
- A higher compressive strength is observed in samples with higher slag contents; and an optimum strength (from 86.4 to 72.3 MPa) is shown in mixtures with an activator modulus of 1.4 in all cases. Mixes with higher slag contents exhibit lower porosities (around 2%) in general, and an increase of the activator modulus within the range of 1.0 and 1.8 shows a positive effect on the pore refinement
- Both raw materials' composition and activator modulus show remarkable influence on the shrinkage behaviour; and the 28 d drying shrinkage can be varied from -2168×10^{-6} to -4864×10^{-6}. The incorporation of fly ash into slag can effectively reduce the shrinkage of mortar samples; also the drying shrinkage can be reduced to certain extent by decreasing the additional silicate content from the activator.

8.2 Hybrid fiber reinforced alkali activated materials

8.2.1 Introduction

The application of steel fiber in Portland cement systems has proved its advantages in improving the flexural strength, fracture toughness, impact and fatigue resistance (Sahmaran and Yaman, 2007; Bencardino et al, 2010), as well as the efficiency of reducing the shrinkage behavior of the brittle matrix (Corinaldesi and Moriconi, 2004). The randomly dispersed fibers within the matrix reduce the extension and growth of micro-cracks by providing a stress transfer capacity, by which the generated inner stress can be transferred into other stable areas of the matrix (Yazici et al, 2007). Additionally, it should be noted that steel fibers with different lengths play distinct roles in inhibiting the cracks, namely short fibers are mainly for bridging the micro-cracks while long fibers are more efficient in reducing the macro-cracks (Grunewald, 2004; Markovic, 2006).

Those improved properties may also indicate the potential of using steel fiber in alkali activated systems. Steel fiber with dosages of 40 and 120 kg/m^3 was applied in waterglass activated slag, the results showed that the flexural strength was largely improved and there was a reduction in compressive strength when increasing the fiber content; also water absorption and permeable porosity were reduced (Bernal et al, 2010). Both long and short steel fibers with the volume fraction up to 2% were used in waterglass activated slag-silica fume blends, and it is reported that as the fiber content increases, there is a reduction on workability and drying shrinkage; while mixes with a higher fiber content and longer length exhibit higher compressive and flexural strength (Aydin and Baradan, 2013). Improvements in mechanical properties because of the steel fiber addition were also reported (Bernal et al, 2009; Rashad, 2013). However, there presents limited mechanism study and performance evaluation regarding the effect of hybrid steel fiber on the blended alkaline system.

The objective of this work is to design and evaluate cement free high performance alkali activated slag-fly ash composites; steel fibers of two different lengths are applied for strength reinforcement and shrinkage inhibiting. The mixtures are designed by applying the modified Andreasen & Andersen particle packing model, in order to achieve an optimal packing of the granular ingredients and therefore a condensed matrix. The influences of fiber length and dosage, as well as the utilization of hybrid fibers on workability, compressive strength, flexural strength, porosity and drying shrinkage are investigated.

8.2.2 Flowability

The solid precursors used in this study were ground granulated blast furnace slag and Class F fly ash. Limestone powder was used as a filler. Two types of sand were used as fine aggregates: a micro sand (0-1 mm) and a normal sand with the fractions of 0-2 mm. Besides, two types of straight steel fibers were applied: (1) fiber length of 13 mm with diameter of 0.2 mm; (2) fiber

length of 6 mm with diameter of 0.16 mm. The activator used in this study has an equivalent sodium oxide (Na_2O) content of 5% by mass of the powder and an activator modulus of 1.4. The water/powder ratio was kept constant as 0.4 in all mixtures. A slag/fly ash ratio of 80/20 by mass is used in all mixtures. Steel fiber contents up to 1% (by volume of the mortar) with an interval of 0.25% are applied. Samples with only long fiber or short fiber are prepared as references, and mixes with long/short fiber ratios of 80/20, 60/40, 40/60 and 20/80 are studied. The applied mix design methodology follows the one described in Section 8.1.2, and the detailed mix proportions of the used materials are listed in Table 8.2-1.

Table 8.2-1: Mix proportion of AA slag-fly ash composites with steel fibers (kg/m^3)

Mix	Activator	Slag	Fly ash	Limestone	Sand 0-1	Sand 0-2	Short fiber	Long fiber
Ref	379.8	461.9	115.5	144.3	270.6	811.9	0	0
LF-0.25	378.9	460.7	115.2	143.9	269.9	809.9	0	19.5
LF-0.50	377.9	459.6	114.9	143.6	269.2	807.8	0	39
LF-0.75	377.0	458.4	114.6	143.2	268.6	805.8	0	58.5
LF-1.00	376.0	457.3	114.3	142.9	268.0	803.8	0	78
SF-0.25	378.9	460.7	115.2	143.9	269.9	809.9	19.5	0
SF-0.50	377.9	459.6	114.9	143.6	269.2	807.8	39	0
SF-0.75	377.0	458.4	114.6	143.2	268.6	805.8	58.5	0
SF-1.00	376.0	457.3	114.3	142.9	268.0	803.8	78	0
L/S-8/2	376.0	457.3	114.3	142.9	268.0	803.8	62.4	15.6
L/S-6/4	376.0	457.3	114.3	142.9	268.0	803.8	46.8	31.2
L/S-4/6	376.0	457.3	114.3	142.9	268.0	803.8	31.2	46.8
L/S-2/8	376.0	457.3	114.3	142.9	268.0	803.8	15.6	62.4

The slump flows of the fresh alkali activated slag-fly ash mortars with long and short fiber additions are depicted in Figure 8.2-1. It is clear that as the steel fiber content increases, the slump flow exhibits a gradual decrease in general, and the long steel fiber shows a more significant effect on the slump flow than the short ones. For samples without fiber addition, the slump flow is 25.9 cm; and it slightly decreases to 23.1 cm when the short fiber content increases to 1%. Similar trends are also shown in mixes containing long steel fibers. As the

fiber content increases from 0% to 1%, the slump flow gradually decreases from 25.9 cm to 20.6 cm, which shows a higher decrement when compared to the short fiber. This result is in line with the previous researches that the steel fiber addition presents a negative effect on flowability in both Portland cement system and alkali activated system (Rashad, 2013; Yu et al, 2014).

It is well known that the effects of steel fibers on workability can be concluded as: the elongated shaped steel fiber with relatively high surface area increases the cohesive forces between the fibers and the matrix; stiff fibers push apart the particles that larger than the fiber length and change the structure of the granular skeleton to some extent; the deformed steel fiber improves the anchorage between the fiber and matrix. Considering that only straight fibers with different lengths are used in this study, the decrease of slump flow here is due to the increased surface area and the resulting higher cohesive forces within the matrix. And long steel fibers have a relatively significant influence on this cohesive force. Because of the fact that the long fiber presents a relatively smaller surface area (compared to short fiber, with the same volume) but a more significant effect on flowability in this case, it seems that the internal cohesive forces play a more important role than surface area on the workability.

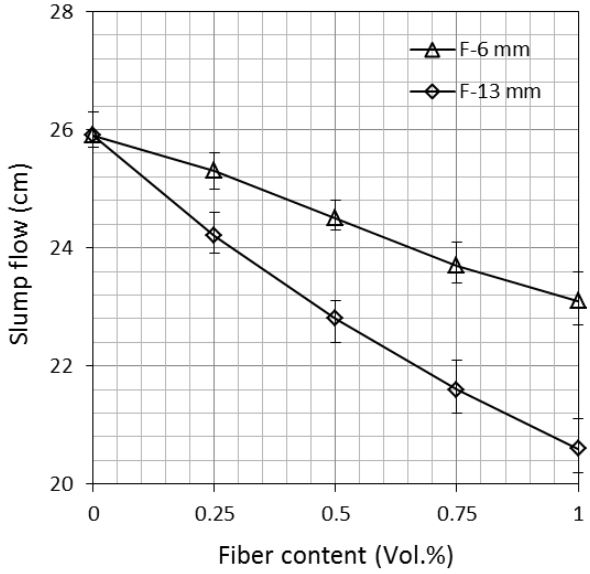

Figure 8.2-1: Slump flow of AA slag-fly ash composites with steel fiber addition

The slump flows of samples with 1% fiber content and different long/short fiber ratios (80/20, 60/40, 40/60 and 20/80) are also tested, and those values are all in between of the samples with 1% pure long and short fibers (20.6 and 23.1 cm), following the tendency that a higher long/short fiber ratio exhibits a relatively low slump flow. It should be noticed that one previous study mentioned that there is an optimum long/short fiber ratio in terms of

workability in Portland cement based system (Yu et al, 2014), while this phenomenon is not observed in this study. It may imply that the slump flow in hybrid fiber conditions may also be influenced by other factors such as total fiber content, binder types, water dosage and utilization of superplasticizers.

8.2.3 Compressive strength

The 7 and 28 d compressive strengths of mixtures with different long and short fiber contents are depicted in Figure 8.2-2. Generally, there is a significant increase in strength when the steel fiber is incorporated; and mixtures with long steel fiber exhibit slightly higher compressive strength than the ones with short fibers. For the reference sample, the compressive strength is 65.4 MPa at 7 d, and it increases to 81.1 MPa after 28 d of curing. When short fibers up to 1% are added, the compressive strength increases to 73.35 MPa and 89.9 MPa at 7 and 28 d, respectively. It indicates that although the steel fiber is well known for improving the tensile or flexural strength, it can also bridge the cracks and retard their propagation to some extent during the compression loads. It should be noted that the mixes with 0.75% and 1% fiber content do not show significant difference in strength, which reveals that there is a limitation in contributing the compressive strength by steel fibers.

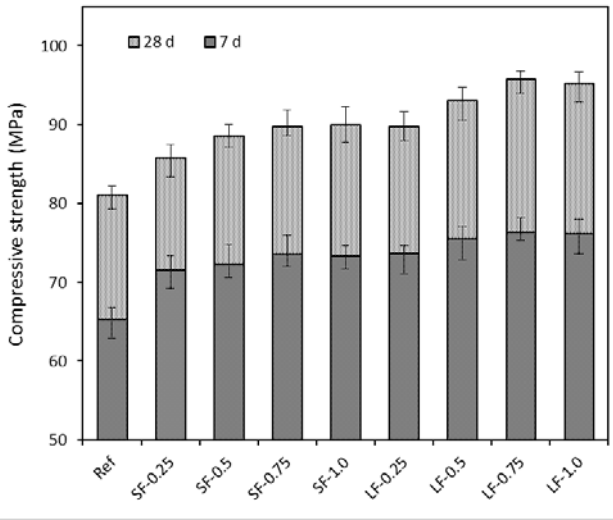

Figure 8.2-2: 7 and 28 d compressive strength of AA slag-fly ash composites with long or short fiber addition

The limited increase or even decrease in strength because of the fiber addition is also reported in the previous studies (Aydin and Baradan, 2013; Rashad, 2013), it is suggested that this phenomenon is due to the combined effect of fiber addition and porosity. The optimum fiber

content in terms of compressive strength may vary from different cases, and for a certain application, the relation between fiber dosage and compressive strength should be taken into consideration during the mix design process.

Similar to the effect of short fibers, the incorporation of long fibers leads to a relatively sharp increase with a dosage of 0.25%, followed by a continuous but slight increase of strength up to around 1%. Also no significant difference in compressive strength is shown in the mixes with 0.75% and 1% long fiber content. The replacement of short and long fibers by 1% results in a strength increment of 11% and 17.5%, respectively; showing ideal fiber efficiency. It is important to notice that mixes with long fibers present higher strengths than the short fiber in general, which is due to the higher efficiency of long steel fibers in inhibiting the growth of macro-cracks.

A total fiber content of 1% is chosen for investigating the effect of hybrid steel fibers. Mixtures with four different long/short fiber ratios (80/20, 60/40, 40/60 and 20/80 by volume) are applied and the 7 and 28 d compressive strengths are presented in Figure 8.2-3. With a fixed total amount of fiber dosage, the compressive strength firstly increases when lowering the long/short fiber ratio, reaching the maximum strength in mixes with long/short ratio of 60/40, followed by a gradual decrease. This result indicates the beneficial effect of using hybrid steel fiber on compressive strength, by doing so a higher strength can be achieved with the same fiber content, and a certain fraction of long/short fibers may exhibit the optimum performance. Additionally, the relatively high strength of all mixes in general is also due to the utilization of particle packing methodology.

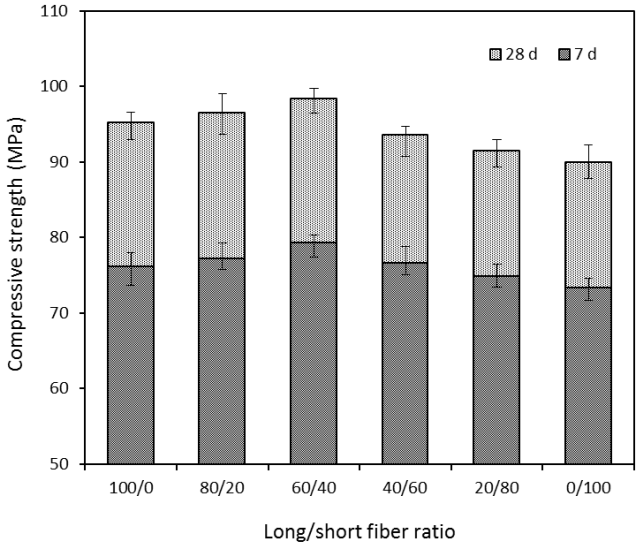

Figure 8.2-3: 7 and 28 d compressive strength of AA slag-fly ash composites with hybrid fiber addition

8.2.4 Flexural strength

The 28 d flexural stress-strain curves of mixtures with short, long and hybrid steel fibers are shown in Figures 8.2-4 to 8.2-6. The stress–strain relation is collected by the default program in the instrument, which is then exported for analysis. It can be seen from Figure 8.2-4 that the addition of only short steel fiber increases the ultimate flexural strength. The flexural strength for samples without fiber incorporation is 8.5 MPa, which gradually increases to 11.2 MPa when increasing the short fiber content up to 1%, showing a relative strength increase of 31.8%. A slight but detectable increase in strain is also observed. However, the fracture mode of the mixtures with short fibers remains the same as the reference sample: the brittle fracture. Moreover, the addition of only short fibers exhibits very limited influence on the energy absorption capacity. The influence of short fiber on the stress-strain behaviors is attributed to shape of this fiber, the relatively short length and diameter makes this fiber capable of inhibiting the micro cracks under flexural loads, thus the flexural strength is increased as a result (for instance, with a 1% fiber addition a relative strength increase of 31.8% is resulted). However, as the loading continues to increase, the micro cracks develop and merge into larger ones and short fiber becomes less effective in macro crack bridging due to its limited length, therefore the failure mode remains the same as plain concrete, i.e. brittle fracture.

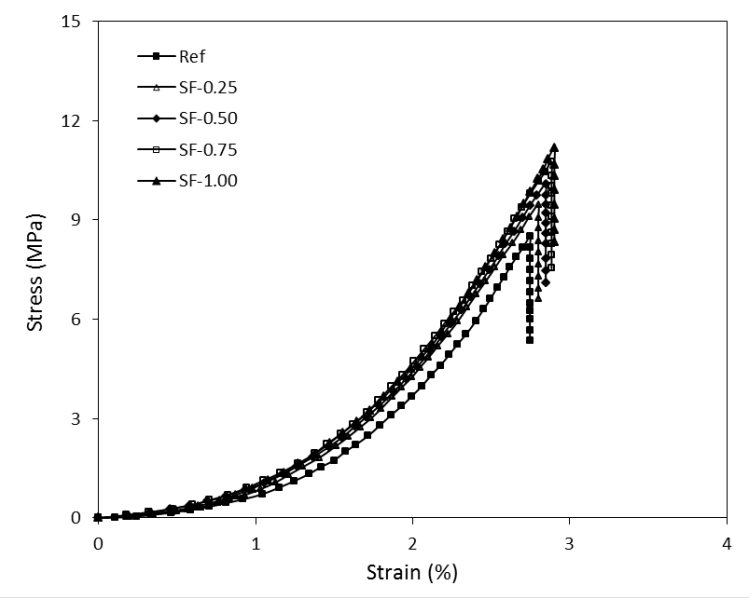

Figure 8.2-4: Flexural stress-strain curve of AA slag-fly ash composites with short fiber

Figure 8.2-5 depicts the stress-strain curves of samples with long fibers. Compared to the effect of short fibers, a more significant improvement in ultimate flexural strength and plastic fracture is presented. For instance, when only 0.25% (by volume) long fiber is incorporated, the

flexural strength increases from 8.5 MPa to 10.0 MPa, showing a more obvious increase (17.6% improvement) compared to the ones with the same amount of short fiber. It indicates that long fibers are more effective in improving the flexural strength. This is attributed to the longer size of long fibers which makes them more oriented between two imaginary borders, thus a better capacity of preventing the growth of macro cracks can be achieved. The sudden stress loss after the peak load is caused by the occurrence of initial failure crack, and the following stress increase is due to the bonding force between the steel fiber and the matrix, then the stress starts to decrease again until the fiber cannot hold the imposed force anymore. It should be noted that the addition of short and long fibers by 1% increases the flexural strength by 31.3% and 58.5%, respectively; showing much higher increments than the compressive strength.

The influence of hybrid steel fiber on flexural strength is presented in Figure 8.2-6. The fiber content for all mixes is fixed at 1% and samples with only long or short fibers are used as references. For mixes with long fiber contents no lower than 40%, plastic fracture is presented. As the long fiber friction increases, mixes show generally a higher energy absorption capacity and a lower stress drop rate after reaching the stress peak; which shows again the higher efficiency of long fibers in bridging the macro-cracks and therefore a more stable post-peak response. However, although mixes show an increased energy absorption capacity with the increasing long fiber content, samples with 60% to 100% long fiber present a comparable post-peak response in general, and the highest flexural strength is shown in mixes with a short/long fiber ratio of 40/60. It confirms that the ultimate flexural strength is not well linked to the toughness.

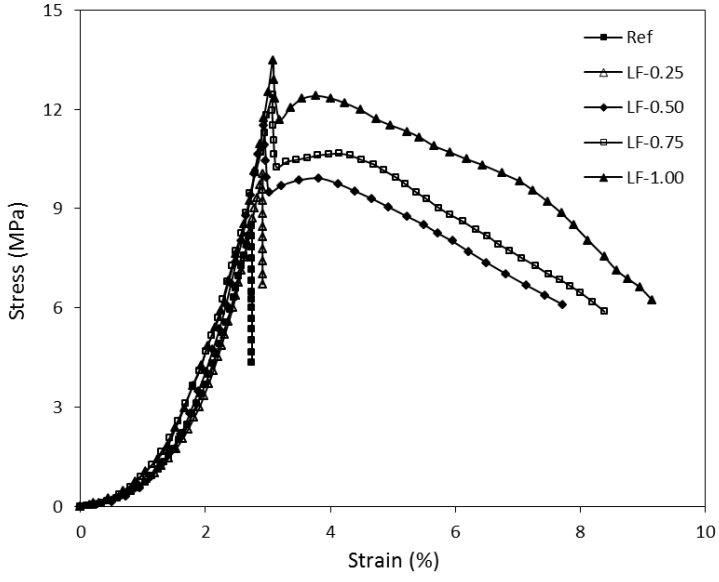

Figure 8.2-5: Flexural stress-strain curve of AA slag-fly ash composites with long fiber

Besides, it can be noticed that the initial elastic period is not linear, which is caused by the limitations of the used testing machine, namely a certain period before stable loading is still needed after the initial load and clamp, and meanwhile the stress-strain curve is already collected. Nevertheless, since all the mixtures share a constant testing procedure, it is scientifically reliable to evaluate the effect fiber addition by investigating the shifts in stress-strain curves; and reasonable comparisons within the tested samples can still be made.

It is well known that the main contribution of steel fibers in reinforcing the mechanical properties is their ability to bridge the cracks and to retard their propagation; and short fibers are efficient in bridging the micro-cracks while long fibers are more effective in inhibiting the macro-cracks.

The positive effect of hybrid fiber on mechanical properties is assigned to the different mechanisms of short and long fibers in restricting the cracks: 1) The short steel fiber can bridge the micro cracks in a more efficient manner, because with the same fiber addition volume, short fibers will have higher number due to their smaller individual volume. While as the micro cracks merge into larger ones with higher crack widths, short fibers may become less active due to their limited length. 2) Long fibers are more oriented between two imaginary borders, which are more efficient in preventing the macro cracks by nature. Besides, they can also form a barrier for short fibers and confine their rotation, thus the short fiber can be better oriented together with long fiber. Therefore, the hybrid usage of long and short fibers inhibit the cracking process from both micro and macro levels, and the synergetic effect of these two facts results in a higher resistance to the loading. The results also show that the fibers work in a similar role in alkali activated binder systems as in Portland cement system.

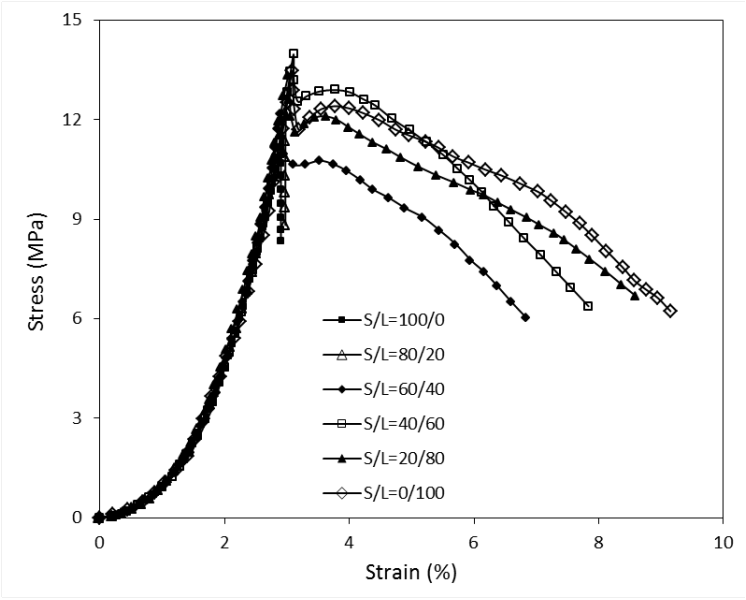

Figure 8.2-6: Flexural stress-strain curve of AA slag-fly ash composites with hybrid fiber

8.2.5 Water permeable porosity

The influences of fiber length and hybrid steel fibers on 28 d water permeable porosity are shown in Figure 8.2-7. All mixtures show similar levels of porosity in overall, and the fiber addition shows limited but detectable influence on the porosity. For samples without fiber addition, the porosity is 17.2% at 28 d; when short fiber is added up to 1%, the porosity increases almost linearly to 17.8%. Similarly, the incorporation of long fibers also leads to a slight increase of porosity up to 18.1%. The increment of porosity due to the fiber addition is in constant with the previous study on other binding system (Yu et al, 2012), showing that the effect is independent of the binder type. It is suggested that the increased porosity due to the fiber addition is attributed to the internal forces between the fibers and aggregates, and/or the fibers themselves, which change the structure of the granular skeleton and reduce the packing density. With the same fiber dosage, the long steel fiber exhibits a more significant influence on porosity than the short ones; indicating that longer fibers may present a more obvious effect on changing the granular skeleton, while the short ones can be relatively better dispersed within the matrix thanks to their smaller length and diameter.

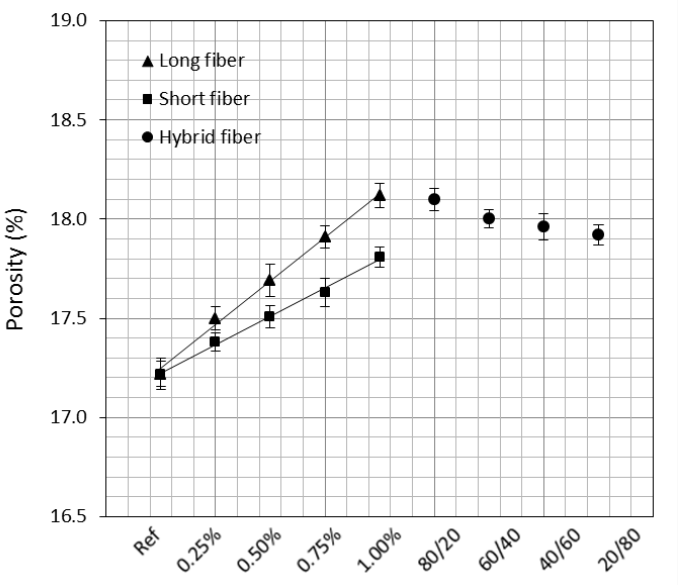

Figure 8.2-7: Effect of fiber length and hybrid fiber on 28 d porosity

Concerning the effect of hybrid fibers, as shown in Figure 8.2-7, that the relation between the porosity and fiber composition seems to follow a similar tendency as the effect of single fibers, and samples with a higher fraction of long fibers exhibit a higher porosity. It seems that the porosity of the hybrid mixes is only a physical combination of the ones with single fibers, and the hybrid usage of these two fibers does not show any synergetic effect on porosity. It can be

seen that both compressive and flexural strength increase with the increasing fiber content in general, but the porosity also increases at the same time. It is suggested that the final mechanical property is the apparent result of the combined effect of steel fiber and porosity. On the one hand, the addition of steel fiber can efficiently inhibit the generating and growing of cracks, especially when hybrid fiber is applied, thus the mechanical properties are improved in general; while on the other hand, the increased porosity due to the fiber addition may lead to the strength reduction. It is obvious that within the applied fiber dosage in this study, the crack-bridging behavior due to the fiber addition seems to present a stronger effect than the porosity increment, and then the mechanical properties exhibit an increase in general. It should also be noticed that beyond the fiber dosage of 1%, the increment of compressive strength is no longer significant; it could be an indication that the increased porosity may show a more obvious effect over the crack-bridging effect at higher fiber contents. It is believed that the relatively poor flowability of the long fiber mixes is also a reason for the higher porosity.

8.2.6 Drying shrinkage

Figure 8.2-8 depicts the drying shrinkage results of mixes with only long or short steel fibers until 28 d and each value is an average of two measurements. It is apparent that the reference sample exhibits an obvious length change over time, especially during the first few days. As shown in the Figure, the shrinkage decreases with the increasing steel fiber content up to 1%. It reveals that the fiber addition can be used as an efficient approach of inhibiting the drying shrinkage of alkali activated materials in this case.

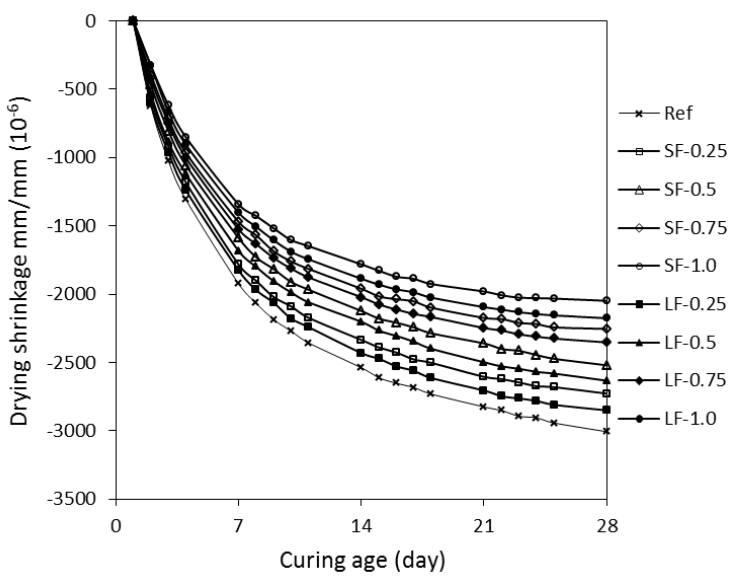

Figure 8.2-8: Shrinkage of AA slag-fly ash mortars with different fiber length and dosage

It can be observed that for a fixed fiber dosage, mixes with long fiber present relatively high values compared to the ones with short fiber, indicating that the long fiber is slightly less effective than short fiber in inhibiting the shrinkage; but a long fiber addition of 1% still exhibits a shrinkage reduction rate of 27.6% compared to the reference sample. The present results are in agreement with the general conclusions from the previous works that the steel fiber addition can effectively reduce the drying shrinkage (Choi et al, 2014; Cao et al, 2014); however, drying shrinkage that is independent of the fiber length was also reported in (Aydin and Baradan, 2013). It reveals that the origin of the starting materials (both the applied binders and steel fibers), sample shape and testing conditions may also show an influence on the final results.

Considering the fiber addition slightly increases the porosity, it is more likely that the significantly reduced drying shrinkage is assigned to the efficiency of steel fibers in maintaining the volume stability of the matrix. The evaporation of free water from the matrix can result in a reduction on the absolute volume, and meanwhile tensile stresses may arise from the resulted internal restraints (Mindess et al, 2003). When steel fiber is incorporated, the generated tensile stresses will be imposed on the fiber (on the matrix as well), due to the high elastic modulus and bridging effect of steel fiber, the influence of this inner force on shrinkage can be suppressed to some extent.

Concerning the effect of hybrid fiber, the tested mixes are having the constant total fiber content (1 vol.%) with different long/short fiber ratios (0/100, 20/80, 40/60, 60/40, 80/20 and 100/0 wt.%). The results show that samples with higher short/long fiber ratios exhibit a slightly lower shrinkage, while all mixtures present a similar level of drying shrinkage in general; which indicates that the fiber content possesses a more significant influence than the fiber type, and the utilization of hybrid fiber seems not to show obvious synergetic effect regarding shrinkage. Concerning the effect of hybrid fiber is limited; their relations with shrinkage are not shown in the form of figure in this study, as presented above.

8.2.7 Other remarks

The fiber content used in this case is limited to 1% by volume, aiming at investigating the effect of fiber length the use of hybrid fiber on those discussed properties, without significantly increasing the total costs of the developed materials. Nevertheless, it is also interesting to investigate the mixes with higher fiber contents in the future studies, since higher fiber dosages are commonly used in the case of high performance cement based composites and then comparisons between different binder systems can be made with convenience. The increased total fiber content may show different effects on different issues, the flowability may continuously decrease and the porosity keeps increasing, since the fiber addition only presents physical effect. To what extent can the steel fiber inhibit the drying shrinkage is another issue that deserves further investigations. Besides, for the applied particle packing methodology, it can be seen from Figure 8.1-1 that the optimized mix still exhibits a lower amount of fine

particles within the range between 0.3 and 20 um compared to the target curve. This is due to the limited amount of fine particles of the provided materials. Thus if additional fine materials can be used in the future studies, a better packing can be achieved, and thus the porosity and other related performances can be further improved. In overall, by using the hybrid steel fiber, a certain combination of the discussed properties can be achieved; also the advantages of both long and short fibers can be taken, especially in improving the stress stain behaviors and reducing the shrinkage, which will brings this type of alternative binder a brighter future in high performance applications.

8.2.8 Conclusions

This section investigates the performances of alkali activated slag-fly ash composites that are reinforced by long and/or short steel fibers, and the mortar samples are designed by applying the modified Andreasen & Andersen particle packing model. Based on the experimental results, the following conclusions can be drawn:

- The addition of long and short fibers (up to 1% by volume) decreases the slump flow from 25.9 cm to 20.6 and 23.1 cm, respectively. The utilization of long steel fiber presents a more significant effect because of the higher influence on the cohesive forces within the matrix. Nevertheless, the designed mixes show in overall relatively good workability.
- The compressive strength is increased by 10.3%/16.8% when short/long steel fiber is incorporated, respectively. The fiber content of around 1% by volume reaches the limit of strength improvement. The hybrid usage of long and short fibers presents a synergetic effect by inhibiting the cracks from both micro and macro levels, resulting in the presence of an optimum strength.
- The addition of long fiber with contents higher than 0.25% by volume changes the fracture mode from brittle into plastic, and the flexural strength and toughness are also remarkably increased by the long fiber incorporation. The addition of short fiber increases the flexural strength in a relatively small level without changing the fracture mode. Synergetic effect of long and short fibers is also shown in flexural behaviors.
- The addition of long and short fibers up to 1% leads to the water permeable porosity increment of 0.6% and 0.9% respectively, attributed to the change of the granular skeleton. The deployment of hybrid fibers leads to a slightly reduced porosity.
- Due to the ability of effectively suppressing the generated inner forces, the utilization of long and short steel fiber significantly reduces the 28 d drying shrinkage up to 27.6% and 31.9%, respectively. The hybrid usage of long and short fibers exhibits more a physical combination rather than synergetic effect.

8.3 Development of sustainable lightweight alkali activated materials

8.3.1 Introduction

Lightweight concrete has been widely applied as both structural and nonstructural components in a wide range of weights and strengths for various applications (Yu et al, 2015), due to its properties such as low density, good thermal insulation and fire resistance. Lightweight concrete can be categorized into three grades in general, depending on the density: low density ones with densities lower than 800 kg/m^3, moderate ones with densities between 800 kg/m^3 and 1400 kg/m^3 and structural ones with densities between 1400 kg/m^3 and 2000 kg/m^3 (ACI committee, 2003). In addition, Portland cement is commonly used as binding material for lightweight concrete, but its production is responsible for around 7% of the global carbon emissions and high energy costs. Some efforts have been spent on applying alkali activated materials in producing lightweight products. For instance, the study of design methodologies of ultra-lightweight geopolymers by applying the particle packing approach, the effect of key factors such as suitable ratios between binder, activator and aggregates (Huiskes et al, 2016); the development of lightweight geopolymers with foaming agent especially for thermal insulating properties (Panias et al, 2010); investigating the relations between density, mechanical properties and thermal conductivity of geopolymers with medium to low densities (Posi et al, 2013; Lee et al, 2014; Escalante-Garcia et al, 2010); the utilization of different alkali binders and uncommon aggregates (Cui et al, 2010; Drchalova et al, 2010; Alengaram et al, 2013).

This study evaluates a lightweight composite that using blended alkali activated binder; also a green olivine nano-silica based alkali activator is applied in order to achieve a better sustainability. The used lightweight aggregate is based on a natural expanded silicate. The lightweight composites are designed to have moderate densities, and to achieve a good balance between mechanical, thermal and acoustic properties. Special focuses are paid on the efficient usage of activators and the effect of alkaline conditions on the lightweight aggregate, because the silica based, porous structure of lightweight aggregate may show an interaction with the pastes due to either dissolution of silica or absorption of activator solution. The effect of activator dosages, addition of lightweight aggregates on early age reaction, gel structure, and aggregates-binder transition zones are investigated; and the effect of the alkali content on mechanical properties, thermal conductivity and sound absorption properties are evaluated.

8.3.2 Compressive strength

Commercial lightweight aggregates (natural expanded silicate, provided by Rotocell) with three particle sizes are applied: 0.5-1 mm, 1-2 mm and 2-4 mm. CEN standard sand is also used as fine aggregates. The olivine nano silica based activator is produced following the description shown in Chapter 5. Three levels of sodium oxide (Na_2O) content were used in this

study: 2.0%, 3.5% and 5.0% (by mass of the binder). A fixed activator modulus of 1.4 and a slag/fly ash mass ratio of 8/2 were used based on the previous experiences. Mixtures are designed to have oven dry densities between 1200 and 1500 kg/m^3, i.e. within the desnity class of D1,4 and D1,6 according to the standard of EN 206-1. The detailed mix proportions are presented in Table 8.3-1.

The 7 and 28 d compressive strength of mixtures with different density levels and a Na_2O content of 3.5% are shown in Figure 8.3-1. The relations between the oven dry density and strength are briefly depicted. It can be seen that as the density decreases, there is an obvious reduction in strength at both 7 and 28 d. The highest 28 d strength reaches 30.7 MPa in mixtures with a density of 1471 kg/m^3, and it gradually reduces to 20.6 MPa in samples with a density of 1163 kg/m^3.

Table 8.3-1: Mix proportion of the designed lightweight composites (kg/m^3)

Sample	Precursors		Activator			Sand	LWA		
	Slag	Fly ash	Nano-s	NaOH	H_2O	0-2	2-4	1-2	0.5-1
D15-5.0	384	96	170.8	30.9	77.7	370	200	150	30
D15-3.5	384	96	119.6	21.7	119.1	380	200	150	30
D15-2.0	384	96	68.3	12.4	170.7	390	200	150	30
D12-5.0	384	96	170.8	30.9	77.7	0	240	180	30
D12-3.5	384	96	119.6	21.7	119.1	10	240	180	30
D12-2.0	384	96	68.3	12.4	170.7	20	240	180	30
D14-3.5	384	96	119.6	21.7	119.1	260	230	140	30
D13-3.5	384	96	119.6	21.7	119.1	135	245	150	30

The relation between density and strength in this study is in line with previous studies concerning the lightweight aggregate based composites (Alduaij et al, 1999; Kralj, 2009; Liu et al, 2010), while the strength results shown here are higher in general than the alkali activated lightweight composites reported in literatures (Xu et al, 2012; Yang et al, 1998; Kockal et al, 2011). Considering the fact that those mixtures are having the same binder content, the reduced compressive strength is mainly attributed to the replacement of normal sand by lightweight aggregates, and a less overall capacity of the aggregates against compressive loading is resulted.

The 7 d strengths share a similar tendency with the 28 d's, which decreases from 27.4 MPa to 18.5 MPa within the density range of around 1500 to 1200 kg/m^3. The 7 d compressive strengths shown in Figure 8.3-1 are all above 88% of the 28 d strength. This is because of the nature of the alkali activated binder system and the ceiling effect of the lightweight aggregates, which presents a relatively fast reaction process and exhibits large percent of the strength at early ages. It should be noticed that key parameters such as activator type and dosage, binder composition and fineness, curing conditions also strongly influence the reaction process, and therefore the strength development.

Figure 8.3-2 depicts the effect of the equivalent Na_2O content on 28 d compressive strength of mixtures with two density levels: 1500 and 1200 kg/m^3. As stated in the introduction part, the alkali activator contributes to a large fraction of the overall environmental issue of alkali activated materials, thus an efficient usage of the activator is of significance. For mixtures with a Na_2O content of 5% in this study, the additionally provided silicate from the activator accounts for around 14.9% of the total silicate within the system, and this activator dosage is a commonly used one in achieving a high strength (Rashad, 2013; Lee et al, 2013; Puertas et al, 2000).

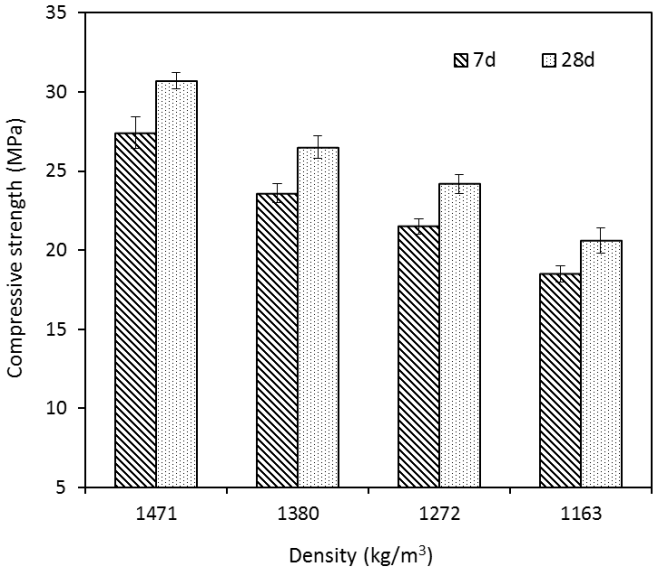

Figure 8.3-1: Compressive strength of AA slag-fly ash lightweight composites with different densities

When reducing the Na_2O content to 3.5% and 2.0%, the silicate fraction from the activator decreases to 10.9% and 6.6%, respectively. Concerning its influence on strength, as can be seen in Figure 8.3-2 that there is an obvious increment of strength when increasing the Na_2O content from 2.0% to 3.5%, and the increase of strength exhibits a limited scale when further

increasing the Na_2O content to 5.0%. To specify, in mixtures with a density level of 1500 kg/m^3, the 28 d strength is increased from 24.0 MPa to 30.7 MPa when shifting the Na_2O dosage from 2.0% to 3.5%, namely a relative increase of 27.9%, and this value is 32.5 MPa in mixtures with a Na_2O content of 5.0%, with a relative increase of only 5.9%. This phenomenon reveals that both Na_2O content and density show an important influence on strength. On the one hand, increasing the alkalinity (Na_2O %) will promote the activation of the binder and therefore result in a higher strength from the aspect of the binder matrix; while on the other hand, the usage of lightweight aggregate limits the strength development by the relatively low crushing strength of the aggregate. Investigating the effect of both density and alkalinity provides insights concerning how the strength would vary within the designed parameter ranges, which also gives information on tailoring the strength with certain densities and reasonable activator dosages for different application requirements.

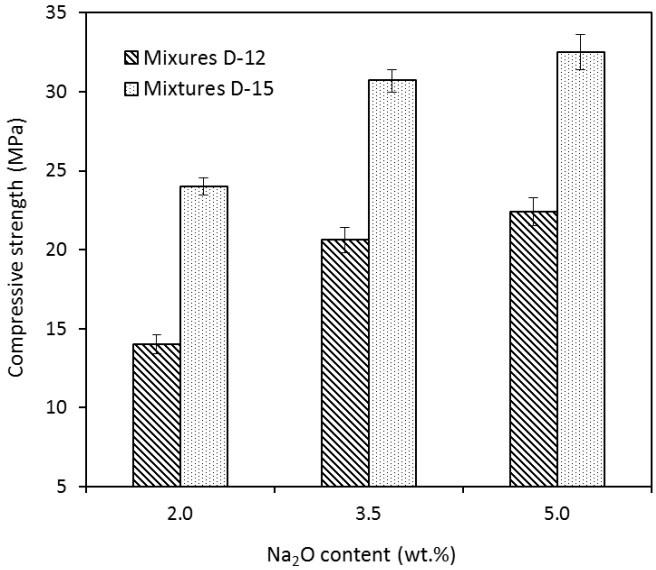

Figure 8.3-2: Compressive strength of AA slag-fly ash lightweight composites with different Na_2O contents

8.3.3 Reaction kinetics

The isothermal calorimeter test was performed on mixtures with the Na_2O content of 2.0%, 3.5% and 5.0%, respectively, and lightweight aggregates were added with an aggregate/binder ratio of 0.8 (based on the mixture proportions shown in Table 8.3-1), in order to evaluate their effect on the early age reaction. Figure 8.3-3 illustrates the normalized heat flows of samples with and without lightweight aggregates during the first 6 d; the heat flow is normalized by mass of the binder (slag and fly ash). It can be seen that the mixtures with a Na_2O content of 5% exhibit

a main reaction peak at around 16 h, with a peak intensity of 1.35 mW/g. The induction stage shows an induction period between around 6 and 10 h, followed by an evident increase of heat flow representing the intensive chemical reaction. When reducing the Na_2O content to 3.5%, a significantly retarded reaction process can be observed. The induction period appears at around 9 to 22 h, the beginning of this stage is 3 h later than the one in sample with a Na_2O content of 5%, also the duration of this stage is more than 3 times longer. The location of the main reaction peak is also delayed to 37 h, which is 21 h later than the 5% Na_2O mixtures. Besides, the peak intensity is reduced to 0.63 mW/g and the deceleration period exhibits a more moderate reduction of heat release.

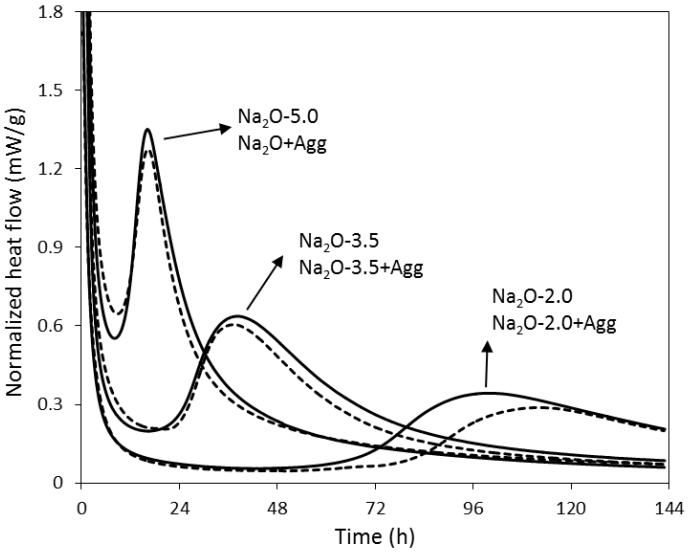

Figure 8.3-3: Normalized heat flows of AA slag-fly ash pastes with different Na_2O contents and lightweight aggregates

A further lower Na_2O dosage of 2.0% results in a dramatic delay of the reaction process. For instance, the induction period lasts more than 48 h; the main reaction peak exhibits an obviously broader covered area with a low peak intensity of about 0.34 mW/g, indicating a gradual and slow formation of the reaction products. Until the testing age of 144 h, the deceleration stage is still ongoing. Thus it can be concluded that the reduction of the reaction process does not present a linear relation with the Na_2O content, the shift of Na_2O concentration effectively influences the characters of the reaction process such as induction time, reaction intensity, the location and duration of main reaction period. Similar tendencies are also shown in previous researches regarding the effect of activator modulus, while the reduction of peak intensity and the delay of the main reaction process is rather limited compared to the case of this study, which suggests that the activator characters such as

additional silicate content and the alkalinity strongly control the activation process of the precursors.

The reaction kinetics results can be somehow related to the compressive strength results in this study, where mixtures with a Na_2O content of 2.0% show an obviously lower strength than the ones with higher Na_2O contents. It is concluded that the delayed reaction process together with lower intensities provide a reduced activation effect of the starting materials, resulting in an overall lower reaction degree and strength. The heat release curves with dash lines refer to the mixtures with lightweight aggregate additions. For mixes with a Na_2O content of 5.0%, the aggregate incorporation slightly reduces the intensity of the main reaction peak without significant effect on its location, and there is also a very slight delay of the induction period. Similar trends are also shown in samples with 3.5% Na_2O content, indicating that the effect of lightweight aggregate on the early age reaction is minor, and those slight effects are probably attributed to the absorption of small amount of activator during the initial mixing. Mixes with a Na_2O content of 2.0% exhibits an evident delay of the main reaction peak, which indicates that under low alkalinity conditions, the effect of lightweight aggregate is magnified.

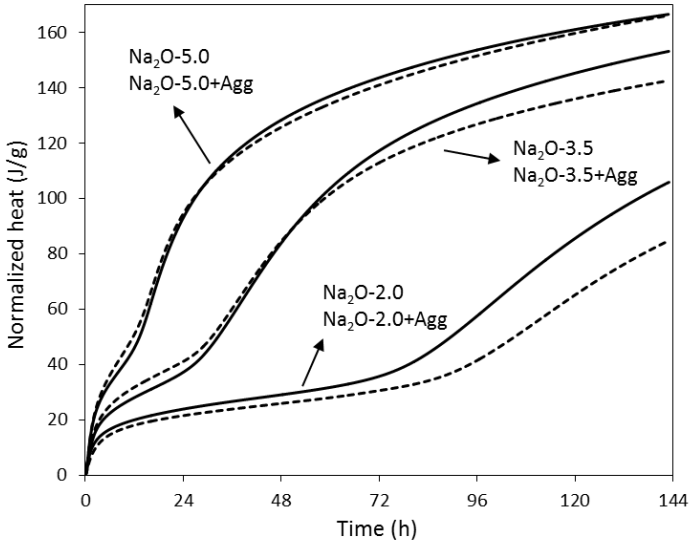

Figure 8.3-4: Normalized heat releases of AA slag-fly ash mortars with different Na_2O contents and lightweight aggregates

The cumulative heat release of all mixtures is shown in Figure 8.3-4. Differences in heat release processes caused by Na_2O content and aggregate addition are clearly depicted. Mixtures with a Na_2O content of 5.0% present the highest cumulative heat of about 166 J/g till the testing age of 144 h. Samples with 3.5% Na_2O show a slightly lower heat release of 153 J/g, while the heat release of mixes with a Na_2O dosage of 2.0% is significantly lower: 106 J/g,

which is also partly because that the main reaction process is still processing. When lightweight aggregate is incorporated, similar heat release is shown in 5% Na_2O mixtures. Similar to the results shown in Figure 8.3-3, as the Na_2O content decreases, the effect of lightweight aggregate on heat release becomes more significant.

8.3.4 Gel structure

In order to investigate to the effect of the Na_2O content on the gel compositions, the TG/DTG analyses were performed and the results are shown in Figures 8.3-5 and 8.3-6, respectively. As shown in Figure 8.3-5 that mixtures with 3 levels of Na_2O content exhibit an evident mass loss before around 100 °C, owing to the evaporation of physically bound water. Another significant loss in mass is shown between about 250 and 450 °C, which are attributed to the decomposition of the reaction products. Afterwards, a gradual decrease in mass is presented in general until 1000 °C; while the remarkable mass loss between 600 and 800 °C is assigned to the decomposition of carbonates.

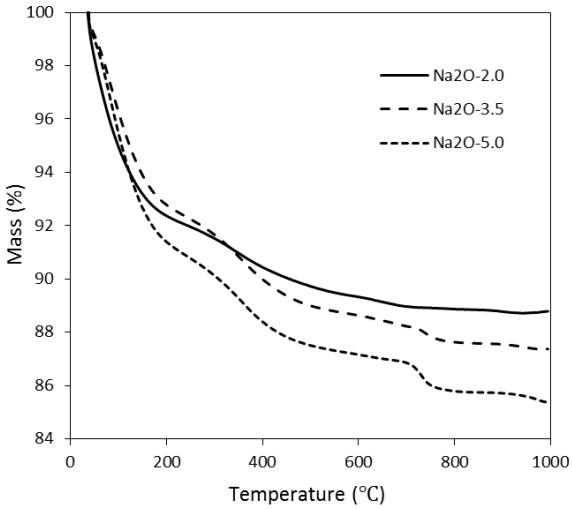

Figure 8.3-5: TG analysis of AA slag-fly ash blends with different Na_2O contents

Three mixtures exhibit similar mass loss before 100 °C (mainly evaporable water), which is 4.9%, 4.0% and 5.3% for samples with a Na_2O content of 5.0%, 3.5% and 2.0%, respectively. This value can be slightly influenced by sampling and variations, thus it is difficult to precisely identify the effect of Na_2O dosage in this mass loss range. The mass loss between 100 and 600 °C, which can be mainly attributed by the decomposition of reaction products, is 8.0% for mixes with a Na_2O content of 5.0%. It slightly decreases to 7.4% in mixes of 3.5% Na_2O; while this value is 5.4% in the case of 2.0% Na_2O, showing a significant reduction. It indicates

that besides the delayed reaction process within the first 144 h, the amount of reaction products in 2.0% Na_2O mixes after 28 d of curing is also obviously lower. The mass loss between 600 °C and 1000 °C is partly attributed to the decomposition of reaction products, while the carbonates also play a role. A detailed calculation in the temperature range of 600 °C and 800 °C shows that when increasing the Na_2O dosage from 2.0% to 5.0%, the mass loss in this range is increased from 0.5% to 1.0% and then 1.4%, which could be an indication that high alkaline condition contributes to the carbonation of alkali activated materials.

The DTG curves shown in Figure 8.3-6 present three evident peaks, the one that located around 100 °C refers to the obvious mass loss of bound water. The shift of this peak to higher temperatures indicates a gel structure with more tightly bound water and finer pore structures (Abdelrazig et al, 1992; Nochaiya et al, 2010). The peaks shown between 250 and 450 °C verify the decomposition of certain reaction products, which are reported to be the dehydration of hydrotalcite that is typically formed from alkali activated slag (Ben et al, 2011). The intensity of the peaks around 600 °C and 800 °C indicates deferent degrees of carbonation caused by the Na_2O dosage.

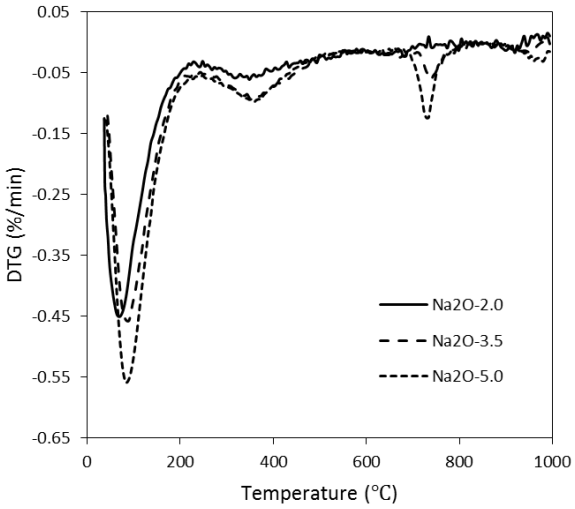

Figure 8.3-6: DTG analysis of AA slag-fly ash blends with different Na_2O contents

8.3.5 Thermal conductivity

In terms of the building materials, a low thermal conductivity contributes to an enhanced indoor thermal comfort, saving the energy cost and preventing the fire caused collapses; while lightweight concrete products based on alkali activated materials are capable of achieving those requirements with a low environmental impact. Figure 8.3-7 shows the thermal conductivity of samples with a Na_2O content of 3.5% and different density levels used in this study, and a

comparison with the available literature. A reduction of thermal conductivity with the decrease of the density can be observed in general. For mixtures with a density level of round 1500 kg/m^3, the thermal conductivity (k-value) is 0.37 W/(m·k), this value is lower than the ones from the obtained literatures. This is because that besides the density, the differences in matrix composition, type of binder and aggregates also show an influence on the property of thermal insulation (De Korte et al, 2010; Zehner et al, 1970). The thermal conductivity reduces to 0.29 W/(m·k) in samples with a density level of 1400 kg/m^3, with a reduction rate of 21.6%. As can be seen from the mix proportions, once the Na_2O content is fixed, the difference between different mixes lies in the aggregate type and dosage. The reduction of density from around 1500 to 1400 kg/m^3 results in a decreased standard sand dosage of 31.6% by mass, indicating its negative influence on thermal insulation. Further reduction of the density to around 1300 and 1200 kg/m^3 leads to further reduced thermal conductivities of 0.22 and 0.16 W/(m·k), respectively. It should be noticed that the thermal conductivity of 0.2 W/(m·k) can be classified to the T2 level of thermal insulation products based on the standard of EN 998-1. It can be seen from Figure 8.3-7 that the thermal conductivity values from this study are lower than that from the literature, which may indicate the advantage of using the alternative binder system together with the lightweight aggregate in this case. Overall, the compressive strengths of around 20 to 30 MPa together with moderate densities and ideal thermal conductivities indicate a wide and promising application potential of this lightweight concrete.

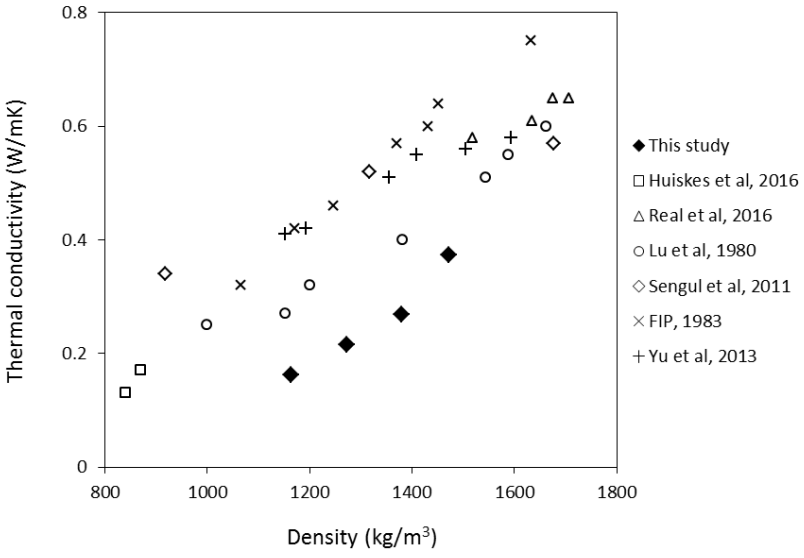

Figure 8.3-7: Thermal conductivity of mixtures with different densities

8.3.6 Acoustical absorption

Owing to the massive addition of the porous lightweight aggregates, the resulting alkali activated lightweight concrete is expected to exhibit good sound absorption behaviors. Figure 8.3-8 exhibits the sound absorption coefficient as a function of frequency, four mixtures with a Na_2O content of 3.5% with different density levels were tested. Generally speaking, the absorption coefficient is significantly increased with the decrease of density, in another word with the increase of lightweight aggregate content within the matrix; and all mixtures mainly show absorption of sound with medium frequencies between around 300 to 1700 Hz. Specifically, mixtures with a density of round 1500 kg/m^3 present a peak absorption coefficient of 0.2, between 800 and 1000 Hz. The peak absorption coefficient increases to around 0.35 and 0.52 in samples with a density about 1400 and 1300 kg/m^3 respectively, while the main absorption frequency range remains similar. A further reduction of density to around 1200 kg/m^3 results in an increased absorption coefficient to above 0.7, with shifted main absorption frequency to higher values. In terms of the low frequency and high frequency ranges, this lightweight product shows limited sound absorption effect. It should be mentioned that the medium frequency usually refers to the sound from humans and daily life.

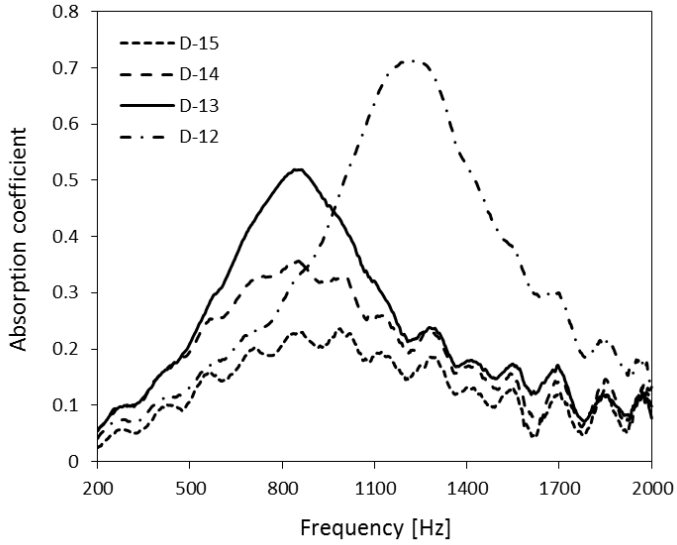

Figure 8.3-8: Acoustic absorption of mixtures with different densities

8.3.7 SEM analysis

Scanning electron microscopy images are used to characterize the applied lightweight aggregate and the interfacial transition zones (ITZ) of the reaction products. Due to the fact that

the effect of Na_2O content on micro scale characteristics is not significant, the reaction products shown in Figure 8.3-9 are having a constant Na_2O content of 3.5%. Fig. 8.3-9-A presents the micro graph of the lightweight aggregate surface, porous structures with irregular shaped surfaces can be observed. This porous structure may already result in a direct link of the aggregate surface and the internal areas. Fig. 8.3-9-B depicts a sectional view of the internal structure of the lightweight aggregate, micro pores with different sizes and shapes are clearly presented. It is easy to understand that this lightweight aggregate exhibits a high porosity, which would result in excellent thermal insulation and sound absorption properties in macro scale. This sectional view also demonstrates that the micro pores within the aggregate are more like single-direction distributed tube shaped structures, rather than individual spherical ones.

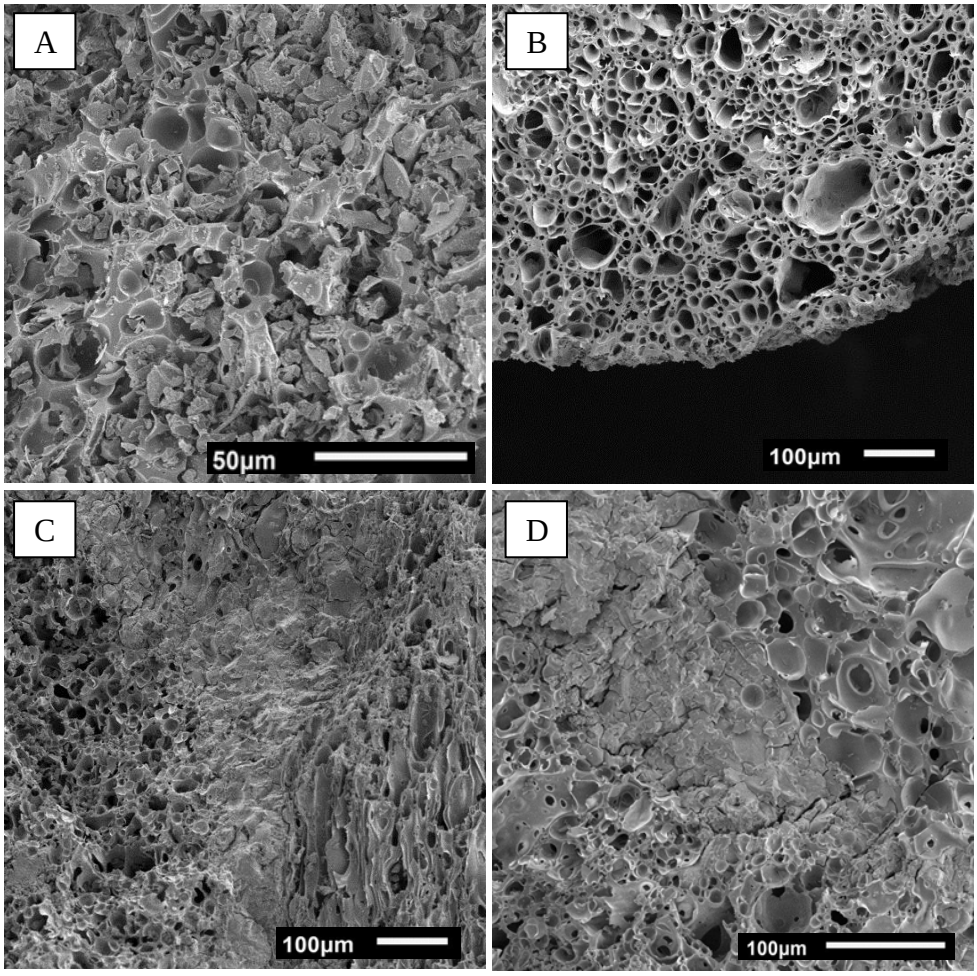

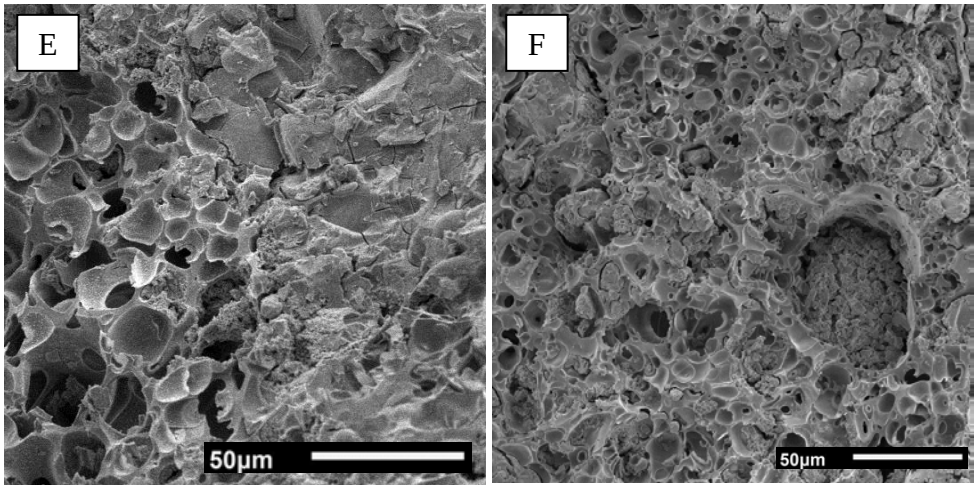

Figure 8.3-9: SEM images of lightweight aggregates (A,B) and the transition zones (C-F)

The ITZ shown in Fig. 8.3-9-C verifies the existence of tube shaped pore structures, as can be seen that two lightweight aggregates that are separated by the binder matrix exhibit different morphology. Together with Fig. 8.3-9-D it can be observed that the boundary between aggregate and the pastes is not clearly defined. Fig. 8.3-9-E shows that certain amount of reaction products is grown within the porous structures that are close to the ITZ. However it is difficult to identify its effect on the mechanical properties, since on the one hand the reaction products break the original structure of aggregate, while on the other hand the formed reacted gels at those areas strengthen the ITZ by densifying the original porous surface of the aggregates. Lightweight aggregates with smaller particle sizes experience a more evident interaction with the binder matrix, as can be seen from Fig. 8.3-9-F that the porous structure of smaller sized lightweight aggregates are partly (sometimes fully) occupied with the reacted gels. This may lead to an increment of the density compared to the designed one, and may slightly reduce the thermal insulation and sound absorption properties.

8.3.8 Conclusions

This section evaluates the mechanical properties, thermal property, acoustical absorption and interfacial transition zones of alkali activated slag-fly ash lightweight composites with densities around 1200 to 1500 kg/m^3 and the effect of alkali content on these properties. In terms of the binder system, the effect of Na_2O contents and the utilization of alternative silica source on early age reaction, gel characters are assessed. Mixtures with 28 d compressive strength up to 32.5 MPa and densities between 1200 and 1500 kg/m^3 are prepared, a direct relation between strength and density is observed. The reduction of Na_2O content from 5% to 2% significantly

prolongs the reaction process, reduces the content of bound water, hydrotalcite and carbonates, but shows negligible effect on the silicate structure. The lightweight concretes exhibit very low thermal conductivity between 0.16 and 0.37 W/(m·k), as well as good sound absorption coefficient up to 0.7 for medium frequencies. The application of alkali activated binders and applying this activator to lightweight concrete suggests an additional approach of preparing building materials with multi-functional properties and reduced environmental impacts.

Chapter 9

Conclusions and recommendations

9.1 Conclusions

This thesis addresses the design and development of ambient temperature cured alkali activated slag-fly ash blends. In order to develop an applicable product with tailored properties, reduced environmental impacts, and achieve a better understanding on the blended binding system, several research steps were carried out. Firstly the physical and chemical properties of the starting materials are characterized in detail, including the used activator, powder materials and aggregates. Then the key synthesizing factors during the production of alkali activated slag-fly ash blends are identified, the effect of those factors on early age reaction, mechanical properties, gel strucutres is evaluated, which provides profound information for later steps. After the key parameters are determined, limestone powder and nano silica are applied individually as substitute of the binders, for the purpose of modifying the binder system to achieve either enhanced sustainability or improved performance (two different application directions). Their influences on fresh and hardened properties are characterized. Besides the modification of the binders, the utilization of a green silica source based activator would results in a mixture with further reduced environmental impacts. Performace comparision is carried out between commercial water glass based activator and olivine nano-silica based ones, on various issues such as gel characteristics, engineering properties and environmental impacts.
Incorporating industrial solid wastes in alkali activated materials brings another approach of making sustainable products. The reuse of incinerated bottom ash could result in reducing the treating costs of solid waste and immobilizing hazardous heavy metals; the reuse of granite powder takes advantage of a local solid waste and provides anther option for the available fine powders for cementious materials. Additionally, by comparing the properties of waste glass powder and silica fume based mixtures, the reactivity and application potential of waste glass powder can be identified. In order to further understand the structure of the blended binder, the reaction degree and gel composition of the reaction products are investigated by using ^{29}Si, ^{27}Al MAS NMR together with selective dissolution, which quantifies the effect of activator and binder composition. The proposed reaction models based on the NMR investigations provide additional information and indications on the gel formation and the effect of blended binder. As for the applications, mortar and concrete mixtures are designed for two application directions, one is the steel fiber reinforced alkali activated materials for high performance applcations, mixtures are designed by using the particle packing model; another one is lightweight alkali activated composites that focus on functional properties.The effects of

starting parameters on several key performances related to engineering application are identified and discussed.
The main conclusions drawn from the performed study are elaborated in the following sections.

9.1.1 Design and modification of the binding materials

Evaluating the effects of activator modulus and slag/fly ash ratios on a number of widely noticed characteristics of the reaction proudcts provides a clear view on their significancy.
The early age reaction results indicate that increasing the slag fraction or lowering the activator modulus would obviously increase the reaction intensity and shorten the main reaction processes, showing a faster reaction. The main reaction product is identified as chain structure C-A-S-H type gels, due to the large amount of incorporated slag and the resulting available calcium, typical polymerized N-A-S-H structures are not obviously observed. The starting compostion shows limited influence on the gel structures, as well as the thermal properties such as bound water content and typical temperatures of phase decomposition. As for the compressive strength, there exsists an optimum activator modulus, either too high or too low modulus will lead to relatively low strength. Also the slag/fly ash mass ratios show an effect on the optimum strength. Thus in order to obtain a desired mechanical property, these two parameters is suggested to be considered simultaneously. Studying the key factors in the manufacturing of alkali activated blends provides indicative information for futher designs.
Two supplementary materials are used for modifying the binding system for different modification purposes, one is nano-silica and the other one is limestone powder. These two materials show different effect on fresh behaviors, for instance nano-silica significantly decreases the slump flow while the flowability increases when limestone powder is added; the setting times are slightly increased with the increase of nano-silica content, while limestone powder shows a negligible effect. The nano-silica addition results in a reduced porosity, indicating its positive effect on pore refinement, while an optimum content of around 2% is shown in terms of porosity. Besides, the nano-silica slightly retards the early age reaction process, while limestone powder slightly accelerates the reaction; and addition of both nano-silica and limestone powder slightly increases the bound water content. From the aspect of mechanical property, a nano-silica addition up to around 2% benefits the compressive strength, and further higher content shows negative effects; the strength show a increase with an increasing limestone powder content up to 30%.

9.1.2 Application of a green alternative activator

A green olivine nano-silica was synthesized in the laboratory, attempting to be used as an alternative silica source for the alkali activator. The produced olivine nano-silica can be well dissolved in NaOH solutions to prepare activators between the modulus of 1.0 and 1.8; the soluble silicate in the nano-silica based activators is above 98%. Compared to the commercial sodium silicate based activator, the olivine nano-silica based one show relatively high

percentage of Q3 sites, indicating a slight difference in Q compositions. For a fixed activator modulus, the alternative activator based mixes show similar reaction process compared to the commercial waterglass based ones but with slightly reduced reaction intensity. Solid-state MAS NMR together with TG analysis demonstrates the gel structure differences in samples that are derived from different activator type and modulus. For instance the slag reactivity is reduced with the increase of activator modulus, and therefore results in reduced Al incorporation within the C-A-S-H gels; and nano-silica based mixes show an increase of Q3(1Al)+Q4(4Al) contents with reduced bound water, while those groups in commercial waterglass based ones remain stable. Compared to the commercial sodium silicate based mixes, the alternative activator based pastes show increased setting times, flowability, porosity, shrinkage, and slightly reduced strength. Additionally, the calculation on the carbon footprint indicates that when olivine nano-silica is used as an alternative silicate source, the CO_2 emission from activator is reduced by up to 29.0% (in samples with Ms of 1.8).

9.1.3 Reusing solid wastes in alkali activated materials

The suitability of using three solid wastes (i.e. bottom ash, granite powder, glass powder) in alkali activated materials is investigated. Important physical and chemical properties of the applied MWSI bottom ash, granite powder and waste glass powder are thoroughly characterized. It is not surprsing that the addition of MWSI bottom ash negatively affects the strength because of its porous structure, compressive strengths between around 20 and 70 MPa can be achieved by using bottom ash with the replacement up to 50%, and the addition of granite powder with the content no higher than 20% results in slightly reduced strengths. Both bottom ash and granite powder slightly delays the early age reaction, they can be considered as non-reactive components in this case. Clarifying the effect of MWSI bottom ash on reaction kinetics is nessesary since the potential reactivity is highly related to the ash origin. Most of the recipes can pass the Dutch legislation that limits the leaching of the heavy metals. But additional treatment to remove the chloride and sulfate is still nessesary; and economically feasible methods of treating thoese two ions are suggested. Applying the solid waste in alkali activated materials shows advantages in sustainable development and reduces the costs of handling the heavy metals and metallic aluminate.

The suitability of reusing waste glass powder as binder substitutes is also discussed. In order to have a clear impression on the efficiency of glass powder, silica fume is applied as a reference. Also Portland cement based mixes are used as references to investigate whether glass powder plays different role in different binding systems. The addition of waste glass powder slightly increases the slump flow, while the silica fume significantly reduces workability. Its addition up to 20% does not show negative effect in terms of compressive strength, and slightly inceases the strength with a dosage of around 20%. In terms of the early age reaction, waste glass powder works as silica enriched precursor and slightly delays the reaction process in alkali activated system, while in Portland cement system it slightly accelerates the reaction and

affects the process of AFm formation. And for the gel compositions, the waste glass powder addition reduces the content of portlandite in a Portland cement system, indicating its contribution to the secondary reaction; while in the alkali activated system, glass powder addition increases the bonud water content, but shows limited effect on gel characteristics.

9.1.4 NMR investigations and modeling

By using a combined analytical method of ^{29}Si MAS NMR spectra deconvolution and selective dissolution, the reaction degree and gel composition of alkali activated slag, fly ash and slag-fly ash blends with different activator moduli are identified in detail. It can be known from this combined application that in alkali activated slag, increasing the activator modulus results in the reduction of slag reactivity, also with the reduced Q2(1Al) content and increased Q3(1Al) content, hydrotalcite type phases are also observed. In alkali activated fly ash, increasing the activator modulus also results in a reduced reaction degree, together with increased content of Q4 groups. Both polymerized Q4 structures and short ranged Q sites are formed. In slag-fly ash blends, both C-A-S-H and N-A-S-H type gels are identified within the reaction products. For a fixed activator modulus, the slag reactivity is reduced while the reaction degree of fly ash is increased compared to the individual systems. The gel interaction can be indicated by comparing the slag-fly ash blends with the physically mixed alkali activated slag and alkali activated fly ash. The blended system presents higher contents of newly formed Q4 groups with increased Al incorporation. The proposed model of gel formation based on the NMR results provides further insights in understanding the microstructure and phase composition of alkali activated slag, fly ash and their blends.

9.1.5 Mix design and applications

The properties of alkali activated slag-fly ash mortars/concretes that are designed by using the modified Andreasen and Andersen packing model are addressed. Important fresh and hardened properties are investigated, for instance the slump flow, setting times, compressive strength, porosity and drying shrinkage. A large range of slump flow and setting times can be caused by the slag-fly ash ratios and activator moduli, while the activator modulus exhibits a more considerable effect. Slag enriched samples show a higher compressive strength, and the optimum strength tends to show in mixtures with an activator modulus of 1.4. An increase of the activator modulus within the range of 1.0 and 1.8 shows a positive effect on the pore refinement. The increase of fly ash content or the decreae of the activator modulus can effectively reduce the shrinkage of mortar samples.

Hybrid fiber reinforced alkali activated slag-fly ash composites are then produced by using the packing model. The addition of long and short fibers slightly decreases the slump flow, and the long steel fiber presents a more significant effect. The addition of steel fiber leads to a compressive strength increament up to around 17%, and the fiber content of around 1% by

volume reaches the limit of strength improvement. The hybrid usage of long and short fibers results in the presence of an optimum strength. The flexural strength and toughness are significantly increased by the long fiber addition, and the use of short fiber increases the flexural strength in a relatively small level without changing the fracture mode. Synergetic effect of long and short fibers is also shown in flexural behaviors. The addition of steel fibers slightly increases the water permeable porosity attributed to the change of the granular skeleton, but can significantly reduce drying shrinkage.

Another application is the lightweight composites with moderate densities, targeting at achieving a good balance between properties such as strength, thermal insulation and acoustical absorption. The used activators are olivine nano-silica based ones that are introduced in Chapter 5. A direct relation between strength and density is observed. The reduction of the used Na_2O content obviously prolongs the reaction process, reduces the content of bound water, hydrotalcite and carbonates, but shows negligible effect on the silicate structure. The lightweight concretes exhibit very low thermal conductivity and good sound absorption coefficient mainly in the range of medium frequencies. Those results suggest a promising lightweight product with multi-functional properties and reduced environmental impacts.

9.2 Recommendations for future research

The present PhD project was focused on the design of ambient temperature cured slag-fly ash blends, with detailed indentifications on the reaction kinetics, gel structures of the binders, everal important fresh and hardened behaviors concerning the mortar/concrete products. The presented results positively indicate the achievements of the performed study, but further researches are still necessary, the following work is summarized as the recommendations for the future investigations.

- The development of suitable water reducers for alkali activated binding systems. Up to now there are no ideal superplastisizers available for this system, because the traditional ones that are usually used for Portland cement system will be decomposed under high alkali conditions at the initial stage, and then cannot efficiently disperse the solid particles. The lack of suitable superplastisizers greatly limits the water to soild ratio in alkali activated mortar/concrete to reach lower values, and then limits this product to reach further higher performances. Therefore, develop applicable water reducers in high alkali environment has great significancy
- Seeking or developing new precursors for alkali activated materials. Theoretically any raw materials that contain amorphous calcium, silica and alumina can be used for alkaliactivation. Nowadays the most widely used precursors are blast furnace slag, fly ash and metakaolin, due to their availability and stable properties. However, the production scale of those three precursors is not comparable to Portland cement, and all of them are also important supplementary cementing materials of Portland cement systems. Therefore,

finding new precursors with cheaper costs and larger availability will promote the application of alkali activated materials.

- At this stage the alkali activated materials are mostly prepared in the laboratory scale with very limited case studies. Considering that the concrete products are usually designed for serving decades or more than 100 years, the durability related issues must be extensively understood. For instance the carbonation, sulfate attack, chloride penetration and freeze/thaw cycles.
- Achieving a more application friendly system. Alkali activated materials are usually prepared with the process of transporting and mixing high alkalinity solutions, handling this chemical may casue safey issues to the users, and thus require higher standard (sometimes higher costs) during the manufacturing. Besides, the relatviely fast hardening process making this material difficult to pre-mix during transportation. Thus developing methods that help to achieve better application friendly products can be interesting to both industry and academia.
- Advanced applications of alkali activated materials. Alkali activated Si+Ca, Si+Al and Si+Ca+Al systems show similar and distinguish performances, which can be used for important part of functional applications such as fire resistant component, heavy metals binding, ceramics synthesizing and alloys synthesizing. Investigate and apply alkali activated materials for more application direction is nessesary and of great interest.

Bibliography

Abbas Z, Moghaddam AP, Steenari BM. Release of salts from municipal solid waste combustion residues. Waste Management. 2003;23:291-305.

Abdelrazig BEI, Main SD, Nowell DV. Hydration studies of modified OPC pastes by differential scanning calorimetry and thermogravimetry. Journal of Thermal Analysis and Calorimetry. 1992;38:495-504.

ACI Committee 213. Guide for structural lightweight-aggregate, concrete; 2003.

Adak D, Sarkar M, Mandal S. Effect of nano-silica on strength and durability of fly ash based geopolymer mortar. Construction and Building Materials. 2014;70:453-9.

Alduaij J, Alshaleh K, Naseerd M, Ellaithy K. Lightweight concrete in hot coastal areas, Cement and Concrete Composite. 1999;21:453-58.

Alengaram UJ, Jumaat MZB, Nikraz H, Kupaei RH. Mix design for fly ash based oil palm shell geopolymer lightweight concrete. Construction and Building Materials. 2013;43:490-96.

Anand S, Vrat P, Dahiya RP. Application of a system dynamics approach for assessment and mitigation of CO_2 emission from the cement industry. Environmental Management. 2006;79(4):383-98.

Andreasen AHM, Andersen J. Über die Beziehungen zwischen Kornabstufungen und Zwischenraum in Produkten aus losen Körnern (mit einigen Experimenten). Kolloid-Zeitschrift 1930;50:217-28 [in German].

Antonia M, Rossena J, Martirena F, Scrivener K. Cement substitution by a combination of metakaolin and limestone. Cement and Concrete Research. 2012;42:1579-89.

Aubert JE, Husson B, Vaquier A. Metallic aluminum in MSWI fly ash: quantification and influence on the properties of cement-based products. Waste Management. 2004;24:589-96.

Aydin S. A ternary optimization of mineral additives of alkali activated cement mortars. Construction and Building Materials. 2013;43:131-8.

Aydin S, Baradan B. The effect of fiber properties on high performance alkali-activated slag/silica fume mortars. Composites Part B: Engineering. 2013;45:63-9.

Bakharev T, Sanjayan JG, Cheng YB. Alkali activation of Australian slag cements. Cement and Concrete Research. 1999;29:113-20.

Balczar I, Korim T, Dobradi A. Correlation of strength to apparent porosity of geopolymers, Understanding through variations of setting time. Construction and Building Materials. 2015;93:983-8.

Bencardino F, Rizzuti L, Spadea G, Swamy RN. Experimental evaluation of fiber reinforced concrete fracture properties. Composites Part B: Engineering. 2010;41:17-24.

Ben Haha M, Lothenbach B, Saout GL, Winnefeld F. Influence of slag chemistry on the hydration of alkali-activated blastfurnace Slag-Part I: Effect of MgO. Cement and Concrete Research. 2011;41:955-63.

Ben Haha M, Saout GL, Winnefeld F, Lothenbach B. Influence of activator type on hydration kinetics, hydrate assemblage and microstructural development of alkali activated blast-furnace slags. Cement and Concrete Research. 2011;41:301-10.

Bernal SA, et al. MgO content of slag controls phase evolution and structural changes induced by accelerated carbonation in alkali-activated binders. Cement and Concrete Research. 2014;57:33-43.
Bernal SA, Mejia de Gutierrez R, Delvasto S, Rodriguez E. Performance of an alkaliactivated slag concrete reinforced with steel fibers. Construction and Building Materials. 2010;24:208-14.
Bernal SA, Mejia de Gutierrez R, Rodriguez E, Delvasto S, Puertas F. Mechanical behavior of steel fiber-reinforced alkali-activated slag concrete. Materiales de Construccion 2009;29:53-62.
Bernal SA, Provis JL, Rose V, Mejia de Gutierrez R. Evolution of binder structure in sodium silicate activated slag metakaolin blends. Cement and Concrete Composite. 2011;33:46-54.
Bernal SA, Provis JL, Walkerly B, et al. Gel nanostructure in alkali-activated binders based on slag and fly ash, and effects of accelerated carbonation. Cement and Concrete Research. 2013;53:127-44.
Bernal SA, Rodriguez ED, Mejia de Gutierrez R, Provis JL, Delvasto S. Activation of metakaolin/slag blends using alkaline solutions based on chemically modified silica fume and rice husk ash. Waste and Biomass Valorization. 2012;3:99-108.
Bertolini L, Carsana M, Cassago D, Curzio A, Collepardi M. MSWI ashes as mineral additions in concrete. Cement and Concrete Research. 2004;34:1899-906.
Birgisdottir H, Pihl KA, Bhander G, Hauschild MZ, Christensen TH. Environmental assessment of roads constructed with and without bottom ash from municipal solid waste incineration. Transportation Research Part D. 2006;11:358-68.
Boghetich G, Liberti L, Natarnicola M, Palma M, Petruzzelli D. Chloride extraction for quality improvement of municipal solid waste incinerator ash for the concrete industry. Waste Management and Research. 2005;23:57-61.
Bonavetti VL, Rahhal VF, Irassar EF. Studies on the carboaluminate formation in limestone filler-blended cements. Cement and Concrete Research. 2001:31:853-9.
Bonk F, Schneider J, Cincotto MA, Panepucci H. Characterization by multinuclear high-resolution NMR of hydration products in activated blast-furnace slag pastes. Journal of the American Ceramic Society. 2003;86(10):1712-9.
Boshehrian A, Hosseini P. Effect of nano-SiO_2 particles on properties of cement mortar applicable for ferrocement elements. Concrete Research Letter. 2011;2(1):167-80.
Bosmans A, Vanderreydt I, Geysen D, Helsen L. The crucial role of waste-toenergy technologies in enhanced landfill mining: a technology review. Journal of Cleaner Production. 2013;55:10-23.
Brindley GW, Nakahira M. A new concept of the transformation sequence of kaolinite to mulite. Nature. 1958;1333-4.
Brindley GW, Nakahira M. The kaolinite–mullite reaction series: IV, The coordination of Aluminum. Journal of the American Ceramic Society. 1961;44:506-7.
Brough AR, Atkinson A. Sodium silicate-based alkali-activated slag mortars: Part I. Strength, hydration, microstructure. Cement and Concrete Research. 2002;32:865-79.
Brough AR, Holloway M, Sykes J, Atkinson A. Sodium silicate-based alkali-activated slag mortars Part II. The retarding effect of additions of sodium chloride or malic acid. Cement and Concrete Research. 2000;30:1375-79.

Brouwers HJH, Radix HJ. Self-compacting concrete: theoretical and experimental study. Cement and Concrete Research. 2005;35:2116-36.
Buchwald A, Hilbig H, Kaps C. Alkali-activated metakaolin-slag blends, performance and structure in dependence of their composition. Journal of Materials Science. 2007;42:3024-32.
Cao ML, Zhang C, Lv HF. Mechanical response and shrinkage performance of cementitious composites with a new fiber hybridization. Construction and Building Materials. 2014;57:45-52.
Chen G, Lee H, Young KL, Yue PL, Wong A, Tao T. Glass recycling in cement production-an innovative approach. Waste Management. 2002;22:747-753.
Chen W, Brouwers HJH. The hydration of slag. Part 1: Reaction models for alkali-activated slag. Journal of Materials Science. 2007;42:428-43.
Chen W. Hydration of slag cement: theory, modeling and application. Ph.D. Thesis, University of Twente, The Netherlands, 2007.
Chen ZT, Liu YQ, Zhu WP, Yang EH. Incinerator bottom ash (IBA) aerated geopolymer. Construction and Building Materials. 2016;112:1025-31.
Chi M, Huang R. Binding mechanism and properties of alkali-activated fly ash/slag mortars. Construction and Building Materials. 2013;40:291-8.
Chithiraputhiran S, Neithalath N. Isothermal reaction kinetics and temperature dependence of alkali activation of slag, fly ash and their blends. Construction and Building Materials. 2013;45:233-42.
Chimenos JM, Segarra M, Fernandez MA, Espiell F. Characterization of the bottom ash in a municipal solid waste incinerator. Journal of Hazardous Materials. 1999;64:211-22.
Choi SJ, Hong BT, Lee SJ, Won JP. Shrinkage and corrosion resistance of amorphous metallic-fiber-reinforced cement composites. Composite Structures. 2014;107:537-43.
Cimpan C, Wenzel H. Energy implications of mechanical and mechanical-biological treatment compared to direct waste-to-energy. Waste Management. 2013;33:1648-58.
Collins F. Inclusion of carbonation during the life cycle of built and recycled concrete: influence on their carbon footprint, The International Journal of Life Cycle Assessment. 2010;15:549-56.
Collins F, Sanjayan JG. Effect of pore size distribution on drying shrinking of alkali activated slag concrete. Cement and Concrete Research. 2000;30:1401-6.
Collins F, Sanjayan JG. Effects of ultra-fine materials on workability and strength of concrete containing alkali-activated slag as the binder. Cement and Concrete Research. 1999;29:459-62.
Corinaldesi V, Moriconi G. Durable fiber reinforced self-compacting concrete. Cement and Concrete Research. 2004;34:249-54.
Criado M, Fernandez A, Palomo A, Sobrados I, Sanz J. Effect of the SiO_2/Na_2O ratio on the alkali activation of fly ash. Part II: ^{29}Si MAS-NMR Survey. Microporous Mesoporous Material. 2008;109:525-34.
Cui X, Qiu S, Yu J, Zhang L, Liu L. Preparation of phosphoric acid-based porous geopolymers. Applied Clay Science. 2010;50:600-3.
Cwirzen A, Provis JL, Penttala V, Cwirzen KH. The effect of limestone on sodium hydroxide-activated metakaolin-based geopolymers. Construction and Building Materials. 2014;66:53-62.

Davidovits J. Synthetic Mineral Polymer Compound of the Silicoaluminates, Family and Preparation Process, US Patent 4472199, 1984.
De Korte ACJ, Brouwers HJH. Calculation of thermal conductivity of gypsum plasterboards at ambient and elevated temperature. Fire and Materials. 2010;34:55-75.
De weerdt K, Ben Haha M, Le Saout G, Kjellsen KO, Justnes H, Lothenbach B. Hydration mechanisms of ternary Portland cements containing limestone powder and fly ash. Cement and Concrete Research. 2011;41:279-91.
Deb PS, Nath P, Sarker PK. The effects of ground granulated blast-furnace slag blending with fly ash and activator content on the workability and strength properties of geopolymer cured at ambient temperature. Materials and Design. 2014;62:32-9.
Deira E, Gebregziabiher BS, Peethamparan S. Influence of starting material on the early age hydration kinetics, microstructure and composition of binding gel in alkali activated binder systems. Cement and Concrete Composite. 2014;48:108-17.
Deja J. Immobilization of Cr^{6+}, Cd^{2+}, Zn^{2+} and Pb^{2+} in alkali-activated slag binders. Cement and Concrete Research. 2002;32:1671-9.
Douglas E, Brandstetr J. A preliminary study on the alkali activation of ground granulated blast-furnace slag. Cement and Concrete Research. 1990;20:746-56.
Drchalova J, Rovnanik P, Bayer P, Kersner Z, Cerny R, Zuda L. Alkali-activated aluminosilicates composite with heat-resistant lightweight aggregates exposed to high temperatures: mechanical and water transport properties. Cement and Concrete Composite. 2010;32:157-163.
Duxson P, Van Deventer JSJ. Commercialization of geopolymers for construction opportunities and obstacles. In: Provis J, Van Van Deventer J, editors. Geopolymers, structure, processing, properties and applications. Cambridge (UK): Woodhead Publishing Limited, Abington Hall; 2009.
Duxson P, Provis JL. Designing precursors for geopolymer cements. Journal of the American Ceramic Society. 2008;91(12):3864-9.
Duxson P, Provis JL, Lukey GC, Mallicoat SW, Kriven WM, Van Deventer JSJ. Understanding the relationship between geopolymer composition, microstructure and mechanical properties. Colloids and Surfaces A. 2005;269:47-58.
Duxson P, Fernandez A, Provis JL, Lukey GC, Palomo A, Van Deventer JSJ. Geopolymer technology: the current state of the art. Journal of Materials Science. 2007;42:2917-33.
Duxson P, Provis JL, Lukey GC, Separovic F, Van Deventer JSJ. ^{29}Si NMR study of structural ordering in aluminosilicate geopolymer gels. Langmuir, 2005;21:3028-36.
Eikelboom RT, Ruwiel E, Goumans JJ. The building materials decree: an example of a Dutch regulation based on the potential impact of materials on the environment. Waste Management. 2001;21:295-302.
EN 1015-3:1999. Methods of test for mortar for masonry Part 3: Determination of consistence of fresh mortar.
EN 196-1:2005. Methods of testing cement Part 1: Determination of strength.
EN 196-3:2005. Methods of testing cement Part 3: Determination of setting times and soundness.
Escalante-Garcia JI, Burciaga O, Aguilar R. Lightweight concretes of activated metakaolin-fly ash binders, with blast furnace slag aggregates. Construction and Building Materials. 2010;24:1166-75.

Escalante-Garcia JI, Campos K, Gorokhovsky A, Fernandez A. Cementitious composites of pulverised fuel ash and blast furnace slag activated by sodium silicate: effect of Na_2O concentration and modulus. Advances in Applied Ceramics. 2006;105:201-8.
European Commission. Reference document on best available techniques for the manufacture of large volume inorganic chemicals -solids and others industry, 2007.
Faimon J. Oscillatory silicon and aluminum aqueous concentrations during experimental aluminosilicate weathering. Geochimica et Cosmochimica Acta. 1996;60,2901-7.
Fan Y, Yin S, Wen Z, Zhong J. Activation of fly ash and its effects on cement properties. Cement and Concrete Research. 1999;29:467-72.
Faucon P, Delagrave A, Petit JC, Richet C, Marchand JM, Zanni H. Aluminum incorporation in calcium silicate hydrates (C-S-H) depending on their Ca/Si ratio. Journal of Physical Chemistry B. 1999;103(37):7796-802.
Fennis SAM, Walraven JC, Uijl JA. The use of particle packing models to design ecological concrete. Heron. 2009;54:185-204.
Fernandez-Jimenez A, Palomo A. Composition and microstructure of alkali activated fly ash binder: effect of the activator. Cement and Concrete Research. 2005;35(10):1984-92.
Fernandez-Jimenez A, Palomo A, Criado M. Microstructure development of alkali-activated fly ash cement: A descriptive model. Cement and Concrete Research. 2005;35(6)1204-9.
Fernandez-Jimenez A, Palomo A, Lopez HC. Engineering properties of alkali-activated fly ash concrete. ACI Materials Journal. 2006;103:106-12.
Fernandez-Jimenez A, Puertas F. Alkali-activated slag cements: Kinetic studies. Cement and Concrete Research. 1997;27(3):359-68.
Fernandez-Jimenez A, Puertas F. Structure of calcium silicate hydrates formed in alkaline-activated slag: influence of the type of alkaline activator. Journal of the American Ceramic Society. 2003;86(8):1389-94.
Fernandez-Jimenez A, Torre AG, Palomo A, Lopez G, Alonso M, Aranda M. Quantitative determination of phases in the alkali activation of fly ash. Part I. Potential ash reactivity. Fuel. 2006;85:625-34.
Fernandez-Jimenez A, Torre AG, Palomo A, Lopez G, Alonso MM, Aranda MAG. Quantitative determination of phases in the alkaline activation of fly ash. Part II: Degree of reaction. Fuel. 2006;85:1960-9.
FIP. Manual of Lightweight Aggregate Concrete, second ed., Surrey University Press, Glasgow, UK, 1983.
Forteza R, Far M, Segui C, Cerda V. Characterization of bottom ash in municipal solid waste incinerators for its use in road base. Waste Management. 2004;24:899-909.
Funk JE, Dinger DR. Predictive process control of crowded particulate suspensions, applied to ceramic manufacturing. Kluwer Academic Publishers, Boston, the United States, 1994.
Gadsden JA. Infrared spectra of minerals and related inorganic compounds, Ed. Butterworths, London, England, 1975.
Gaitero JJ, Campillo I, Guerrero A. Reduction of the calcium leaching rate of cement paste by addition of silica nanoparticles. Cement and Concrete Research. 2008;38:1112-8.
Gao K, Lin KL, Wang DY, Hwang CL, Tuan BL, Shiu HS, Cheng TW. Effect of nano-SiO_2 on the alkali-activated characteristics of metakaolin-based geopolymers. Construction and Building Materials. 2013;48:441-7.
Gao X, Yu QL, Brouwers HJH. Properties of alkali activated slag-fly ash blends with limestone addition. Cement and Concrete Composite. 2015;59:119-28.

Garcia-Loderio I, Aparicio E, Fernandez A, Palomo A. Effect of calcium on the alkaline activation of aluminosilicate glass. Ceramics International. 2016;42:7697-707.

Garcia-Loderio I, Fernandez A, Blanco MT, Palomo A. FTIR study of the sol-gel synthesis of cementitious gels: C-S-H and N-A-S-H. Journal of Sol-Gel Science and Technology. 2008;45:63-72.

Garcia-Loderio I, Fernandez A, Palomo A, Macphee DE. Effect of calcium additions on N-A-S-H cementitious gels. Journal of the American Ceramic Society. 2010;1-7.

Garcia-Loderio I, Fernandez A, Palomo A. Variation in hybrid cements over time. Alkaline activation of fly ash-portland cement blends. Cement and Concrete Research. 2013;52,112-22.

Garcia-Loderio I, Macphee DE, Palomo A, Fernandez A. Effect of alkalis on fresh C-S-H gels. FTIR analysis. Cement and Concrete Research. 2009;39:147-53.

Garcia-Loderio I, Macphee DE, Palomo A, Fernandez A. Effect on fresh C-S-H gels the simultaneous addition of alkali and aluminium. Cement and Concrete Research. 2010;40:27-32.

Garcia-Loderio I, Palomo A, Fernandez A, Macphee DE. Compatibility studies between N-A-S-H and C-A-S-H gels. Study in the ternary diagram Na_2O-CaO-Al_2O_3-SiO_2-H_2O. Cement and Concrete Research. 2011;41:923-31.

Gartner E. Industrially interesting approaches to low-CO_2 cements. Cement and Concrete Research. 2004;34:1489-98.

Granizo ML, Alonso S, Blanco-Varela MT, Palomo A. Alkaline activation of metakaolin: effect of calcium hydroxide in the products of reaction. Journal of the American Ceramic Society. 2002;85(1):225-31.

Grunewald S. Performance-based design of self-compacting fibre reinforced concrete. Ph.D. Thesis. Delft University of Technology, The Netherlands, 2004.

Glukhovsky VD, Rostovskaja GS, Rumyna GV. High strength slag alkaline cements. In: Proceedings of the seventh international congress on the chemistry of cement. 1980;3:164-8

Guerrieri M, Sanajayan JG. Behavior of combined fly ash/slag-based geopolymers when exposed to high temperatures. Fire and Materials. 2009. 34;163-175.

Hai YZ, Venkatesh Kodur, Shu LQ, Liang C, Bo W. Development of metakaolin-fly ash based geopolymers for fire resistance applications. Construction and Building Materials. 2014;55:38-45.

Hajimohammadi A, Provis JL, Van Deventer JSJ, Time-resolved and spatially resolved infrared spectroscopic observation of seeded nucleation controlling geopolymer gel formation. Journal of Colloid and Interface Science. 2011;357:384-92.

Hakkinen T. The influence of slag content on the microstructure, permeability and mechanical properties of concrete: Part 1. Microstructural studies and basic mechanical properties. Cement and Concrete Research. 1993;23(2),407-21.

Hendriks CA, Worrell E, Jager D, Blok K, Riemer P. Emission reduction of greenhouse gases from the cement industry. In: Proceedings of the 7th international conference on greenhouse gas control technologies, IEA GHG R&D Probram, Vancouver, Canada, 2004.

Hjelmar O, Holm J, Crillesen K. Utilisation of MSWI bottom ash as sub-base in road construction: first results from a large-scale test site. Journal of Hazardous Materials. 2007;139:471-80.

Huiskes DMA, Keulen A, Yu QL, Brouwers HJH. Design and performance evaluation of ultra-lightweight geopolymer concrete. Materials and Design. 2016;89:516-26.
Hunger M. An integral design concept for ecological self-compacting concrete. 2010. PhD Thesis. Eindhoven University of Technology, Eindhoven, the Netherlands.
Hunger M, Entrop AG, Mandilaras I, Brouwers HJH, Founti M. The behavior of a microencapsulated phase change material in concrete. Cement and Concrete Composite. 2009;31:731-43.
Husken G. A multifunctional design approach for sustainable concrete with application to concrete mass products. 2010. PhD Thesis. Eindhoven University of Technology, Eindhoven, the Netherlands.
Husken G, Brouwers HJH. Earth-moist concrete: application of a new mix design concept. Cement and Concrete Research. 2008;38:1246-59.
Iler RK. The Chemistry of Silica: Solubility, Polymeri- zation, Colloid and Surface Properties, and Biochemis- try. John Wiley and Sons, New York, 1979.
Islam A, Alengaram UJ, Jumaat MZ, Bashar II. The development of compressive strength of ground granulated blast furnace slag-palm oil fuel ash-fly ash based geopolymer mortar. Materials and Design. 2014;56:833-41.
Ismail I, Bernal SA, Provis JL, Hamdan S, Van Deventer JSJ. Microstructural changes in alkali activated fly ash/slag geopolymers with sulfate exposure. Materials and Structure. 2013;46:361-73.
Ismail I, Bernal SA, Provis JL, San Nicolas R, Hamdan S, Van Deventer JSJ. Modification of phase evolution in alkali-activated blast furnace slag by the incorporation of fly ash. Cement and Concrete Composite. 2014;45:125-35.
Jang JG, Lee NK, Lee HK. Fresh and hardened properties of alkali-activated fly ash/slag pastes with superplasticizers. Construction and Building Materials. 2014;50:169-176.
Jansson H, Bernin D, Ramser K. Silicate species of water glass and insights for alkali-activated green cement. AIP Advances. 2015;5;067167,1-9.
Jonckbloedt RCL. The dissolution of olivine in acid, a cost effective process for the elimination of waste acids. PhD Thesis, Utrecht University, The Netherlands, 1997.
Juric B, Hanzic L, Ilic R, Samec N. Utilization of municipal solid waste bottom ash and recycled aggregate in concrete. Waste Management. 2006;26:1436-42.
Kakali G, Tsivilis S, Aggeli E, Bati M. Hydration products of C_3A, C_3S and Portland cement in the presence of $CaCO_3$. Cement and Concrete Research. 2000;30:1073-77.
Mackenzie KJD, Meinhold RH, Sherriff BL, Xu Z, ^{27}Al and ^{25}Mg solid-state magic-angle spinning nuclear magnetic resonance study of hydrotalcite and its thermal decomposition sequence. Journal of Materials Chemistry. 1993;3(12):1263-9.
Khmiri A, Chaabouni M, Samet B. Chemical behaviour of ground waste glass when used as partial cement replacement in mortars. Construction and Building Materials. 2013;44:74-80.
Kockal NU, Ozturan T. Strength and elastic properties of structural lightweight concretes. Materials and Design. 2011;32:2396-403.
Kovalchuk G, Fernandez A, Palomo A. Alkali-activated fly ash: Effect of thermal curing conditions on mechanical and microstructural development Part II. Fuel. 2007;86:315-22.
Ko MS, Chen HY, Lyu SJ, Wang TT, Ueng TH. Permeation characteristics and impact factors of geopolymers made of kaolin. Construction and Building Materials. 2015; 93:301-8.

Kralj D. Experimental study of recycling lightweight concrete with aggregates containing expanded glass. Process Safety and Environmental Protection. 2009;87:267-73.
Krizana D, Zivanovic B. Effects of dosage and modulus of water glass on early hydration of alkali slag cements. Cement and Concrete Research. 2002;32:1181-8.
Kumar S, Kumar R, Mehrotra SP. Influence of granulated blast furnace slag on the reaction, structure and properties of fly ash based geopolymer. Journal of Materials Science. 2010;45(3):607-15.
Kuo WT, Lin KL, Chang WC, Luo HL. Effects of nano materials on properties of waterworks sludge ash cement paste. Journal of Industrial and Engineering Chemistry. 2006;12(5):702-9.
Lancellotti I, Ponzoni C, Barbieri L, Leonelli C. Alkali activation processes for incinerator residues management. Waste Management. 2013;33:1740-9.
Larrard F, Sedran T. Mixture-proportioning of high-performance concrete. Cement and Concrete Research. 2002;32:1699-704.
Lazaro A, Brouwers HJH, Quercia G, Geus JW. The properties of amorphous nano-silica synthesized by dissolution of olivine. Chemical Engineering Journal. 2012;211:112-21.
Lazaro A. Nano-silica production at low temperatures from the dissolution of olivine. Ph.D. Thesis. Eindhoven University of Technology, The Netherlands, 2014.
Lazaro A, Quercia G, Brouwers HJH, Geus JW. Synthesis of a green nano-silica material using beneficiated waste dunites and its application in concrete. World Journal of Nano Science and Engineering. 2013;3:41-51.
Lazaro A, Vegas LB, Brouwers HJH, Geus JW, Bastida J. The kinetics of the olivine dissolution under the extreme conditions of nano-silica production. Applied Geochemistry. 2015;52:1-15.
Lee HK, Kim HK, Hwang EA. Utilization of power plant bottom ash as aggregates in fibre-reinforced cellular concrete. Waste Management. 2010;30:274-84.
Lee K, Song J, Gong M, Yang K. Properties and sustainability of alkali-activated slag foamed concrete. Journal of Cleaner Production. 2014;68:226-33.
Lee NK, Jang JG, Lee HK. Shrinkage characteristics of alkali-activated fly ash/slag paste and mortar at early ages. Cement and Concrete Composite. 2014;53:239-48.
Lee NK, Lee HK. Setting and mechanical properties of alkali-activated fly ash/slag concrete manufactured at room temperature. Construction and Building Materials. 2013;47:1201-9.
Lee WKW, Van Deventer JSJ. Use of infrared spectroscopy to study geopolymerization of heterogeneous amorphous aluminosilicates, Langmuir. 2003;19:8726-34.
Le Saout G, Ben Haha M, Winnefeld F, Lothenbach B. Hydration degree of alkali-activated slags: a ^{29}Si NMR study. Journal of the American Ceramic Society. 2011;94:4541-7.
L'Hopital E, Lothenbach B, Le Saout G, Kulik D, Scrivener KL. Incorporation of aluminium in calcium-silicate-hydrates. Cement and Concrete Research. 2015;75,91-103.
Li C, Sun HH, Li LT. A review: The comparison between alkali-activated slag (Si+Ca) and metakaolin (Si+Al) cements. Cement and Concrete Research. 2010;40:1341-9.
Liu X, Chia KS, Zhang MH. Development of lightweight concrete with high resistance to water and chloride-ion penetration. Cement and Concrete Composite. 2010;32:757-66.
Lothenbach B, Le Saout G, Gallucci E, Scrivener K. Influence of limestone on the hydration of Portland cements. Cement and Concrete Research. 2008;38:848-60.

Luciano S, Joao L, Ferreira VM, Dachmir H, Wellington R. Effect of nano-silica on rheology and fresh properties of cement pastes and mortars. Construction and Building Materials. 2009;23:2487-91.

Lu SK, Man QS, Xing SS, Yun XL. Research on several physicomechanical properties of lightweight aggregate concrete. International Journal of Cement composites and Lightweight Concrete. 1980;2:185-91.

Ma Y. Microstructure and engineering properties of alkali activated fly ash. PhD Thesis. Delft University of Technology, Delft, The Netherlands, 2013.

Ma Y, Ye G. The shrinkage of alkali activated fly ash. Cement and Concrete Research. 2015;368:75-82.

Markovic I. High-performance hybrid-fibre concrete development and utilization. Ph.D. Thesis. Delft University of Technology, The Netherlands, 2006.

McLellan BC, Williams RP, Lay J, van Riessen A, Corder GD. Costs and carbon emissions for geopolymer pastes in comparison to ordinary portland cement. Journal of Cleaner Production. 2011;19:1080-90.

Melo AA, Cincotto MA, Repette W. Drying and autogenous shrinkage of pastes and mortars with activated slag cement. Cement and Concrete Research. 2008;38:565-74.

Merwin LH, Sebald A, Rager H, Schneider H. ^{29}Si and ^{27}Al MAS NMR spectroscopy of mullite. Physics and Chemistry of Minerals. 1991;18:47-52.

Mindess S, Francis YJ, Darwin D. Concrete. 2nd ed. NJ (USA): Prentice Hall; 2003.

Mukharjee BB, Barai SV. Assessment of the influence of Nano-Silica on the behavior of mortar using factorial design of experiments. Construction and Building Materials. 2014;68:416-25.

Myers RJ, Bernal SA, San Nicolas R, Provis JL. Generalized structural description of calcium-sodium aluminosilicate hydrate gels: the cross-linked substituted tobermorite model. Langmuir. 2013;29:5294-306.

Nath P, Sarker PK. Effect of GGBFS on setting, workability and early strength properties of fly ash geopolymer concrete cured in ambient condition. Construction and Building Materials. 2014;66:163-71.

NEN 10304-2:1996. Water quality: determination of dissolved anions by liquid chromatography of ions. Part 2: Determination of bromide, chloride, nitrate, nitrite, orthophosphate and sulfate in waste water.

NEN 6966:2005. Environment-analysis of selected elements in water, evaluates and destruates - atomic emission spectrometry with inductively coupled plasma.

NEN 7383:2003. Uitloogkarakteristieken-Bepaling van de cumulatieve uitloging van anorganische componenten uit poeder-en korrelvormige materialen met een vereenvoudigde procedure voor de kolomproef - vaste gronden steenachtige materialen (in Dutch).

Ng TS, Foster SJ. Development of a mix design methodology for high-performance geopolymer mortars. Structural Concrete.2013;14(2):148-56.

Nochaiya T, Wongkeo W, Pimraksa K, Chaipanich A. Microstructural, physical, and thermal analyses of Portland cement-fly ash-calcium hydroxide blended pastes. Journal of Thermal Analysis and Calorimetry. 2010;100:101-8.

NT Build 492. Concrete, mortar and cement-based repair materials: chloride migration coefficient from non-steady-state migration experiments.

Oh JE, Jun YB, Jeong Y. Characterization of geopolymers from compositionally and physically different fly ashes. Cement and Concrete Composite. 2014;50:16-26.

Pacheco F, Miraldo S, Ding Y, Labrincha JA. Targeting HPC with the help of nanoparticles: an overview. Construction and Building Materials. 2013;38:365-7.

Palacios M, Puertas F. Effect of carbonation on alkali-activated slag paste. Journal of the American Ceramic Society. 2006;89(10):3211-21.

Palomo A, Alonso S, Fernandez A. Sobrados A, Sanz J. Alkaline activation of fly ashes: NMR study of the reaction products. Journal of the American Ceramic Society. 2004;87(6):1141-5.

Palomo A, Fernandez A, Lieyda JL. Railway sleepers made of alkali activated fly ash concrete. Revista Ingenieria de Construccion. 2007;22(2):75-80.

Panias D, Vaou V. Thermal insulating foamy geopolymers from perlite. Minerals Engineering. 2010;23:1146-51.

Pardal XL, Brunet F, Charpentier T, Pochard I, Nonat A. ^{27}Al and ^{29}Si solid-state NMR characterization of calcium aluminosilicates hydrate. Inorganic Chemistry. 2012;51:1827-36.

Peng ZH, Vance K, Dakhane A, Marzke R, Neithalath N. Microstructural and ^{29}Si MAS NMR spectroscopic evaluations of alkali cationic effects on fly ash activation. Cement and Concrete Composite. 2015;57:34-43.

Pera J, Husson S, Guilhot B. Influence of finely ground limestone on cement hydration. Cement and Concrete Composite. 1999;21(2):99-105.

Phair JW, Van Deventer JSJ, Smith JD, Mechanism of polysialation in the incorporation of zirconia into fly ash-based geopolymers. Industrial and Engineering Chemistry Research. 2000;39:2925-34.

Phoo T, Chindaprasirt P, Sata V, Hanjitsuwan S, Hatanaka S. The effect of adding nano-SiO_2 and nano-Al_2O_3 on properties of high calcium fly ash geopolymer cured at ambient temperature. Materials and Design. 2014;55:58-65.

Posi P, Teerachanwit C, Tanutong C, Limkamoltip S, Lertnimoolchai S, Sata V, Chindaprasirt P. Lightweight geopolymer concrete containing aggregate from recycle lightweight block. Materials and Design. 2013;52:580-586.

Provis JL, Van Deventer JSJ. Alkali-Activated Materials State-of-the-Art Report, RILEM TC 224-AAM. 2014.

Provis JL, Van Deventer JSJ. Geopolymers: Structure, Processing, Properties and Industrial Applications, Woodhead Publishing Limited, UK, 2009.

Provis JL, Duxson P, Van Deventer JSJ, Lukey GC. The role of mathematical modeling and gel chemistry in advancing geopolymer technology. Chemical Engineering Research & Design. 2005;83:853-60.

Provis JL, Lukey GC, Van Deventer JSJ. Do geopolymers contain nanocrystalline zeolites? A reexamination of existing results. Chemistry of Materials. 2005;17(12):3075-85.

Puertas F, Martinez S, Alonso S, Vazquez E. Alkali-activated fly ash/slag cement. Strength behaviour and hydration products. Cement and Concrete Research. 2000;30:1625-32.

Puertas F, Torres-Carrasco M. Use of glass waste as an activator in the preparation of alkali-activated slag. Mechanical strength and paste characterization. Cement and Concrete Research. 2014;57:95-104.

Puligilla S, Mondal P. Co-existence of aluminosilicate and calcium silicate gel characterized through selective dissolution and FTIR spectral subtraction. Cement and Concrete Research. 2015;70,39-49.

Qing Y, Zenan Z, Deyu K, Rongshen C. Influence of nano-SiO_2 addition on properties of hardened cement paste as compared with silica fume. Construction and Building Materials. 2007;21:539-45.

Quercia G. Application of nanosilica in concrete. 2014. PhD Thesis. Eindhoven University of Technology, Eindhoven, the Netherlands.

Rajaokarivony AZ, Thomassin JH, Baillif P, Touray JC. Experimental hydration of two synthetic glassy blast furnace slags in water and alkaline solutions (NaOH and KOH 0.1 N) at 40 ℃: structure, composition and origin of the hydrated layer. Journal of Materials Science. 1990;25(5):2399-410.

Rangan BV, Hardjto D. Development and properties of low calcium fly ash based geopolymer concrete. Research report GC-1, Faculty of Engineering, Curtins University of Technology, Perth, Australia, 2005.

Rashad AM. A comprehensive overview about the influence of different additives on the properties of alkali-activated slag-A guide for Civil Engineer. Construction and Building Materials. 2013;47:29-55.

Rashad AM, Bai Y, Basheer PAM, Collier NC, Milestone NB. Chemical and mechanical stability of sodium sulfate activated slag after exposure to elevated temperature. Cement and Concrete Research. 2012;42:333-43.

Rashad AM. Properties of alkali-activated fly ash concrete blended with slag. Iranian Journal of Materials Science and Engineering, 2013;10(1):57-64.

Rashad AM, Zeedan SR. The effect of activator concentration on the residual strength of alkali-activated fly ash pastes subjected to thermal load. Construction and Building Materials. 2011;25:3098-107.

Ravikumar D, Neithalath N. Reaction kinetics in sodium silicate powder and liquid activated slag binders evaluated using isothermal calorimetry. Thermochimica Acta. 2012;546:32-43.

Real S, Gomes MG, Rodrigues AM, Bogas JA. Contribution of structural lightweight aggregate concrete to the reduction of thermal bridging effect in buildings. Construction and Building Materials. 2016;121:460-70.

Richardson IG. The calcium silicate hydrates. Cement and Concrete Research. 2008;38:137-58.

Richardson IG. Tobermorite/jennite- and tobermorite/calcium hydroxide-based models for the structure of C-S-H: applicability to hardened pastes of tricalcium silicate, β-dicalcium silicate, Portland cement, and blends of Portland cement with blast-furnace slag, metakaolin, or silica fume. Cement and Concrete Research. 2004;34:1733-77.

Rimer JD, Lobo RF, Vlachos DG. Physical basis for the formation and stability of silica nanoparticles in basic solutions of monovalent cations. Langmuir. 2005;21:8960-71.

Robie RA, Hemingway BS, Takei H. Heat capacities and entropies of Mg_2SiO_4, Mn_2SiO_4, and Co_2SiO_4 between 5 and 380 K, American Mineralogist. 1982;67:470-82.

Rodriguez ED, Bernal SA, Provis JL, Paya J, Monzo JM, Borrachero MV. Effect of nanosilica-based activators on the performance of an alkali-activated fly ash binder. Cement and Concrete Composite. 2013;35:1-11.

Rothstein D, Thomas JJ, Christensen BJ, Jennings HM. Solubility behavior of Ca-,S-, Al-, and Si-bearing solid phases in Portland cement pore solutions as a function of hydration time. Cement and Concrete Research. 2002;32:1663-71.
Rovnanik P, Bayer P, Rovnanikova P. Characterization of alkali activated slag paste after exposure to high temperatures. Construction and Building Materials. 2013;47:1479-87.
Roy DM, Jiang WM, Silsbee MR. Chloride diffusion in ordinary, blended, and alkali-activated cement pastes and its relation to other properties. Cement and Concrete Research. 2000;30:1879-84.
Rozineide A, Santa AB, Soares C, Riella HG. Geopolymers with a high percentage of bottom ash for solidification/immobilization of different toxic metals. Journal of Hazardous Materials. 2016;318:145-153.
Sahmaran M, Yaman IO. Hybrid fiber reinforced self-compacting concrete with a high-volume coarse fly ash. Construction and Building Materials. 2007;21:150-6.
Said A, Zeidan M, Bassuoni M, Tian Y. Properties of concrete incorporating nano-silica. Construction and Building Materials. 2012;36:838-44.
Sengul O, Azizi S, Karaosmanoglu F, Tasdemir MA. Effect of expanded perlite on the mechanical properties and thermal conductivity of lightweight concrete. Energy and Buildings. 2011;43:671-76.
Schilling PJ, Butler LG, Roy A, Eaton AH. ^{29}Si and ^{27}Al MAS-NMR of NaOH activated blast-furnace slag. Journal of the American Ceramic Society. 1994;77(9):2363-8.
Shaikh FUA, Supit SWM, Sarker PK. A study on the effect of nano silica on compressive strength of high volume fly ash mortars and concretes. Materials and Design. 2014;60:433-42.
Shen WG, Wang YH, Zhang T, Zhou MK, Li JS, Cui XY. Magnesia modification of alkali-activated slag fly ash cement. Journal of Wuhan University of Technology-Mater. Sci. Ed. 2011:121-5.
Shi CJ, Day RL. A calorimetric study of early hydration of alkali-slag cements. Cement and Concrete Research. 1995;25:1333-46.
Shi CJ, Day RL. Early strength development and hydration of alkali-activated blast furnace slag/fly ash blends. Advances in Cement Research. 1999;11(4):189-96.
Shi CJ, Fernandez A, Palomo A. New cements for the 21st century: The pursuit of an alternative to Portland cement. Cement and Concrete Research. 2011;41:750-763.
Shi CJ, Krivenko PV, Roy D. Alkali-activated cements and concretes. USA and Canada: Taylor and Francis; 2006.
Shi CJ, Xie P. Interface between cement paste and quartz sand in alkali activated slag mortars. Cement and Concrete Research. 1998;28:887-96.
Shi CJ, Zheng K. A review on the use of waste glasses in the production of cement and concrete. Resources Conservation and Recycling. 2007;52:234-247.
Shi CJ. Strength, pore structure and permeability of alkali-activated slag mortars. Cement and Concrete Research. 1996;26:1789-9.
Shih JY, Chang TP, Hsiao TC. Effect of nanosilica on characterization of Portland cement composite. Materials Science and Engineering: A. 2006;424:266-74.
Soil Quality Decree, 2008. https://zoek.officielebekendmakingen.nl/stb-2/.
Song Q, Wang Z, Li J. Environmental performance of municipal solid waste strategies based on LCA method: a case study of Macau. Journal of Cleaner Production. 2013;57:92-100.

Song S, Jennings HM. Pore solution chemistry of alkali-activated ground granulated blast-furnace slag. Cement and Concrete Research. 1999;29:159-70.
Sun GK, Young JF, Kirkpatrick RJ. The role of Al in C-S-H: NMR, XRD, and compositional results for precipitated samples. Cement and Concrete Research. 2006;36(1):18-29.
Sugama T, Brothers LE. Acid resistant cements for geothermal wells: sodium silicate activated slag/fly ash blends. Advances in Cement Research. 2005;17(2):65-75.
Tang P, Florea MVA, Spiesz P, Brouwers HJH. Application of thermally activated municipal solid waste incineration (MWSI) bottom ash fines as binder substitute. Cement and Concrete Composite. 2016;70:194-205.
Taylor HFW. Cement chemistry. London: Thomas Telford; 1997.
Taylor M, Gielen D. Energy efficiency and CO_2 emissions from the global cement industry. Int. Energy Agency; 2006.
Thongsanitgarn P, Wongkeo W, Chaipanich A, Poon CS. Heat of hydration of Portland high-calcium fly ash cement incorporating limestone powder: Effect of limestone particle size. Construction and Building Materials. 2014;66:410-7.
Topcu IB, Canbaz M. Properties of concrete containing waste glass. Cement and Concrete Research. 2004;34:267-74.
Torres-Carrasco M, Puertas F. Waste glass as a precursor in alkaline activation: Chemical process and hydration products. Construction and Building Materials. 2017;139:342-354.
Torres-Carrasco M, Puertas F. Waste glass in the geopolymer preparation, mechanical and microstructural characterization. Journal of Cleaner Production. 2015;90:397-408.
Tsivilis S, Chaniotakisb E, Badogiannis E, Pahoulasa G, Ilias A. A study on the parameters affecting the properties of Portland limestone cements. Cement and Concrete Composite. 1999;21:107-16.
Turner LK, Collins FG, Carbon dioxide equivalent (CO2-e) emissions: a comparison between geopolymer and OPC cement concrete. Construction and Building Materials. 2013;43:125-30.
Tyditat V, Matas T, Cerny R. Effect of w/c and temperature on the early-stage hydration heat development in Prortland-limestone cement. Construction and Building Materials. 2014;50:140-7.
USGS. Mineral commodity summaries, United States Geological Survey, Reston, Virginia, 2017;202.
Vail JG. Soluble Silicates: Their Properties and Uses. 1952; New York, Reinhold.
Van Jaarsveld JGS, Van devnter JSJ, Lukey GC. The effect of composition and temperature on the properties of fly ash- and kaolinite-based geopolymers. Chemical Engineering Journal. 2002;89;63-73.
Van Jaarsveld JGS. The physical and chemical characteristics of fly ash based geopolymers. PhD Thesis, The University of Melbourne; 2000.
Voglis N, Kakali G, Chaniotakis E, Tsivilis S. Portland-limestone cements. Their properties and hydration compared to those of other composite cements. Cement and Concrete Composite. 2005;7:191-6.
Walkley B, et al. Phase evolution of C-(N)-A-S-H/N-A-S-H gel blends investigated via alkali-activation of synthetic calcium aluminosilicate precursors. Cement and Concrete Research. 2016;89:120-135.
Wang HY, Huang WL. A study on the properties of fresh self-consolidating glass concrete (SCGC). Construction and Building Materials. 2010;24:619-24.

Wang SD, Scrivener KL. Hydration products of alkali activated slag cement. Cement and Concrete Research. 1995;25:561-71.
Wang SD, Scrivener KL, Pratt PL. Factors affecting the strength of alkali-activated slag. Cement and Concrete Research. 1994;24(6):1033-43.
Wang SD, Scrivener KL. ^{29}Si and ^{27}Al NMR study of alkali-activated slag. Cement and Concrete Research. 2003;33:769-74.
Weerdt K, Kjellsen KO, Sellevold E, Justnes H. Synergy between fly ash and limestone powder in ternary cements. Cement and Concrete Composite. 2011;33:30-8.
Wiles CC. Municipal solid waste combustion ash: state-of-the-knowledge. Journal of Hazardous Materials. 1996;47:325-44.
Xie TY, Ozbakkaloglu T. Behavior of low-calcium fly and bottom ash-based geopolymer concrete cured at ambient temperature. Ceramics International. 2015;41(4):5945-58.
Xie Z, Xi Y. Use of recycled glass as a raw material in the manufacture of Portland cement. Materials and Structure. 2002;35:510-515.
Xu H, Van Deventer JSJ, The geopolymerisation of alumino-silicate minerals. International Journal of Mineral Processing. 2000;59:247-66.
Xu Y, Jiang L, Xu J, Li Y. Mechanical properties of expanded polystyrene lightweight aggregate concrete and brick. Construction and Building Materials. 2012;27:32-38.
Yang CC, Huang R. Approximate strength of lightweight aggregate using micromechanics method. Advanced Cement Based Materials. 1998;7:133-38.
Yang KH, Song JK, Ashour AF, Lee ET. Properties of cementless mortars activated by sodium silicate. Construction and Building Materials. 2008;22:1981-9.
Yang KH, Song JK, Lee KS, Ashrour AF. Flow and compressive strength of alkali-activated mortars. ACI Materials Journal. 2009;106:50-8.
Yang T, Yao X, Zhang ZH, Wang H. Mechanical property and structure of alkali-activated fly ash and slag blends. Journal of Sustainable Cement-Based Materials 2012;1:167-78.
Yang X, Zhu W, Yang Q. The viscosity properties of sodium silicate solutions. Journal of Solution Chemistry. 2008;37:73-83.
Yazici S, Inan G, Tabak V. Effect of aspect ratio and volume fraction of steel fiber on the mechanical properties of SFRC. Construction and Building Materials. 2007;21:1250-3.
Ye Q, Zhang ZA, Kong DY, Chen RS. Influence of nano-SiO_2 addition on properties of hardened cement paste as compared with silica fume. Construction and Building Materials. 2007;21:539-45.
Yilmaz B, Olgun A. Studies on cement and mortar containing low-calcium fly ash, and limestone. Cement and Concrete Composite. 2008;30(3):194-201.
Yip CK, Lukey GC, Van Deventer JSJ. The coexistence of geopolymeric gel and calcium silicate hydrate at the early stage of alkaline activation. Cement and Concrete Research. 2005;35:1688-97.
Yip CK, Provis JL, Lukey GC, Van Deventer JSJ. Carbonate mineral addition to metakaolin-based geopolymers. Cement and Concrete Composite. 2008;30(3):979-85.
Yousuf M, Mollah A, Hess TR, Tsai YN, Cocke DL. An FTIR and XPS Investigations of the effects of carbonation on the solidification/stabilization of cement based systems-portland type V with zinc. Cement and Concrete Research. 1993;23(4):773-84.
Yu P, Kirkpatrick RJ, Poe B, McMillan PF, Cong X. Structure of calcium silicate hydrate (C-S-H): near-, mid-, and far-infrared spectroscopy. Journal of the American Ceramic Society. 1999;82(3):742-8.

Yu R, Spiesz P, Brouwers HJH. Mix design and properties assessment of Ultra-High Performance Fibre Reinforced Concrete (UHPFRC). Cement and Concrete Research. 2014;56:29-39.
Yu R, Spiesz P, Brouwers HJH. Static properties and impact resistance of a green Ultra-High Performance Hybrid Fibre Reinforced Concrete (UHPHFRC): Experiments and modeling. Construction and Building Materials. 2014;68:158-71.
Yu QL, Brouwers HJH. Development of a self-compacting gypsum-based lightweight composite. Cement and Concrete Composite. 2012;34:1033-43.
Yu QL. Brouwers HJH. Microstructure and mechanical properties of β-hemihydrate produced gypsum: An insight from its hydration process. Construction and Building Materials. 2011; 25:3149-57.
Yu QL. Design of environmentally friendly calcium sulfate-based building materials, Ph.D. Thesis, Eindhoven University of Technology, The Netherlands, 2010.
Yu QL, Spiesz P, Brouwers HJH. Ultra-lightweight concrete: conceptual design and performance evaluation. Cement and Concrete Composite. 2015;61:18-28.
Zajac M, Rossberg A, Le Saout G, Lothenbach B. Influence of limestone and anhydrite on the hydration of Portland cements. Cement and Concrete Composite. 2014;46:99-108.
Zehner P, Schlunder EU. Thermal conductivity of granular materials at moderate temperatures. Chemie Ingenieur Technik. 1970;42:933-41.
Zhang DJ, Liu WS, Hou HB, He XH. Strength, leach ability and microstructure characterization of Na_2SiO_3-activated ground granulated blast-furnace slag solidified MSWI fly ash. Waste Management and Research. 2007;25:402-7.
Zhang MH, Islam J, Peethamparan S. Use of nano-silica to increase early strength and reduce setting time of concretes with high volumes of slag. Cement and Concrete Composite. 2012;34:650-62.
Zhang ZH, Wang H, Provis JL, Bullen F, Reid A, Zhu YC. Quantitative kinetic and structural analysis of geopolymers. Part 1. The activation of metakaolin with sodium hydroxide. Thermochimica Acta. 2012;539:23-33.
Zivica V. Effectiveness of new silica fume alkali activator. Cement and Concrete Composite. 2006;28:21-5.

List of symbols and abbreviations

Abbreviations

AAM	Alkali Activated Materials
BA	Bottom Ash
DSC	Differential Scanning Calorimetry
DTG	Differential Thermal Gravimetric
EDX	Energy-dispersive X-ray spectroscopy
FA	Fly Ash
FTIR	Fourier Transform Infrared Spectroscopy
GGBS	Granulated Ground Blast furnace Slag
GP	Glass Powder
IC	Isothermal Calorimeter
ICP	Inductively Coupled Plasma
ITZ	Interfacial Transition Zone
LCA	Life Cycle Analysis
LSM	Least Squares Method
LWA	Light Weight Aggregates
MAS	Magic Angle Spinning
MCL	Mean Chain Length
MSWI	Municipal Solid Waste Incineration
NMR	Nuclear Magnetic Resonance
NS	Nano Silica
NVG	Niet Vorm Gegeven (in Dutch)
PSD	Particle Size Distribution
OES	Optical Emission Spectrometry
OPC	Ordinary Portland Cement
RD	Reaction Degree
RH	Relative Humidity
RSS	Sum of the Squares of the Residuals
SCM	Supplementary Cementitious Material
SEM	Scanning Electron Microscope
SF	Silica Fume
TEM	Transmission Electron Microscopy
TG	Thermal Gravimetric
WG	Water Glass
XRD	X-ray Diffraction
XRF	X-ray Fluorescence

Symbols

D	Particle size
d	Diameter
L_i	Effective initial length of the sample
L_n	Length at a certain testing age
L_o	Initial length
Me	Alkali ions
Ms	Activator modulus
M_d	Mass of oven dried sample
M_s	Mass of saturated sample in surface-dry condition in air
M_w	Mass of water-saturated sample in water
max	Maximum
min	Minimum
NO_x	Nitric oxide and nitrogen dioxide
$Si_{(Or)}$	Si from the starting material
$Si_{(Un)}$	Si from the unreacted material
$Si_{(Res)}$	Si from the residuals after selective dissolution
$Si_{(Ac)}$	Si from the activator

Summary

Alkali activated slag-fly ash binders: design, modeling and application

This thesis addresses the design of ambient temperature cured alkali activated slag-fly ash composites, including the determination of key manufacturing factors in the blended systems; modification of the binding materials by nano-silica and limestone powder, modifying the activators by using an alternative silica; assessment of reusing solid wastes (bottom ash, granite powder, glass powder) in alkali activated binder; mechanism study and modeling of the reaction process by using NMR; application of alkali activated materials in steel fiber reinforced high performance products and lightweight functional products.

Fundamental research on the starting materials is carried out in the first place. Then the effect of slag/fly ash ratios and activator modulus on early age reaction, mechanical properties, T-O bond and thermal characters of the blended pastes are analyzed in detail, providing guide information for the binder design. Afterwards, two additives are used to modify the binders, one is nano-silica for the purpose of performance improvement; another one is limestone powder in order to achieve enhanced sustainability. Their effects on fresh behaviors, mechanical property, porosity and potential chemical effect on reaction process/products are discussed in depth. Modification is also carried out on the activator, aiming at developing an activator with reduced environmental impacts. A green olivine nano-silica is used as alternative silica, comprehensive comparison is performed between the alternative activator and waterglass based one, discussed issues include gel characteristics, engineering properties and environmental issues like costs, energy and carbon footprint. Using industrial wastes shows advantages in sustainable development. Incorporating incinerated bottom ash results in reduced the treating costs; the reuse of granite powder makes full use of local waste and avoids landfilling; and the utilization of waste glass powder provides another option for the supplementary binding materials.

In order to acquire a deep insight on the reaction degree and gel composition of the blended binder, ^{29}Si, ^{27}Al NMR together with selective dissolution are investigated. By using these combined analysis method, the effect of activator and binder composition on the Si related gel structure can be quantified. Subsequently Ca-Si-Mg-Al related phase changes are modeled based on the NMR quantification results, which provide additional information on the gel interaction of blended binder. At the final stage, two practical application studies are carried out. One is the fiber reinforced alkali activated materials for high performance applications, another one is lightweight composites for functional properties. Key performances related to application in each compsite are identified and discussed in detail.

List of publications

Peer-reviewed Journals

1. **X. Gao**, Q.L. Yu, A. Lazaro, H.J.H. Brouwers. Investigation on a green olivine nano-silica source based activator in alkali activated slag-fly ash blends: reaction kinetics, gel structure and carbon footprint. *Cement and Concrete Research*. 2017; 100:129-39.
2. **X. Gao**, B. Yuan, Q.L. Yu, H.J.H. Brouwers. Applying waste incineration bottom ash and waste granite powder in alkali activated slag: micro-scale characterization, leaching behavior and carbon footprint. *Journal of Cleaner Production*. 2017; 164:410-19.
3. **X. Gao**, Q.L. Yu, R. Yu, H.J.H. Brouwers. Evaluation of hybrid steel fiber reinforcement in high performance geopolymer composites. *Materials and Structures*. 2017; 50:165.
4. **X. Gao**, Q.L. Yu, H.J.H. Brouwers. Apply ^{29}Si, ^{27}Al MAS NMR and selective dissolution in identifying the reaction degree of alkali activated slag-fly ash composites. *Ceramics International*. 2017; 43:12408-19.
5. **X. Gao,** Q.L. Yu, A. Lazaro, H.J.H. Brouwers. Evaluating an eco-olivine nano-silica as alternative silica source in alkali activated composites. *Journal of Materials in Civil Engineering*. (Accepted)
6. **X. Gao**, Q.L. Yu, H.J.H. Brouwers. Assessing the porosity and shrinkage of alkali activated slag-fly ash composites designed applying a packing model. *Construction and Building Materials*. 2016; 119:175-184.
7. **X. Gao**, Q.L. Yu, H.J.H. Brouwers. Properties of alkali activated slag-fly ash blends with limestone addition. *Cement and Concrete Composites*. 2015; 59:119-128.
8. **X. Gao**, Q.L. Yu, H.J.H. Brouwers. Characterization of alkali activated slag-fly ash blends containing nano-silica. *Construction and Building Materials*. 2015; 98:397-406.
9. **X. Gao**, Q.L. Yu, H.J.H. Brouwers. Reaction kinetics, gel character and strength of ambient temperature cured alkali activated slag-fly ash blends. *Construction and Building Materials*. 2015; 80:105-115.
10. **X. Gao**, Q.L. Yu, H.J.H. Brouwers. Phase evolution of alkali activated slag, fly ash and their blends under autoclaved conditions. *Cement and Concrete Composite*. (Under review)
11. **X. Gao,** Q.L. Yu, J.T. van den Heuvel, H.J.H. Brouwers. Evaluation of an eco silica source based alkali activated lightweight composites. (In preparation)
12. **X. Gao**, Q.L. Yu, H.J.H. Brouwers. A comparison study on the role of waste glass powder and silica fume in Portland cement and alkali activated systems. (In preparation).

Conference proceedings

1. **X. Gao**, Q.L. Yu, R. Yu, H.J.H. Brouwers, Z.H. Shui. Investigation on the effect of slag and limestone powder addition in alkali activated metakaolin. Proceedings of the International Conference of Non-Traditional Cement and Concrete (NTCC2014), June 16-19, 2014, Brno, Czech Republic (pp. 21-26).
2. **X. Gao**, Q.L. Yu, H.J.H. Brouwers. Properties of alkali activated slag-fly ash blends with limestone addition. 19th Internationale Baustofftagung, Tagungsbericht / IBAUSIL, September 16-18, 2015, Weimar, Germany (pp. 771-779).
3. **X. Gao**, Q.L. Yu, R. Yu, H.J.H. Brouwers. Properties of hybrid steel fiber reinforced alkali activated slag-fly ash composites. Proceedings of the 9th international concrete conference, July 4-6, 2016, Dundee, Scotland, UK (pp. 625-634).
4. **X. Gao**, Q.L. Yu, H.J.H. Brouwers. Development of alkali activated slag-fly ash mortars: mix design and performance assessment. Proceedings of the 4th International Conference on Sustainable Construction Materials and Technologies (SCMT4), August 7-11, 2016, Las Vegas, Nevada, USA (pp 423-431).
5. **X. Gao**, Q.L. Yu, A. Lazaro, H.J.H. Brouwers. Application of an alternative nano-silica based activator in alkali activated materials. Proceedings of the 4th International Conference of Non-Traditional Cement and Concrete, June 19-22, 2017, Brno, Czech. (pp. 126-131).

Curriculum Vitae

Xu Gao was born on 10th March, 1988 in Wuhan, Hubei Province, China. After finishing high school education in ShuiGuoHu high school in 2006, Wuhan, he started to study at Wuhan University of Technology (WHUT) in Wuhan, China. In June 2010 he graduated and received his bachelor degree in major of material science, with graduate project about modifying the proton exchange membrane of lithium ion battery. Then he continued his graduate study at WHUT and received his Master of Science degree about silicate based materials in June 2013, and his research topic was metakaolin based geopolymers. From October 2013 he started a PhD project under the supervision of prof.dr.ir. H.J.H. Brouwers and dr. QingLiang Yu. The study was supported by China Scholarship Council and the department of Build Environment in Eindhoven University of technology, the Netherlands. His research interests include the development alkali activated materials, lightweight concrete, high performance concrete and the reuse of industrial wastes. During his spare time, he likes to hang out with friends dinning and shopping, he also likes having party and playing texas holden poker.

Alkali activated slag-fly ash blends are investigated. Determination of key manufacturing factors provides guide information for further designs; modifications of the binder and the activator are achieved by using green nano-silica and limestone powder, resulting in further reduced environmental impacts such as overall costs, energy consumption and carbon footprint. Suitability of reusing solid wastes like incinerated bottom ash, waste glass and glass powder is evaluated. Mechanism study and modeling of the reaction process are also addressed. Eventually, high performance and lightweight functional products are designed and applied.

F A C

B W K

E H T

/ Department of the Built Environment

TU/e Technische Universiteit Eindhoven University of Technology